



HAL
open science

Protection, Fault Location and Isolation in Smart Grids

Tran The Hoang

► **To cite this version:**

Tran The Hoang. Protection, Fault Location and Isolation in Smart Grids. Electric power. Université Grenoble Alpes [2020-..], 2020. English. NNT : 2020GRALT026 . tel-03065960

HAL Id: tel-03065960

<https://theses.hal.science/tel-03065960>

Submitted on 15 Dec 2020

HAL is a multi-disciplinary open access archive for the deposit and dissemination of scientific research documents, whether they are published or not. The documents may come from teaching and research institutions in France or abroad, or from public or private research centers.

L'archive ouverte pluridisciplinaire **HAL**, est destinée au dépôt et à la diffusion de documents scientifiques de niveau recherche, publiés ou non, émanant des établissements d'enseignement et de recherche français ou étrangers, des laboratoires publics ou privés.

THÈSE

Pour obtenir le grade de

DOCTEUR DE L'UNIVERSITE GRENOBLE ALPES

Spécialité: **GENIE ELECTRIQUE**

Arrêté ministériel: 25 mai 2016

Présentée par

Tran The HOANG

Thèse dirigée par **Yvon BESANGER-MOLERES**, Professeur des
Universités, Grenoble INP, et
Quoc-Tuan TRAN, Professeur, INSTN, CEA/INES

préparée au sein du **Laboratoire de Génie Electrique**
dans l'**École Doctorale Electronique, Electrotechnique,**
Automatique, Traitement de Signal (EEATS)

Protection, Localisation et Isolement de Défauts dans les Réseaux Intelligents

Thèse soutenue publiquement le **23 Juin 2020**,
devant le jury composé de:

Monsieur Bruno FRANÇOIS

Professeur des Universités, École centrale de Lille, Président

Monsieur Mircea EREMI

Professeur, Universitatea Politehnica din București, Rapporteur

Monsieur Marc PETIT

Professeur, CentraleSupélec, Rapporteur

Monsieur Quoc-Tuan TRAN

Professeur, INSTN, CEA/INES, Directeur de thèse

Monsieur Yvon BESANGER-MOLERES

Professeur des Universités, Grenoble INP, Directeur de thèse



In memory of my grandfather and my uncle.

*This thesis is dedicated to all of my family members for their love,
endless support, encouragement & sacrifices.*

CONTENTS

ACRONYMS	xi
ACKNOWLEDGMENT	xiii
ABSTRACT	xv
RESUME	xvii
1 INTRODUCTION	1
1.1 Context, problem statement and research objectives	2
1.2 Grid codes applicable to PV systems	7
1.2.1 Static voltage support requirement	7
1.2.2 Dynamic grid support requirement	8
1.2.3 Frequency control via active power regulation	10
1.3 Thesis contributions	11
1.4 Thesis structure	13
2 MODELING OF DISTRIBUTION NETWORKS WITH PV SYSTEMS	15
2.1 Introduction	17
2.2 Overview of distribution systems	17
2.2.1 LV distribution networks	18
2.2.1.1 Overhead lines and underground cables	18
2.2.1.2 MV/LV distribution transformers	18
2.2.1.3 LV neutral system	18
2.2.2 MV distribution networks	19
2.2.2.1 Urban and rural networks	19
2.2.2.2 HV/MV distribution transformers	20
2.2.2.3 MV neutral systems	20
2.3 Overview of distribution protection	21

2.3.1	LV distribution protection	21
2.3.1.1	Underground-cable networks	21
2.3.1.2	Overhead-line networks	22
2.3.2	MV distribution protection	22
2.3.2.1	Protection against phase faults	23
2.3.2.2	Protection against earth faults	24
2.3.2.3	Time setting	24
2.3.2.4	Other protections	25
2.3.2.5	Recloser application	25
2.4	Studied distribution networks	26
2.4.1	Description of Grid-1	26
2.4.2	Description of Grid-2	27
2.4.3	Description of Grid-3	30
2.5	DIgSILENT PowerFactory	30
2.6	System impedance valuemodeling	31
2.6.1	HV external grid	31
2.6.2	Substation transformer	31
2.6.3	Overhead lines and underground cables	32
2.6.4	Load	32
2.7	PV systems	33
2.7.1	Structural configuration of a PV system	33
2.7.2	PV module equivalent circuit	34
2.7.3	PV array and MPPT algorithm	35
2.7.4	PV model for steady-state studies	36
2.7.5	PV model for transient studies	37
2.7.5.1	Selection of the control scheme	37
2.7.5.2	AC-side dynamic models	39
2.7.5.3	DC-bus dynamics	39
2.7.5.4	Current reference derivation	40
2.7.5.5	Power reference determination	41
2.7.5.6	DC-link voltage control	42
2.7.5.7	PS and NS current controls in dual dq-frame	44
2.7.5.8	Model validation	45
2.8	Battery energy storage system	47

2.8.1	Battery model	47
2.8.2	Frequency controller	48
2.8.3	Active/Reactive power controller	48
2.8.4	Battery charge control	49
2.9	Overview of IEC 61850 standard	49
2.10	Conclusion	50
3	DIRECTIONAL APPROACH FOR DISTRIBUTION NETWORKS WITH HIGH PV PENETRATION	51
3.1	Introduction	53
3.2	State-of-the-art	53
3.2.1	Fundamental operation of a RDIR element	53
3.2.2	Torque-product-based RDIR element	54
3.2.2.1	Phase voltage-based polarization	54
3.2.2.2	Sequence voltage-based polarization	55
3.2.2.3	Sequence current-based polarization	56
3.2.3	Impedance-based directional RDIR element	56
3.2.4	Superimposed component-based RDIR element	56
3.2.5	ANN-based RDIR element	57
3.2.6	Application of directional methods for distribution networks	57
3.3	PV fault characteristics	59
3.3.1	Equivalent sequence circuits of PV systems	60
3.3.2	Evaluation of the angles of PV fault sequence impedances	61
3.3.3	Evaluation of the magnitudes of PV fault sequence impedances	61
3.4	Formulation of the proposed directional algorithm	62
3.5	Evaluation of the proposed RDIR by analytical approach	63
3.5.1	Single-phase-to-ground fault	63
3.5.1.1	Forward fault	64
3.5.1.2	Reverse fault	64
3.5.2	Two-phase fault	65
3.5.2.1	Forward fault	65
3.5.2.2	Reverse fault	66
3.5.3	Two-phase-to-ground fault	66
3.5.3.1	Forward fault	67

3.5.3.2	Reverse fault	67
3.5.4	Conclusion	68
3.5.5	Preliminary numerical calculation	68
3.5.5.1	Component impedance value investigation	68
3.5.5.2	Overall results and conclusion	69
3.6	Evaluation of the proposed algorithm by simulations	70
3.6.1	Single-phase-to-ground fault	70
3.6.1.1	Impacts of fault resistances and PV penetration level	70
3.6.1.2	Impacts of faults closed to RDIR location	74
3.6.1.3	Impacts of load imbalance	74
3.6.1.4	Impacts of external grids	76
3.6.1.5	Impact of variation of solar irradiation	77
3.6.1.6	Overall evaluation considering all affecting factors	78
3.6.2	Two-phase faults	79
3.6.3	Two-phase-to-ground fault	81
3.6.4	Summary evaluation of the proposed method for all kinds of un- balanced fault	82
3.7	Procedure for fault direction determination	83
3.8	Conclusion	85
4	DEVELOPMENT OF DISTRIBUTION PROTECTION SCHEMES WITH HIGH PV PENETRATION	87
4.1	Introduction	88
4.2	State-of-the-art of distribution protection	89
4.2.1	LV microgrid protection	89
4.2.1.1	Protection schemes without communication requirement	89
4.2.1.2	Adaptive protection	90
4.2.1.3	Impedance/Admittance protection	91
4.2.1.4	Protection schemes considering the FRT requirements	91
4.2.1.5	Conclusion	91
4.2.2	MV network protection	92
4.2.2.1	Adaptive protection	92
4.2.2.2	Differential protection	93
4.2.2.3	Multiagent-based protection scheme	94
4.2.2.4	Distance protection	95

4.2.2.5	Conclusion	95
4.3	Proposition of PV FRT-compliant interface protection	95
4.3.1	Voltage-based protection settings	96
4.3.2	Frequency-based protection settings	96
4.4	Protection scheme for LV microgrids	97
4.4.1	Considered LV microgrid	97
4.4.2	Proposition of the developed protection scheme	98
4.4.3	Protection scheme for grid-connected mode	100
4.4.3.1	Lateral protection	100
4.4.3.2	PV protection system	100
4.4.3.3	LV feeder protection	101
4.4.3.4	Secondary transformer protection	102
4.4.3.5	Protection against external faults	102
4.4.4	Protection algorithm for the islanded mode	102
4.4.4.1	Lateral protection	102
4.4.4.2	PV and BESS interface protection	102
4.4.4.3	Feeder protection	103
4.4.5	Case study	103
4.4.5.1	Grid-connected mode	103
4.4.5.2	Islanded mode	110
4.5	Protection scheme for MV networks	113
4.5.1	Proposition of the protection scheme	113
4.5.1.1	MV/LV transformers and the associated LV microgrids	113
4.5.1.2	PV protection	114
4.5.1.3	MV feeder protection	114
4.5.1.4	MV busbar protection	116
4.5.1.5	HV/MV transformer protection	117
4.5.2	Case study	117
4.6	Conclusion	119
5	FAULT LOCATION AND ISOLATION SYSTEM FOR ACTIVE DISTRIBUTION NETWORKS	121
5.1	Introduction	123
5.2	State-of-the-art	124

5.3	Proposition of FLISs for active distribution networks	125
5.4	Proposed ANN-based FLIS	126
5.4.1	Multi-layer perceptron classifier-based artificial neural network . .	126
5.4.2	Data measurement and feature extraction	129
5.4.3	Data set for training and testing the designed ANN	130
5.4.4	Evaluation results	130
5.5	Proposed MAS-based FLIS with IEC 61850-oriented design	130
5.5.1	Multi-agent system	131
5.5.1.1	Definition	131
5.5.1.2	Layer structure in MAS applications	131
5.5.2	Proposed system	132
5.5.3	Functional structure of required FIED and agents	134
5.5.3.1	Required functionalities of FIED	135
5.5.3.2	Required functionalities of the designed agent	136
5.5.4	Operating principle of the proposed scheme	136
5.5.4.1	Normal operation	136
5.5.4.2	Transient faults	136
5.5.4.3	Permanent faults	139
5.5.4.4	Switch failure protection	140
5.5.4.5	Operation of the proposed FLIS in case of no PV generation . .	140
5.5.4.6	Restoration of power to customer downstream the fault location	141
5.6	Validation using cosimulation approach	141
5.6.1	Fundamental of cosimulation method and the proposed system . .	141
5.6.2	Design of MAS for co-simulation system	141
5.6.3	MatrikonOPC server for cosimulation	143
5.6.4	Optimal placement of controlled switches for Grid-1	144
5.6.5	Results and discussion	144
5.6.5.1	Faults on Feeder 1	144
5.6.5.2	Fault on Feeder 2	144
5.6.5.3	Switch failure	144
5.6.6	Conclusion	146
5.7	Validation using CHIL approach	146
5.7.1	Overview of DRTS and CHIL approach in power system domain .	146
5.7.2	Description of the MAS for the CHIL platform	148

5.7.3	CHIL testing platform	149
5.7.3.1	Studied feeder	149
5.7.3.2	Feeder IED and agents	149
5.7.4	Results and discussion	150
5.7.4.1	Evaluation of data exchange	150
5.7.4.2	Evaluation of the proposed scheme	151
5.7.5	Conclusion	152
5.8	Conclusion	153
6	CONCLUSION AND PERSPECTIVE	155
6.1	Conclusion	155
6.2	Perspectives	156
	BIBLIOGRAPHY	176
	APPENDIX A MODEL PARAMETERS	1
	APPENDIX B PV MODELING	3
B.1	Transformation from abc- to dual PS and NS dq-frames	3
B.2	Formulation of PV equivalent sequence circuits	3
B.3	Equations of angles of PV fault sequence impedances	4
B.4	Equations of magnitudes of PV fault sequence impedances	5
	APPENDIX C SIGNAL PROCESSING AND DATA MEASUREMENT	7
C.1	Signal processing	7
C.2	Measurement of criterion values	7
C.3	Measurement of symmetrical sequence quantities	8
	APPENDIX D ANALYSIS OF FAULT CIRCUITS CONTAINING PV SYSTEMS	9
D.1	Superposition principle and superimposed quantities	9
D.2	Equivalent sequence circuits	10
D.2.1	PS equivalent circuit	10
D.2.2	NS equivalent circuit	11
D.2.3	ZS equivalent circuit	11
	APPENDIX E EVALUATION RESULTS OF THE PROPOSED DRIR METHOD	13
E.1	Two-phase fault	13

E.2 Two-phase-to-ground fault	15
APPENDIX F IMPACTS OF HIGH PENETRATION OF DERs ON DISTRIBUTION PROTECTION	19
F.1 Blinding tripping	19
F.2 False tripping	21
F.3 Impacts on reclosing performance	21
F.4 Impacts on coordination between recloser and fuse	22
F.5 Impacts on distance protection	22
F.6 Issues related to low level of PV fault currents	23
F.7 Overvoltage of healthy phases during ground faults	24
F.8 Impacts of inverter-based PV systems on the conventional directional method	24
APPENDIX G LV DISTRIBUTION PROTECTION	27
G.1 Protection configuration for grid-connected mode	27
G.1.1 MCCB time-current curve settings	27
G.1.2 Feeder protection setting thresholds	27
G.1.3 Transformer protection setting thresholds	28
G.1.4 Interface protection setting thresholds	28
G.2 Protection coordination for islanded operation	29
G.2.1 MCCB time current curve settings	29
G.2.2 DER and BESS protection settings	29
G.2.3 Feeder protection setting thresholds	29
G.3 Results for grid-connected mode	30
G.4 Results for islanded mode	34
APPENDIX H MV DISTRIBUTION PROTECTION	39
APPENDIX I OVERVIEW OF THE IEC 61850 STANDARD	45
I.1 General overview of the standard	45
I.2 Data modeling in IEC 61850	46

Acronyms

ANN Artificial Neural Network.

CAIDI Customer Average Interruption Duration Index.

CHIL Controller Hardware-in-the-Loop.

DER Distributed Energy Resource.

FLIS Fault Location and Isolation System.

FRT Fault Ride Through.

GOOSE Generic Objective Oriented Substation Event.

LN Logical Node.

LV Low Voltage.

MAS Multiagent System.

MV Medium Voltage.

NS Negative Sequence.

PS Positive Sequence.

RCS Remotely Controlled Switch.

RDIR Directional Element.

SAIDI System Average Interruption Duration Index.

ZS Zero Sequence.

Acknowledgment

I am deeply indebted to Professor Yvon Besanger and Professor Quoc Tuan Tran for their excellent supervision, brilliant ideas, and positive encouragement. It has been a real privilege to pursue my doctoral research under their supervision. I would also like to extend my deepest gratitude to Professor Tuan for his acceptance of supervision, unwavering guidance, constructive advice, strong motivation, insightful suggestions, and patience that cannot be underestimated. The completion of my dissertation would not have been possible without his support. His extensive expertise in the power system domain and considerable experience in conducting research have been the most valuable thing I received. Professor Tuan is my role model not only in work but also in life. My experiences about the warm dinners at his home as well as his caring about my family and my son will always be in my mind. I am also grateful to Professor Besanger for his relentless support, belief in my abilities, and precious suggestions during the planning, development, and writing of this thesis. His willingness to devote time to me and to contact the people I need was greatly appreciated.

Many thanks to Cédric Boudinet for his valuable experience and practical contributions. He played a decisive role in the implementation of my experimental platforms. Thanks should also go to Dr. Tung Lam Nguyen for his unrelenting assistance, to Dr. Duong Quoc Bao for his effective collaboration, to Professor Stéphane Mocanu for his practical suggestions, to Professor Raphael Caire for his helpful advice, and to the administrative and informative staff of G2Elab for their helpful assistance.

Special thanks to my Vietnamese friends from G2Elab as well as from Grenoble for their friendship, enthusiastic support, and the exciting moments we spent together.

I also gratefully acknowledge the help of all my friends, my colleagues, and other people I probably forgot to mention here.

I would like to recognize the financial support that I received from the Vietnamese

government, the PPinterop and the Ergirid Projects.

I am extremely grateful to my family for supporting me spiritually throughout my studies and my life in general. Mom and dad, thank you for your wholehearted support in caring for my son. My parents-in-law, thank you for your understanding and constant encouragement. My brother, my sister-in-law, and my little sister, a big thank to you for raising my son and your unconditional love for him. My brother, thank you so much for all that you have done for my son and also for me. I know perfectly well that you must put a lot of time and effort into it.

Finally, I would like to express my deepest appreciation to my wife for her love, continuing encouragement, and the other things she has done for me. Special thanks also to my beloved son, who has been a driving motivation for me. The time you spent with me in France will be one of the most memorable moments in my life. Thank you for coming into my life; you are my miracle.

Abstract

In the light of recently approved grid codes, photovoltaic (PV) systems connected to distribution networks in the event of a fault must remain connected and actively support the grid voltage recovery. These requirements have imposed various challenges on not only protection schemes but also Fault Location and Isolation Systems (FLIS) of distribution networks, especially when PV penetration reaches a certain high level. Therefore, the work presented in this thesis focuses on the development of solutions to these issues. This task is approached as follows.

First, the thesis studies all new grid codes applicable to PV systems connected to both medium voltage (MV) and low voltage (LV) networks. Then, a detailed analysis of the control strategy for PV inverters meeting all of the above grid requirements is provided. In addition, the study briefly describes main components, such as load, transformer, battery energy storage system. To evaluate solutions proposed in the thesis, models of three real MV grids, including Grid-1 with three LV microgrids, Grid-2, and Grid-3 are built either in DIgSILENT | PowerFactory or in Matlab | Simulink, depending on the study purposes. Finally, the unconventional fault behavior of PV systems with the designed control method and the impacts of their high integration on distribution protection schemes and FLISs are analyzed and discussed.

From the knowledge of the drawbacks indicated above, there is a proposition of a directional method based on the measurement of prefault voltage and during-fault negative sequence current. Equations describing the proposed method for different fault types are first derived by using circuit theory and then used for numerical analysis. The next step is the evaluation of the proposed method when being applied for Grid-2 by simulations in DIgSILENT | PowerFactory. Results obtained from the simulations indicate that the utilization of these above quantities provides an highly efficient polarization method for detecting fault direction, even for extremely high PV integration.

Afterwards, by using the above directional method, together with other protection principles, the thesis further presents various protection strategies suitable for MV distribution networks with connected LV microgrids. The protection strategies are developed starting from PV interface protection to ensure their fault ride-through capability and requirements for successful islanding of the LV microgrids. Special attention also focuses on the protection elements for primary and backup functions, the coordination between different protection levels, and the need for communication assistance. Additionally, a grid control facility is mentioned to achieve the smooth transition of LV microgrids to the islanded mode in the event of external faults. Indeed, the simulation results of the proposed protection schemes provide evidences of high effectiveness.

Furthermore, two FLISs are constructed. One is founded on an artificial neural network whereas the other relies on a Multi-Agent System (MAS) with an IEC 61850-oriented design. Requiring only a small number of measuring points, the former FLIS allows simple implementation while ensuring high accuracy and low computation time. On the other hand, the latter solution depends on the data exchange between neighboring agents and their ability to make operational decisions locally. A comprehensive description of the agents' structure and their operational logic is offered. To assess the MAS-based FLIS, the thesis offers two different methods. The first is a cosimulation system comprising DIgSILENT | PowerFactory simultaneously coupled with several Python programs via an OPC server. The second is the implementation of a Controller-Hardware-in-the-Loop platform. Various case studies show high effectiveness of the operational coordination and the interoperability between agents. Finally, the evaluation results indicate that the two proposed FLISs correctly identify concerned faulty sections with reduced operation time, improving several system reliability indices, such as SAIDI and CAIDI.

Key words: Protection, fault location, fault isolation, smart grids, renewable energy

Resume

À la lumière des codes de réseau récemment approuvés, les systèmes photovoltaïques (PV) connectés aux réseaux de distribution en cas de panne doivent rester connectés et soutenir activement le rétablissement de la tension du réseau. Ces exigences ont imposé divers défis non seulement aux systèmes de protection, mais aussi aux systèmes de localisation des pannes et d'isolement (FLIS) des réseaux de distribution, en particulier lorsque la pénétration du photovoltaïque atteint un certain niveau élevé. Par conséquent, les travaux présentés dans cette thèse se concentrent sur le développement de solutions à ces problèmes. Cette tâche est abordée de la manière suivante.

Tout d'abord, la thèse étudie tous les nouveaux codes de réseau applicables aux systèmes PV connectés à la fois aux réseaux moyenne tension (MT) et basse tension (BT). Ensuite, une analyse détaillée de la stratégie de contrôle pour les onduleurs PV répondant à toutes les exigences du réseau ci-dessus est fournie. En outre, l'étude décrit brièvement les principaux composants, tels que la charge, le transformateur, le système de stockage d'énergie par batterie. Pour évaluer les solutions proposées dans la thèse, des modèles de trois réseaux MT réels, dont le Grid-1 avec trois micro-réseaux BT, le Grid-2 et le Grid-3 sont construits soit dans DIgSILENT | PowerFactory soit dans Matlab | Simulink, selon les objectifs de l'étude. Enfin, le comportement non conventionnel des systèmes PV en cas de défaut avec la méthode de contrôle conçue et les impacts de leur intégration élevée sur les schémas de protection de la distribution et les FLIS sont analysés et discutés.

À partir de la connaissance des inconvénients indiqués ci-dessus, il est proposé une méthode directionnelle basée sur la mesure de la tension avant défaut et du courant de séquence négative en cas de défaut durable. Les équations décrivant la méthode proposée pour différents types de défauts sont d'abord dérivées en utilisant la théorie des circuits, puis utilisées pour l'analyse numérique. L'étape suivante consiste à évaluer la méthode proposée lorsqu'elle est appliquée au réseau 2 par des simulations dans PowerFactory. Les résultats obtenus à partir des simulations indiquent que l'utilisation des quantités susmentionnées fournit une méthode de polarisation très efficace pour détecter

la direction des défauts, même pour une intégration PV extrêmement élevée.

Ensuite, en utilisant la méthode directionnelle ci-dessus, ainsi que d'autres principes de protection, la thèse présente en outre diverses stratégies de protection adaptées aux réseaux de distribution MT avec des micro-réseaux BT connectés. Les stratégies de protection sont développées à partir de la protection de l'interface PV pour assurer leur capacité à surmonter les défauts et les exigences pour un îlotage réussi des micro-réseaux BT. Une attention particulière est également accordée aux éléments de protection des fonctions primaires et de secours, à la coordination entre les différents niveaux de protection et à la nécessité d'une assistance en matière de communication. En outre, une installation de contrôle du réseau est mentionnée pour assurer la transition en douceur des micro-réseaux BT vers le mode îloté en cas de défaillances externes. En effet, les résultats de simulation des schémas de protection proposés attestent d'une grande efficacité.

En outre, deux FLIS sont construits. L'un est fondé sur un réseau neuronal artificiel, tandis que l'autre repose sur un système multi-agent (MAS) dont la conception est orientée vers la norme CEI 61850. Ne nécessitant qu'un petit nombre de points de mesure, l'ancien FLIS permet une mise en œuvre simple tout en garantissant une grande précision et un faible temps de calcul. En revanche, la seconde solution dépend de l'échange de données entre agents voisins et de leur capacité à prendre des décisions opérationnelles au niveau local. Une description complète de la structure des agents et de leur logique opérationnelle est proposée. Pour évaluer le FLIS basé sur MAS, la thèse propose deux méthodes différentes. La première est un système de cosimulation comprenant PowerFactory simultanément couplé à plusieurs programmes Python via un serveur OPC. La seconde est la mise en œuvre d'une plate-forme de type Controller-Hardware-in-the-Loop. Diverses études de cas montrent une grande efficacité de la coordination opérationnelle et de l'interopérabilité entre les agents. Enfin, les résultats de l'évaluation indiquent que les deux FLIS proposés identifient correctement les sections défectueuses avec un temps de fonctionnement réduit, ce qui entraîne l'amélioration de plusieurs indices de fiabilité du système, tels que SAIDI et CAIDI.

Mots clés: Protection, localisation de défauts, isolement des défauts, énergie renouvelable, réseaux intelligents.

Chapter 1

Introduction

Contents

1.1	Context, problem statement and research objectives	2
1.2	Grid codes applicable to PV systems	7
1.2.1	Static voltage support requirement	7
1.2.2	Dynamic grid support requirement	8
1.2.3	Frequency control via active power regulation	10
1.3	Thesis contributions	11
1.4	Thesis structure	13

1.1 Context, problem statement and research objectives

The history of the power system dates back to the end of the 19th century, when the first complete DC power system was built by Thomas Edison in September 1882. This network consisted of a DC generator supplying electricity to 59 households [1]. However, with the invention of the transformer and AC transmission by L. Gaulard and J.D. Gibbs in Paris, the AC system had dominated the DC system. The first complete three-phase AC electrical network came into service in 1893. It was a simple, small-scale system with a few generators and loads located in a small geographical area. In parallel with economic and population growth in many countries, electricity production worldwide has increased significantly, as shown in Figures 1.1a, [2]. This figure shows that global electricity production at the end of 2017 was three times higher than in 1980.

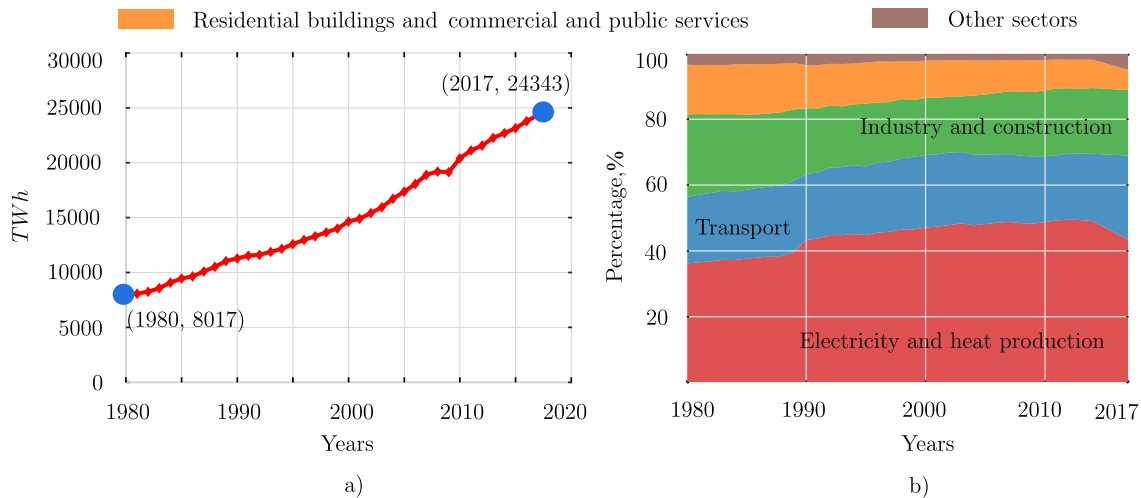


Figure 1.1 – (a) Global electricity production, and (b) Carbon dioxide emissions by sectors

To meet such a high demand for energy, it was necessary to build a large, centralized power generation facility. Some countries have successfully operated a variety of giant power generation complexes with nominal capacities in multiples of tens of *GW*. High electricity consumption would result in high greenhouse gas emissions, as sizeable centralized power plants typically operate with polluting primary energy sources such as fossil fuels, except for nuclear and hydroelectric plants. Several studies, such as [3], have indicated that electricity and heat production are responsible for the highest emissions of greenhouse gases (Figure 1.1b), accounting for up to half of global emissions.

As a result, many countries have targeted their efforts on climate change mitigation. The Kyoto Protocol, in 1998, was the first international agreement to facilitate the reduction of greenhouse gas emissions. This attempt and other subsequent negotiations, including the *COP25* negotiation in Paris in 2015, put increased pressure on the governments of many countries to introduce new energy policies aimed at reducing their level of dependence on fossil fuels such as coal for power generation. Many solutions have been proposed, and some are at the research stage. Among the others, the development of renewable energies is considered to be the highest priority. Renewable sources can

include different types of energy, such as low-impact hydropower, wind power, solar power, and other minor energy sources such as biofuels, tidal, geothermal, wave power, and so on. These renewable sources, which are normally small in size, can be categorized in **Distributed Energy Resource (DER)** group. [4, 5]. In other words, **DER** can be defined as the production of electricity that takes place at or near customer locations to meet their energy demand. **DER** can range from a few *kW* to tens of *MW*. **DER** technologies can be based on fossil fuels, renewable sources, and waste heat.

The installation of **DERs** can offer various advantages. By increasing the integration of **DERs**, nations can address their carbon emissions, achieving sustainability goals for long-term socio-economic development. In addition, in some countries with limited capacity or natural resources, generating electricity from renewable energy can reduce their dependence on imported fuels. Technically, the efficient use of renewable energy can help local utilities to diversify energy supply, reduce congestion on high-load transmission lines during peak hours, provide several ancillary services such as frequency and voltage control, and reduce transmission and distribution losses. In addition, the construction of **DER**-based generating units can provide a redundant reserve for critical loads during outages. The ability to peak shaving during the high tariff period is also a decisive advantage of **DERs**.

On the other hand, compared with other **DER**, inverter-interfaced PV systems that are based on solar energy and wind turbines that lie on wind energy have achieved more significant technological advancements and cost reduction. The future dominance of solar and wind energy is a clear trend in the total share of global electricity generation. It is predicted that 40% of electricity generation will come from wind and solar power combined with low-impact hydro-power and other energy sources by 2040, almost double the 21% share in 2017. The increase in the cumulative capacity of PV systems and wind turbines in recent years can be seen in Figure 1.2a, [6]. Globally, the cumulative capacity of wind turbines reached 656 *GW* in 2019, about 14 times more than in 2004. The cumulative PV capacity even shows a more remarkable rise of 174 times over the same period, from only 3.7 *GW* in 2004 to about 647 *GW* in 2019. It is worth mentioning that although wind energy has dominated solar energy in the last period, the overall cumulative PV capacity is expected to exceed that of wind turbines in 2020 with 789 *GW* and 782 *GW*, respectively.

Furthermore, unlike wind turbines, which are mainly installed on High Voltage (HV) transmission grids, the majority of PV systems are interfaced with **Medium Voltage (MV)** and **Low Voltage (LV)** distribution grids. For example, the data provided by [7, 8] indicate that, at the end of 2015, about 94% of the cumulative installed PV capacity in Germany was connected to the **LV** and **MV** grids (Figure 1.2b). Distribution System Operators (DSO) have historically planned and operated their networks passively with less investment and application of advanced intelligent technologies compared to transmission networks. As a result, DSOs may find it more difficult to work on the integration of **DERs** in general, and PV systems in particular, and on quality of service compared to Transmission System Operators (TSO). Therefore, the study only aims to consider in detail the **DER** technology that relies on solar energy, i.e., inverter-based PV systems. Wind energy,

whose generating units are connected to the distribution networks via power electronic inverters, is also considered.

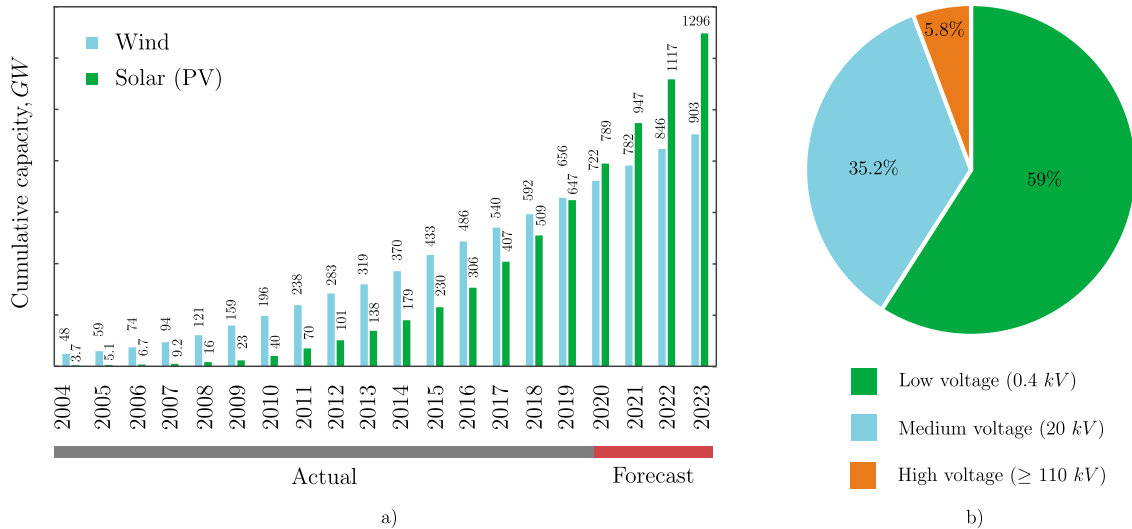


Figure 1.2 – (a) Global cumulative capacity of wind turbines and solar PV systems, and (b) Distribution of PV capacity across voltage levels in Germany by 2015

Over the last decade, many standards, such as those described in [9, 10, 11], have suggested that PV inverters should not actively regulate the voltage at their Points of Common Coupling (PCC). Moreover, these grid codes have required the connected PV systems to operate at a power factor at least greater than 0.9 under the control of the Maximum Power Point Tracking (MPPT) system to extract as much energy as possible from the PV panels [12, 13]. As a result, these systems have been primarily operated as active power sources without reactive power capability. At the same time, PV systems had to disconnect from the grid when faults were detected in the grids [9, 10, 11]. These requirements were valid when the penetration level of PV systems was low.

Nevertheless, due to the rapid reduction in the price of photovoltaic cells and advances in power electronics technology, the penetration of photovoltaic systems into the MV and LV grids can reach such a level that it can lead to a violation of grid integration [14, 15, 16]. One of these problems is the potential overload or overvoltage that can be observed in both MV and LV feeders, especially when a very large part of the PV systems is realized, due to the intermittent solar radiation and the resulting imbalance between PV generation and load consumption [17, 18, 19]. Thus, several suggestions were put forward. A solution has been proposed in [20] where the maximum power extracted from PV systems should be limited. However, this solution runs counter to the policies on the reduction in greenhouse gas emissions supported by most governments around the world. As a result, many countries have proposed specific grid codes for integrated PV systems to participate in steady-state voltage regulation through reactive power control. Specifically, connected PV systems should be able to inject or absorb reactive power to control voltage locally. This functional capability is called static voltage support or voltage var control and recently mentioned in various studies, [21, 22, 23, 24].

Another problem is that the disconnection of a large number of PV systems by the operation of the anti-islanding protection can lead to more serious events, such as a large-scale power outage. For example, IEEE 1547, UL 1741 or VDE-AR-N 4105 required all PV systems in LV networks to disconnect within 0.2 s if the voltage at their Points of Common Coupling (PCC) falls below 0.8 p.u [9, 10, 11]. If this requirement is met, faults on transmission systems, which can lead to widespread voltage drops, would present serious risks to the post-fault active power balance. In particular, the disconnection of PV systems following the transmission faults can create an additional voltage drop within the MV and LV grids, which would cause more PV systems to be dropped out. Therefore, in response to grid violations, PV systems must remain connected in terms of Fault Ride Through (FRT) and simultaneously support the grid voltage during the faults in terms of dynamic grid support by injecting reactive power, [21, 22, 23, 24, 25, 26, 27]. This new capability of PV systems can stabilize the grid in case of faults and prevent the large-scale disconnection of PV systems. In addition, the new grid codes also require the PV systems to offer other advanced functional capabilities, including frequency control, power quality control, remote demand response, and communication with intelligent inverters [27]. However, these new functional capability of the PV systems, especially the dynamic voltage support capability, has made the fault contribution of PV systems unneglectable. Moreover, their fault behaviors have changed due to the reactive power injection during faults. Many potential problems caused by the high PV integration have been reported in [28, 29, 30, 31, 32]. Most of these problems are mainly related to radial distribution networks, and their extent depends on the penetration and size of the PV systems.

First, the PV systems in distribution networks are installed along the MV and LV feeders. As a result, fault currents sensed by the distribution protective devices, such as feeder relays, become bidirectional since they are fed by both the external grids and the downstream connected PV systems. When the fault currents injected by the PV systems reach a high level, they may cause several problems for the distribution protections, such as false or sympathetic tripping. In addition, the coordination between the recloser and the fuse is also affected since the PV systems can remain connected to feed the fault even when the feeder CB is open. Details of these impacts are investigated in Appendix F. Besides, the current Fault Location and Isolation System (FLIS)s that are mainly based on non-directional fault indicators should be revised due to the effects of bidirectional fault currents. If no appropriate action is considered, system reliability indices such as System Average Interruption Duration Index (SAIDI), Customer Average Interruption Duration Index (CAIDI) obviously deteriorate.

Next, for dealing with the false tripping issue, one may suggest supplementing the conventional overcurrent protections with Directional Element (RDIR). The operating principle of the commercially digital directional relays is mainly based on the phase displacement between the measured fault currents and voltages. These operating quantities are primarily imposed by synchronous machines. Therefore, for these RDIR elements to properly operate when being applied for distribution networks with high PV penetration, the fault currents and voltages should be similar to those of conventional synchronous machines. However, the amplitude and waveform of PV fault currents may be different.

According to the most recent studies, the fault behaviors of inverter-based PV systems are mainly determined by their control schemes [33, 34]. Hence, these sources act as current-controlled voltage sources under fault conditions rather than as voltage sources as synchronous machines usually do. Unconventional characteristics and the wide variety of fault signals can cause malfunction to the existing directional relays. These impacts are demonstrated in Appendix F.8.

Further, one increasing trend in the smart grid research is that small networks consisting of DERs and loads are encouraged to be designed and operated in a deliberate and controlled manner to maximize the benefits of DERs and reduce the technical issues associated with their high penetration. Such sub-networks are referred to as “LV microgrids”, which were first proposed in [35]. These LV microgrids must be able to operate properly in both modes of operation, including grid-connected and islanded operation modes. However, in LV microgrids with high penetration of inverter-based PV systems, their protection systems may suffer from low fault current levels when the microgrids are operated in islanded mode. In fact, the fault currents contributed by the PV systems are limited due to the thermal withstanding limit of their electronic inverters, e.g., only about 1.2 times the inverter rated currents [33]. Therefore, in the islanded mode, the short-circuit capacity of the microgrids with high PV penetration can be considerably lower than that of a conventional grid with synchronous generators of the same power. The overcurrent relays applied may not be sensitive enough to detect this fault condition. The problem may be aggravated by the PV intermittent nature.

Finally, the slow operation of the overcurrent-based protection schemes presently being used in distribution networks cannot guarantee the FRT requirements of the connected PV systems. For instance, in France, faults on MV feeders in urban networks are only eliminated after 0.5 s [36]. Such long time delay may cause the PV systems connected to adjacent healthy feeders to be tripped unnecessarily. Another problem is that, the current fuse-based protection schemes of the LV microgrids cannot ensure their successful islanding in the case of an external fault because the fault currents contributed by PV systems installed inside the concerned microgrid are not large enough.

Hence, we can conclude that the increased integration of PV systems in the MV and LV distribution networks has profoundly influenced their protection systems as well as their Fault Location and Isolation System (FLIS). A entire revision of the traditional philosophy of distribution protection, which was supposed to operate in a radial configuration with unidirectional power flow, [28, 37] is required. The question of how to integrate PV systems into distribution networks without impacting their protection systems and FLIS is one of the main directions of smart grid research. Therefore, the objectives of the thesis are the following:

- 1 To review all new grid code requirements imposed by countries worldwide;
- 2 To comprehensively investigate the impacts of high PV penetrations on the distribution protection as well as fault location and isolation systems in the context of new grid code requirements;

- 3 To formulate a PV detailed model with a control strategy that not only facilitates the fault detection but also fulfills the grid code requirements;
- 4 To develop a directional algorithm for fault direction detection within distribution networks with high PV penetration;
- 5 To propose protection settings for PV interface protection in order to avoid them from unwanted tripping and also be used as a foundation for developing **MV** and **LV** distribution protection;
- 6 To propose different protection schemes for **LV** microgrids and **MV** distribution networks with the consideration of the new grid code requirements applicable for PV systems. The proposed schemes should be able to operate in a selective and coordinated manner. The successful islanding of the connected **LV** microgrids can be ensured in the event of external faults;
- 7 To develop an **Artificial Neural Network (ANN)**- and a **Multiagent System (MAS)** based **FLISs** for **MV** distribution network with high penetration of PV systems;
- 8 To develop a cosimulation system, and to implement a **Controller Hardware-in-the-Loop (CHIL)** platform with IEC 61850-based communication infrastructure for validating the proposed **MAS**-based **FLIS**.

1.2 Grid codes applicable to PV systems

Many new grid codes require PV systems to have a wide range of advanced functional capabilities, as summarized in [26, 38]. Among these capabilities, this study aims to detail only the static voltage support, the dynamic grid support, and finally, the frequency control requirements because of their relevance to the research topic.

1.2.1 Static voltage support requirement

According to [24], static voltage support or voltage var control means controlling the voltage in the **MV** grid under normal conditions, when slow voltage variations in the distribution network are kept within the allowed limits. In particular, in case of operational requirements and upon request of the system operator, PV systems must participate in the control of the static voltage in the **MV** grid. The implementation of a static voltage support capability for PV systems connected to the **MV** grid has long proven itself.

However, in most countries, the requirement for static voltage support is still not applied for PV systems connected to **LV** grids, except in Italy and Austria [27, 39], due to their comparatively high costs. Nevertheless, the relevance of PV systems in **LV** grids is still increasing. Thus, newly installed PV systems within **LV** grids must, in the future, take over the control of the grid voltage. The German Network Technology Forum has revised the code of practice "Power plants connected to the low-voltage grid" (VDE-AR-N 4105) for this [40].

In terms of steady-state voltage support, PV systems should be able to provide reactive power control capability (reactive power injection or absorption) based on the power factor ($\cos \varphi$) at PCC. The values of $\cos \varphi$ can vary from $0.95_{\text{underexcited}}$ to $0.95_{\text{overexcited}}$ corresponding to the second and third quadrants as shown in Figure 1.3, [24]. The operating value of reactive power can be set by either:

- 1 fixed power factor, i.e. constant $\cos \varphi$;
- 2 variable set-point defined by $\cos \varphi(P)$ -characteristic;
- 3 fixed value in $MVar$, i.e. constant Q ;
- 4 controlled value defined by $Q(V)$ characteristic.

Implementation of the PV static voltage support can be varied in a wide range between different countries, even among DSOs in one country. Examples of $Q(V)$ and $\cos \varphi(P)$ characteristics required by different German DSOs are shown in Figure 1.3, [41].

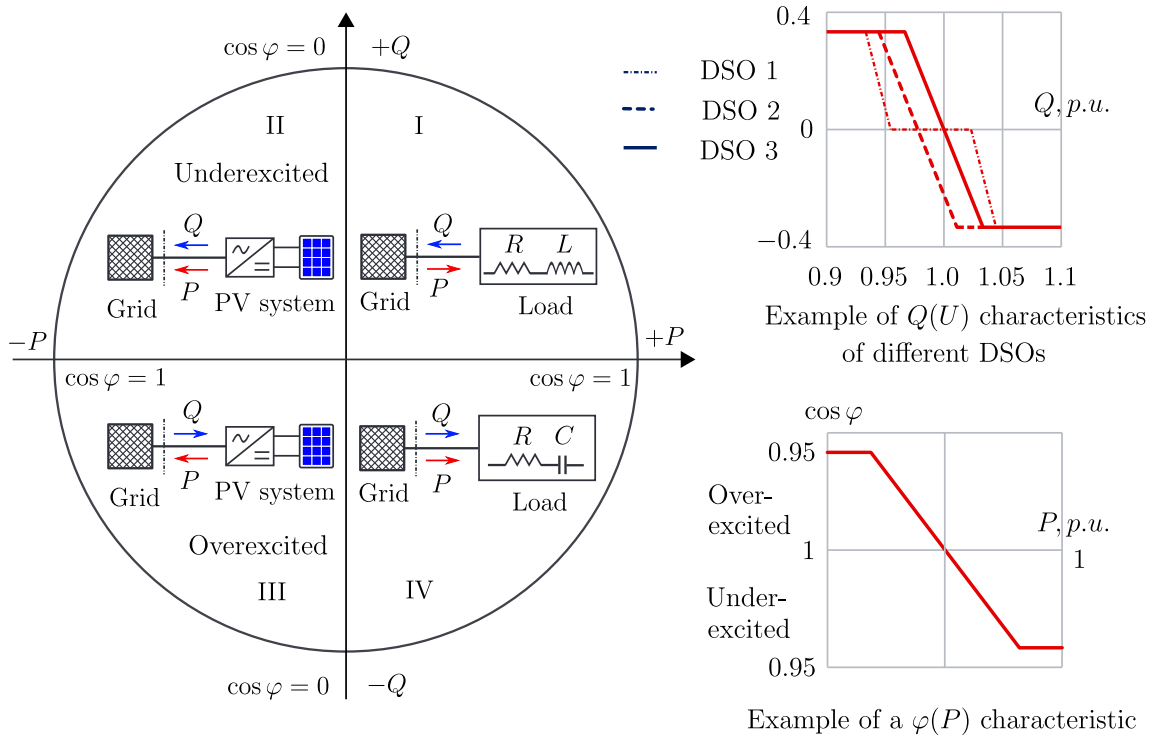


Figure 1.3 – PV static voltage support

1.2.2 Dynamic grid support requirement

In terms of the dynamic grid support capability, the PV systems should be capable of:

- 1 staying connected in the event of faults in external grids (FRT requirement);
- 2 feeding a reactive current to the network to support the grid voltage;
- 3 controlling the postfault reactive power consumption to not exceed the pre-fault value.

The **Fault Ride Through (FRT)** requirements vary from country to country. For example, the French grid code stipulates that only generating units with a maximum power greater than 5 *MV* should remain connected during external faults. In contrast, the Italian grid operators require that generating units connected to the **Low Voltage (LV)** grid with a rated power greater than 6 *kVA* should be able to overcome external grid faults [22]. Similarly, in addition to the grid connection obligation [24, 42], the German grid legislation also comes into force for grid-connected PV systems [43] at **LV** level. Moreover, several recent studies in Japan have also proposed **FRT** requirements for PV systems located in **LV** distribution networks [39, 44, 45]. Figure 1.4 illustrates different **FRT** characteristics during a fault imposed on PV systems in various countries [46, 47].

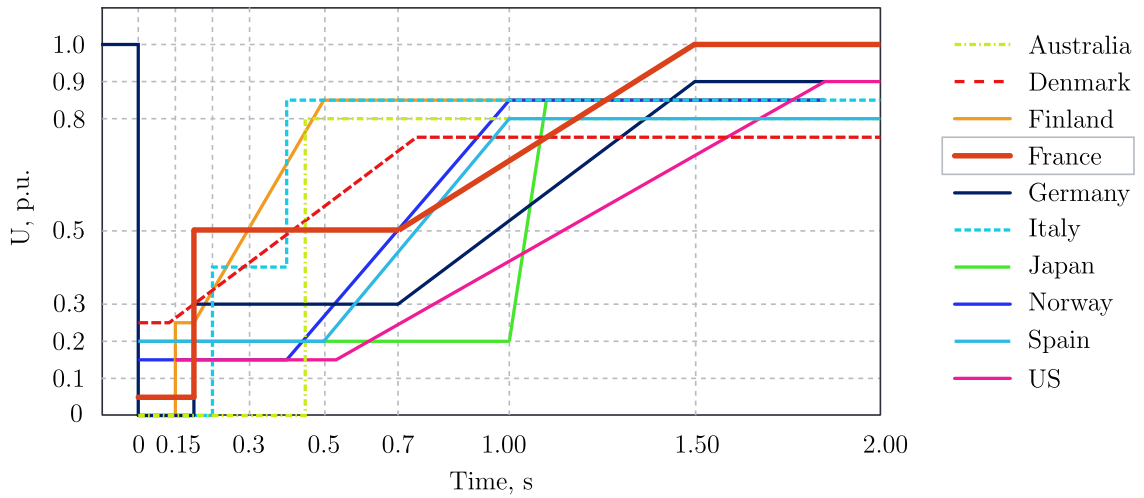


Figure 1.4 – FRT requirements in various countries

Concerning the requirement of reactive current injection under grid faults, its aims are twofold: first, to prevent the inverter from being tripped by its over-current protection and second to help the grid voltage recovery. The reactive current control should be triggered in case of the grid voltage decrease of more than 10% of the nominal voltage (i.e., in case of voltage drops below 0.9 *p.u.*). The reactive current required to be injected should be kept equal to at least 2% of the PV inverter rated current per each percent of voltage drop as shown in Figure 1.5, and can be expressed as follows, [48]:

$$I_q = \begin{cases} \text{deadband} & \text{if } 0.9 \leq V/V_n < 1.1 & (1.1a) \\ k \frac{V - V_0}{V_n} I_n + I_{q0} & \text{if } 0.5 \leq V/V_n < 0.9 & (1.1b) \\ -I_n & \text{if } V/V_n < 0.5 & (1.1c) \end{cases}$$

where V is instantaneous grid voltage during a fault, V_0 is grid voltage before fault occurrence, and V_n is the nominal voltage. I_q is reactive current, I_n is the nominal current, and I_{q0} is reactive current prior to fault inception.

In the event of an unbalanced fault, the amount of reactive current injected should be confined in a range not to cause the voltage on the healthy phases higher than $1.1V_n$, where V_n is the nominal voltage at the Points of Common Coupling (PCC). Additionally,

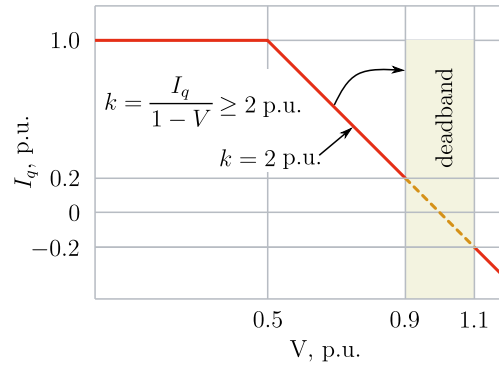


Figure 1.5 – Dynamic voltage support requirement in the event of fault for PV systems

the PV systems should be able to provide a reactive current of at least equal to the inverter rated current if required. Opposed to the static voltage support requirement that is applied to both **MV** and **LV** systems, the dynamic voltage support is just required for **MV** PV systems in most countries. However, in the study, it is assumed that the PV systems connected to both **MV** and **LV** grids can offer dynamic voltage support during faults.

1.2.3 Frequency control via active power regulation

Due to the highly intermittent characteristics of solar energy, the active power supplied by PV systems depends upon the external environmental conditions and therefore be uncertain. When the amount of connected PV systems is high, their fluctuation in power output may cause frequency deviation from the permitted range or even grid instability [49, 50]. Moreover, the potential disconnection of a large number of PV systems due to the operation of their interface protection may degrade the situations. Thus, many authorities in different countries have modified and updated their grid codes, to which the frequency control requirement through active power regulation has been added. For instance, the authorities in Germany have required that the connected PV system must be able to decrease its power production at over-frequency.

In detail, when the system frequency exceeds 50.2 Hz , each PV system should reduce its active power output with a gradient of 40%/ Hz of the generated power [24]. If the system frequency is above 51.5 Hz or below 47.5 Hz , the PV systems should be disconnected from the grid by their interface protection. The requirement active power reduction in the event of over-frequency can be observed in Figure 1.6. The amount active power reduction that should be regulated by the PV inverter controller is defined as:

$$\Delta P = \begin{cases} 0 & \text{if } 47.5 < f \leq 50.2 \\ 0.4P_m(50.2 - f) & \text{if } 50.2 < f < 51.5 \\ \text{PV shall be disconnected from the grid} & \text{if } f \leq 47.5 \text{ or } f \geq 51.5 \end{cases} \quad (1.2)$$

where P_m is the instantaneous available power delivered by the PV systems, and f is the system frequency in Hz .

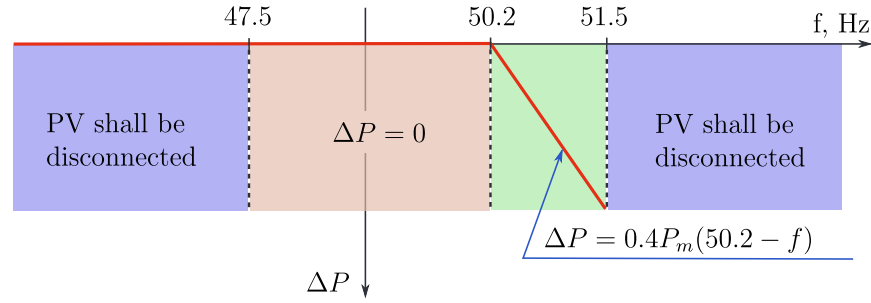


Figure 1.6 – Active power control at over-frequency

Table 1.1 represents several selected grid codes from European countries for PV systems connected to distribution networks.

Table 1.1 – Grid code requirement for PV systems in different countries

Country	Requirement					
	Static voltage support		Dynamic voltage support		Active power reduction	
	MV	LV	MV	LV	MV	LV
Germany	Yes	Yes	Yes	No	Yes	Yes
Austria	Yes	optional	Yes	No	Yes	Yes
Italy	Yes	>6 kVA	Yes	>6 kVA	Yes	Yes
Spain	>2 MW	No	>2 MW	No	>2 MW	Yes
France	Yes	No	>5 MW	No	No	No

1.3 Thesis contributions

Taking into account all the above, the contribution of the thesis can be summarized as follows:

- 1 A detailed description of a PV inverter control strategy, which meets the dynamic voltage supports imposed by the new grids codes on the PV systems connected to the **Medium Voltage (MV)** and **Low Voltage (LV)** distribution networks, is offered. Moreover, the PV systems are proposed to inject **Negative Sequence (NS)** currents in the event of unbalanced faults to mitigate the oscillation of active power. The injection mechanism of **NS** currents can facilitate the detection of these kinds of faults. Next, based on this control algorithm, a fault model of PV systems is derived. Finally, the equation expressing the magnitudes and angles of PV fault sequence impedances are obtained and their possible values are evaluated by analytic analysis.
- 2 The thesis further develops a directional algorithm dedicated for distribution networks with high PV penetration. One of the salient feature of the proposed approach is that it can deal with the non-conventional patterns of PV

fault current and voltage waveforms. Moreover, it can be immune from the high penetration of inverter-based PV systems as well as other influencing factors such as load imbalances, short circuit power of external grid, faults close to measurement location, fault types, and fault impedances. The proposed directional method is then deployed for developing effective protection schemes and [Fault Location and Isolation System \(FLIS\)](#)s.

- 3 Strategy for the coordination of protection schemes between [MV](#) and [LV](#) distribution networks is provided. These schemes can operate in a selective and coordinated manner. One element can serve as redundant protection for the others and can differentiate between forward and reverse faults. The coordination between [MV](#) and [LV](#) protections not only allow the connected [LV](#) microgrids to achieve successful islanding in the event of external faults, but also ensure the [Fault Ride Through \(FRT\)](#) requirements of the connected PV systems.
- 4 The thesis develops two [FLIS](#)s for [MV](#) distribution networks with high PV penetration. The first system is based on the [Artificial Neural Network \(ANN\)](#) method that can achieve high accuracy of faulty line-section location with short time computation. The second approach is [Multiagent System \(MAS\)](#)-based system, in which decision-making on faulty line-section is made locally by the respective agents, based on the fault direction information exchange among them. Normally, the number of affected customers on the second stage of power restoration process (the operation phase of [Remotely Controlled Switch \(RCS\)](#) in traditional [FLIS](#)) can be large. By applying the proposed [FLIS](#), the DSOs can reduce the duration of this stage, and thus significantly improve the system [System Average Interruption Duration Index \(SAIDI\)](#) and [Customer Average Interruption Duration Index \(CAIDI\)](#) indices.
- 5 The thesis designs a cosimulation system consisting of [DIgSILENT | PowerFactory](#), Python, and OPC-DA server. The network is simulated in [PowerFactory](#), the agents are simulated by using Python language. The agents hosted in Python engine receive measured signals from [PowerFactory](#) via OPC-DA server, process them and then return the results back to the [PowerFactory](#). As a result, the obtained system allows to evaluate the proposed [MAS](#)-based [FLIS](#) within the pure software environments.
- 6 Finally, the thesis implements a [Controller Hardware-in-the-Loop \(CHIL\)](#) platform for testing the [MAS](#)-based [FLIS](#). The interoperability of the equipment involved is verified with the inclusion of IEC 61850 communication as well as real controllers (Raspberry PIs) and digital relays.

1.4 Thesis structure

The thesis has been organized in 5 chapters, and 9 appendixes as follows:

In the first chapter, the thesis statement and objectives are mentioned. We also summarize the thesis contributions in this chapter.

Chapter 2 presents the models of all common system components such as overhead lines, underground cables, transformer, external grids as well as loads that are needed for the transient studies. The loads modeled are a combination of static and dynamic types that make the load transient behaviors as close as possible to "real life". Additionally, since the requirements of new grid codes are the foundation of the research, we conduct a thorough investigation on the new grid codes applicable to the PV systems in different countries. The objectives of the analysis is to integrate the grid code requirements into the PV models for obtaining proper PV transient behaviors for studies in the following chapters. Then, a control strategy for PV systems that fulfills the PV voltage dynamic support requirement is developed and validated by simulations.

Chapter 3 presents a new directional algorithm for distribution networks with high penetration of PV systems. First, the algorithm is evaluated by applying analytical approach for the fault equivalent circuits involving the PV models developed in Chapter 2. The proposed direction method is then evaluated by simulations in the software environment DigSILENT|PowerFactory. Different fault scenarios are conducted in order to evaluate the performance of the proposed methods.

Chapter 4 develops different protection schemes for both MV and LV networks. The developed MV protection scheme can not only provide the accurate operation for fault within the protected MV network but also ensure the selective operation with the connected LV microgrids. Such a selectivity between two protection levels enables that successful islanding of the LV microgrids in the event of faults in external HV or MV networks. On the other hand, the LV microgrid protection schemes are designed to have different setting groups adaptable to both operation modes of the protected microgrids. The FRT requirements of the connected PV systems are also met.

Chapter 5 proposes two FLIS systems. The first method is based on a state-of-the-art ANN network. A Multi-layer Perceptron (MPL) is used for classifying the faulty line-sections. The designed ANN network is first trained with a partial data set and then is test by the remaining. The second approach is based on a MAS system with a IEC 61850-based design. The MAS-based FLIS is evaluated first by a co-simulation system and then by a CHIL platform.

Appendices from A to I are included at the end of the thesis.

Chapter 2

Modeling of distribution networks with PV systems

Contents

2.1	Introduction	17
2.2	Overview of distribution systems	17
2.2.1	LV distribution networks	18
2.2.2	MV distribution networks	19
2.3	Overview of distribution protection	21
2.3.1	LV distribution protection	21
2.3.2	MV distribution protection	22
2.4	Studied distribution networks	26
2.4.1	Description of Grid-1	26
2.4.2	Description of Grid-2	27
2.4.3	Description of Grid-3	30
2.5	DIgSILENT PowerFactory	30
2.6	System impedance value modeling	31
2.6.1	HV external grid	31
2.6.2	Substation transformer	31
2.6.3	Overhead lines and underground cables	32
2.6.4	Load	32
2.7	PV systems	33
2.7.1	Structural configuration of a PV system	33
2.7.2	PV module equivalent circuit	34
2.7.3	PV array and MPPT algorithm	35
2.7.4	PV model for steady-state studies	36
2.7.5	PV model for transient studies	37

- 2.8 Battery energy storage system 47
 - 2.8.1 Battery model 47
 - 2.8.2 Frequency controller 48
 - 2.8.3 Active/Reactive power controller 48
 - 2.8.4 Battery charge control 49
- 2.9 Overview of IEC 61850 standard 49
- 2.10 Conclusion 50

2.1 Introduction

The algorithms toward the distribution protection schemes as well as [Fault Location and Isolation System \(FLIS\)](#), which will be developed in the subsequent chapters, should be validated. Within the scope of this thesis research, we make use of three different real distribution networks with parameters provided by local utility companies. Besides, several [Low Voltage \(LV\)](#) microgrids with detailed data on loads and other component parameters are offered. Thus, in this chapter, the models of all components involved in the three given networks for electro-mechanical and electro-magnetic simulations in the software environments [DIgSILENT | PowerFactory](#) and [Matlab/Simulink](#) are presented. The purpose of the simulations is twofold. The first objective is to generate fault data that emulate the measured currents and voltages from real distribution networks for validation of the directional algorithm developed in [Chapter 3](#) and the [Artificial Neural Network \(ANN\)](#)-based [FLIS](#) proposed in [Chapter 5](#). The second goal is to create fault operation scenarios for the evaluation of the protection schemes in [Chapter 4](#) and the [Multiagent System \(MAS\)](#)-based [FLIS](#) in [Chapter 5](#). Moreover, the networks being modeled are used for validation by using the developed [CHIL](#) platform in [Chapter 5](#).

2.2 Overview of distribution systems

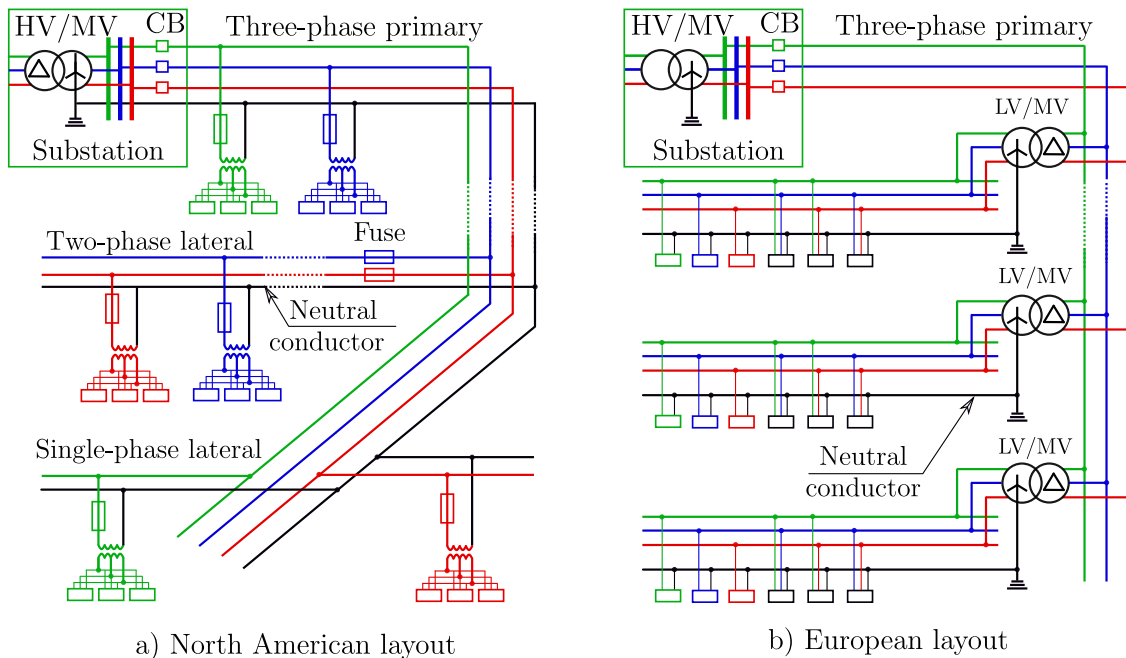


Figure 2.1 – North American vs European distribution network layouts

Distribution systems are the part of the power systems that are connected with High Voltage (HV) transmission networks via HV/MV transformers located at primary distribution substations. Distribution networks receive electricity from HV transmission networks and deliver it to ultimate customers. There are two main structures of distribution networks, including European and North American. The main differences lie on their layouts, as shown in [Figure 2.1](#), [\[51\]](#). The [Medium Voltage \(MV\)](#) feeders in North Amer-

ica use 3-phase, 4-wire multi-grounded systems while in Europe 3-phase, 3-wire systems are dominant. Moreover, European MV/LV distribution transformers are mostly three-phase with a rating of 50 to 1000 kVA , whereas the common North American ones are single-phase with much fewer ratings of 25 or 50 kVA .

As the studied networks provided by the local utility companies are operating on the European layout, we would focus only on this type of network structure. Figure 2.1 illustrates two levels of distribution networks, one is MV network, and the other is Low Voltage (LV) network. HV/MV transformers at each primary distribution substation transforms the HV power to the MV power. Originated from the secondary bus-bar systems of the HV/MV transformers, the outgoing MV feeders deliver this power to MV/LV transformers. Each HV/MV substation can offer a connection of up to 20 MV feeders. Close to end-users, MV/LV transformers receive the power on the MV voltage and steps it down to LV circuits. From the LV side of the MV/LV transformers, the LV distribution circuits connect to the end-users via distribution service boards.

2.2.1 LV distribution networks

2.2.1.1 Overhead lines and underground cables

LV networks represent the final level in a power system and are often operated manually. The connection group of distribution transformer windings are mostly $DYn-11$ group, [52]. Similar to MV networks, for LV networks, underground cable lines are used in urban areas, while overhead lines are preferred in rural areas. The LV feeders may consist of lots of laterals and sub-laterals. The structure of LV networks can be categorized into three levels, depending on the supply reliability requirement of connected loads [4].

For the first level, the MV side of a distribution transformer is connected to an incoming MV feeder. The LV conductors are radial. The layout of the second level is similar; however, the outgoing LV feeders can be open-ring or can be doubled where each is connected to a single transformer. LV network loads can be three-phase, two-phase, or single phase. The connection of two-phase/single-phase customers leads to inherently unbalanced characteristics of LV networks. Typical cross-sectional areas used for LV feeder are twisted overheads 70 and 150 mm^2 Al with neutral 54.6 or 70 mm^2 ; and underground cables 150 and 240 mm^2 Al with neutral 50, 70 or 95 mm^2 .

2.2.1.2 MV/LV distribution transformers

MV/LV transformers have standard ratings of 50, 100, and 160 kVA for the pole-mounted type, and 160, 250, 400, 630, and 1,000 kVA for the pad-mounted type.

2.2.1.3 LV neutral system

Concerning the earthing systems for LV networks, the IEC 60364-5-54 standard has defined three main categories described by two letters, including IT, TT, and TN systems as shown in Figure 2.2, [53]. For the first letter, which is identified by the earthing mode

of the transformer neutral, "I" is the acronym of the French word "isolé" meaning isolated from earth, and "T" stands for "terre" meaning directly connected to the earth. For the second letter, which is defined by the earthing method of the exposed conductive parts of installations, T indicates that the conductive parts of equipment frames are directly earthed, whereas N (neutre) implies that conductive parts of the equipment frame are directly connected to the neutral conductor. The third earthing method, i.e. TN, may further be divided into three sub-categories. The first subgroup is named TN-C if the network-neutral and protective earth conductors of customer installations are the same. The second subgroup is called TN-S if these two conductors are independent. The last one is abbreviated as TN-C-S if the TN-C method is applied between the neutral point of network transformer and the TN-C system.

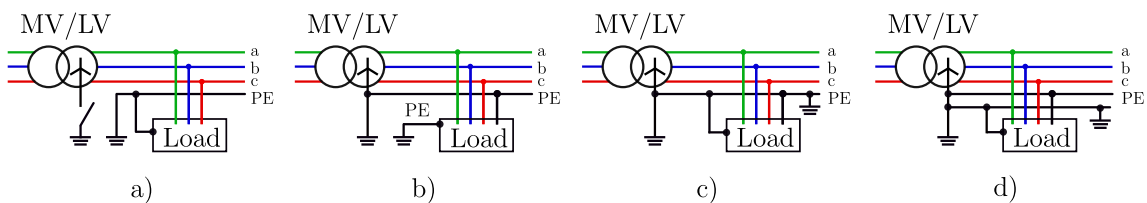


Figure 2.2 – LV earthing systems with (a) IT, (b) TT, (c) TN-C, and (d) TN-S

2.2.2 MV distribution networks

2.2.2.1 Urban and rural networks

MV networks are usually operated in a radial configuration. However, they are also designed such that a loop can be quickly established by using normally opened switches. This architecture enables one feeder to be reserved for one or several adjacent lines. Two kinds of MV networks are currently used in practice, including urban and rural networks. The urban networks are mainly underground cables and are used in densely populated areas. They consist of cables, usually three-phase, with synthetic or paper insulation. This type of network is used to meet the needs of improving the quality of the power supply and the environment, such as visual impact and insensitivity to weather conditions. On the other hand, the rural networks are primarily overhead lines and used in regions with low load density, for instance, rural areas, small towns, or villages.

Urban feeders are usually shorter in length compared with rural ones. Average length of urban feeders ranges from 3 to 10 km with cross-sectional areas of 150 or 240 mm². Mean length of rural feeders vary from 10 to 35 km with cross-sectional areas typically of 240 mm² for the substation outlet, and 148 mm² and 54 mm² for the main and lateral, respectively, [54]. The maximum allowable power for each outgoing MV feeder is 5 MVA for rural networks and 6 MVA for urban networks. This value is imposed by the limit of 400 A on the outgoing bay from the HV/MV substation. The value of the Positive Sequence (PS) reactance per unit length of overhead lines is normally equal to 0.3 or 0.35 Ω/km. The Zero Sequence (ZS) capacitance per unit length of overhead lines is usually taken as 5 pF/m, and that of underground cables is much higher, which is often equal to 0.155 μF/km for a 50 mm² section.

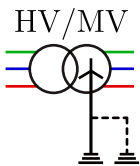
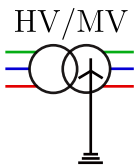
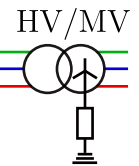
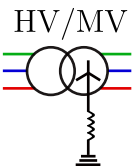
2.2.2.2 HV/MV distribution transformers

Ratings of the HV/MV substation may range from 5 *MVA* for a small rural substation to over 280 *MVA* for urban one [51]. Within a HV/MV distribution substation, the number of HV/MV transformers is often limited to 2 in rural areas and 3 in urban areas.

2.2.2.3 MV neutral systems

The method of earthing, whether neutral or not, is a crucial element as it determines the main characteristics of earth faults. This kind of fault may account for up to 80% of the total number of faults and can cause the local increase of the ground voltages on the healthy phases when they occur. Currently, for earthing the neutral of *MV* networks, utility companies around the world are applying five main earthing approaches, according to [4, 55, 56], as shown in Table 2.1. None of these methods are dominant throughout the world. Some methods are specific to some countries, while several systems can be found within a single country.

Table 2.1 – MV earthing systems in several typical countries

Country	Method				
	Distributed earthed	Solidly and undistributed earthed	Impedance earthed	Designed earthed	Unearthed
					
Australia	x				
Canada	x				
US		x			
Spain		x	x	x	x
France			x		
Japan					x

The neutral system has a direct impact on the planning of the networks in order to ensure the safety of personnel and property, and on the quality of the power supply. The dielectric strength of all the networks and their components is notably determined according to the rise in the ground voltage in the event of a fault, whether it occurs on the HV, *MV*, or *LV* networks. The main differences between these methods reflect in the response of the networks once ground-faults occur. Therefore, the selection of a neutral earthing system is of significant importance because it directly defines the levels of the ground fault current and also the voltage surge that are usually contradictory. Hence, the choice of earthing system is usually resulted from the compromise between technical requirements and operating expenses.

2.3 Overview of distribution protection

2.3.1 LV distribution protection

LV network protection schemes are very different depending on the operations and traditions of the Distribution System Operators (DSO). The main schemes used by ENEDIS (main french DSO) are described below.

2.3.1.1 Underground-cable networks

An underground type LV network that is used in urban areas has the following protections in series, from the customer location to the HV side of the MV/LV transformer. A protection scheme of a typical LV urban network is illustrated in Figure 2.3.

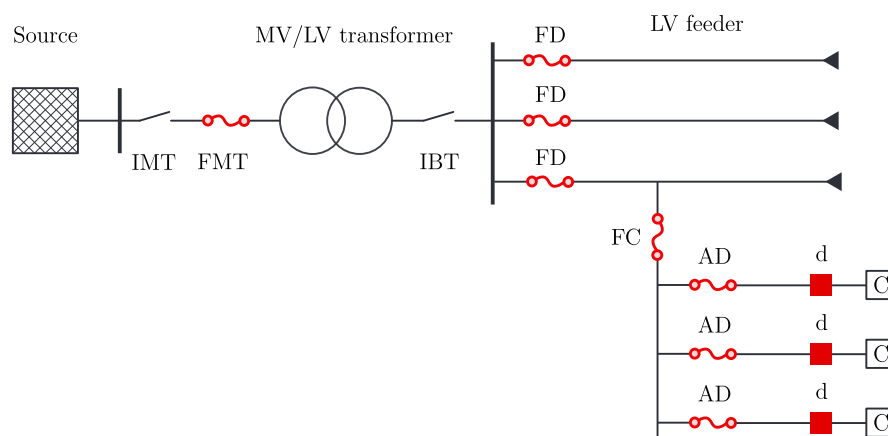


Figure 2.3 – A protection scheme of a typical French LV underground-cable network

Customer: A circuit breaker denoted by letter "d" is used to disconnect the LV system from the customer's facilities when a fault or overload affects them. The standard rated currents of customer circuit breakers are 30, 45, 60, and 90 A. These values represent the upper limits of the setting current. There is also a fuse signified by AD and placed at the beginning of each entrance service. It is designed to interrupt those fault currents that exceed the breaking capacity of the customer circuit breaker. In France, the standard values of its rating are 45, 60, and 90 A.

Distribution board of building: A fuse denoted by FC is deployed to clear faults within a distribution board of a building to prevent LV outgoing feeders from unnecessary disconnection. In France, the standard ratings of the fuse FC are limited to 125, 200, 250, and 400 A.

LV outgoing feeder: A fuse denoted by FD is installed at the beginning of the LV feeder. The fuse FD is in charge of eliminating faults that are located between itself and the distribution board of the building. In France, the standard ratings of the fuse FD are confined to 200, 250, and 400 A.

MV/LV transformer: A fuse FMT is used for protecting the MV/LV transformer

against damage in distribution transformers or providing backup protection for LV feeders. In networks with operating voltages between 12 and 24 kV, its ratings are 3, 6, 16, 43, and 63 A. There are also disconnecting switches for low voltage (IBT) and medium voltage (IMT) on both sides of the transformer.

2.3.1.2 Overhead-line networks

An overhead line network, which is mainly used in rural areas, is equipped with the following protections, as shown in Figure 2.4.

- 1 Customer's circuit breaker d;
- 2 Customer's circuit breaker d and a fuse AD accompanying this circuit breaker;
- 3 FD of the LV outgoing feeders, if applicable;
- 4 Circuit breaker D for a pole-mounted substation and switch I or the circuit breaker D in the case of a cabin-type substation (simplified low-level substation). On this type of network, no fuse or circuit breaker has been installed for the MV/LV secondary distribution transformer, but their installation is being considered;
- 5 A surge arrester for protecting transformers against atmospheric disturbances.

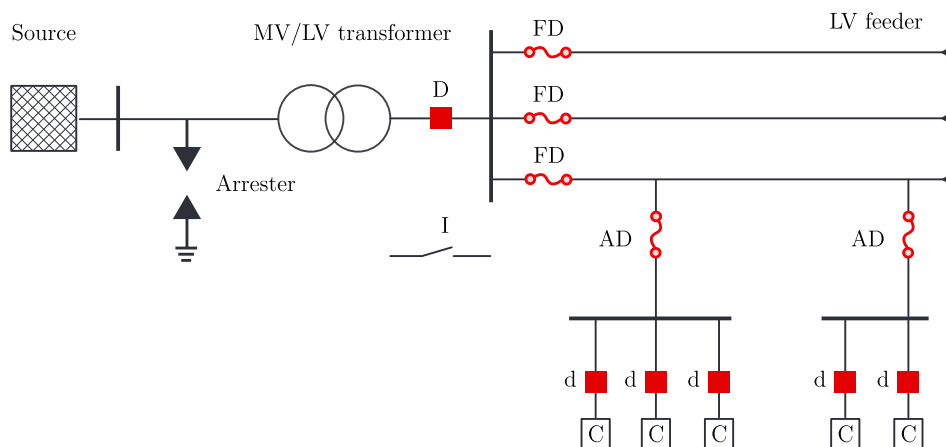


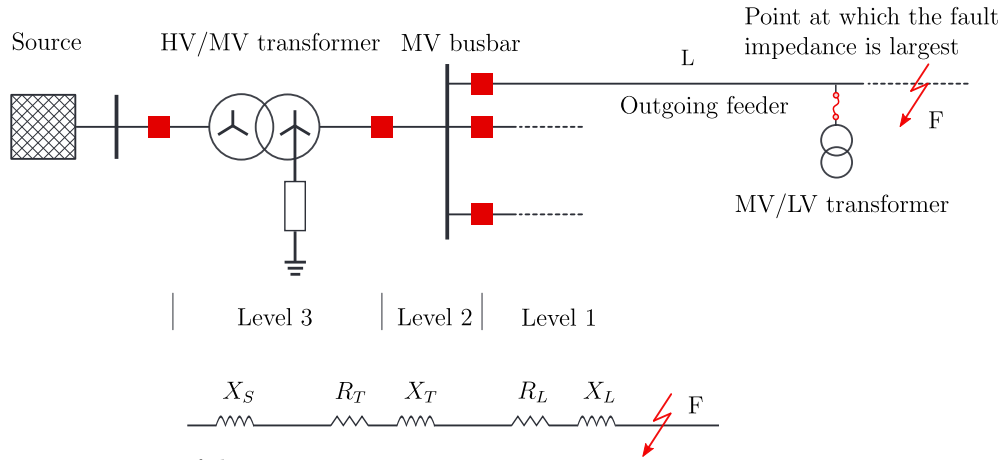
Figure 2.4 – A protection scheme of a typical French LV overhead-line network

2.3.2 MV distribution protection

In general, the MV protection schemes are intended for the detection and elimination of faults of all kinds: phase faults and ground faults. According to [57], the French MV protection scheme is structured in three levels as follows, Figure 2.5:

- 1 **Level 1:** Protection of the outgoing feeder;
- 2 **Level 2:** Protection of MV busbar whose purpose is to protect the busbar and be a backup of the possible failure of the outgoing feeder circuit breakers. This protection is to trip the Circuit Breaker (CB) on the MV side of the transformer;

- 3 **Level 3:** Protection of HV/MV transformer and associated equipment whose role is to protect the auxiliary equipment connected to the transformer on the **MV** side. This protection is to trip the CB on the HV side of the transformer.



X_s : reactances of the source

R_T and X_T : resistance and reactance of the HV/MV transformer, respectively

R_L and X_L : resistance and reactance of the MV feeder, respectively

Figure 2.5 – A French typical MV radial network and its different protection levels

Moreover, each level has two protection types that are phase and ground protections. The former, which is independent of the network ground system, is to deal with phase faults. The phase protection is mainly composed of phase overcurrent relays, either definite or inverse time. On the other hand, the latter, which should be adapted to the network earthing system, is against the ground faults. The earth protection utilizes different types of protection depending on the network grounding system and the protection levels mentioned above.

2.3.2.1 Protection against phase faults

The principles for calculating phase fault currents are identical for any radial network. Fault calculation aims to determine the lowest possible fault current, from which the current setting threshold is derived. The setting threshold is determined by considering the current of two-phase fault, which is lower than that of three-phase fault. According to Figure 2.5, the two-phase fault current can be defined by, [57]:

$$I_F^{(2)} = \frac{V_n}{2\sqrt{R_L^2 + (X_s + X_T + X_L)^2}} \quad (2.1)$$

where $I_F^{(2)}$ is the two-phase fault current and V_n is the grid nominal voltage;

Level 1: The setting current should be lower than $0.8I_F^{(2)}$, but it must be higher than the maximum load current of the protected feeder. It also should be higher than the inrush current in the event of load recovery connected to the feeder.

Level 2: The busbar protection should not trip before the feeder protection if the fault is located on the feeder. The most straightforward setting is to refer to the rated current of the HV/MV transformer or MV busbar fed from the feeder, i.e., 1.6 times the rated current of the transformer or 1.3 times the rated current of the busbar. The lower value is selected after verifying that this setting is higher than 1.2 times the highest setting current of the outgoing feeders.

Level 3: The setting depends on that chosen for MV busbar. It is either twice the rated current of the transformer (in the case of a setting equal to 1.6 times the rated current of the transformer) or 1.6 times the rated current of the busbar (in the case of a setting equal to 1.3 times the rated current of the busbar).

2.3.2.2 Protection against earth faults

The earthing system in French MV distribution networks is primarily low-resistance grounded. In rural distribution networks, the ground-fault current is limited to 150-300 A primary. In the urban networks, which have higher capacitive currents, the resistor is selected to limit the ground fault current to a maximum of 1000 A. The reduction of ground-fault current avoids high constraints on the equipment.

Level 1: The ground overcurrent function is set to 1.2 times the capacitive current of the feeder. A margin of 20% is selected to prevent the protection from false tripping.

Level 2: The current threshold is set to be equal to 1.2 times the maximum current among the setting currents of **Level 1**.

Level 3: HV/MV transformers are mainly protected from non-electrical quantities that do not distinguish between multi-phase and single-phase faults. This kind of protection typically includes a Buchholz relay.

2.3.2.3 Time setting

The principles of time selectivity settings described in this paragraph are only valid for networks equipped with definite time overcurrent protection, as is the case in Europe.

Constraints: It is required to ensure at least an interval of 0.3 s between two protection levels. However, it can be reduced to 0.25 s when digital or numerical relays are used. The time delay of the protection on the customer side is fixed at 0.2 s according to the standard NF C13-100. This value should be taken into account when determining the time delay of the outgoing feeder protection.

Level 1: ENEDIS uses only one time-delay of 0.5 s. This value helps to ensure the minimum time interval between the user delay of 0.2 s and network protections. Delay of 0.5 s also can help to avoid the impacts of the inrush current caused by the load reconnection during the operation of reclosing function.

Level 2: The time delay of the protection level is set at 0.8 s that ensures the selectivity

interval of 0.3 s with the protection of outgoing feeder. This value is quite long, which may cause severe impacts on the busbar system. Hence, an alternative method is using a direct transfer trip that will be presented in more detail in the subsequent section.

Level 3: Based on **Level 2** time delay, the time delay of this level is fixed at 1.1 s.

2.3.2.4 Other protections

Apart from the above protections, there are other protection functions as follows, [57]:

- 1 Protection of the link between HV/MV transformer and MV busbar;
- 2 Resistive earth detector measures the current flowing in the transformer neutral, i.e. ground current on transformer MV side. It backs up the ground protection of outgoing feeders and trips incoming CB after a time delay;
- 3 Internal protection of the transformer acting on the CB on the HV side;
- 4 Tank earth protection of the transformer acting on the CB on the HV side.

2.3.2.5 Recloser application

In the present practice, the utilities often implement reclosers at the beginning of MV overhead feeders to clear temporary faults without causing prolonged power interruption to customers [54]. Its operating principle is as follows. When a feeder relay detects a fault, it issues a trip signal to open the respective feeder CB. It should be noted that, for those feeders to which a recloser is applied, the time delay of their relays is reduced to 0.15 s instead of 0.5 s, as previously mentioned, Figure 2.6. However, after the first trip, the feeder relay moves to delayed trips for further trips if the fault is permanent. The time delay of the second and third consecutive trips of the relay is usually 0.5 s

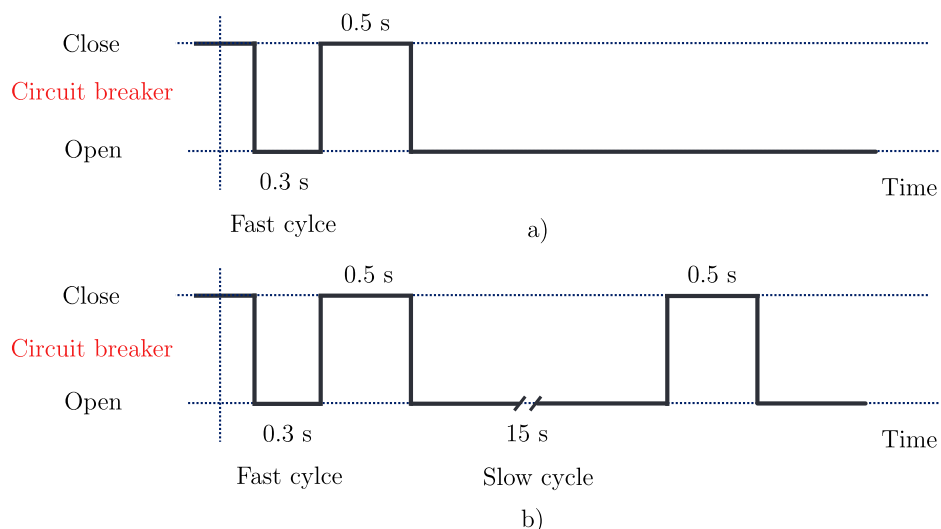


Figure 2.6 – Recloser cycles for (a) a transient fault, and (b) a permanent fault

After a predefined time delay, the recloser automatically commands the CB to reclose.

If the fault is transient, it has already been cleared. The supply is restored to the customer connected to the affected feeder; otherwise, the feeder relay trips the CB again. The reclosing cycles for a transient and a permanent faults are depicted in Figure 2.6, [57]. Typically, the process of recloser operation is as follows:

- 1 Fast cycle: recloses the CB within about 0.3 to 1 s after the feeder CB opening;
- 2 Slow cycle: If the fault still exists, the feeder relay trips the CB again. Then, the recloser is delayed for about 15 to 30 s before reclosing the CB.
- 3 The CB is finally reopened if the fault still exists after 0.5 s by the feeder relay.

There may be cases where a third closing attempt is made after about 20 s or 30 s , e.g. to give the **Remotely Controlled Switch (RCS)** installed on the affected feeder time to operate, or to burn the tree branch or bird which provoked the fault. This is the case in France where switches take advantage of the second power outage to open when the loads are dropped out, as they are unable to operate on short-circuit currents, [58].

2.4 Studied distribution networks

There are three real distribution grids, provided by three utility companies, two (Grid-1 and Grid-3) from France, and one (Grid-2) from Vietnam. The studied networks are operating at 20 kV for **MV** level and 0.4 kV for **LV** level for French networks, and 22 kV and 0.4 kV for Vietnamese network.

2.4.1 Description of Grid-1

Figure 2.7 sketches the single-line diagram of Grid-1. The network is supplied by either External Grid A or B via 63/20 kV transformers. There are 4 feeders, but only two of them are modeled in detail with complete inputs of line sections and **LV** loads. All the feeders are underground cables with the cross-section area decreasing for sections located further from the HV/MV substation. Several laterals tapped from the feeder backbones to feed local **LV** loads via MV/LV transformers. **LV** loads consist of both three-phase and single-phase loads making the **LV** networks unbalanced in nature. The total rating capacity of loads is 7 MVA with a power factor to be assumed equal to 0.9. The daily load consumption, which is shown in Figure A.1, varies according to 24 h -time characteristics, and the peak and lowest loading conditions occur at 19 h and 04 h , respectively.

Three **LV** microgrids that contain various PV systems are included at nodes "06", "10", and "16". These grids could be operated in both operation modes, including grid-connected and islanded modes, even if the latter operation mode is not allowed today. In grid-connected mode, the frequency is imposed by the external grid. However, in an isolated mode, it is required to install a Battery Energy Storage System (BESS) within each grid for frequency and voltage control. The microgrid concerned in the study is **LV** microgrid 1. This network consists of several PV systems and one BESS unit as presented in Figure 2.8. The control algorithms of these generating units have already been developed in Chapter 2 that fulfill the new grid code requirements. One diesel generator is also im-

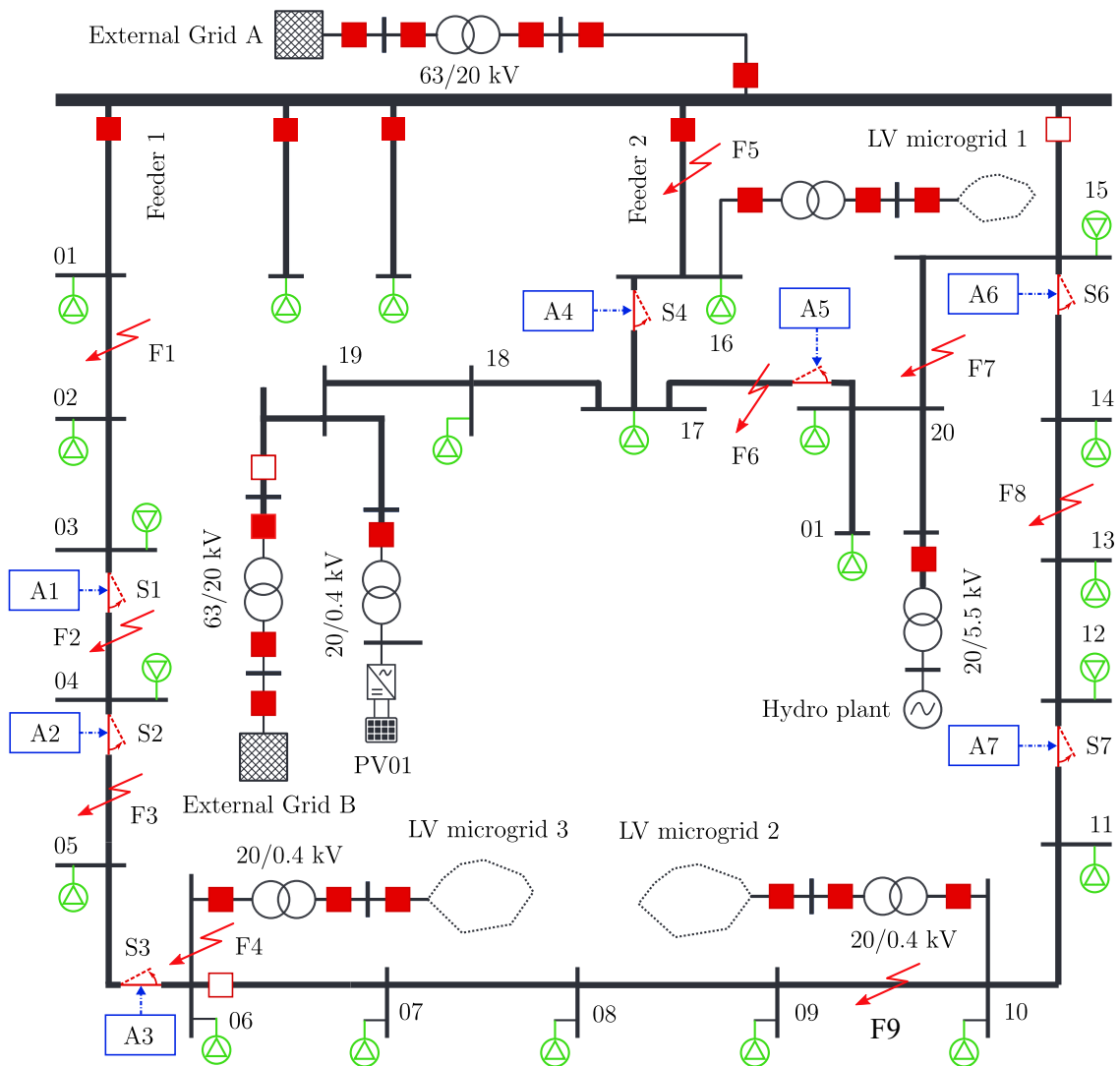


Figure 2.7 – Single-line diagram of Grid-1

plemented to serve as a reserve supply in case of long term islanding. However, the grid services, such as frequency control, is still held by the BESS unit. It is noted that in the study, the LV microgrid is mainly operated grid-connected mode. It is only turned into isolated operation when a fault occurs on the external grid or on the host MV feeder. The LV grid earthing is the TN type. According to [59], the TN system is the most appropriate approach for LV microgrids since the tough voltages at the faulted bus are smaller than those of the TT and IT types. Moreover, in the TN system, an earthed fault, in principle, provides sufficient current to operate an overcurrent device.

2.4.2 Description of Grid-2

Grid-2 is an isolated MV network whose operating voltages are 22 and 0.4 kV. Single-line diagram of Grid-2 is shown in Figure 2.9. The original form of the network consisted of only 7 transformer-diesel generator units. The later installation of solar and wind energy-based DERs and a BESS is proposed according to the investment of the national

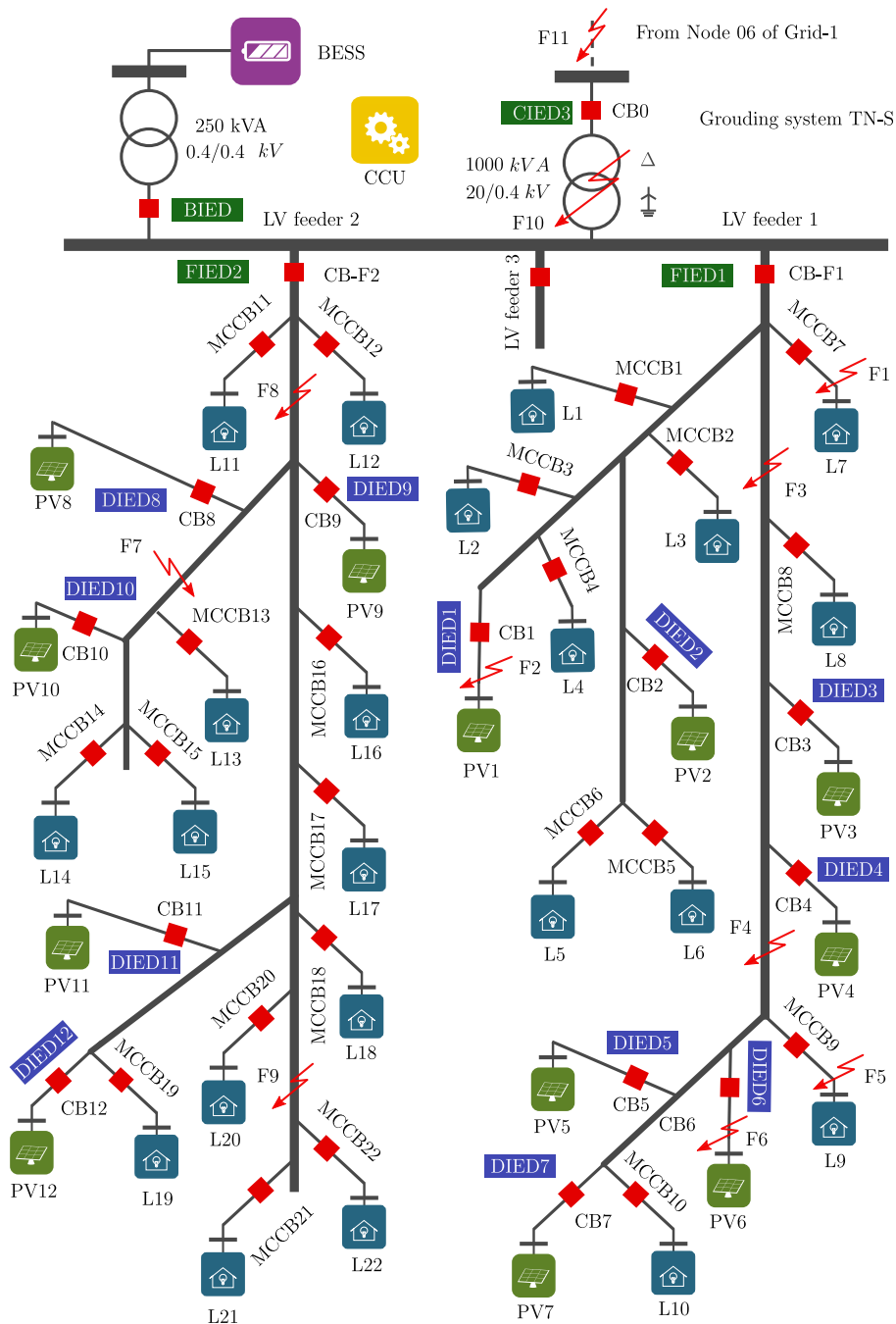


Figure 2.8 – Single-line diagram of LV microgrid 1

electricity corporation and some local private companies. The total installed capacity of PV systems and wind turbine are intended to reach 6.8 MW and 3 MW, respectively.

The structure of Grid-2 is similar to that of Grid-1, where three radial feeders originated from the 22 kV busbar systems of the generation center and supply various single-phase and three-phase LV loads. Besides, feeder 1 and feeder 2 are meshed at several points by normally-open switches. The earthing system used for Grid-2 is a solidly and undistributed earthed method.

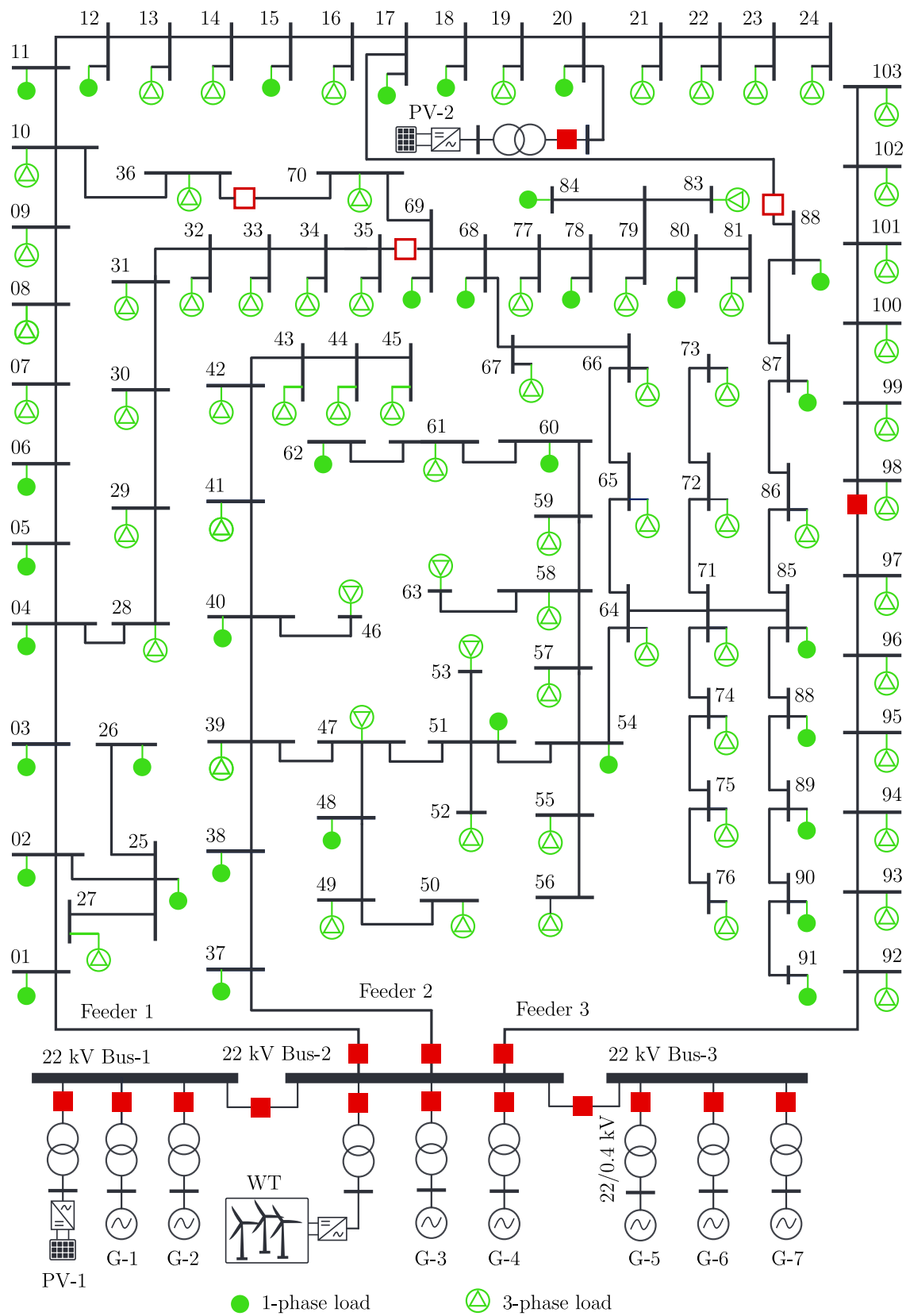


Figure 2.9 – Single-line diagram of Grid-2

2.4.3 Description of Grid-3

Grid-3, which is depicted in Figure 2.10 is a rural French MV distribution network supplied from a 63 kV external grid via a 63/20 kV transformer. There are 6 MV feeders, in which each feeder is modeled by several line sections based on the PI model. Only Feeder 1 with total active and reactive powers of 4401 kW and 829 kVar, respectively, is detailed as shown in Figure 2.10. The loads are distributed along the feeder. The feeder is divided into 4 zones by 3 switches from S1 to S3. Four PV systems of 440 kW each are integrated into these 4 zones.

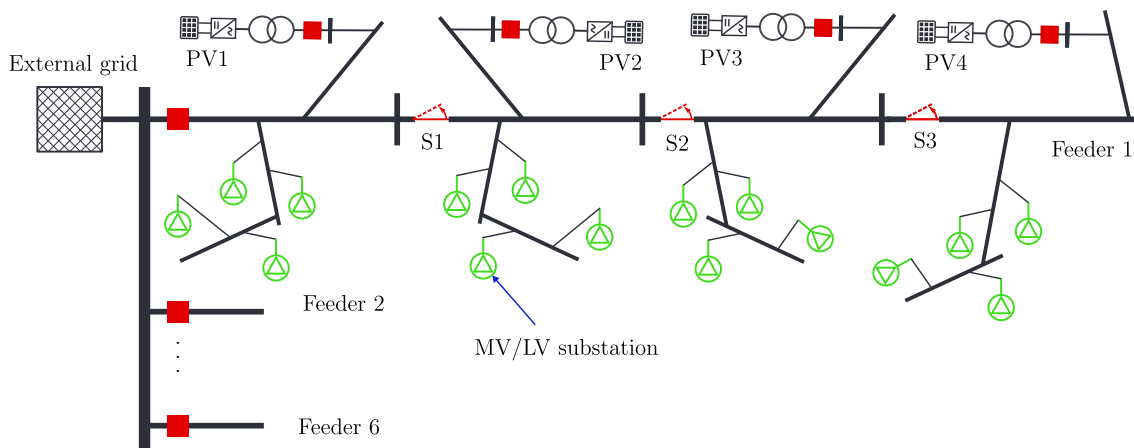


Figure 2.10 – Single-line diagram of Grid-3

2.5 DIgSILENT | PowerFactory

DIgSILENT | PowerFactory is a leading power system analysis computer-aided tool for many applications in generation, transmission, distribution and industrial analysis. It provides a wide range of calculation functionality, even for highly complicated problems, with state-of-the-art algorithms including real-time simulation ability. An abundant number of pre-defined and tested models of power system components can be found in its component library.

Depending on the purposes of study, DIgSILENT | PowerFactory requires different sets of component inputs with a user-friendly graphic interface. The data management system in DIgSILENT | PowerFactory would be highly appreciated thanks to its flexibility and effectiveness, allowing users to model and simulate large networks with thousands of components. In particular, data in DIgSILENT | PowerFactory are classified and stored in a multi-variable database concept, enabling the data entering, filtering, sorting as well as importing and exporting as simple as possible.

On the other hand, the Digsilent Programming Language is provided for creating automated and integrated solutions. Users can design and build new calculation functions for their calculation purposes. In transient studies, the Digsilent Programming Language is used for generating control blocks of several system components such as synchronous generators, PV and wind systems, protection and control systems ...

DIgSILENT | PowerFactory can be interfaced with many programming languages like Python via integrated API (Application Program Interface). The Python scripting language can be employed for generation of automatic tasks and user-defined calculation commands and integration of PowerFactory into other applications. By combining Python and PowerFactory, users can access to extensive standard libraries and third-party modules, e.g. interface to external database and web service.

In the study, many calculation functionalities of DIgSILENT | PowerFactory are used ranging from simple tasks such as load flow, quasi-dynamic simulation to more complex applications like optimal power flow, optimal RCS placement, electro-mechanical and electro-magnetic transient simulations. Cosimulation between PowerFactory and Python via OPC DA communication protocol is also put in use.

2.6 System impedance valuemodeling

2.6.1 HV external grid

As the thesis mainly focuses on the distribution network, the HV external grid is modelled as a voltage source with an internal impedance. The model implies that all synchronous generating units connected to the grid are at remote areas far from the distribution networks under study. The transient response of these generators therefore can be neglected except for those synchronous machine-based distributed generators installed inside the studied distribution networks like diesel generators.

2.6.2 Substation transformer

In the study, we model both primary and secondary distribution transformers by using a three-phase two-winding transformer model. Due to the inherent unbalance of the studied networks and also the requirement of unbalanced fault analysis, the transformer should be modeled in detail for each symmetrical sequence circuit. The **Positive Sequence (PS)**, **Negative Sequence (NS)**, and **Zero Sequence (ZS)** equivalent circuits of the simulated transformer are illustrated in Figure 2.11, [60].

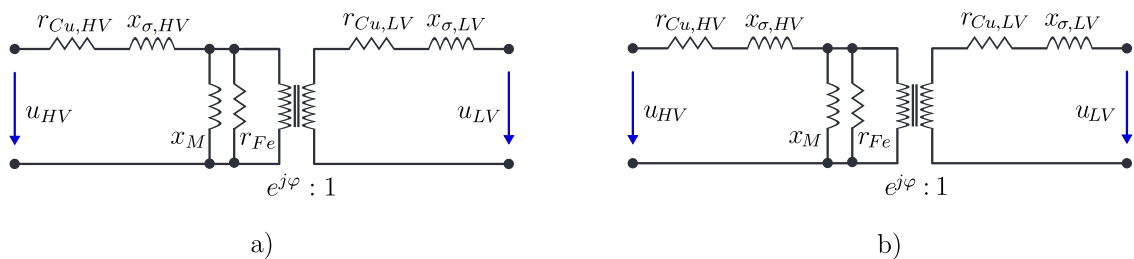


Figure 2.11 – (a) PS/NS and (b) ZS equivalent circuits of a transformer

The leakage reactances and winding resistances are included on the primary and secondary sides, and the magnetizing branch accounts for core losses. The magnetizing reactance and parallel resistance represent these losses. The transformer rating depends on the maximum total load capacity of all the connected feeders that generally takes up

the exact composition of loads could be found very difficult and varies in a wide range depending on many factors such as season, time of day, etc. For electro-mechanical and electro-magnetic transient studies, a three-phase load can be modeled as a combination of static and dynamic loads in which the portion of each load type can be manually set. The single-phase load, on the other hand, can only consist of the static type. The static load can be divided into three types including constant power, constant current, and constant impedance and represented in a common form by using three polynomial terms as, [60]:

$$P = P_0 \left[a_P \left(\frac{v}{v_0} \right)^{e_{aP}} + b_P \left(\frac{v}{v_0} \right)^{e_{bP}} + c_P \left(\frac{v}{v_0} \right)^{e_{cP}} \right] \quad (2.4)$$

$$Q = Q_0 \left[a_Q \left(\frac{v}{v_0} \right)^{e_{aQ}} + b_Q \left(\frac{v}{v_0} \right)^{e_{bQ}} + c_Q \left(\frac{v}{v_0} \right)^{e_{cQ}} \right] \quad (2.5)$$

where $a_P + b_P + c_P = 1$, $a_Q + b_Q + c_Q = 1$, and v is the voltage at the load connection point in $p.u$, v_0 is the nominal voltage.

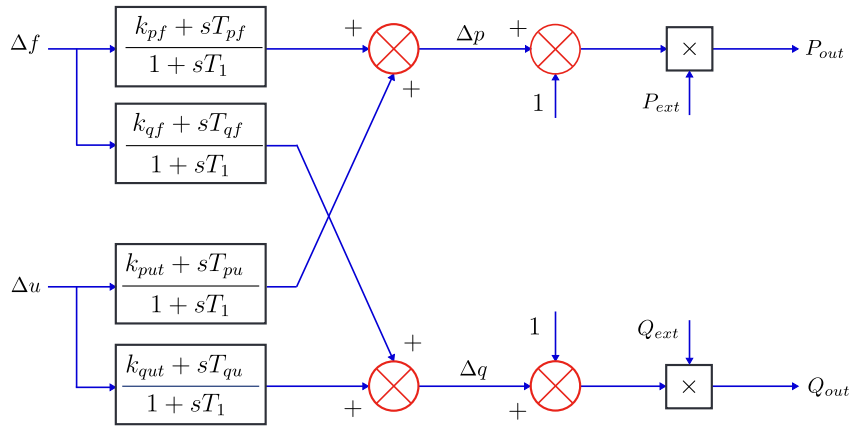


Figure 2.13 – Block diagram of the dynamic load model

The type of static load is selected by specifying respective exponents $e_{aP}/e_{bP}/e_{cP}$ and $e_{aQ}/e_{bQ}/e_{cQ}$. In the study, the constant impedance type is obtained by assigning $a_P = b_P = a_Q = b_Q = 0$ and $e_{cP} = e_{cQ} = 2$. Dynamic loads depend on grid voltage and frequency variations, and its model can be represented by the block diagram illustrated in Figure 2.13, [60]. In the three studied networks, all loads connected to one MV/LV transformer are represented by one aggregated load except for the LV loads in the three LV microgrids included inside Grid-1. These loads will be modeled in detail. The rating capacity of the aggregated load is equal to the summary of those of all the loads.

2.7 PV systems

2.7.1 Structural configuration of a PV system

PV systems are interfaced with the AC network through power electronic Voltage Source Inverter (VSI). As indicated in [61], there are two typical structures of PV systems. The first configuration is the two-stage system containing a boost DC/DC converter that

decouples the direct connection between the PV panels and the AC output for preventing ripples of AC output power from being included in PV voltage. Nevertheless, once achieving a necessary DC voltage level by a proper number of PV modules connected in series, the boost DC/DC converter can be removed, and the structure becomes the single-stage scheme. This topology is more efficient, low-price, and easier implementation compared with the former [61] and therefore, would be considered in this study. Figure 2.14 shows simplified diagrams of the two structures.

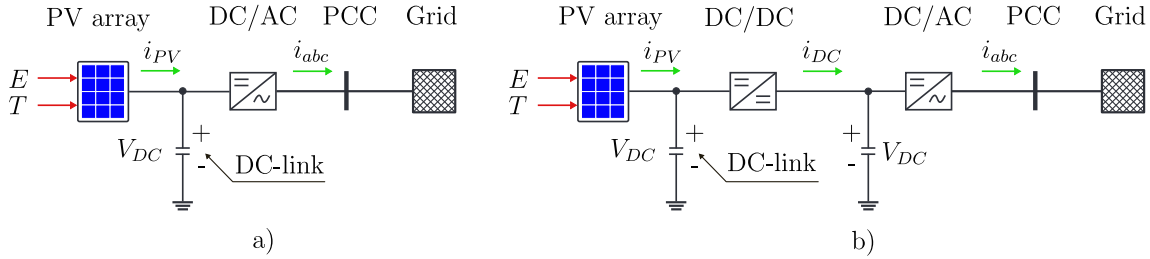


Figure 2.14 – Single-line structural diagram of (a) single-stage and (b) two-stage structures for grid-connected PV systems

As it can be seen from Figure 2.14a, the single-stage PV system consists of a PV array, a DC-link capacitor, and a three-phase DC/AC inverter connected with the grid via a filter, and then a step-up transformer. Moreover, a controller called Maximum Power Point Tracking (MPPT) system is installed for extracting maximum available power from the PV panels. The MPPT operating point is not constant but rather depends on the atmospheric conditions, including temperature and solar irradiation. In the applied PV configuration, the DC/AC inverter performs the DC-link voltage control and other functional features imposed by grid codes such as static and dynamic grid supports, and power quality commitment. In this section, the modeling and simulation of PV systems that are compliant with the grid requirements presented in Subsection 1.2 are investigated.

2.7.2 PV module equivalent circuit

Solar cells are the building element of PV modules; their equivalent circuit is depicted in Figure 2.15. The relationship between output current and voltage of a PV module, i.e. I_{PV} and V_{PV} , can be expressed by the following equations [62]:

$$I_{PV} = I_{Ph} - I_{sat} \left[\exp \left(\frac{qV_{PV}}{N_{cell}nK_bT} \right) - 1 \right] - \frac{mI_{PV}R_S + V_{PV}}{mR_P} \quad (2.6)$$

$$I_{Ph} = \left[I_{sc,STC} \frac{R_P + R_S}{R_P} + \alpha_i (T - T_{STC}) \right] \frac{E}{E_{STC}} \quad (2.7)$$

$$I_{sat} = \frac{I_{sc,STC} + \alpha_i (T - T_{STC})}{\exp \left[q \left(\frac{V_{oc,STC} + \alpha_v (T - T_{STC})}{N_{cell}K_bT} \right) - 1 \right]} \quad (2.8)$$

where N_{cell} is the cell number of the PV module; $q = 1.6e^{-19}$; C is magnitude of electron charge, $K_b = 1.38e^{-23}$ is Boltzmann constant; n is diode factor; α_i and α_v are temperature correction factor for current and voltage, respectively, $1/K$; T the temperature, K ; T_{STC} is the temperature at the Standard Test Condition (STC), K ; E is solar irradiation, W/m^2 ;

I_{sat} is the cell saturation current, A; I_{Ph} is the photo-current at the STC, A; R_S and R_P are the series and shunt resistances, respectively, Ω ; $I_{sc,STC}$, A and $V_{oc,STC}$, V are the short circuit current and open-circuit voltage at the STC, respectively.

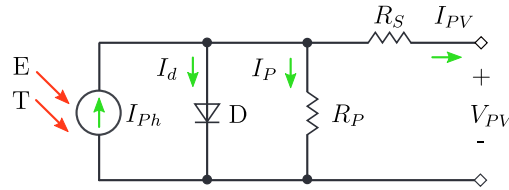


Figure 2.15 – Equivalent circuit of a PV cell

All the values of the parameters involved in Equations 2.6, 2.7, and 2.8, which are required for the modeling of the PV module in the study, are provided in Table A.1. These parameters are offered by manufacturers at STC with standard irradiation $E_{STC} = 1000 \text{ W/m}^2$ and temperature $T_{STC} = 25 \text{ }^\circ\text{C}$. Based on the above mathematical equation and given parameters, the I-V and P-V characteristic curves of a PV module at different values of solar irradiation can be determined, as shown in Figure 2.16.

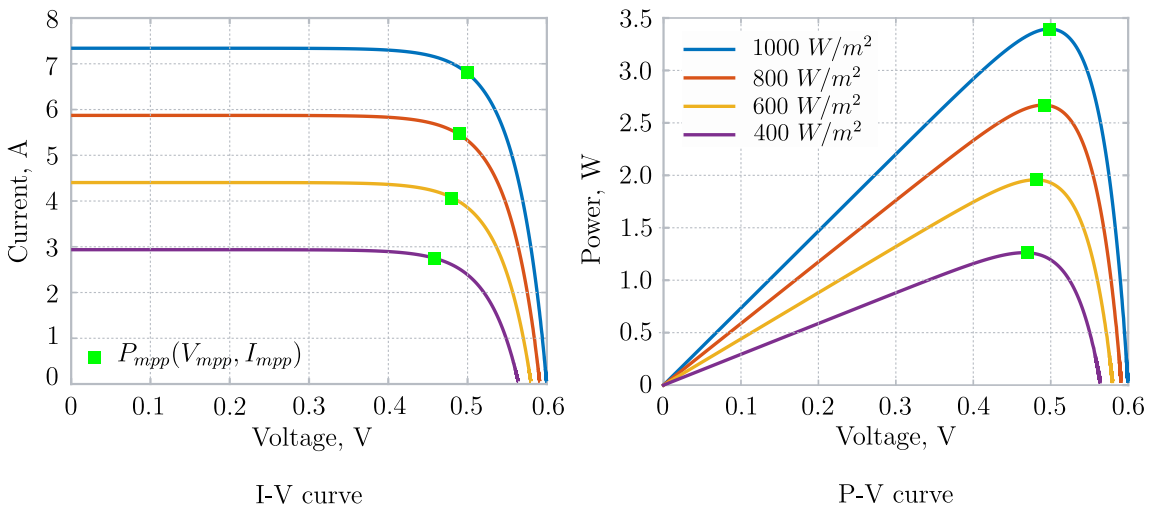


Figure 2.16 – PV characteristic curves at different solar irradiation

2.7.3 PV array and MPPT algorithm

The model of PV array is constructed by assembling an appropriate number of the above PV modules. For example, in our study, 20 modules connected in series in a string and 140 parallel strings are considered. As it can be observed on Figure 2.16, the maximum output active power of the PV array varies with the solar irradiation and solar cell temperature. Hence, a tracking system named MPPT system is implemented for tracking the maximum power point of the PV array. Various MPPT algorithms have been developed in which two commonly used are Perturb and Observe method and Incremental Conductance method [63]. The MPPT system will track the operating voltage of the PV array to extract as much active power as possible, enabling the PV system operating at its highest efficiency. In the study, the operating mechanism of the MPPT system is sim-

plified. The voltage V_{mpp} and current I_{mpp} at maximum power point corresponding to each simulation operating point, i.e., simulation hour during a day, are adjusted by the temperature and irradiation correction factors as:

$$V_{mpp} = V_{mpp,PV,STC} \cdot \frac{\ln E}{\ln E_{STC}} \cdot \alpha_v \quad (2.9)$$

$$I_{mpp} = I_{mpp,PV,STC} \cdot \frac{E}{E_{STC}} \cdot \alpha_i \quad (2.10)$$

where $V_{mpp,PV,STC}$ and $I_{mpp,PV,STC}$ are the voltage and current at the maximum power point at the STC, respectively.

Then, the maximum output active power of the PV array corresponding to the operating point with MPPT control would be:

$$P_{mpp} = V_{mpp} \cdot I_{mpp} \quad (2.11)$$

The preliminary theoretical results of the modeled PV array with solar irradiation of 1000 W/m^2 and the ambient temperature of 33° are shown in Table A.2.

2.7.4 PV model for steady-state studies

Time-domain transient simulations require the initial parameters of the studied network to be specified in advance, which can be derived only from valid power flow calculations. These initial conditions describe the network steady-state operating status at the beginning of the transient simulation, satisfying the requirements of zero-derivatives of all state variables of the components involved in the study, such as load, generators, controller, etc. Hence, before developing transient models for generating units of the studied networks, i.e., PV systems and BESS, their presentations in steady-state operation should be developed first. For power flow simulations, the active power delivered by the installed PV systems should be given. In the study, the active power output of the PV systems for each simulation scenario is calculated in advance according the equations given in Subsections 2.7.2 and 2.7.3 under normal condition with the MPPT control.

Concerning reactive power capacity requirement, as discussed in Subsection 2.6.1, in most countries, the PV systems connected to LV and MV distribution network should offer the static voltage support feature. Hence, we propose that each PV system has a local controller that can control the PV reactive power injection following the laws imposed by local authorities. As mentioned above, there are several operation modes for PV reactive power controllers. In the thesis, we assume that all the PV deliver reactive power capacity following the $Q(V)$ characteristic, in particular, voltage Q-droop control mode. The control algorithm means that the amount of reactive power required to be injected is proportional to the deviation of the grid voltage from the set-point value. Nonetheless, the reactive power output should not exceed the maximum inverter value defined in Equation 2.13 to prevent PV inverter from thermal damage. The block diagram and characteristic of the control unit are shown in Figure 2.17 [24].

Based on the control characteristic illustrated in Figure 2.17, the additional reactive power that should be delivered by the PV systems for local voltage regulation can be determined by:

$$\Delta Q = Q_{ref} - Q = -Q_{droop} S_n \frac{V_{ref} - V}{V_n} = -\frac{100 S_n}{ddroop} \frac{\Delta V}{V_n} \quad (2.12)$$

where: V is the actual voltage, V ; V_{ref} is the voltage reference dictated by local operator, V ; Q is the actual output reactive power of the PV systems, Var ; $Q_{setpoint}$ is the specified dispatch reactive power of the PV system, Var ; S_n is the PV nominal apparent power, VA ; Q_{droop} is the reactive power increment for 1% voltage deviation, %; $ddroop$ is the droop value needs to be assigned in the PV model, %.

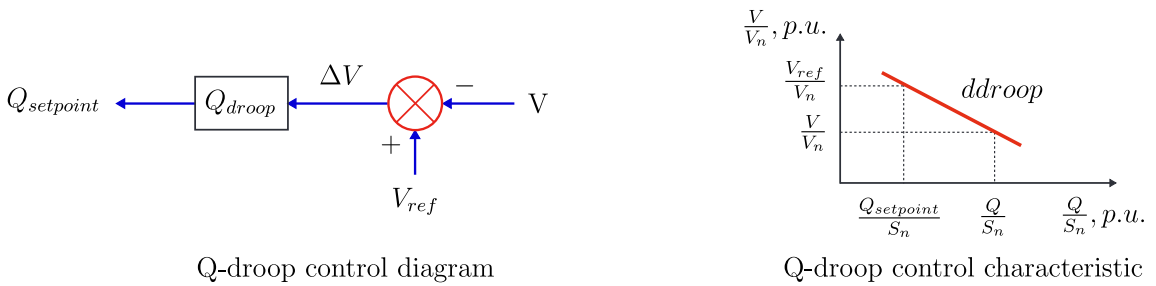


Figure 2.17 – PV voltage Q-droop control

In the study, the $ddroop$ value is selected equal to 2% as recommended by many national grid codes that will result in an increase of reactive power by 50% of the PV nominal apparent power in case of a voltage drop of 0.1 $p.u.$ However, the reactive power capacity delivered by the PV system depends on its nominal inverter rating current [47]. Particularly, the maximum value of reactive power that the inverter can inject during normal operation with the Maximum Power Point Tracking (MPPT) scheme is restricted to:

$$Q_{max} \leq \sqrt{S_n^2 - P_{mpp}^2} \quad (2.13)$$

where P_{mpp} is the PV active power at the maximum-power operating point regulated by the MPPT controller; S_n is the inverter rating apparent power.

2.7.5 PV model for transient studies

2.7.5.1 Selection of the control scheme

The transient response of the Voltage Source Inverter (VSI)-based PV systems to grid faults largely depends upon their control algorithms. Hence, when conducting transient studies under fault conditions in the presence of VSI-based PV systems, the correct models of their inverter control scheme are of essential importance. Various control algorithms dedicated to PV inverter control under fault conditions, which have realized their dynamic support requirement, as specified in Subsection 1.2, have been investigated. Among numerous methods, the control algorithm under double Synchronous Reference Frame (SFR) reported in [64] is found as the most common technique in sev-

eral recent pieces of research. Double SFR means that there are two control sub-systems, one controls **PS** current in positive-sequence SFR, and another regulates the **NS** current in the negative-sequence SFR, simplifying the estimation of reference current for the decoupling relationship between the active and reactive powers. In the case of symmetrical faults, the **NS** current reference equals zero.

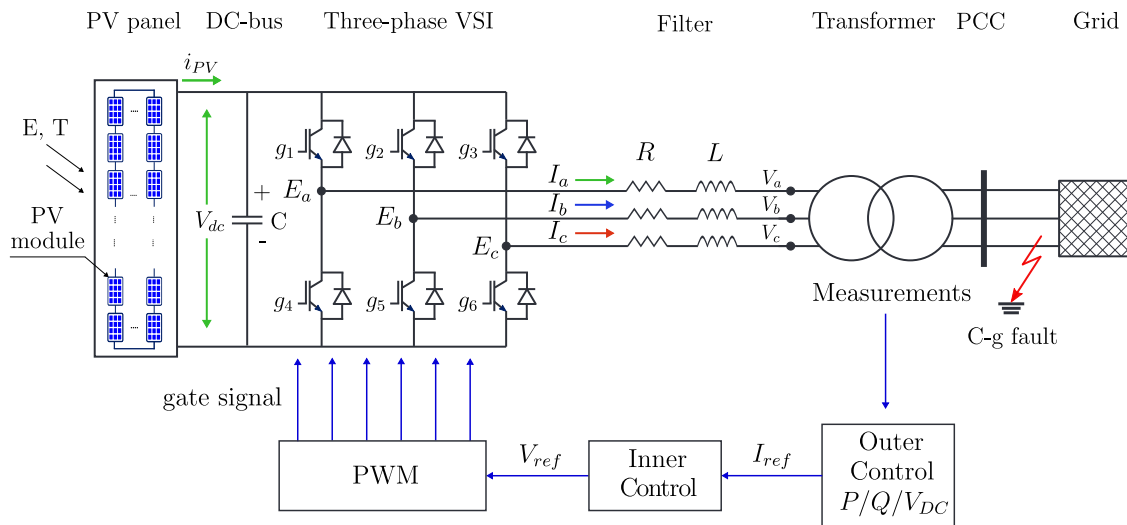


Figure 2.18 – Schematic diagram of the PV system

The above control frame is used by [65], in which the active power output quality is improved, but its side effect is the oscillation of the reactive power output and the introduction of **NS** current. In contrast, a control algorithm developed in [66] can eliminate the **NS** current, but results in the oscillation of both active and reactive output powers. The suppression of such power oscillations can be achieved as demonstrated in [67], but with current distortion. Other approaches, such as presented in [68] and [69], can satisfy the **Fault Ride Through (FRT)** requirements by generating the necessary inverter currents, but in the case of unbalanced voltage drops, such a control scheme may result in the risk of excessively high inverter output current. Consequently, the selection of control algorithms is the compromise between the power oscillation and the current quality.

For realizing the dynamic grid support requirement as presented in Section 1.2, the control algorithm used for the PV inverters in this study involves two control loops as illustrated in Figure 2.18. The first loop is named the inner current control loop, and the second one is called the outer voltage control loop, [70]. The outer loop regulates the inverter DC current and maintains the voltage of the DC-bus. The output of this control loop, which is the reference current, is delivered to the inner control loop. Then, the inner control loop regulates the current according to the reference current provided by the outer control loop to achieve the maximum output active current. Besides, the inner control loop also controls the injection of PV reactive current for supporting grid voltage during fault. The structural diagram of a three-phase VSI-based PV system is provided in Figure 2.18. In the following, the control scheme of the PV systems is presented.

2.7.5.2 AC-side dynamic models

Based on the schematic diagram of the considered PV in Figure 2.18, the relationship between the grid voltage and the VSI AC-side current is described by:

$$V_{dq} = E_{dq} + L \frac{dI_{dq}}{dt} + RI_{dq} \quad (2.14)$$

where L and R are the inductance and resistance of the filter, respectively; E_{dq} is the voltage at the terminal of the VSI, V_{dq} is the grid voltage, and I_{dq} is the VSI AC-side current, all in dq-frame.

By applying Equation B.1 for Equation 2.14, we obtain the expressions of the grid PS and NS voltages in Synchronous Reference Frame (SFR) frame as:

$$E_{dq}^+ = L \frac{dI_{dq}^+}{dt} + RI_{dq}^+ + j\omega LI_{dq}^+ + V_{dq}^+ \quad (2.15)$$

$$E_{dq}^- = L \frac{dI_{dq}^-}{dt} + RI_{dq}^- - j\omega LI_{dq}^- + V_{dq}^- \quad (2.16)$$

Then, applying Equations B.3 and B.4 to these above equations and rewriting them in separate d- and q-components, we can obtain the formulae describing the dynamics of PS and NS components in the dq-frame as, [64]:

$$L \frac{dI_d^+}{dt} = \omega LI_q^+ - RI_d^+ + E_d^+ - V_d^+ \quad (2.17)$$

$$L \frac{dI_q^+}{dt} = -\omega LI_d^+ - RI_q^+ + E_q^+ - V_q^+ \quad (2.18)$$

$$L \frac{dI_d^-}{dt} = -\omega LI_q^- - RI_d^- + E_d^- - V_d^- \quad (2.19)$$

$$L \frac{dI_q^-}{dt} = \omega LI_d^- - RI_q^- + E_q^- - V_q^- \quad (2.20)$$

where I_d^+ , I_q^+ , I_d^- and I_q^- are the control outputs; E_d^+ , E_q^+ , E_d^- and E_q^- are the control inputs; and V_d^+ , V_q^+ , V_d^- and V_q^- are the disturbances.

2.7.5.3 DC-bus dynamics

In a VSI-based PV system, the DC-link voltage should be regulated to extract as much active power as possible. Hence, the formulas describing the DC-link voltage are required. As presented in [71], the DC-bus dynamics of the PV systems can be obtained from the power balance principle and from Figure 2.14 as:

$$P_{PVarray} - \frac{d}{dt} \left(\frac{1}{2} CV_{DC}^2 \right) = P_{DC} \quad (2.21)$$

where C is the capacity of the DC link; V_{DC} is the DC link voltage; P_{DC} is the DC-side power of the PV inverter; $P_{PVarray}$ is the power delivered by the PV array.

In Equation 2.21, $P_{PVarray}$ varies according to the atmospheric conditions, so cannot be controlled by the control system. Therefore the control objective should be via P_{DC} . If we ignore the loss in switching processes, the DC-side power of the inverter can be assumed to equal its AC-side terminal power, i.e., P_{VSI} . Therefore, the equation describing the dynamics of the DC-bus is derived from the Equation 2.21 as:

$$\frac{C}{2} \frac{dV_{DC}^2}{dt} = P_{PVarray} - P_{VSI} \quad (2.22)$$

where P_{VSI} is the AC-side power of the PV inverter.

In the above equation, V_{DC} is the state variable and also the control output. On the other hand, P_{VSI} is control input, and $P_{PVarray}$ is the disturbance. Since the study aims to control the power delivered by the PV system, i.e., P_S and Q_S , the AC-side terminal power of the PV inverter, i.e., P_{VSI} , should be expressed in terms of these two power quantities, as follows, [71]:

$$P_{VSI} = P_S + \left(\frac{2L}{3V_S^2} \right) P_S \frac{dP_S}{dt} + \left(\frac{2L}{3V_S^2} \right) Q_S \frac{dQ_S}{dt} \quad (2.23)$$

where V_S is the voltage at the PV coupling point.

Substituting for P_{VSI} from Equation 2.23 in Equation 2.22, we obtain the equation expressing the dynamic of the DC-bus voltage as:

$$\frac{dV_{DC}^2}{dt} = \frac{2}{C} P_{PVarray} - \frac{2}{C} \left[P_S + \left(\frac{2LP_{S0}}{3V_S^2} \right) \frac{dP_S}{dt} \right] + \frac{2}{C} \left(\frac{2LQ_{S0}}{3V_S^2} \right) \frac{dQ_S}{dt} \quad (2.24)$$

where P_{S0} and Q_{S0} are active and reactive power under a steady-state condition of the PV systems, respectively.

From Equation 2.24, we can deduce that V_{DC} is the output, P_S is the control input, and $P_{PVarray}$ and Q_S are the disturbance inputs.

2.7.5.4 Current reference derivation

The inverter apparent power under unbalanced grid faults is defined by, [64]:

$$S = \left(e^{j\omega t} V_{dq}^+ + e^{-j\omega t} V_{dq}^- \right) \left(e^{j\omega t} I_{dq}^+ + e^{-j\omega t} I_{dq}^- \right)^* = P + jQ \quad (2.25)$$

By applying Equations B.3 and B.4 for V_{dq}^+ , V_{dq}^- , I_{dq}^+ , and I_{dq}^- in Equation 2.25, the descriptions of active and reactive powers of the considered PV systems under unbalanced fault conditions can be formulated as:

$$\begin{cases} P = P_0 + P_{c2} \cos(2\omega t) + P_{s2} \sin(2\omega t) \\ Q = Q_0 + Q_{c2} \cos(2\omega t) + Q_{s2} \sin(2\omega t) \end{cases} \quad (2.26)$$

Equation 2.26 indicates that apart from the fundamental components, i.e. P_0 and Q_0 , the active and reactive powers generated by VSI-based PV systems under unbalanced fault conditions also contain second-order harmonic cosine and sine coefficients, i.e. P_{c2} , P_{s2} , Q_{c2} , and Q_{s2} . These harmonic components are caused by the voltage unbalance. As presented in [64], these coefficients P_{c2} , P_{s2} , Q_{c2} , and Q_{s2} can be computed by:

$$\begin{bmatrix} P \\ Q \\ P_{c2} \\ P_{s2} \\ Q_{c2} \\ Q_{s2} \end{bmatrix} = \frac{3}{2} \begin{bmatrix} V_d^+ & V_q^+ & V_d^- & V_q^- \\ V_q^+ & -V_d^+ & V_q^- & -V_d^- \\ V_d^- & V_q^- & V_d^+ & V_q^+ \\ V_q^- & -V_d^- & -V_q^+ & V_d^+ \\ V_q^- & -V_d^- & V_q^+ & -V_d^+ \\ -V_d^- & -V_q^- & V_d^+ & V_q^+ \end{bmatrix} \begin{bmatrix} I_d^+ \\ I_q^+ \\ I_d^- \\ I_q^- \end{bmatrix} \quad (2.27)$$

Six components in Equation 2.27 need to be controlled while there are only four controlling current quantities. Our objective in the study is to maintain the quality of PV active power output with zero ripples, so the coefficients P_{c2} and P_{s2} should be canceled out or, in other words, should be equal to zero. Therefore, we can remove the two last rows of the coefficient matrix in Equation 2.27, leaving the reactive power ripples of PV systems uncontrolled. Assigning the values P and Q to P_{ref} and Q_{ref} respectively, we can obtain the reference quantities as follows.

$$\begin{bmatrix} I_{dref}^+ \\ I_{qref}^+ \\ I_{dref}^- \\ I_{qref}^- \end{bmatrix} = \frac{2}{3} \begin{bmatrix} V_d^+ & V_q^+ \\ V_q^+ & -V_d^+ \\ V_d^- & -V_q^- \\ V_q^- & V_d^- \end{bmatrix} \begin{bmatrix} P_{ref}/D \\ Q_{ref}/G \end{bmatrix} \quad (2.28)$$

where I_{dref}^+ and I_{qref}^+ , I_{dref}^- and I_{qref}^- are reference currents in PS and NS SFR, respectively; $D = (V_d^+)^2 + (V_q^+)^2 + (V_d^-)^2 + (V_q^-)^2$; $G = (V_d^+)^2 + (V_q^+)^2 - (V_d^-)^2 - (V_q^-)^2$.

The determination of P_{ref} and Q_{ref} is detailed in the following.

2.7.5.5 Power reference determination

The value of P_{ref} is derived from the output of the MPPT system, whereas that of Q_{ref} is obtained following the characteristic of the dynamic voltage support requirement presented in Figure 1.5. In the study, a value of 2 for variable k in Equation 1.1b is chosen. Nonetheless, opposed to the static voltage support requirement as discussed in subsection 2.7.4, particularly, in Equation 2.13, in the event of a fault, the connected PV systems should assign the highest priority to reactive power injection for supporting the grid voltage recovery. The PV maximum reactive current during a fault can reach the nominal inverter current if the voltage drops below 0.5 p.u. Therefore, the PV systems can work at maximum power point only in case of enough available capacity. The flowchart of power reference determination is illustrated in Figure 2.19. Note that in all the equations in the flowchart, subscript n denotes nominal values.

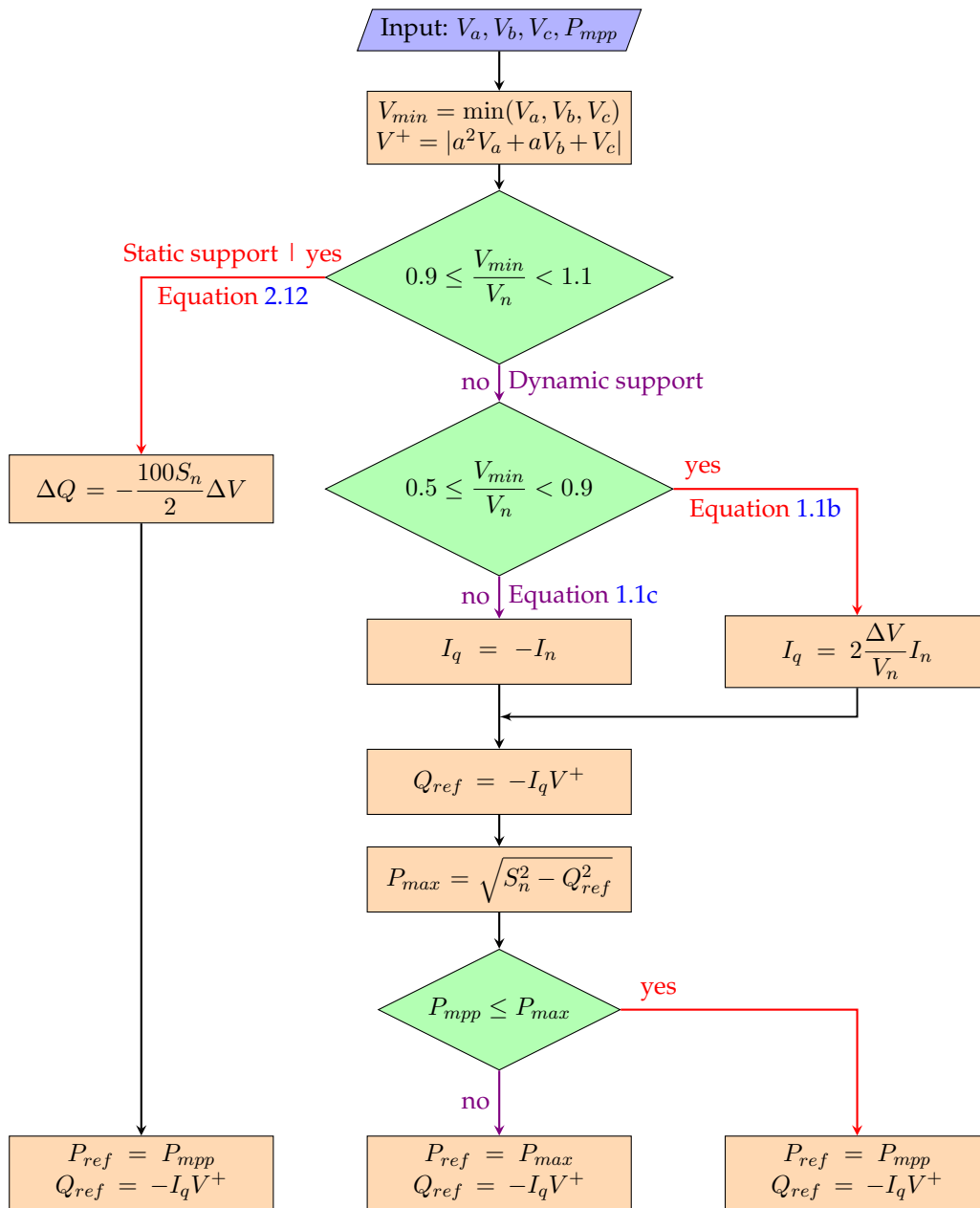


Figure 2.19 – Flowchart of the power reference generation process

2.7.5.6 DC-link voltage control

The control of DC-link voltage can be seen in the Figure 2.20. In practical operation, the outer voltage control loop regulates the DC-link voltage at the reference voltage $V_{mpp,ref}$ at the maximum power point dynamically determined by the MPPT system according to the change of weather conditions. However, in the transient study, because of the very short duration of the considered fault scenarios, the weather conditions, and hence, the reference voltage $V_{mpp,ref}$ can be regarded as unchanged. Consequently, in this study, during a fault, the $V_{mpp,ref}$ is assumed to be constant and the MPPT algorithm remains as presented in Subsection 2.7.3. By applying Laplace transformation to Equation

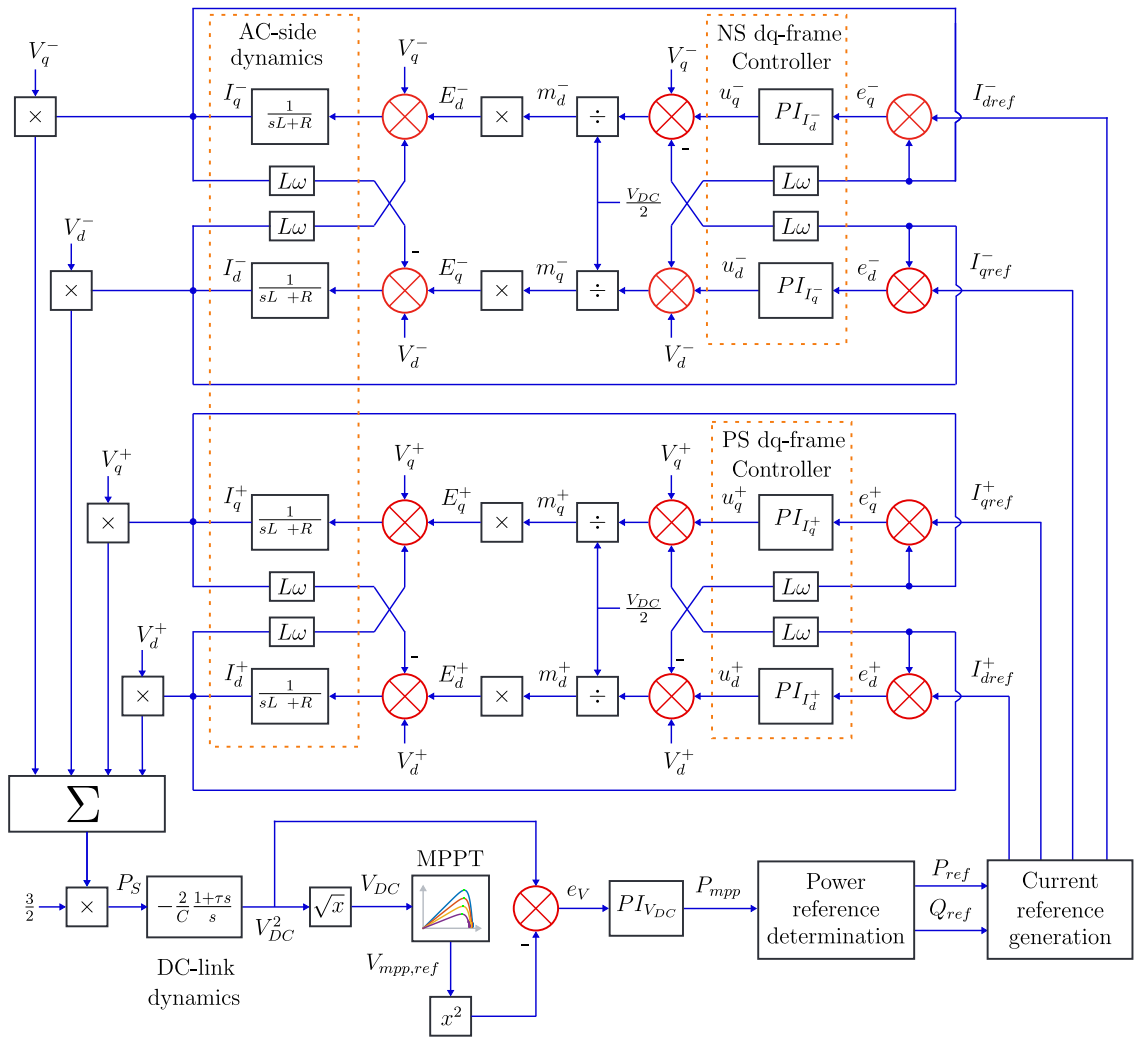


Figure 2.20 – Control block diagram of the modeled PV system in dual dq-frame

2.24, and consider $P_{PVarray}$ and Q_S as disturbance inputs, one can deduce the transfer function of DC-link dynamics [71], as follows:

$$sV_{DC}^2 = -\frac{2}{C} \left(1 + \frac{2LP_{S0}}{3V_S^2} s \right) P_S \quad (2.29)$$

$$G_V(s) = \frac{P_S}{V_{DC}^2} = -\frac{2}{C} \frac{1 + \frac{2LP_{S0}}{3V_S^2} s}{s} = -\frac{2}{C} \frac{1 + \tau s}{s} \quad (2.30)$$

where $\tau = \frac{2LP_{S0}}{3V_S^2}$ is time constant.

In the case of voltage drop during fault, the PV inverter output active current, i.e., the d-component current, should increase to maintain the PV system operating at the maximum power point. At the same time, the PV system should increase the reactive current injection for voltage recovery support. The inverter current, in this case, may exceed its nominal value and should be limited. Hence, the PV output active power shall be limited

to the maximum value, i.e., P_{max} , as presented in Figure 2.19 by increasing the DC-link voltage for keeping a sufficient room for reactive current injection. As indicated in Figure 2.21, DC-link voltage may occasionally reach its highest value, i.e., the open-circuit voltage under STC, and thus the inverter must be chosen to withstand this voltage level. Consequently, the number of the series PV module in a string should be limited to ensure that the overall open-circuit voltage of the PV array is assuredly less than the maximum operating voltage of the PV inverter. Nevertheless, the value of DC-link voltage should be below the maximum permitted value of the inverter, V_{DCmax} , defined by:

$$V_{oc} \leq V_{DCmax} = \frac{V_{max,VSI}}{n_{series}} \quad (2.31)$$

where n_{series} is the number of PV modules per string.

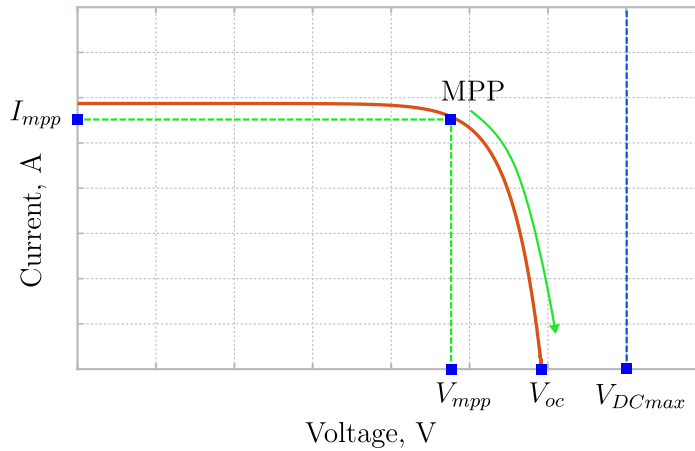


Figure 2.21 – DC-link voltage limit

According to the PV parameters provided in Table A.1, n_{series} is 20, $V_{oc,STC}$ is 43.8 V, so the overall open-circuit of the PV array would be $20 \times 43.8 = 876$ V. The nominal voltage of the VSI modeled in the study should be higher than this value.

2.7.5.7 PS and NS current controls in dual dq-frame

As demonstrated in [71], the relationships between the voltage at inverter terminal and DC-link voltage in dual PS and NS dq-frames are defined as:

$$E_d^+ = \frac{V_{DC}}{2} m_d^+ \quad (2.32)$$

$$E_q^+ = \frac{V_{DC}}{2} m_q^+ \quad (2.33)$$

$$E_d^- = \frac{V_{DC}}{2} m_d^- \quad (2.34)$$

$$E_q^- = \frac{V_{DC}}{2} m_q^- \quad (2.35)$$

where m_d^+ , m_q^+ , m_d^- , and m_q^- are the PWM modulating signals in PS and NS dq-frames.

Because of the appearance of ωL term in Equations 2.17, 2.18, 2.19, 2.20, the dynamic

response of d-component and q-component of each sequence current are coupled. To eliminate these dynamic coupling, we define m_d^+ , m_q^+ , m_d^- , and m_q^- as follows, [71]:

$$m_d^+ = \frac{2}{V_{DC}} (u_d^+ - \omega L I_q^+ + V_d^+) \quad (2.36)$$

$$m_q^+ = \frac{2}{V_{DC}} (u_q^+ + \omega L I_d^+ + V_q^+) \quad (2.37)$$

$$m_d^- = \frac{2}{V_{DC}} (u_d^- + \omega L I_q^- + V_d^-) \quad (2.38)$$

$$m_q^- = \frac{2}{V_{DC}} (u_q^- - \omega L I_d^- + V_q^-) \quad (2.39)$$

where u_d^+ , u_q^+ , u_d^- , and u_q^- are four new control inputs, [71].

Using Equations 2.36, 2.37, 2.38, and 2.39 to substitute for m_d^+ , m_q^+ , m_d^- , and m_q^- in Equations 2.32, 2.33, 2.34, 2.35, and then substituting the obtained expressions of E_d^+ , E_q^+ , E_d^- , and E_q^- to Equations 2.17, 2.18, 2.19, and 2.20, we receive four decoupled, first-order, linear systems as follows:

$$L \frac{I_d^+}{dt} = -R I_d^+ + u_d^+ \quad (2.40)$$

$$L \frac{I_q^+}{dt} = -R I_q^+ + u_q^+ \quad (2.41)$$

$$L \frac{I_d^-}{dt} = -R I_d^- + u_d^- \quad (2.42)$$

$$L \frac{I_q^-}{dt} = -R I_q^- + u_q^- \quad (2.43)$$

These above formulas indicate that the current in dual dq-frame can be regulated by u_d^+ , u_q^+ , u_d^- , and u_q^- respectively. Figure 2.20 illustrates the inner current control loops for PS and NS components in dq-frame. The difference between the reference and measured currents is compensated by the corresponding PI controllers. The outputs of PI controllers will be processed to generate modulating signals for operating the PV inverter, i.e. m_d^+ , m_q^+ , m_d^- , and m_q^- . As it can be seen in Figure 2.20 and Equations 2.40, 2.41, 2.42, and 2.43, the response of the PV systems to four current control loops are the same, hence, their corresponding PI controllers will have the same integral and proportional coefficients, i.e. identical k_p and k_i . Let us consider Equations 2.40 and 2.41, the transfer function of the AC-side dynamics in dual PS/NS dq frames would be as:

$$G_I^+ = G_I^- = \frac{I_d^+}{u_d^+} = \frac{I_q^+}{u_q^+} = \frac{I_d^-}{u_d^-} = \frac{I_q^-}{u_q^-} = \frac{1}{sL + R} \quad (2.44)$$

2.7.5.8 Model validation

In order to validate the proposed PV control scheme, we assume a two-phase fault with $R_f = 10 \Omega$ occurring on Section 03-04 of Figure 2.9. Two fault scenarios are carried out. In the first scenario, PV-1 is a traditional type without dynamic voltage support.

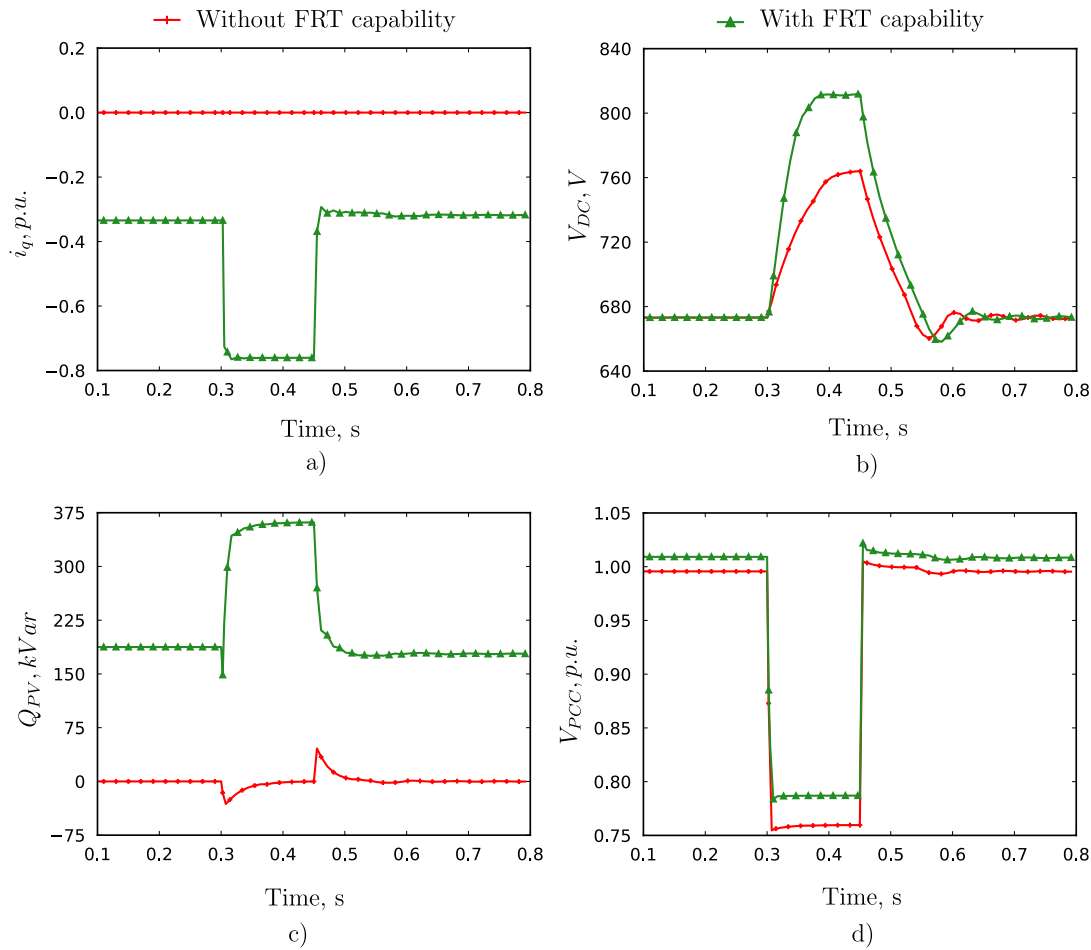


Figure 2.22 – PV response to a single-phase fault under different control strategies with (a) PV-1 reactive current, (b) DC-link voltage, (c) PV-1 reactive power, and (d) Voltage at the PV-1 PCC

In contrast, in the second scenario, the PV-1 participates in system voltage recovery by injecting an additional amount of reactive power. Moreover, in the latter simulation, PV-1 also provides static voltage support. The results obtained from simulations in the software environment DlgSILENT | PowerFactory can be observed in Figure 2.22.

Figure 2.22a shows that PV-1 without **Fault Ride Through (FRT)** capability injects no reactive current during fault as opposed to an increment of about 0.4 p.u. in case of with **FRT** capability. As a result, PV-1 reactive power almost remains at 0 kVar for the former scenario compared with about 370 kVar for the latter one (Figure 2.22c), leading to a significant increase of the voltage at the PV-1 PCC from 0.75 p.u. to just under 0.8 p.u. as demonstrated in Figure 2.22d. It should note that the reactive power plotted in Figure 2.22c is of the fundamental component. Any higher-order components and ripples are removed. Figure 2.22b also reveals that the DC-side voltage increase in the case of **FRT** capability is higher than in case of without **FRT** capability. It is obvious since the PV control loop should increase the DC-link voltage to allow the VSI injecting reactive current for voltage support, as stated in Subsubsection 2.7.5.6. Fortunately, the DC-link voltage increases to just over 800 V that is still less than the maximum permitted level of 876 V .

2.8 Battery energy storage system

The objectives of the Battery Energy Storage System (BESS) implementation in LV microgrids included in Grid-1 of Figure 2.7 is twofold. First, the BESS maintains the voltage and frequency stability of the LV microgrids when being switched from the grid-connected mode to the islanded mode in case of permanent external faults. Second, it regulates the voltage and frequency of the LV microgrids when operated in the islanded mode. For Grid-2, along with offering V/f control, the BESS is also intended to provide a fast inertial response when the overall system inertia is low to maintain frequency stability. The low-inertia issue may occur when most synchronous diesel generators are switched off, and the load demand is mostly covered by the PV systems.

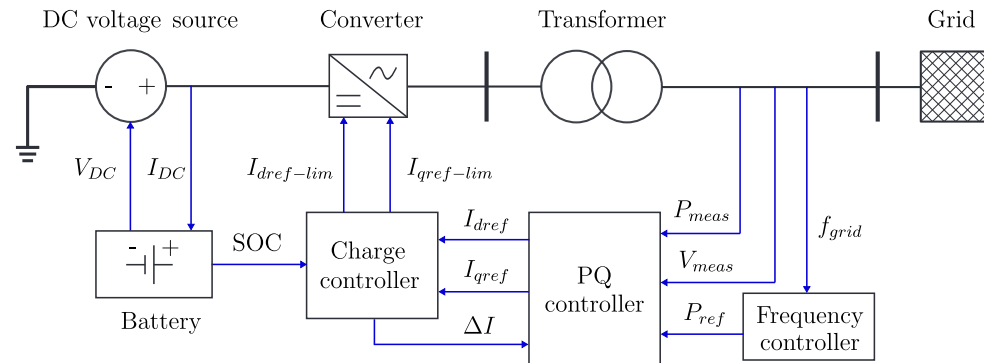


Figure 2.23 – Structural block diagram of the BESS

The study proposes to deploy the BESS model provided in [72]. This model is composed of a battery model, a voltage-sourced converter, and a BESS control system. The battery model can charge/discharge to absorb/inject energy, balancing power supply against load demand. The converter transforms DC power from battery to AC grid and vice versa. The control system ensures the proper operation of the BESS with necessary control purposes, which consists of different controllers as depicted in Figure 2.23, [72].

2.8.1 Battery model

A simplified model of battery in [72], which includes a constant internal resistance (Z_i) connected in series with a SOC-controlled voltage source, is employed. State of Charge (SOC) represents the battery current loading state. An example of set of parameters needed for modelling the battery used in Grid-2 (Figure 2.9) is provided in Table A.3. The DC voltage level at the battery terminal, which is sent to the DC-voltage source, is defined by:

$$V_{DC} = V_{max}SOC + V_{min}(1 - SOC) - I_{bat}Z_i \quad (2.45)$$

where V_{max} is cell voltage of discharge cell, V_{min} is cell voltage of fully charged cell; I_{bat} is current flowing through the battery internal impedance Z_i ; and SOC is the State of Charge of the battery.

2.8.2 Frequency controller

The frequency controller contains two parts, as presented in Figure 2.24, [72, 73]. The first part is based on a traditional droop-based proportional controller with a small dead-band. The droop coefficient determines the amount of active power that should be delivered in case of a frequency deviation, and can be defined by:

$$P - P_{ref} = -\frac{1}{K_s} (f - f_{ref}) \quad (2.46)$$

where P and f are the measured values of the BESS active power and grid frequency, respectively; P_{ref} and f_{ref} are the reference active power and frequency, respectively; and K_s is the droop coefficient.

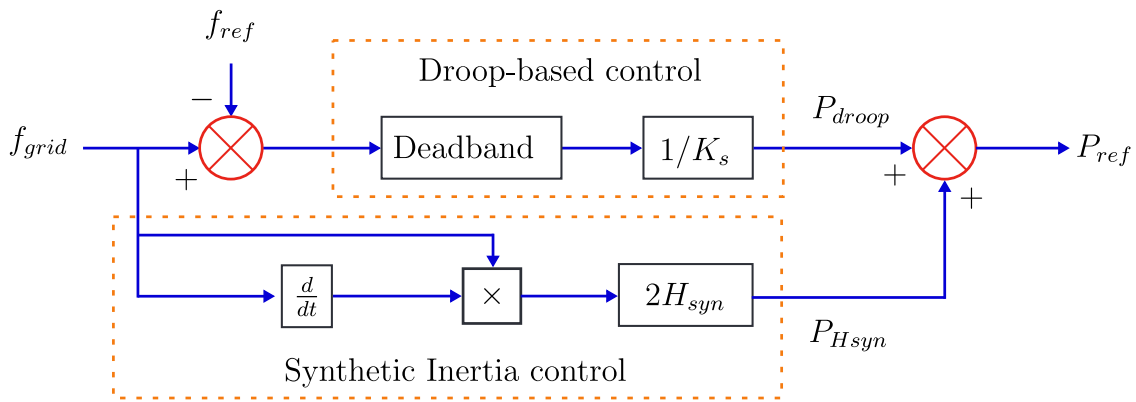


Figure 2.24 – Model of the BESS frequency controller

The second part is to emulate the inertia response that is normally offered by conventional synchronous generators. The inertia response can be adjusted by varying the synthetic inertia constant H_{syn} and represented to the system via an additional active power control signal defined by:

$$P_{H_{syn}} = 2H_{syn}f_{grid}\frac{df_{grid}}{dt} \quad (2.47)$$

where f_{grid} is the measured grid frequency in *p.u.*; H_{syn} is the synthetic inertia constant.

2.8.3 Active/Reactive power controller

The active power reference obtained from the frequency controller is filtered by a first-order integral and then forwarded to the PI control block to generate a d-component current reference. On the other hand, the voltage deviation is compensated by a q-component current reference generated by the combination of a very slow integral control block for tracking the set-point and a slope with a deadband for proportionally supporting voltage. The PQ controller model can be seen in Figure 2.25, [72]. All the needed parameters are provided in Annex A.

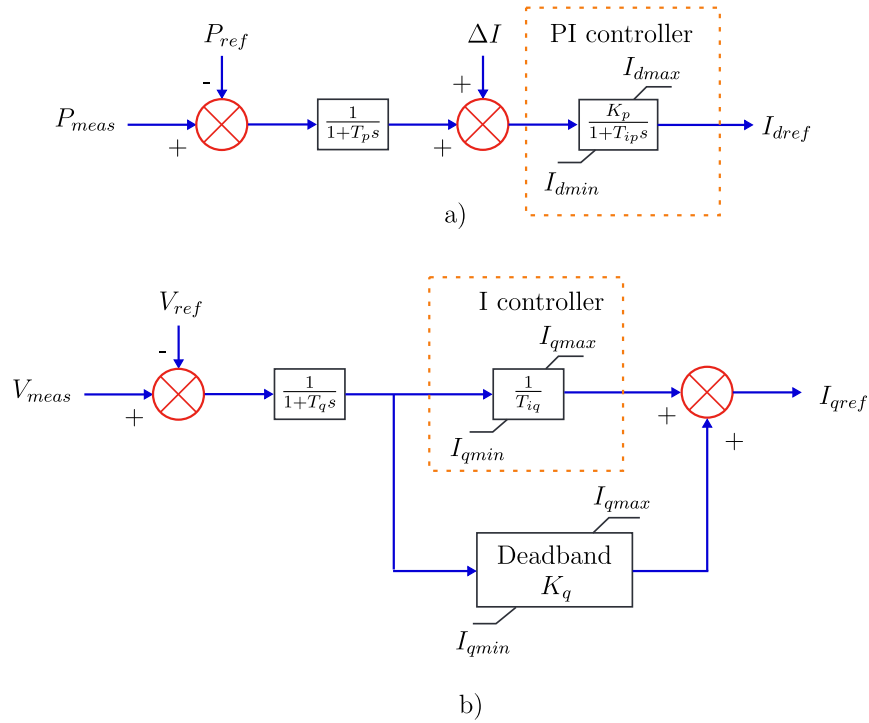


Figure 2.25 – Diagrams of the BESS PQ controller with (a) active, and (b) reactive power loops

2.8.4 Battery charge control

The battery charge control is composed of two components. The first component is a charging controller, which aims at meeting all boundary requirements presented in Table A.3. The control objective of the second component is to restrict the absolute values of the BESS output currents to its converter thermal limit.

2.9 Overview of IEC 61850 standard

IEC 61850 is a comprehensive standard for the design of a substation automation system and its applications. It defines methods for the device description in substations and an information exchange mechanism between these devices at the time of configuration and at the time of execution. IEC 61850 allows the integration of all protection, control, measurement, and monitoring functions through a common protocol. However, IEC 61850 is much more than a new protocol. It describes an engineering process and architecture with many new benefits that affect the design, specification, engineering, operation, and maintenance. In the study, all the elements involved in the protection as well as fault location and isolation systems are modeled by using the model specification in the IEC 61850 standard. We named each function according to the corresponding **Logical Node (LN)** as specified in IEC 61850-5. The names of all standard **LN**s have four characters. The **LN** names used in the study are given in Table 2.2. The overall description of the IEC 61850 standard are provided in Appendix I.

Table 2.2 – LN names in the IEC 61850 standard

LN name	Functionality	LN name	Functionality
<i>Group P: protection functions</i>		<i>Group R: protection-related functions</i>	
PIOC	Instantaneous overcurrent	RDIR	Directional element
PTOC	Time overcurrent	RBRF	Breaker failure
PTUV	Undervoltage	RSWF	Switch failure
PDIR	Direction comparison	RDRE	Fault counter
PTRC	Protection trip conditioning	RREC	Autoreclosing
<i>Group C: control</i>		<i>Group X: switchgear</i>	
CILO	Interlocking	XCBR	Circuit breaker
CSWI	Switch controller	XSWI	Circuit switch
<i>Group G: generic references</i>		<i>Group T: instrument transformers</i>	
GPAC	Generic automatic process control	TCTR	Current transformer
		TVTR	Voltage transformer

2.10 Conclusion

This chapter starts by describing different distribution layouts, along with distribution earthing systems and distribution protection schemes. Moreover, the study also briefly mentions main network components that are needed for the transient studies, such as load, transformer, overhead lines, underground cables. Next, a detailed analysis of the control strategy for PV inverters meeting all of the requirements of new grids is provided. Furthermore, to evaluate solutions proposed in the thesis, models of three given real MV grids, including Grid-1 with three LV microgrids, Grid-2, and Grid-3 are built either in DIgSILENT | PowerFactory or in Matlab | Simulink, depending on the study purposes. Based on these grid models, the proposed control strategy for PV inverters is validated by simulations in DIgSILENT | PowerFactory when being applied for the PV systems of Grid-2. On the other hand, model of the BESS with the necessary controllers is also analysed and constructed in DIgSILENT | PowerFactory. Finally, the chapter ends with the overview of the IEC 61850 standard.

Furthermore, in the next chapter, based on the proposed control strategy of the PV inverter and the component models built in DIgSILENT | PowerFactory, a new directional method will be proposed and validated.

Chapter 3

Directional approach for distribution networks with high PV penetration

Contents

3.1	Introduction	53
3.2	State-of-the-art	53
3.2.1	Fundamental operation of a RDIR element	53
3.2.2	Torque-product-based RDIR element	54
3.2.3	Impedance-based directional RDIR element	56
3.2.4	Superimposed component-based RDIR element	56
3.2.5	ANN-based RDIR element	57
3.2.6	Application of directional methods for distribution networks	57
3.3	PV fault characteristics	59
3.3.1	Equivalent sequence circuits of PV systems	60
3.3.2	Evaluation of the angles of PV fault sequence impedances	61
3.3.3	Evaluation of the magnitudes of PV fault sequence impedances	61
3.4	Formulation of the proposed directional algorithm	62
3.5	Evaluation of the proposed RDIR by analytical approach	63
3.5.1	Single-phase-to-ground fault	63
3.5.2	Two-phase fault	65
3.5.3	Two-phase-to-ground fault	66
3.5.4	Conclusion	68
3.5.5	Preliminary numerical calculation	68
3.6	Evaluation of the proposed algorithm by simulations	70
3.6.1	Single-phase-to-ground fault	70
3.6.2	Two-phase faults	79

3.6.3	Two-phase-to-ground fault	81
3.6.4	Summary evaluation of the proposed method for all kinds of unbalanced fault	82
3.7	Procedure for fault direction determination	83
3.8	Conclusion	85

3.1 Introduction

As discussed in Chapter 1, the integration of **Distributed Energy Resource (DER)**s, especially PV systems, into distribution networks has imposed lots of challenges. The need for the development of a new **Directional Element (RDIR)** element that can be used for protection as well as fault location and isolation of such an active distribution network is rather urgent. In this chapter, firstly, the review of related studies on the directional algorithm is carried out. After, a new method dedicated to distribution networks with high penetration of inverter-based PV systems is proposed. Then, the detailed fault characteristics of the PV system during fault is developed based on the PV model developed in Section 2.7. Finally, the proposed method is evaluated by using analytical analysis and then verified by simulation under different fault conditions in the software environment DIgSILENT | PowerFactory.

3.2 State-of-the-art

3.2.1 Fundamental operation of a RDIR element

Protection engineers have used **RDIR** elements for determining the fault directions regarding relay locations throughout the years. The **RDIR** element should be designed such that faults on different ends of the protected component can be categorized into two types, namely forward and reverse faults. Let us consider a simple two-source network with a Voltage Transformer (TVTR) and a Current Transformer (TCTR) as shown in Figure 3.1a. Faults with currents flowing from bus to line are considered forward. In contrast, faults with the currents leading from line to bus are regarded as reverse.

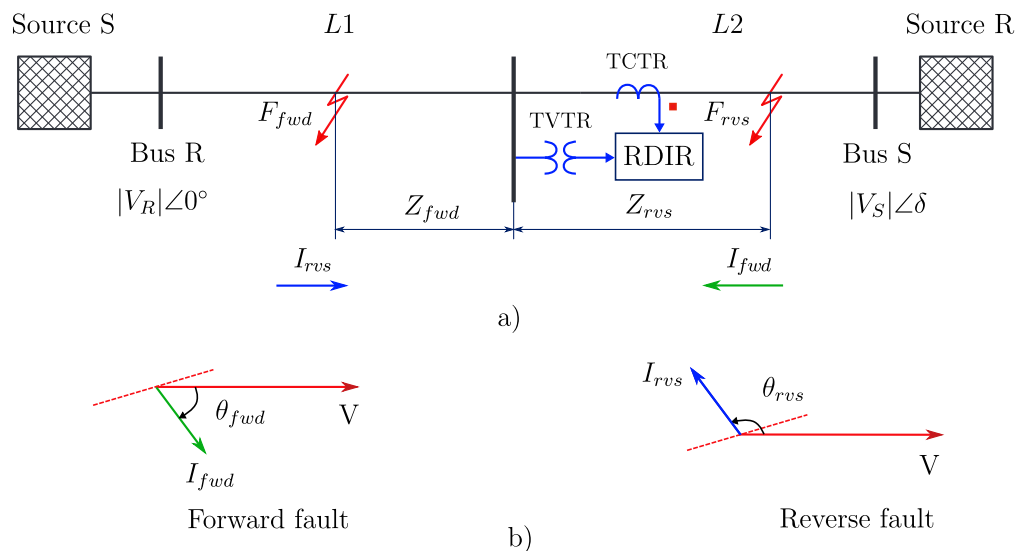


Figure 3.1 – Fundamental operating principle of a RDIR element

The **RDIR** element compares two signals for making direction decisions. The first signal is called operating quantity, and the second one is named reference or polarizing quantity. The latter signal should be able to maintain its polarity regardless of forward

or reverse faults. In contrast, the former quantity should reflect the change in polarity according to two fault locations. Normally, the current phasor is used as the operating signal, while the voltage phasor at the relay location is chosen as the reference quantity. This **RDIR** element is called voltage-polarized **RDIR** element, [74, 75, 76, 77]. However, currents can also be used as reference quantity instead, and the method is referred to as current-polarized or current-only **RDIR** elements, [78, 79, 80, 81].

3.2.2 Torque-product-based **RDIR** element

This type of **RDIR** element is operated based on the calculation of a so-call torque product to identify fault direction:

$$T = |A||B| \cos[\theta_A - (\theta_B + \theta)] \quad (3.1)$$

where A and B are polarizing and operating signals, respectively; θ_A and θ_B are their phase angles.

The polarizing signal may be phase or sequence voltages, or sequence current. The operating quantity is phase or sequence currents. If a voltage signal polarizes a **RDIR** element, it is named voltage-polarized **RDIR** element. In contrast, if a current signal polarizes a **RDIR** element, it is referred to as current-polarized element.

3.2.2.1 Phase voltage-based polarization

The phasor diagram shown in Figure 3.1b describes the fundamental principle of a voltage-polarized **RDIR** element. In case of a forward fault, the operating current lags the reference voltage by an angle θ_{fwd} that is equal to the angle of the fault loop impedance. By contrast, for a reverse fault, the current leads the voltage by an angle approximately equal to 180° minus the angle of the fault loop impedance. The angle displacements between the operating and polarizing quantities for two fault locations are as:

$$\begin{cases} \angle(V, I_{fwd}) = \theta_{fwd} = \theta_{Z_{fwd}}, & \text{in case of a forward fault;} \\ \angle(V, I_{rvs}) = \theta_{rvs} = \theta_{Z_{rvs}} + 180^\circ, & \text{in case of a reverse fault} \end{cases} \quad (3.2)$$

where Z_{fwd} and Z_{rvs} are the fault impedances of the forward and reverse faults, respectively and $\theta_{Z_{fwd}}$ and $\theta_{Z_{rvs}}$ are their phase angles.

To ensure that the phase displacement between operating and reference signals are within the boundaries established for all types of forward and reverse faults, an angle named Maximum Torque Angle (MTA) was introduced [76]. Figure 3.2 shows the performance of the 90° -connect **RDIR** element with 45° MTA for a phase-B-to-phase-C fault. In practical application, the **RDIR** element in each phase calculates a so-called torque value defined by Equation 3.3 to determine the fault direction.

$$T = |V_{pol}||I_{op}| \cos(\theta_{V_{pol}} - \theta_{I_{op}} - MTA) \quad (3.3)$$

where V_{pol} and I_{op} are the measured voltage and current; $\theta_{V_{pol}}$ and $\theta_{I_{op}}$ are their angles.

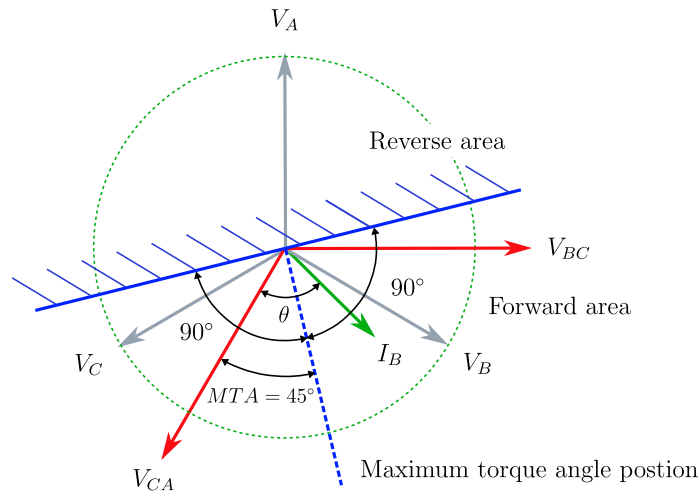


Figure 3.2 – Performance of the 90°-connection RDIR element with MTA of 45°

Equation 3.3 indicates that the obtained torque is highest when the phase difference between the current and voltage inputs is equal to the MTA. This also implies that the current input I_B in Figure 3.2 leads the voltage input V_{CA} by the MTA. A positive produced torque declares a forward fault, and a negative value indicates a reverse fault.

3.2.2.2 Sequence voltage-based polarization

Although achieving high performance in most fault conditions, the above RDIR element may face with incorrect operation in case of a typical reverse phase-to-ground fault within a network providing much dominant Zero Sequence (ZS) fault current over the remaining two sequence currents, [82]. This issue becomes more concerned when the polarization method is applied for distribution networks with grounded neutrals, i.e., short lines and low system ZS impedances. Hence, instead of phase quantities, the latter generations of directional relays use sequence quantities as the reference factor. A study in [83] proposed to use a single Positive Sequence (PS) voltage-polarized RDIR element for coping with balanced fault and another Negative Sequence (NS) or ZS voltage-referenced one for other unbalanced faults. The equation for calculating the torque value of PS voltage-polarized RDIR element is defined as, [83]:

$$T^+ = |V^+||I^+| \cos \left[\theta_{V^+} - (\theta_{I^+} + \theta_{Z_L^+}) \right] \quad (3.4)$$

where V^+ and I^+ are polarizing and operating quantities, θ_{V^+} and θ_{I^+} are their phase angles, and $\theta_{Z_L^+}$ is angle of the protected line impedance.

For detecting fault direction under unbalanced faults, RDIR elements usually make use of sequence quantity inputs. The NS and ZS voltage polarized RDIR elements calculate their sequence torque-products by, [84]:

$$T^- = |V^-||I^-| \cos \left[180^\circ + \theta_{V^-} - (\theta_{I^-} + \theta_{Z_L^-}) \right] = |T^-| \cos \theta_{T^-} \quad (3.5)$$

$$T^0 = |V^0||I^0| \cos \left[180^\circ + \theta_{V^0} - (\theta_{I^0} + \theta_{Z_L^0}) \right] = |T^0| \cos \theta_{T^0} \quad (3.6)$$

where $\theta_{Z_L^-}$ and $\theta_{Z_L^0}$ are the line NS and ZS impedance angles; and $|T^-|$, θ_{T^-} , $|T^0|$ and θ_{T^0} denote magnitudes and phase angles of the NS and ZS torque-products, respectively.

The positive value of the obtained torque-product (T^- or T^0) indicates a forward fault, and its negative value declares reverse faults. Moreover, the value of T^- or T^0 should exceed a minimum threshold to be considered as valid directional decisions. This requirement prevents the RDIR element from incorrect direction decisions in case the magnitudes of either sequence voltage or current are not sufficient to offer reliable outputs. The ZS voltage for direction identification for unbalanced faults involving ground when the NS quantities cannot offer reliable angle characteristics, [85].

3.2.2.3 Sequence current-based polarization

In some typical networks, the magnitude of polarizing sequence voltage may be insufficient to offer reliable reference; thus, polarization based on ZS current can be an alternative approach to determine the direction of ground faults [86, 84]. The torque-product values of this RDIR element is defined as:

$$T^0 = |I_{pol}| |3I^0| \cos(\theta_{I_{pol}} - \theta_{3I^0}) = |T^0| \cos \theta_{T^0} \quad (3.7)$$

where I_{pol} is the polarizing current and $3I^0$ is the operating quantity.

Similarly, positive T^0 indicates forward faults and negative T^0 declares reverse faults.

3.2.3 Impedance-based directional RDIR element

Another solution to the extremely low V_{pol} is to compute the ratio between reference and operating quantities rather than the torque-product of Equation 3.1, [86].

$$z^- = \frac{|V^-|}{|I^-|} \cos [\theta_{V^-} - (\theta_{I^-} + \theta_{Z_L^-})] \quad (3.8)$$

$$z^0 = \frac{|V^0|}{|I^0|} \cos [\theta_{V^0} - (\theta_{I^0} + \theta_{Z_L^0})] \quad (3.9)$$

The RDIR element compares the obtained impedances with the predefined thresholds to establish the fault direction. The fault is forward if the derived value is less than the forward threshold. In contrast, the RDIR element informs a reverse fault if the calculated value exceeds the reverse threshold.

3.2.4 Superimposed component-based RDIR element

For this type of RDIR element, a study in [87] developed a new approach that calculated a superimposed PS impedance for determining fault direction under all fault conditions. The superimposed PS impedance is defined as the ration between the superimposed voltage to the superimposed current:

$$\Delta Z_1 = \frac{\Delta V_1}{\Delta I_1} \quad (3.10)$$

where ΔV_1 and ΔI_1 are the incremental PS voltage and current.

For calculating the voltage and current increments, prefault values of these signals should be memorized for about five cycles prior to the fault inception. The obtained value is expected to be situated in the third quadrant for a forward fault and in the first quadrant for a reverse fault. This method can perform well under close-in fault conditions, i.e., almost zero polarizing voltage, thanks to the prefault voltage values that can offer a more stable and reliable polarization.

3.2.5 ANN-based RDIR element

Apart from these above methods, RDIR elements can also be based on Artificial Neural Network (ANN). A study in [88] proposed to use a multi-layered feed-forward neural network for fault direction detection. The method can avoid the impacts of fault types, prefault loading conditions, fault location, and impedance variations. It was evaluated by implementing a digital signal processing platform and can deal with missing data issues. A back propagation of a Levenberg–Marquardt learning method is presented in [89]. This method proved its advantage by the reduced size of the designed network. Various methods of a similar operating principle can also be found in [90, 91, 92].

The authors in [93] designed a modular neural network to identify the fault direction for transmission line protection. The method was then implemented on a digital processing platform for performance evaluation. The obtained results revealed rather promising effectiveness. ANN with the Levenberg–Marquardt algorithm was also applied in [94] with the time taken for direction decision making less than half cycle of the fundamental frequency. This method can mitigate all issues related to various fault conditions.

3.2.6 Application of directional methods for distribution networks

Conventional distribution networks are normally operated in radial configuration, hence non-directional overcurrent protection is adequate for handling unearthed faults [77, 95, 96]. RDIR elements are only used for protecting distribution networks against ground faults [97, 98]. Generally, directional principles applied for traditional single-source distribution networks are inherited from those developed for transmission networks that are presented in the above subsections. The selection of the most suitable directional methods for ground faults in a distribution network depends on its grounding method [97]. For some networks, for instance, a low-impedance grounded system, several methods are integrated simultaneously, and the best choice is selected during the processing by the RDIR element itself based on the current network configuration.

With the ever-increasing integration of Distributed Energy Resource (DER)s into distribution networks, fault currents have been turned into bidirectional. For dealing with the bidirectional fault currents, there are several solutions. One can suggest differential protection [99], but high investment cost is a substantial disadvantage of this method. Re-

cent studies in [100, 101, 102, 103, 104] proposed to use directional overcurrent or distance protection. However, these researches just reused the existing directional principles that have been used over the years. A thorough analysis of the performance of these RDIR elements under high penetration of DERs was neglected.

On the other hand, various studies toward the development of directional methods dedicated to distribution networks in the presence of DERs have been reported recently. Research in [80] presented a method that determines fault direction by comparing the phase change of PS current in reference to the prefault current. The main advantage of this method is that it does not require a voltage signal, reducing the implementation cost. Similar principle also reported in [105]. In this paper, the authors developed two algorithms for detecting the fault direction. The first one is to compute the ratio of ZS and NS currents of the fundamental frequency, and the second is to calculate the ratio of the ZS and PS components of the fifth harmonic currents. These ratios were then plotted on complex planes for finding the boundaries separating forward and reverse faults. The results showed that when the fault resistances are high, uncertainty areas where forward and reverse faults cannot be distinguished will appear.

Another paper using the ratio of NS and PS currents and also the ratio of their increments over fault duration was presented in [79]. In this study, the authors also developed two fault models of inverter-based DERs. For handling the increased impacts of synchronous generator-based DERs, the authors also designed an approach based on Support Vector Machine technique for realizing optimal decision boundary between forward and reverse areas [106]. The simulation results have demonstrated the high effectiveness of the method. However, the challenges of using the current-only directional algorithm for distribution networks with DERs can also be found in [78]. The authors concluded that this type of directional methods should be used as a secondary choice where voltage signals are not available rather than being considered as a good alternative solution.

A comprehensive study on the development of a directional algorithm for a microgrid with high penetration of DERs has been recently published in [107]. This research considered all types of DERs, including four types of wind turbine generators and inverter-based DERs. After indicating the cases when the traditional directional algorithms may face potential maloperation, the authors proposed two directional algorithms, one for balanced faults and the other for unbalanced faults. These algorithms used the ratios of subtractions between prefault and during-fault values of sequence voltages and currents to obtain operating quantities. Operating zones for the RDIR elements, depending on their locations, were defined. The proposed method showed excellent performance under various fault conditions.

After investigating state-of-the-art studies related to directional algorithms, we have realized that there are a limited number of studies focusing on directional methods dedicated to distribution networks with a high level of inverter-based DERs. A dominant number of researches deployed those principles developed for transmission networks. One of the assumptions when applying the present directional algorithms for distribution networks with a high integration of DERs is that their fault characteristics are similar to

those of conventional synchronous generators. Synchronous generator-based DERs, such as diesel generators, or wind generators of Type 1 (Squirrel Cage Induction Generator) and Type 2 (Wound-Rotor Induction Generator with Variable External Rotor Resistance) may respond to faults in the same way with synchronous generators, [108].

Under unbalanced fault conditions, the NS circuit of these DERs can be assumed to be similar to synchronous generators and, therefore, may be represented by a single NS impedance. Consequently, NS current is defined by the NS voltage caused by the fault condition and the NS impedance of the fault loop. In contrast, full converter-based NS wind turbine generators or inverter-based PV systems have different fault patterns, [108]. The NS currents of these DERs are imposed by the inverter controller [34], leading to an unconventional characteristic of the phase displacements between NS currents and voltages. The application of the existing directional algorithms for unbalanced faults in the context of high penetration of converter-based DERs should be revised.

Moreover, a majority of studies did not consider the Fault Ride Through (FRT) requirement when analyzing the performance of the applied directional algorithms, except for the approach presented in [107]. However, it did not allow the inverter-based DERs to inject NS currents under fault conditions. As stated in [109, 100], no NS injection possibly causes over-voltage issues in healthy phases under unbalanced faults. Additionally, no NS current generation may make the unbalanced faults with a low fault level more difficult to be detected. Therefore, in this chapter, we intend to develop a directional algorithm for distribution networks with a high penetration of inverter-based PV systems. The dynamic voltage support requirement imposed by current grid codes is achieved by the control scheme developed in Section 2.7. This control strategy enables the PV systems to provide NS current during unbalanced faults. The objectives of NS current generation are twofold: (i) to facilitate the detection of unbalanced faults [109], and (ii) to reduce the increased voltage in healthy phases under such fault conditions.

3.3 PV fault characteristics

Let us consider a simplified MV network provided in Figure 3.3. The network consists of two 22 kV overhead lines L1 and L2, connected to an external grid. There is also a three-phase inverter-based PV system coupled with the network via an 22/0.4 kV step-up transformer. A TVTR and a TCTR are implemented for data measurement.

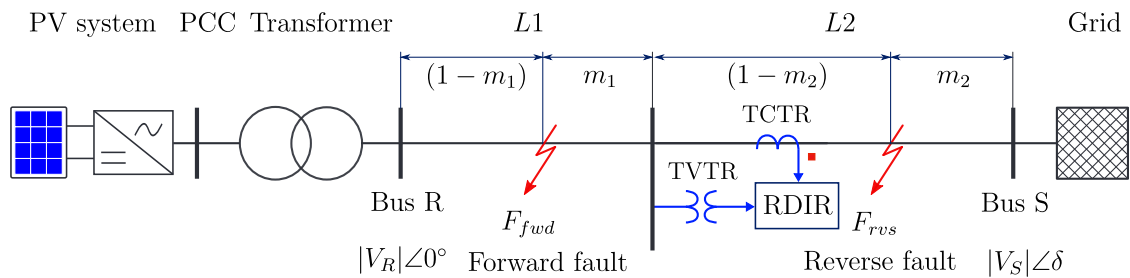


Figure 3.3 – Single-line diagram of the studied network

In Figure 3.3, the red dot at the Current Transformer (TCTR) location indicates its polarity mark. The secondary current of the TCTR is in phase with its primary current if the latter flows in at the polarity mark, i.e., from Bus-S to Bus-R. Conversely, the two currents are in opposite directions. So, for the forward fault (F_{fwd}) of Figure 3.3, the current sensed by the RDIR element is in phase with the current flowing in line L2. By contrast, for the reverse fault (F_{rvs}), the current sensed by the RDIR element is out-of-phase with the primary current flowing in L1. Without loss of generality, we assume that the voltage angle at bus-R is reference phasor, and its phase angle, therefore, is equal to zero. The voltage phasor at bus-S leads that at bus-R by an angle δ .

3.3.1 Equivalent sequence circuits of PV systems

Fault analysis of inverter-dominated grids requires proper transient models of the involved components, in our case inverter-based PV systems. In the study, the sequence circuits of such PV generating units during unbalanced faults are developed and provided in Appendix B.2. It worth mentioning that in the case of an earthed fault, the PV system circuit is open to the Zero Sequence (ZS) current due to the delta connection of at least one of the PV transformer windings. As a result, the part of the circuit that contains PV systems does not conduct the ZS during earthed faults.

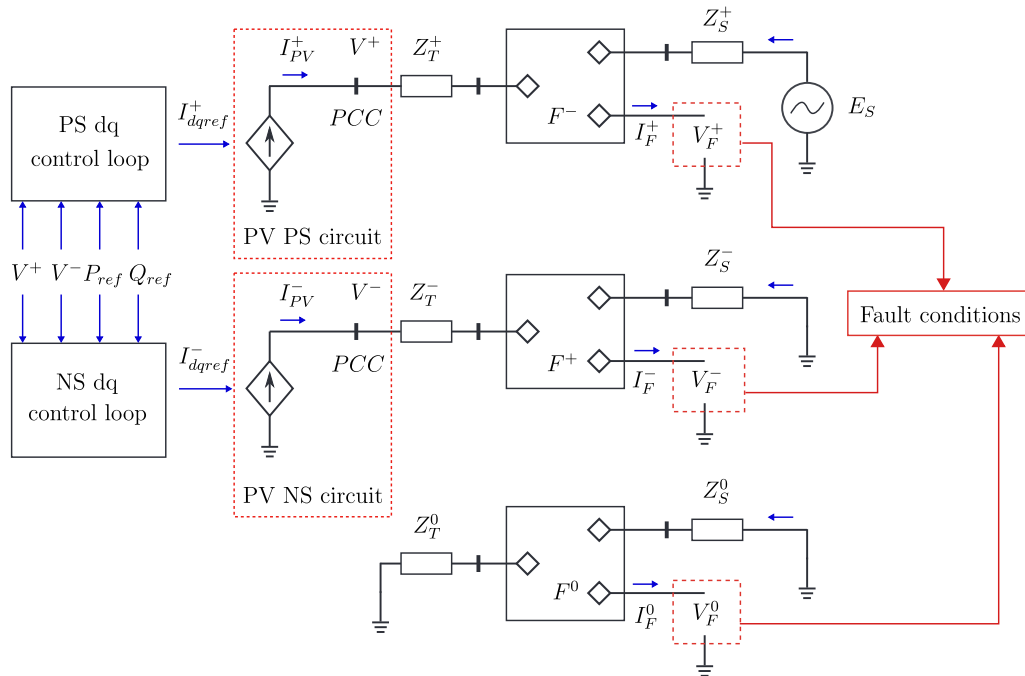


Figure 3.4 – PV equivalent sequence circuits under unbalanced fault conditions

Equations B.7 and B.8 have shown that the sequence currents contributed by the PV systems are controlled separately. The PS current is regulated by the PS dq-frame controller while NS current is controlled by the NS dq-frame controller, following the control scheme in Figure 2.20. Therefore, for all types of unsymmetrical fault, the PV system can be represented by only two separately voltage-controlled current sources, namely PS and NS current sources, [110]. Consequently, the final equivalent sequence circuits of the PV

systems and the external grid during unsymmetrical faults are as illustrated in Figure 3.4. The interconnection pattern of these sequence circuits is defined by the fault types.

3.3.2 Evaluation of the angles of PV fault sequence impedances

The development of the equations representing the angle features of the PV fault sequence impedances is provided in Appendix B.3. By observing these above formulas, we can conclude that the angle characteristics of the PV PS and NS fault impedances are defined by the fault severity, i.e., the voltage drop and the unbalance factor of the voltage at the Point of Common Coupling (PCC). Concerning voltage drop, in some cases, for instance, PV systems and faults are close to the RDIR location, the PV systems may suffer a severe voltage drop, even zero-voltage condition [110]. However, these PV systems should not be disconnected as declared by grid codes and satisfy the requirement on dynamic voltage support. The reactive power injection in such a case may reach inverter nominal apparent power, leading to no active power generation. Consequently, the phase angle of their PS and NS fault impedances are the same and equal to $\pi/2$. Regarding the voltage unbalance factor, the study in [111] indicates that this factor is usually inside the range of $0.1 < \beta < 0.4$ even though higher values can also be observed.

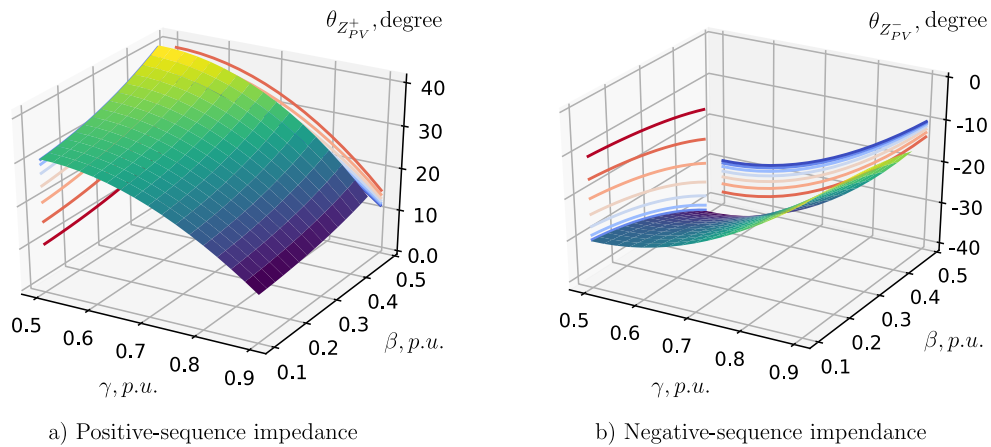


Figure 3.5 – Analytical evaluation of the PV fault angle characteristics

The preliminary analytical evaluation of the PS impedance angle characteristic is included in Figure 3.5. The projections of three-dimension plot of the PS impedance angle characteristic on $\gamma - \theta_{PV}^+$ and $\beta - \theta_{PV}^+$ planes in Figure 3.5 show that the angle characteristic of the PV PS impedance is within the range of 10 to 40° and therefore, that of NS impedance varies from -40 to -10°. Except for those cases when voltage at the PCC drops below 0.5 p.u., the value for PS component is 90° and that for NS component is -90°.

3.3.3 Evaluation of the magnitudes of PV fault sequence impedances

The development of equations expressing the magnitudes of the PV sequence impedances under faults is included in Appendix B.4. Equations B.25a and B.25b have drawn a conclusion that the magnitudes of the PV PS and NS fault impedances, similar to those of their angle characteristics, entirely depend on the voltage unbalance factor and the fault

severity. By changing the values of β and γ by steps within the ranges similar to what being carried out in Subsection 3.3.2, the initial assessment of the magnitudes of PV PS and NS impedances are shown in Figures 3.6.

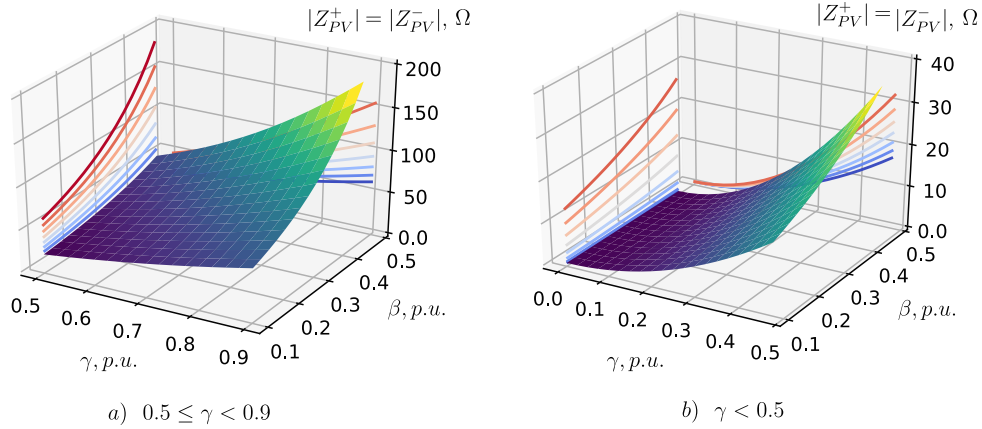


Figure 3.6 – Analytical evaluation of the magnitude of the PV sequence impedances

Figure 3.6 indicates that the magnitudes of the PV sequence impedances can reach 200 Ω in the case of minor voltage drop but can decrease to below 5 Ω if the voltage drops considerably. Hence, we can conclude that the variation of the PV sequence impedances is largely dependent upon the voltage drop level, and in turn, the PV inverter control strategy. Based on these initial evaluation of the PS and NS fault impedances of the PV systems, the study on the impacts of non-conventional PV fault behaviors on the existing NS directional algorithm is provided in Appendix F.8.

3.4 Formulation of the proposed directional algorithm

As demonstrated in Appendix F.8, the traditional NS directional principle cannot guarantee the accurate operation for distribution networks with high penetration of PV systems due to their unconventional current and voltage waveforms during unbalanced faults. Therefore, in the study, we intend to propose a new approach that can offer reliable performance under the condition of high PV penetration. In particular, instead of the NS product-torque, the proposed method calculates an impedance based on the ratio between the prefault voltage and the during-fault NS current, as follows:

$$z_{measured}^- = \frac{V_{Fprefault}}{I^-} \quad (3.11)$$

In Equation 3.11, $V_{Fprefault}$ is the prefault voltage measured at the location of the RDIR element in Figure 3.3. The prefault values of the voltage are deployed because, in steady-state operation, the voltage is normally maintained within a permitted range and therefore, can offer a reliable reference compared with the strange pattern of faulted quantities likes NS voltage in the context of high penetration of inverter-based sources. The use of prefault voltage as polarizing quantity has been applied in previous researches,

such as in [87, 107]. However, these methods are different from the proposed algorithm since they use the subtraction between the prefault and during-fault values to detect the fault direction. Due to the contribution of PV systems to the grid voltage recovery during the fault, in terms of reactive power injection, these methods still face various issues, as discussed in Section 3.2.6.

Another method such as [79] uses the ratio between the increments of PS and NS currents, i.e. $\Delta I^+/\Delta I^-$, to identify the fault direction. The simulation results have demonstrated its effectiveness. However, as recommended in [78], current-only RDIR methods should be regarded as alternative solutions only if one should consider a low-cost implementation. The traditional voltage-polarized directional techniques should have the highest priority over the others. Concerning the operating quantity, despite strange patterns, NS current is still an effective information source for fault description, as demonstrated in the study in [107]. In the following, we evaluate the proposed method by using the analytical approach.

3.5 Evaluation of the proposed RDIR by analytical approach

In this section, we apply the superposition theory presented in Appendix D.1 for evaluating the proposed directional approach. Since the pure-fault circuits provided in Figure D.1c describes the equivalent network for three-phase balanced faults and so cannot be deployed for other unbalanced faults. Therefore, a suitable pure-fault sequence circuit should be developed to investigate various fault types. Moreover, all quantities are denoted by Δ symbol to represent the superimposed-state network. For simplicity, we assume that the PS and NS impedances of network components are identical, except for those of PV systems. Besides, the ZS impedance of the line is assumed to be three times its PS value while that of the transformer remains the same as its PS impedance is. In the case of a forward fault, the RDIR element measures the NS current fed by the external grids. In contrast, for a reverse fault, the RDIR element operates on the NS current contributed by the PV systems. In the following, the formulas describing $z_{measured}^-$ will be investigated separately for each type of unbalanced faults. Depending on the fault type, we need to connect those sequence equivalents diagrams developed in Appendix D.2 in an appropriate way for forming the corresponding sequence connection diagram.

3.5.1 Single-phase-to-ground fault

Figure 3.7 illustrates the interconnected superimposed-state circuit of a phase-A-to-ground fault of Figure 3.3, in which the equivalent PS, NS, and ZS sequence circuits are taken from Appendix D.2. An additional impedance Z_f that stands for fault impedance is added to this circuit.

By applying the second Kirchhoff's law to the overall circuit given in Figure 3.7, one obtains the relationship between the prefault voltage at the RDIR location, i.e. $V_{Fprefault}$, and the fault sequence voltages, as follows:

$$V_{Fprefault} = -\Delta V_F^+ - \Delta V_F^- - \Delta V_F^0 + 3Z_f \Delta I_F^- \quad (3.12)$$

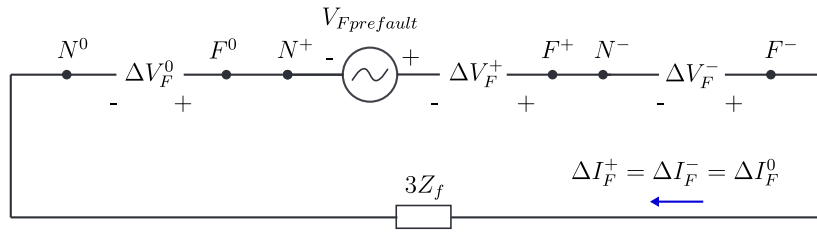


Figure 3.7 – Superimposed circuit for a single-phase-to-ground fault

3.5.1.1 Forward fault

From Figure D.2, the relationship between the PS and NS currents sensed by the RDIR element can be acquired as:

$$\Delta I^+ = \frac{c_{fwd}^-}{c_{fwd}^+} \Delta I^- = c_{fwd} \Delta I^- \quad (3.13)$$

where $c_{fwd} = c_{fwd}^-/c_{fwd}^+$; c_{fwd}^+ and c_{fwd}^- are obtained from Tables D.1 and D.2.

By substituting Equation 3.13 and the related equations provided in Tables D.1, D.2, and D.3 to Equation 3.12, the relationship between the prefault voltage at the Voltage Transformer (TVTR) location and the NS current fed to the RDIR element in case of the single-phase-to-ground forward fault is defined as follows:

$$V_{Fprefault} = \left[c_{fwd} Z_{fwd-2}^+ + Z_{fwd-2}^+ + c_{fwd}^- \left(Z_{\sum fwd}^0 + 3Z_f \right) \right] \Delta I^- \quad (3.14)$$

As indicated in Appendix D.2, the NS current is equal to the corresponding superimposed quantity if we assume that the prefault network is balanced. Hence, ΔI^- is equal to I^- . Based on Equations 3.11 and 3.14, the impedance measured in case of a forward single-phase-to-ground fault with the inputs of $V_{Fprefault}$ and I^- is as follows:

$$z_{measured-fwd}^- = \frac{V_{Fprefault}}{I^-} = Z_{\sum fwd}^- \quad (3.15)$$

where $Z_{\sum fwd}^- = c_{fwd} Z_{fwd-2}^+ + Z_{fwd-2}^+ + c_{fwd}^- \left(Z_{\sum fwd}^0 + 3Z_f \right)$.

3.5.1.2 Reverse fault

Similarly, by analyzing Figure D.2, the relationship between the PS and NS currents sensed by the RDIR element in this fault type can be determined as:

$$\Delta I_{PV}^+ = \frac{c_{rvs}^-}{c_{rvs}^+} \Delta I_{PV}^- = c_{rvs} \Delta I_{PV}^- \quad (3.16)$$

where $c_{rvs} = c_{rvs}^-/c_{rvs}^+$; c_{rvs}^+ and c_{rvs}^- are obtained from Tables D.1 and D.2.

By substituting Equation 3.16 and the related equations provided in Tables D.1, D.2,

and D.3 to Equation 3.12, the relationship between the prefault voltage at the TVTR location and the NS current fed to RDIR element in case of a reverse single-phase-to-ground fault is defined as follows:

$$V_{Fprefault} = [c_{rvs} (Z_{rvs-1}^+ + Z_{PV}^+) + (Z_{rvs-1}^+ + Z_{PV}^-) + c_{rvs}^- (Z_{\Sigma rvs}^0 + 3Z_f)] \Delta I_{PV}^- \quad (3.17)$$

The NS current fed to the RDIR element in this fault scenario is in opposite direction with the primary NS current since it flows into the Current Transformer (CT) at the non-polarity mark as illustrated in Figure 3.3. Hence, based on Equations 3.11 and 3.17, the impedance measured by the RDIR element in case of a reverse single-phase-to-ground fault with the inputs of $V_{Fprefault}$ and $-I_{PV}^-$ is as follows:

$$z_{measured-rvs}^- = \frac{V_{Fprefault}}{-I_{PV}^-} = -Z_{\Sigma rvs}^- \quad (3.18)$$

where $Z_{\Sigma rvs}^- = c_{rvs} (Z_{rvs-1}^+ + Z_{PV}^+) + (Z_{rvs-1}^+ + Z_{PV}^-) + c_{rvs}^- (Z_{\Sigma rvs}^0 + 3Z_f)$.

3.5.2 Two-phase fault

Figure 3.8a illustrates the superimposed-state circuit of the phase-B-to-phase-C fault of Figure 3.3 in which the equivalent sequence diagrams are taken from Subsection D.2. By applying second Kirchhoff's law to the overall circuit given in Figure 3.8, one obtains:

$$V_{Fprefault} = -\Delta V_F^+ + \Delta V_F^- - Z_f \Delta I_F^- \quad (3.19)$$

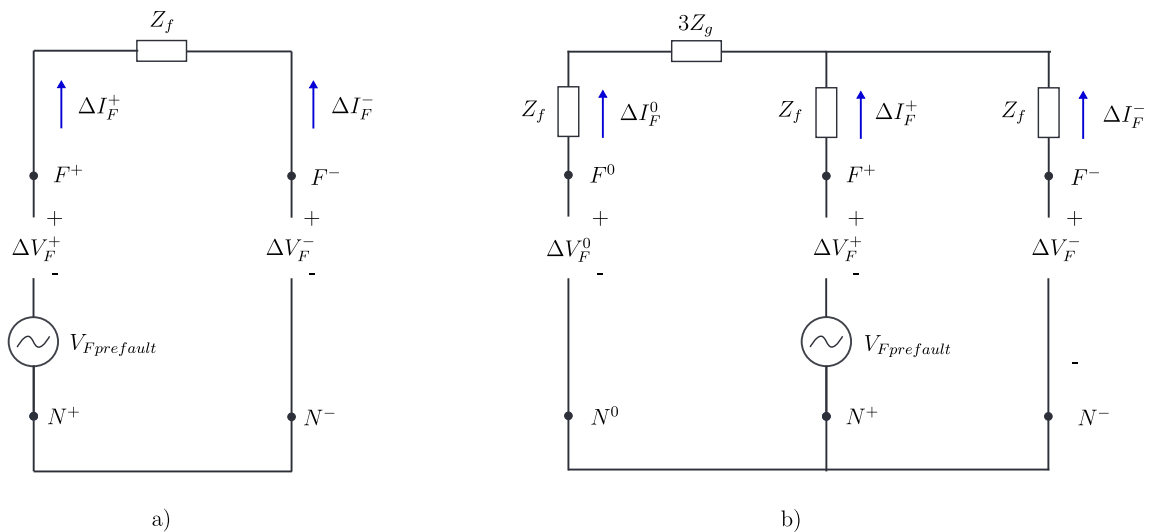


Figure 3.8 – Superimposed circuits for (a) two-phase, and (b) two-phase-to-ground fault

3.5.2.1 Forward fault

For a forward fault, the PS current can be expressed via the NS current as:

$$\Delta I^+ = -\frac{c_{fwd}^-}{c_{fwd}^+} \Delta I^- = c_{fwd} \Delta I^- \quad (3.20)$$

By substituting Equation 3.20, and the related equations, provided in Tables D.1, D.2, and D.3 to Equation 3.19, for a two-phase forward fault, the prefault voltage at the TVTR location can be expressed via the NS current fed to the RDIR element as:

$$V_{Fprefault} = \left(c_{fwd} Z_{fwd-2}^+ - Z_{fwd-2}^+ - c_{fwd}^- Z_f \right) \Delta I^- \quad (3.21)$$

Finally, based on Equations 3.11 and 3.21, the measured impedance is as:

$$z_{measured-fwd}^- = \frac{V_{Fprefault}}{I^-} = Z_{\Sigma fwd}^- \quad (3.22)$$

where $Z_{\Sigma fwd}^- = c_{fwd} Z_{fwd-2}^+ - Z_{fwd-2}^+ - c_{fwd}^- Z_f$.

3.5.2.2 Reverse fault

The PS current sensed by the RDIR element is represented by the NS current as:

$$\Delta I_{PV}^+ = -\frac{c_{rvs}^-}{c_{rvs}^+} \Delta I_{PV}^- = c_{rvs} \Delta I_{PV}^- \quad (3.23)$$

Consequently, the relationship between prefault voltage and NS current sensed by the RDIR element is defined by:

$$V_{Fprefault} = \left[c_{rvs} (Z_{rvs-1}^+ + Z_{PV}^+) - (Z_{rvs-1}^+ + Z_{PV}^-) - c_{rvs}^- Z_f \right] \Delta I_{PV}^- \quad (3.24)$$

Based on Equations 3.11 and 3.24, the reverse measured impedance is defined by:

$$z_{measured-rvs}^- = \frac{V_{Fprefault}}{-I_{PV}^-} = -Z_{\Sigma rvs}^- \quad (3.25)$$

where $Z_{\Sigma rvs}^- = c_{rvs} (Z_{rvs-1}^+ + Z_{PV}^+) - (Z_{rvs-1}^+ + Z_{PV}^-) - c_{rvs}^- Z_f$.

3.5.3 Two-phase-to-ground fault

The superimposed sequence network for a phase-B-to-phase-C-to-ground fault is illustrated in Figure 3.8b. All the expressions determining the involved impedances in this figure can be found in Tables D.1, D.2, and D.3. Impedance Z_f describes fault impedance between two faulted phases and impedance Z_g signifies ground fault impedance. By analyzing the network of Figure 3.8b, one can get:

$$V_{Fprefault} = -\Delta V_F^+ + \Delta I_F^+ Z_f + \Delta V_F^- - \Delta I_F^- Z_f \quad (3.26)$$

3.5.3.1 Forward fault

By applying the first Kirchhoff's law to the network of Figure 3.8b, the relationship between ΔI^+ and ΔI^- can be expressed as:

$$\Delta I^+ = \frac{1}{c_{fwd}^+} \left(\frac{Z_{fwd-2}^+ + c_{fwd}^- Z_f}{Z_{\Sigma fwd}^0 + Z_f + 3Z_g} - c_{fwd}^- \right) \Delta I^- = c_{fwd} \Delta I^- \quad (3.27)$$

Substituting Equation 3.27 and those equations provided in Tables D.1, D.2, and D.3 to Equation 3.26, the desired expression can be realized as:

$$V_{Fprefault} = \left(c_{fwd} Z_{fwd-2}^+ - Z_{fwd-2}^+ + c_{fwd} c_{fwd}^+ Z_f - c_{fwd}^- Z_f \right) \Delta I^- \quad (3.28)$$

Finally, we have the expression for the impedance measured by the RDIR element with the reference quantity $V_{Fprefault}$ and I^- as:

$$z_{measured-fwd}^- = \frac{V_{Fprefault}}{I^-} = Z_{\Sigma fwd}^- \quad (3.29)$$

where $Z_{\Sigma fwd}^- = c_{fwd} Z_{fwd-2}^+ - Z_{fwd-2}^+ + c_{fwd} c_{fwd}^+ Z_f - c_{fwd}^- Z_f$.

3.5.3.2 Reverse fault

Similar to the forward fault, we can derive the necessary formula expressing the relationship between the PS and NS currents measured by the RDIR element as:

$$\Delta I_{PV}^+ = \frac{1}{c_{rvs}^+} \left(-c_{rvs}^- + \frac{Z_{PV}^- + Z_{rvs-1}^+ + c_{rvs}^- Z_f}{Z_{\Sigma fwd}^0 + Z_f + 3Z_g} \right) \Delta I_{PV}^- = c_{rvs} \Delta I_{PV}^- \quad (3.30)$$

Substituting all the above equation and those Equations offered in Tables D.1, D.2, and D.3, the relationship between prefault voltage and the NS current measured by the RDIR element for a two-phase-to-ground reverse fault is defined by:

$$V_{Fprefault} = [c_{rvs} (Z_{rvs-1}^+ + Z_{PV}^+) - (Z_{rvs-1}^+ + Z_{PV}^-) + c_{rvs} c_{rvs}^+ Z_f - c_{rvs}^- Z_f] \Delta I_{PV}^- \quad (3.31)$$

Finally, we have the expression for the impedance measured by the RDIR element with the reference quantity $V_{Fprefault}$ and $-I_{PV}^-$ as:

$$z_{measured-rvs}^- = \frac{V_{Fprefault}}{-I_{PV}^-} = -Z_{\Sigma rvs}^- \quad (3.32)$$

where $Z_{\Sigma rvs}^- = c_{rvs} (Z_{rvs-1}^+ + Z_{PV}^+) - (Z_{rvs-1}^+ + Z_{PV}^-) + c_{rvs} c_{rvs}^+ Z_f - c_{rvs}^- Z_f$.

3.5.4 Conclusion

In this part, we have obtained the expressions of the measured impedances for all kinds of unbalanced faults. The non-linear relation between state variables, i.e., fault current and voltage have been eliminated, leaving only impedances in the final equations. In the following, we evaluate numerically the possible ranges of the measured impedances.

3.5.5 Preliminary numerical calculation

3.5.5.1 Component impedance value investigation

Equations 3.15, 3.18, 3.22, 3.25, 3.29, and 3.32 indicate that the measured impedances are fully defined by the impedances of the associated components. The possible values of all elements involved in the network in Figure 3.3 are given in Table 3.1. As mentioned in Subsection 2.2.2 the length of MV feeders range from about 3 to 50 km. A set of typical types of diverse MV feeders are taken from [112], where their relative impedances are in range of 0.35 to 0.49 Ω/km .

By varying all the involved parameters, we can determine the possible ranges of the measured impedances; and therefore, the thresholds for fault direction determination can be obtained. For simplicity, we assume two operation scenarios of the external source, one for low and one for high loading conditions that correspond the short-circuit capacities of 400 MVA and 1000 MVA, respectively. Hence, the external source impedance is 0.484 Ω for the former scenario and 1.21 Ω for the latter one. The line length varies by a step of 10 km from 3 to 53 km, and the fault resistances are within the range of 0 to 40 Ω .

Table 3.1 – Typical ranges of the network component impedances and its angles

Element						
HV grid		Line		PV transformer		Fault resistance
Z_S, Ω	$\theta_{Z_S}, ^\circ$	Z_L, Ω	$\theta_{Z_L}, ^\circ$	Z_T, Ω	$\theta_{Z_T}, ^\circ$	R_f, Ω
0.484 – 1.21	85	2.33 – 12.5	65 – 85	9.85	75.5	0 – 40

Regarding system state parameters, the voltage unbalance factor, β , is assumed to vary within a range of 0.1 to 0.4 as stated in Subsection 3.3.2. In addition, voltage at the PV terminal is assumed to change from 0.9 p.u. to 0.1 p.u. by a step of 0.1 p.u. The rating capacity of the PV system ranges from 1.6 to 6.4 MW, which emulates the PV portion within an interval of 20 to 80% out of the overall network load capacity. The final possible ranges of PS and NS impedances of the PV system are obtained based on the equations derived in Subsections 3.3.2 and 3.3.3.

For each fault type, there are 1600 values of the measured impedances obtained from 1600 combinations of the involved parameters, in which a half for forward faults and the other half for reverse faults. For all three types of unbalanced fault, we have totally 4800 values of calculated impedances.

3.5.5.2 Overall results and conclusion

We plot all the measured impedances derived from the numerical calculation for all three different unbalanced faults on one R-X plane. Since the obtained values vary in a wide range up to several thousand Ω , only a part of the plot closed to the separation boundary is zoomed in and inserted in Figure 3.9 for a better illustration. We can observe that the reverse impedances are mainly situated in the lower area in contrast with the forward impedances.

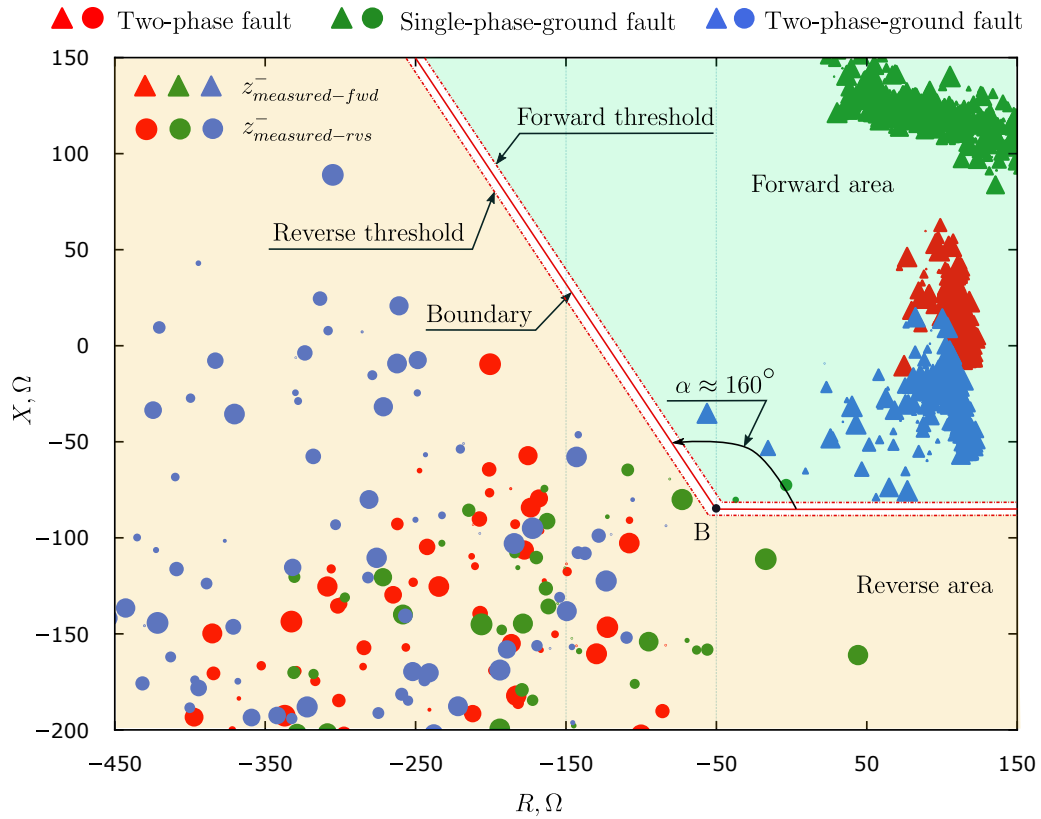


Figure 3.9 – Numerical results of the proposed NS impedances on the R-X plane

It is evident that due to the unconventional behavior of PV systems during faults, the measured impedances in case of reverse faults, which mainly consist of PV impedances, vary in a much more extensive range. A boundary can be drawn as a baseline for realizing setting thresholds, i.e., forward and reverse. It should be noted that the forward limit has to be located on a certain distance from the reverse threshold for preventing any possible overlap between two fault locations, i.e., forward and reverse faults.

Figure 3.9 indicates that the reverse reactances X tend to rise when the reverse resistances R are behind a typical value, in this case, -50Ω . Hence, we can adjust the slopes of these threshold lines to prevent the reverse impedances from invading the forward area. Although there are still a few values located in false areas, the probability of such false location appears to be minimal, only 1 or 2 per a total of 4800 points. The proposed method, therefore, has demonstrated itself as a promising directional candidate.

3.6 Evaluation of the proposed algorithm by simulations

For investigating the effectiveness of the proposed method, Grid-2 (Figure 2.9) is considered. However, for simplification purposes, the PV-01 and WT are disconnected, leaving only PV-02 subject to investigation. The RDIR element is assumed to be placed at Bus-10 with the Current Transformer (TCTR) polarity mark indicated. So, faults on those sections located between Bus-10 and PV-02 are considered as a reverse fault. Conversely, faults placed from 22 kV Bus-1 to Bus-10 are forward faults. However, due to the short length of all the network sections, we also propose to increase the length of sections 04-05 and 14-15 by a step of 2 km for 5 consecutive increments to account for the impacts of feeder length. Fault resistances are assumed to vary within a range of 0 to 90 Ω by a step of 10 Ω following the statistical data on the potential values of fault impedance, [113]. Various fault scenarios on Feeder 1 with parameters tabulated in Table 3.2 are conducted. We use the equations offered in Appendix C for fault data extraction.

Table 3.2 – Set of parameter for simulated fault scenarios

Fault type	
Single-phase-ground fault, two-phase fault, two-phase-ground fault	
Fault location	
Forward fault	10-11, 11-12, 12-13, 13-14, 14-15, 16-17, 17-18, 19-20
Reverse fault	01-03, 03-04, 04-05, 05-06, 06-07, 07-08, 08-09, 09-10
Element parameter	
PV-02 capacity	$P_{PV}, \% \mid 20 \div 80$ by a step of 20
Fault resistance	$R_f, \Omega \mid 0 \div 90$ by a step of 10
Section length	$l, \text{ km} \mid 2 \div 10$ by a step of 2

3.6.1 Single-phase-to-ground fault

3.6.1.1 Impacts of fault resistances and PV penetration level

3.6.1.1.1 Low- and medium-impedance faults

For Medium Voltage (MV) distribution networks, a fault impedance within a range of 0 to 40 Ω can be considered as low- and medium-impedance faults, [113]. Figure 3.10 shows the results for R_f from 0 to 40 Ω with the overall capacity of the connected PV systems equal to 20% out of the total load capacity of the grid. We can witness that there is a relatively wide separation region that allows the developed RDIR element to distinguish between the forward and reverse faults with no effort. It implies that we can easily set the forward and reverse thresholds for the proposed RDIR method. The forward threshold should be higher the reverse one by a reasonable value for preventing the RDIR element from any potential overlap. The proposed algorithm performs well for low- and medium-impedance faults, which are within the range from 0 Ω to 40 Ω . The higher the fault resistance, the further the steady-state values of $z_{measured}^-$ from the separation boundary are located.

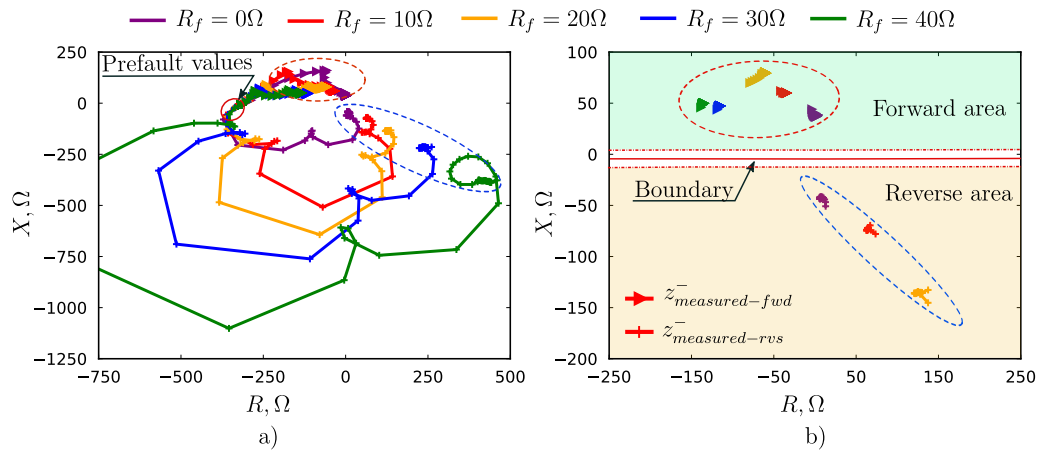


Figure 3.10 – Evaluation results for single-phase fault for $R_f \in [0 : 40] \Omega$ with $P_{PV} = 20\%$, (a) entire trajectory in the R-X plane, and (b) a part zoomed in on R-axis with $R \in [-250 : 250] \Omega$

The results for PV capacity of 40% are shown in Figure 3.11. Here, one noticeable feature, when the penetration level of the PV system increases, is the move to the left of the measured reverse reactances. The values of reactances for reverse fault scenarios of 30 and 40 Ω fault resistances are approximately equal to -1000 and -400 Ω , respectively, compared with positive values for the previous fault scenarios of the same fault resistances. Another additional distinct difference is that the measured NS reactances for forward fault scenarios decrease. For example, as can be witnessed in Figure 3.11, the reactances for this fault locations reduce to establish their stable during-fault values at about only 5 Ω , leading to a narrower area located between forward and reverse thresholds.

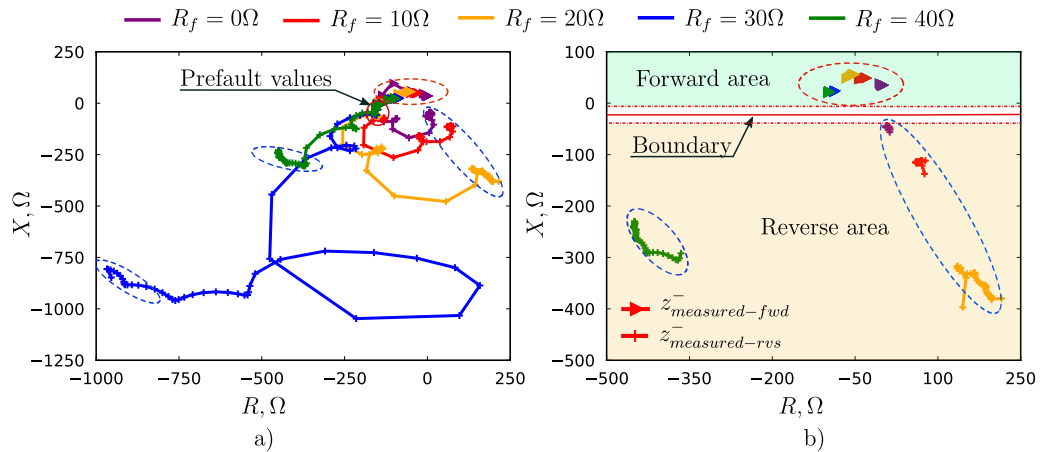


Figure 3.11 – Evaluation results for single-phase fault for $R_f \in [0 : 40] \Omega$ with $P_{PV} = 40\%$, (a) entire trajectory in the R-X plane, and (b) a part zoomed in on R-axis with $R \in [-500 : 250] \Omega$

These changes of the measured NS impedance trajectories can be explained by the greater participation of PV systems in network fault voltage recovery. When the fault resistances are high, the voltage drops during faults are limited, leading to an increased amount of reactive power injected by the PV systems. On the other hand, in case of lower fault impedances of 0, 10, and 20 Ω , although the PV injected reactive currents can reach their nominal currents, the amount of reactive power generation is limited due to

the large drops of the fault voltages. Such a trend can be seen more clearly for the fault scenarios with higher PV portions. However, despite the changes, separating boundary can be realized with no effort, reflecting high effectiveness of the proposed method.

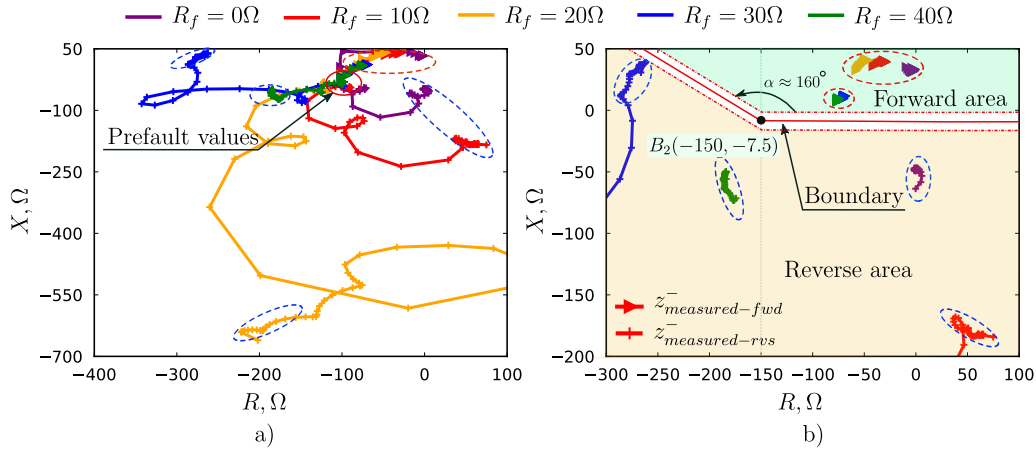


Figure 3.12 – Evaluation results for single-phase fault for $R_f \in [0 : 40]$ Ω with $P_{PV} = 60\%$, (a) entire trajectory in the R-X plane, and (b) a part zoomed in on R-axis with $R \in [-300 : 100]$ Ω

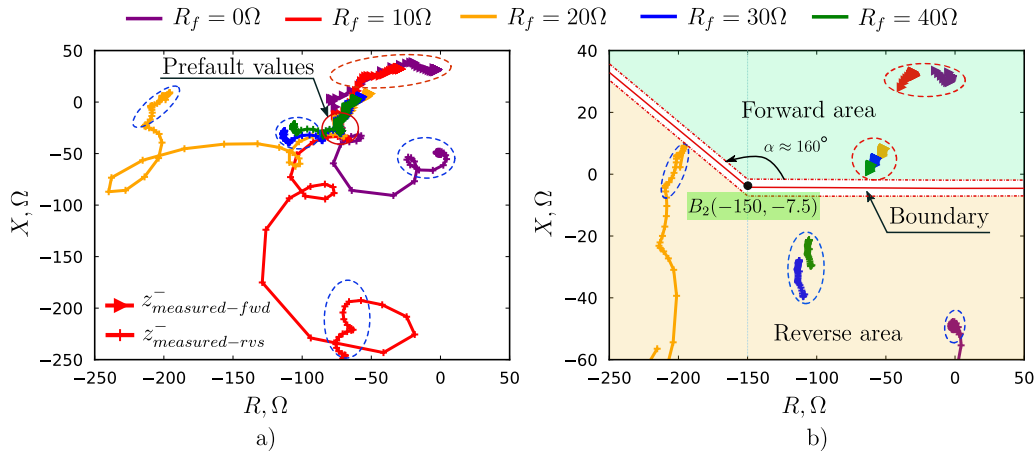


Figure 3.13 – Evaluation results for single-phase fault for $R_f \in [0 : 40]$ Ω with $P_{PV} = 80\%$, (a) entire trajectory in the R-X plane, and (b) a part zoomed in on R-axis with $R \in [-250 : 50]$ Ω

Figure 3.12 represents the results for PV share of 60%. Although the values of the measured NS impedances are established at levels similar to the case of 40 % PV, their trajectories can invade the forward area if the setting boundary remain the same as in the previous cases. For instance, the blue orbit of the measured impedance for 30 Ω reverse fault in Figure 3.12b increases up to about 40 Ω , causing incorrect identification of fault direction. Hence, the boundary separating the forward and reverse areas should be modified. In the study, we propose to decrease the forward area by increasing the slope of its border by an angle of approximately 160° at the resistance equal to 150 Ω as shown in Figure 3.12b. Here, we can observe a similar pattern of the setting thresholds in Figure 3.12b with those in Figure 3.9. The similarity between the numerical calculations conducted in Section 3.5.5 and simulation results have confirmed not only the correctness of the PV models, and the related control algorithms, but also the effectiveness of the proposed directional method. The same evolution of the measured impedances can be

obtained for the case of $P_{PV} = 80\%$, as shown in Figure 3.13. However, in this case, the changes start to happen from the fault resistance equal to $20\ \Omega$ instead of $30\ \Omega$. The correct operation of the proposed method can be achieved with the same setting thresholds.

3.6.1.1.2 High-impedance faults

Results for fault scenarios with $P_{PV} = 20\%$ for higher fault resistances are provided in Figure 3.14. In this case, the reactances of reverse measured impedances are still located in the right of the forward reactances. Hence, for a low level of PV penetration, the trajectory of the measured impedances for high-impedance faults are similar to those for low- and medium-impedance faults. The proposed method, again, successfully detects the fault direction with a high-reliability level reflected via a wide separation area.

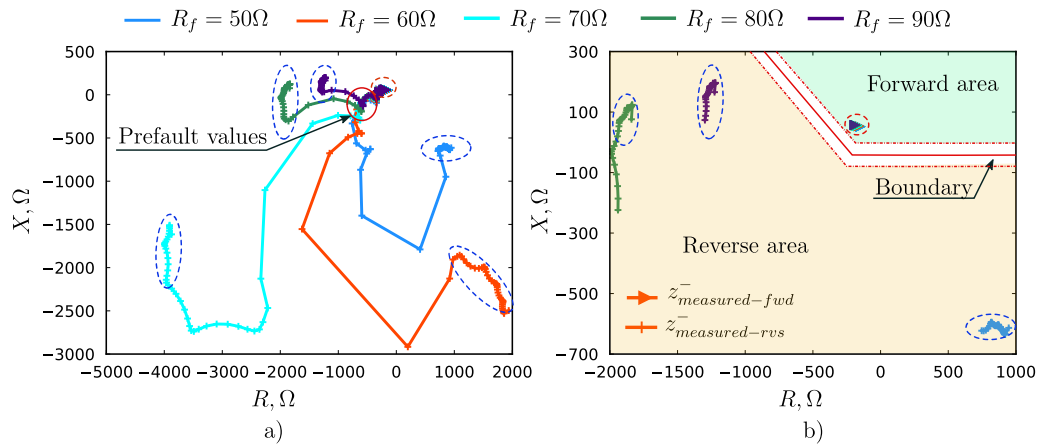


Figure 3.14 – Evaluation results for single-phase fault for $R_f \in [50 : 90]\ \Omega$ with $P_{PV} = 20\%$, (a) Trajectory in the R-X plane, and (b) zoomed in on R-axis with $R \in [-2000 : 1000]\ \Omega$

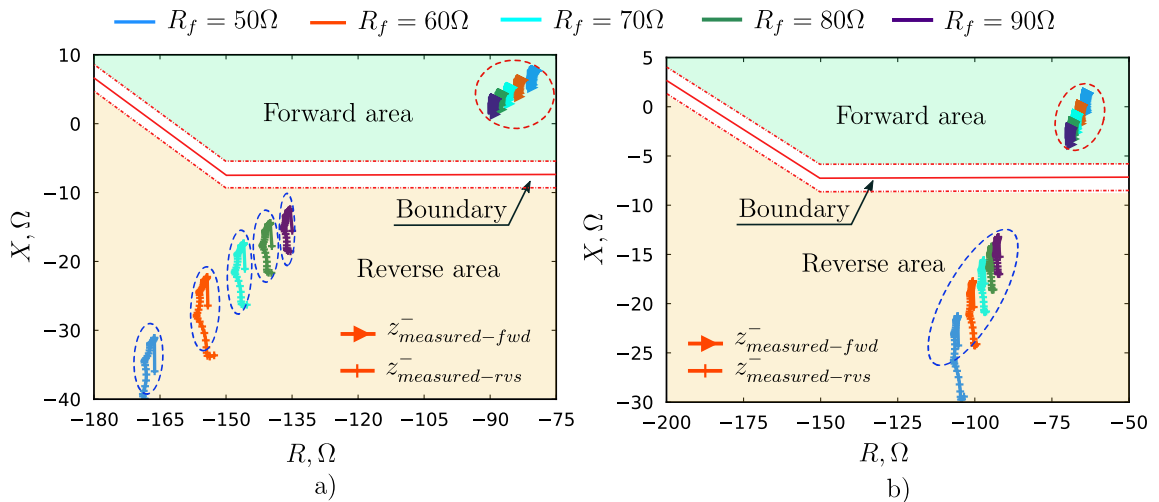


Figure 3.15 – Evaluation results for single-phase fault for $R_f \in [50 : 90]\ \Omega$ with the PV capacity of (a) 40% and (b) 80%, respectively

The trajectories for fault scenarios with higher proportion of PV systems are represented in Figures 3.15. We can see that when the installed capacity of PV systems increases, the impedances measured by the proposed algorithm for reverse faults tend to

move closer to the forward area. However, there is still a sufficient space, in which the setting thresholds that have already been deployed for low- and medium-impedance faults, can achieve a correct performance.

3.6.1.2 Impacts of faults closed to RDIR location

For faults closed to the RDIR location, the measured voltages drop significantly, even equal to zero, which possibly result in false direction identification. Values of traditional torque-product are too small for triggering direction algorithm. The proposed method can avoid these issues by using the prefault values of voltage memorized in two cycles prior to fault application. Let us consider a close-in fault, located on a distance of 0.5% of the section length from the Voltage Transformer (TVTR) location of Figure 2.9.

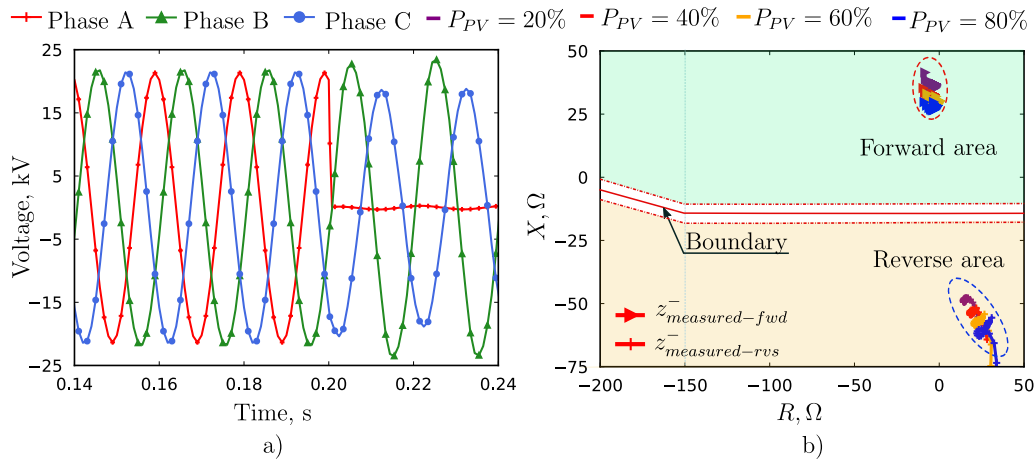


Figure 3.16 – (a) Three phase voltage during close-in phase-A-to-ground fault and (b) the corresponding evaluation results of the proposed RDIR element

Figure 3.16 shows that voltage of the faulted phase reduces to approximately zero; however, the decayed values of the measured impedances have located far from the separation area, allowing the proposed algorithm to realize reliable operation. The setting thresholds for forward and reverse faults can remain the same as above.

3.6.1.3 Impacts of load imbalance

In the theoretical evaluation of the proposed method, we assume balanced loads prior to faults, and therefore the prefault values of NS currents are zero. The superimposed NS current can be considered equal to the NS current measured by the RDIR element. However, the practical operation of distribution networks has indicated that completely balanced loads never can be achieved due to variations of loads over the times. Load changes in each phase are caused by numerous unpredictable factors, for instance, customer consumption characteristics, weather conditions, etc. Consequently, the imbalance is an inherent feature that always exists in distribution networks. Its impacts on the performance of protection units, in particular, the designed RDIR element, therefore, should not be neglected. To investigate such effects, we should modify the loads for obtaining a larger load imbalance level. The details of three-phase loads of Feeder 1 (Figure 2.9)

are provided in Table 3.3. Load in phase A is considered as the base level. Phase B load is assumed to consume by 22% more than the base level, and phase C load, by contrast, decreased by 12%.

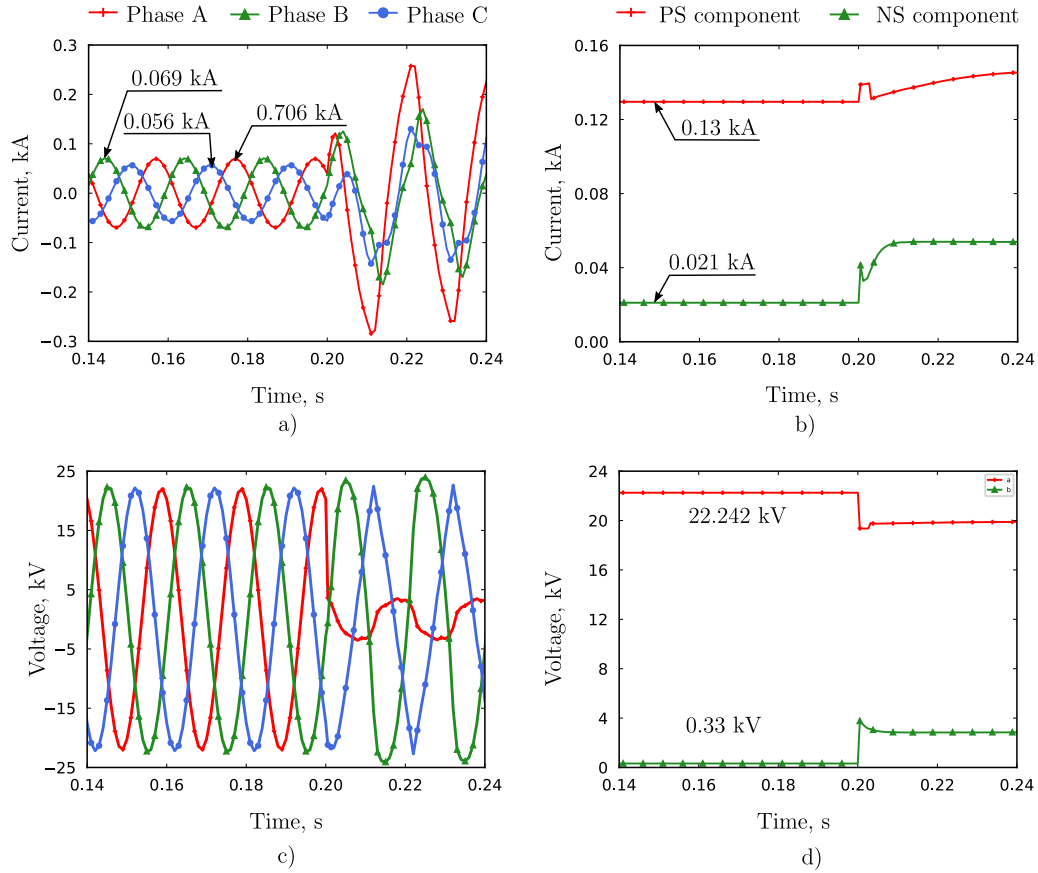


Figure 3.17 – (a) and (b) three-phase currents and their sequence components; and (c) and (d) three-phase voltages and their sequence components

Table 3.3 – Voltage and current imbalance due to unbalanced loads

Phase	$P/P_{base}, \%$	Current, kA	Voltage, kV	Imbalance, %	
				Voltage	Current
A	100	0.069	12.7		
B	122	0.071	13.0	1.48	16.15
C	88	0.056	12.8		

The current and voltage wave-forms and their PS and NS components are represented in Figure 3.17. Based on Figure 3.17c and d, the imbalance levels of voltage and current, which are calculated by [114], are 1.48 and 16.15%, respectively. The voltage imbalance level is less than the permitted range of 2% suggested by [115]. Figure 3.18 depicts the results for 20% PV capacity with fault resistances within a range of 0 to 40 Ω . The patterns of the measured impedances during fault are different from those of Figure 3.10a due to the impacts of pre-fault NS voltage on the pre-fault reference voltage. The presence of NS voltage component in steady-state operation causes the pre-fault voltage phasor to deviate from the position at which the perfectly-balanced pre-fault voltage is located.

Nonetheless, because the imbalance level within the MV grid is normally limited to less than 2% as mentioned previously, the steady-state values of measured impedances are properly placed within proper areas, demonstrating the effectiveness of the proposed algorithm. The setting thresholds for both forward and reverse faults remain the same as the previous settings.

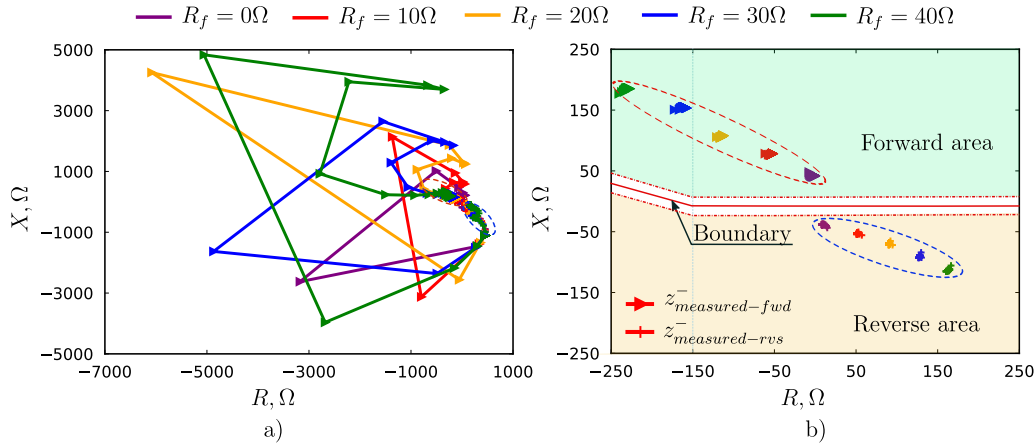


Figure 3.18 – Evaluation results for single-phase fault under 20% unbalanced load conditions with 20% PV capacity

The impacts of load imbalance are also examined for the increasing PV capacities. As can be seen in Figure 3.19, the measured impedances in case of forward faults are located very close to the upper boundary, especially when fault resistances are high. Nonetheless, the proposed method can perform well regardless of the presence of unbalanced loading conditions, even with high fault resistances.

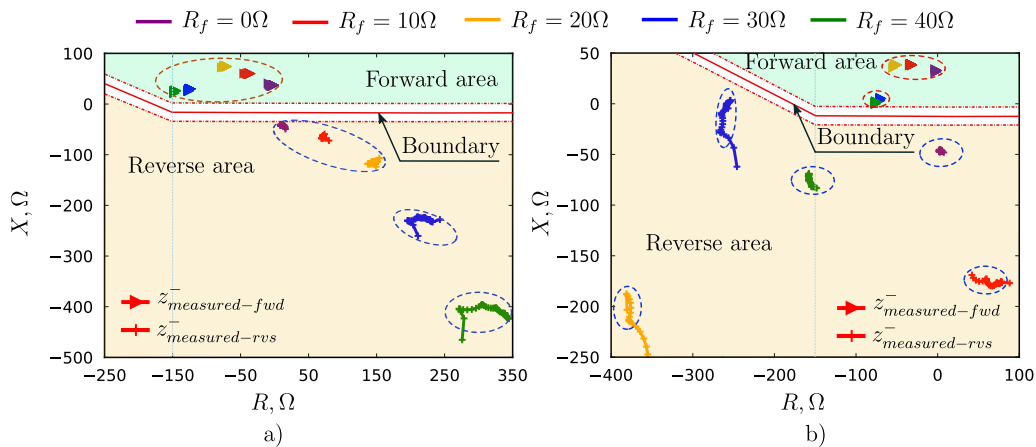


Figure 3.19 – Evaluation results for single-phase fault under 20% unbalanced load conditions with (a) 40%, and (b) 80% PV capacities

3.6.1.4 Impacts of external grids

For estimating the effects of external grids, the diesel generators of Grid-2 are replaced by an external grid with the short-circuit capacity increasing from 400 MVA to 1000 MVA by a 200 MVA step. The traditional NS torque-based RDIR element is affected

when the NS source behind the TVTR location is strong, i.e., low NS impedance. In such a case, the measured NS voltage can be too small that cannot offer a correct polarization, [83]. In contrast, Figure 3.20 has demonstrated the reliable operation of the proposed approach under different network short-circuit powers. The proposed RDIR algorithm can rid this issue thanks to the reliable polarizing signal provided by the prefault memorized voltage. Hence, the effects of grid short-circuit capacity can be minimized.

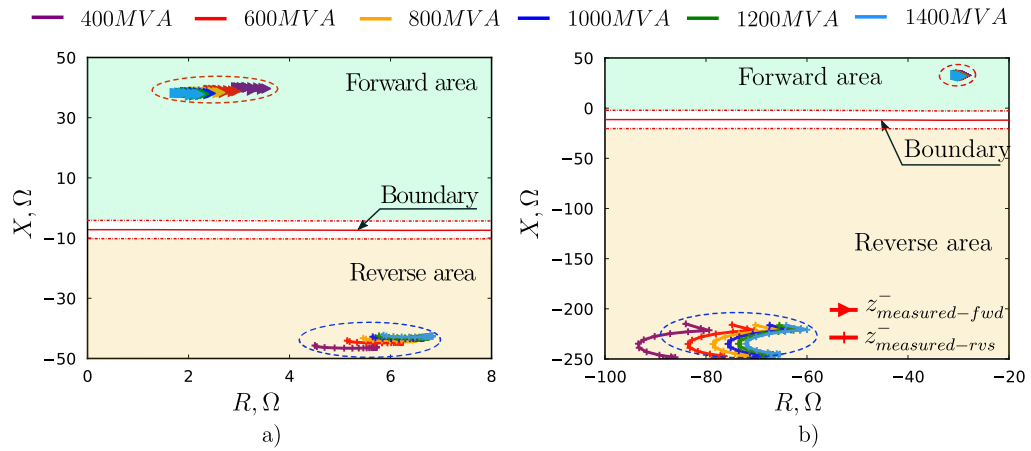


Figure 3.20 – Evaluation results for single-phase fault under the variation of external grid power with (a) $R_f = 0 \Omega$ and $P_{PV} = 20\%$, and (b) $R_f = 10 \Omega$ and $P_{PV} = 80\%$

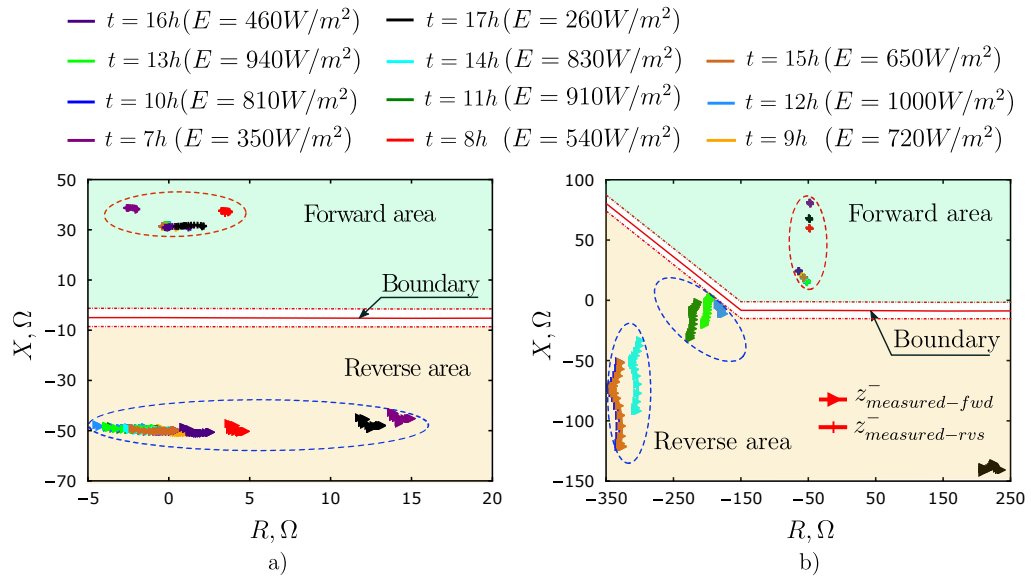


Figure 3.21 – Evaluation results for single-phase fault under the variation of solar irradiation with $P_{PV} = 80\%$, and (a) $R_f = 0 \Omega$, and (b) $R_f = 20 \Omega$

3.6.1.5 Impact of variation of solar irradiation

The impacts of the intermittent nature of solar sources are also evaluated as illustrated in Figure 3.21. The proposed RDIR method has shown a high effectiveness in the case of solid faults with the values of the measured impedances located far away from the separation boundary. In contrast, in case of $R_f = 20 \Omega$, the measured impedances

tend to move closer to the separation border at high hours of solar irradiation. This is because during high hours of solar irradiation, the amount of reactive power injected by the connected PV systems is higher, leading to higher measured reactances.

3.6.1.6 Overall evaluation considering all affecting factors

Figure 3.22 represents one-point-for-one-fault-scenario $z_{measured}^-$ on the R-X complex plane with the variation of fault resistances, PV capacities, line sections, and lastly fault locations on each section. In particular, the fault resistance increases from 0 to 90 Ω by a step of 10 Ω , and the PV capacity varies by step change of 10% from 10% to 80%. We move the fault location along Feeder 1 by a step of 20% of the section length from 20% to 80%. Combined with the two fault locations in reference to the RDIR location, i.e. forward and reverse faults, we receive totally $2 \times 10 \times 8 \times 8 = 1280$ points of $z_{measured}^-$ on Figure 3.22. The marker size in this figure increases corresponding to the increase of the PV capacity.

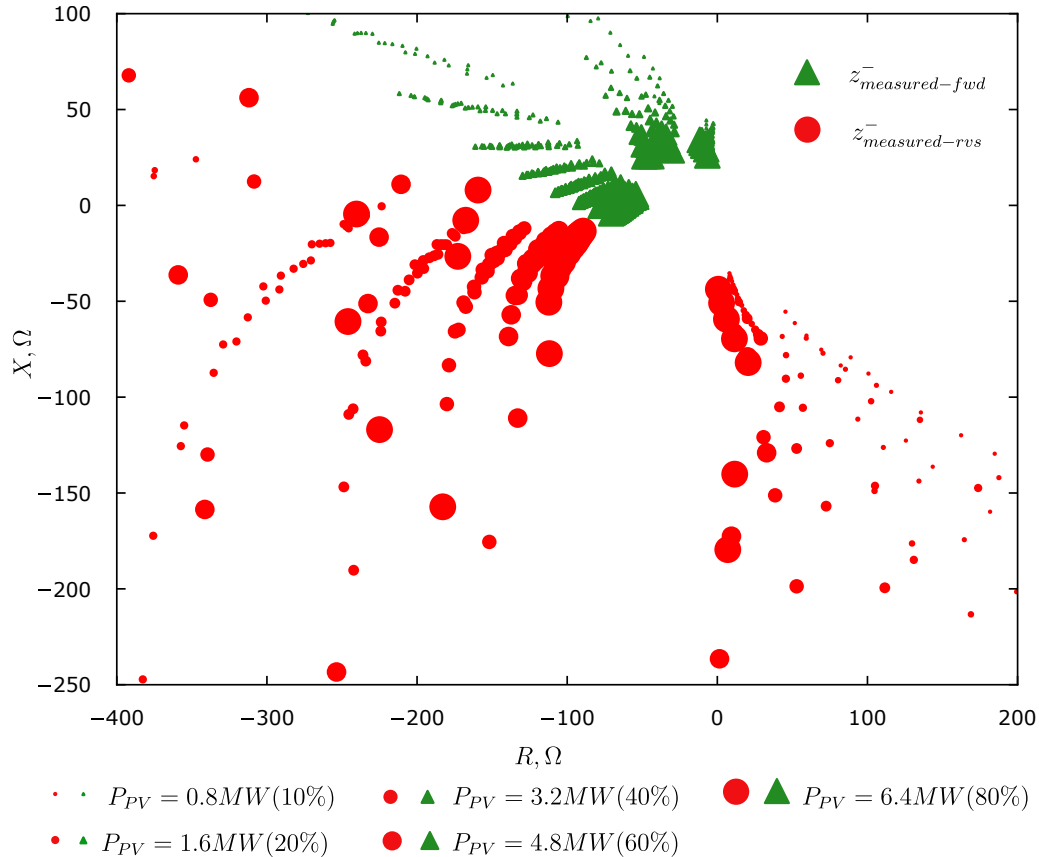


Figure 3.22 – Overall characteristic of $z_{measured}^-$ for single-phase-to-ground fault

For a better illustration, a part of Figure 3.22 closed to the boundary between two areas is zoomed in on the X-axis, as shown in Figure 3.23. We can see that the measured impedance locations for forward and reverse faults are consistent with those numerically evaluated in Section 3.5.5 and shown in Figure 3.9. One more time, we can confirm that the consistency between numerical evaluation and simulation has demonstrated the correctness of the proposed PV models.

Furthermore, as shown in Figure 3.23, it is undemanding to draw appropriate boundary lines in the R-X complex plane to allow the proposed RDIR element to properly detect the fault direction. The boundary line (red solid line) in Figure 3.23 can be realized by giving a coordinate of point B_2 , at which the slope of the boundary lines should increase by an angle of approximately 160° . Afterward, the forward (upper) and reverse (lower) boundary lines can be obtained with a proper distance from the boundary line for ensuring a minimum sensitivity level of the proposed RDIR element. Based on the resulted bounded areas, if the impedance measured by the RDIR element is located inside the upper blue-shaded zone, it declares a forward fault. By contrast, the RDIR element states a reverse fault if the computed impedance is situated inside the lower brown-shaded zone.

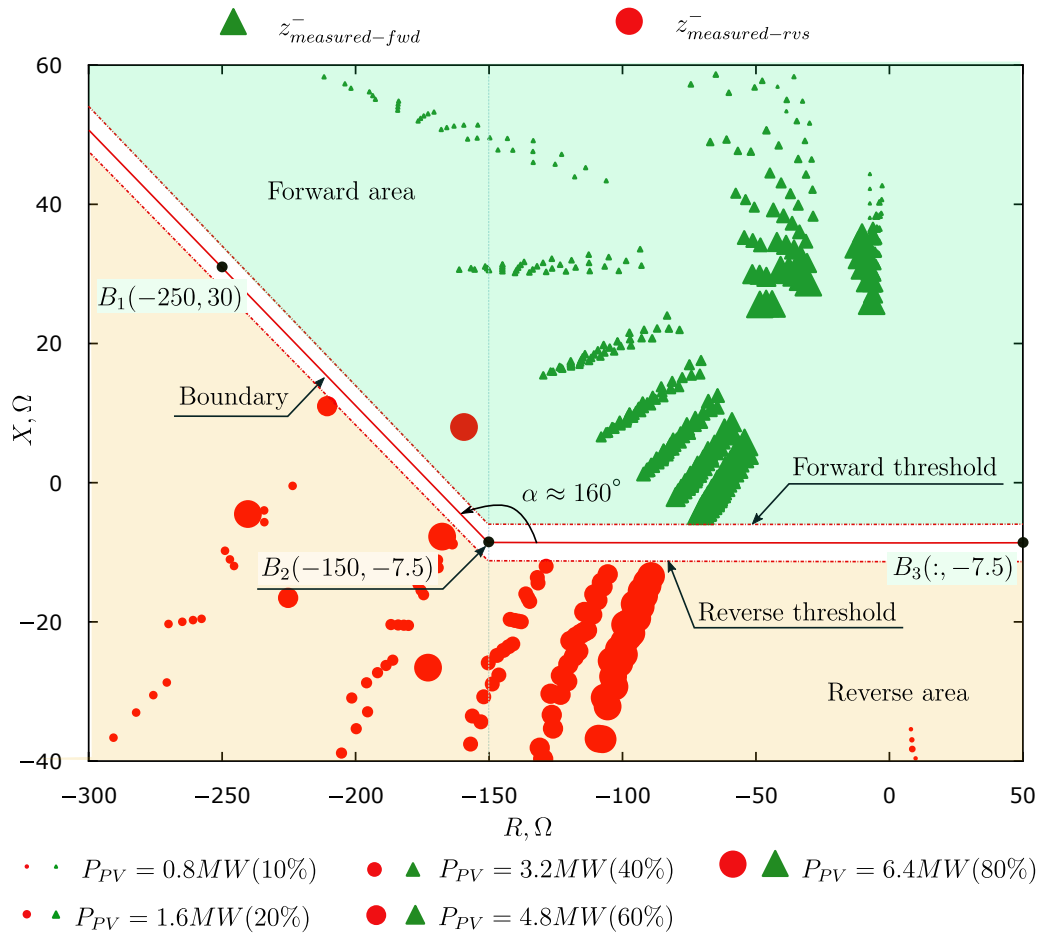


Figure 3.23 – Operating characteristic of the proposed method for one-phase-ground fault

3.6.2 Two-phase faults

Similar to what being presented in Subsection 3.6.1, partially zoomed-in trajectories of the measured impedances in case of two-phase fault for low- and medium-impedance fault are inserted in Figure 3.24. For this kind of fault, the fault voltage only decreases moderately, resulting in a limited contribution of PV systems to the system voltage recovery. In other words, the amount of reactive power injected by PV systems during faults is less than that for single-phase faults. Hence, the trajectories of the measured reverse impedances during faults remain almost the same for different PV installed ca-

capacities, except for the situation when the PV installed capacity reaches the highest level considered, i.e., $P_{PV} = 80\%$. In such generating conditions, the measured impedances for reverse faults are shifted to the left since the amount of reactive power delivered by the PV system has become more considerable, Figure 3.24d.

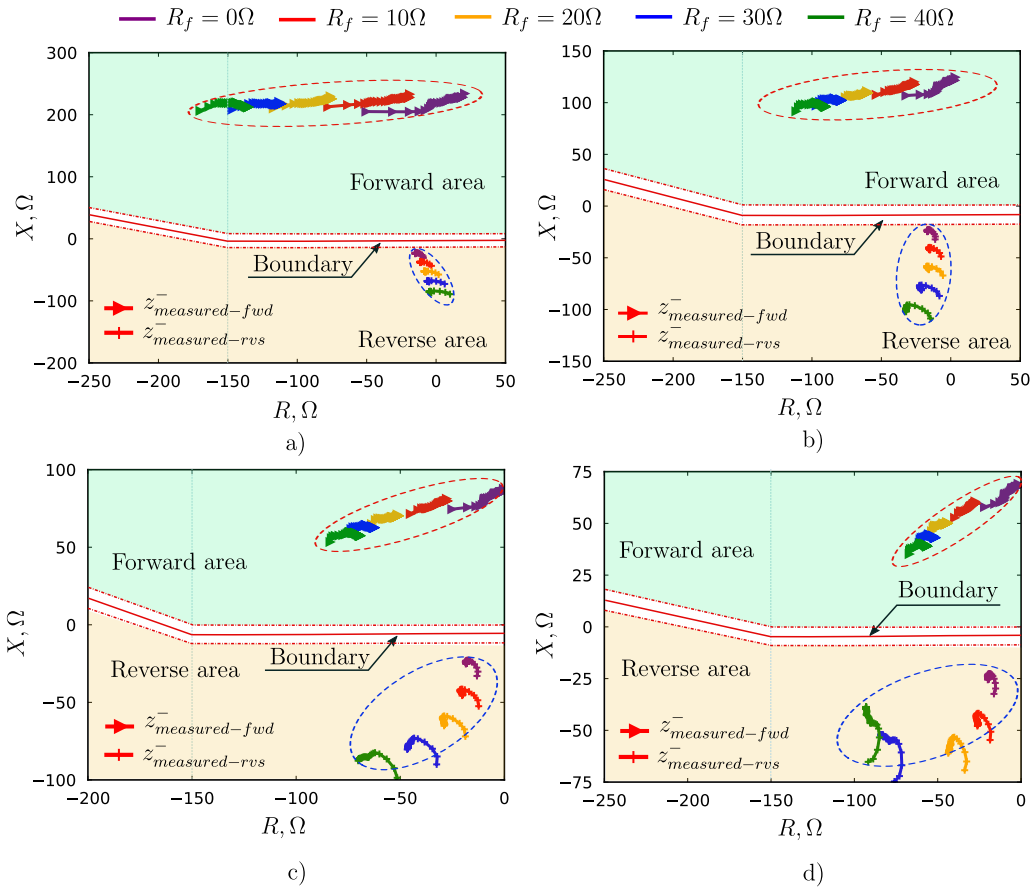


Figure 3.24 – Evaluation of the proposed RDIR element for $R_f \in [0 : 40] \Omega$ with (a) $P_{PV} = 20\%$, (b) $P_{PV} = 40\%$, (c) $P_{PV} = 60\%$, and (d) $P_{PV} = 80\%$

The effects of other factors such as faults with higher impedances, external source power, close-in fault, and unbalanced loads are also taken into consideration. Since the results of the two-phase fault are similar to those of the above single-phase-to-ground fault, all the results are included in the Appendix E.1. Concerning a so-called high-impedance fault, the measured impedances for reverse faults show a homogeneous pattern for different PV capacities. Only for $P_{PV} = 80\%$, these values move closer to the boundary lines. In the remaining cases, forward impedances well distinguish from reverse ones.

The overall evaluation of the proposed RDIR approach for two-phase faults under all possible affecting factors is depicted in Figure 3.25. All the considered fault conditions for this kind of fault are left the same as for single-phase-to-ground fault. The overall figure shows that if we leave the boundary lines unchanged, the reverse impedances are situated rather far from the separation area. In contrast, only a few forward impedances are located very close to the forward boundary line. However, none of these values has entered the false area, i.e., reverse region. The proposed method, therefore, has proven

its high effectiveness for two-phase faults.

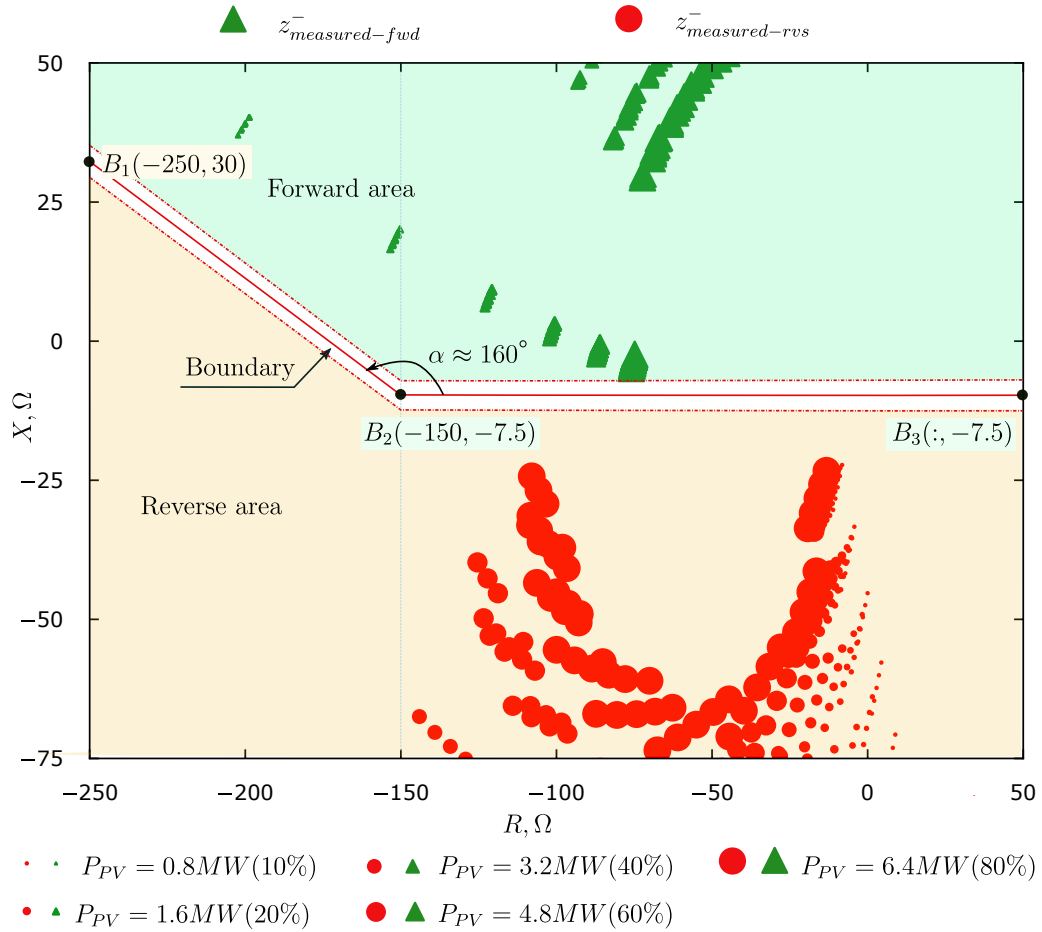


Figure 3.25 – Operating characteristic of the proposed method for two-phase fault

3.6.3 Two-phase-to-ground fault

The detailed results, obtained for each fault scenario taking into account all factors that may affect the performance of the proposed method in the event of a two-phase-to-ground fault, are included in Appendix E.2. In this subsection, only the overall picture is provided in Figure 3.26. Similarly, as can be observed from Figure 3.26, we can reaffirm a consistent characteristic of the proposed impedances derived from simulations with those acquired from the analytical approach illustrated in Figure 3.9. Moreover, the trajectories of the measured impedances are almost similar to those for single-phase-to-ground and two-phase faults. With a high proportion of PV systems, the corresponding substantial injection of reactive power results in the shift of the measured reverse reactances to the left. However, they are still located in the proper region, confirming the high performance of the proposed method. The boundary lines that have been set for the two previous fault types can remain unchanged. The distance between the closest forward and reverse values are long enough for the proposed approach to ensure the correct detection of fault direction. None of the false direction decision may happen based on what we can witness in Figure 3.26. However, for an extremely high PV penetration, for instance $P_{PV} = 80\%$, the values of the measured impedances are situated very close to the boundary line.

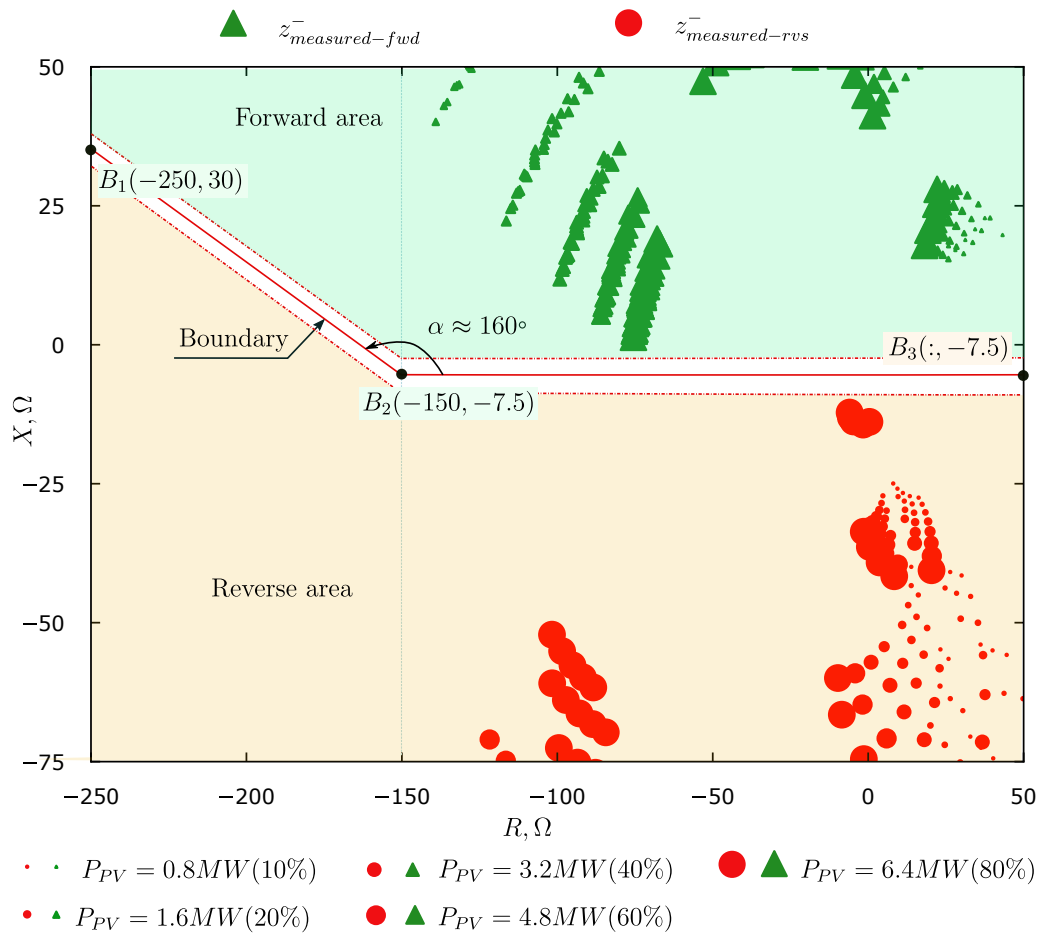


Figure 3.26 – Operating characteristic of the proposed method for two-phase-ground fault

3.6.4 Summary evaluation of the proposed method for all kinds of unbalanced fault

At this stage, the performances of the proposed method for all unbalanced faults have been presented. The results show high accuracy and dependability of the so-called NS impedance-based RDIR element. The high accuracy is verified by the proper locations of the obtained impedance values within the corresponding areas. In other words, values for forward faults are situated in the setting forward area, while those for reverse faults are located in setting reverse areas. Only one or two values in the case of reverse single-phase-to-ground fault are located in the false region. These values are mainly affected by the PV systems since the NS currents fed to the RDIR element in these cases are mostly contributed by the inverter-based PV systems. When the PV capacity reaches its highest level, faults with low impedance, even zero-impedance faults, may lead to massive voltage drop. The FRT-compliant control strategy presented in Section 2.7 has forced the PV systems to generate as much reactive power as possible. The active power production may reduce to zero, resulting in such unusual values of the measured impedance.

The representation of all results in one R-X plane, as shown in Figure 3.27 suggests that one can deploy a unique setting pattern for all kinds of unbalanced faults. There

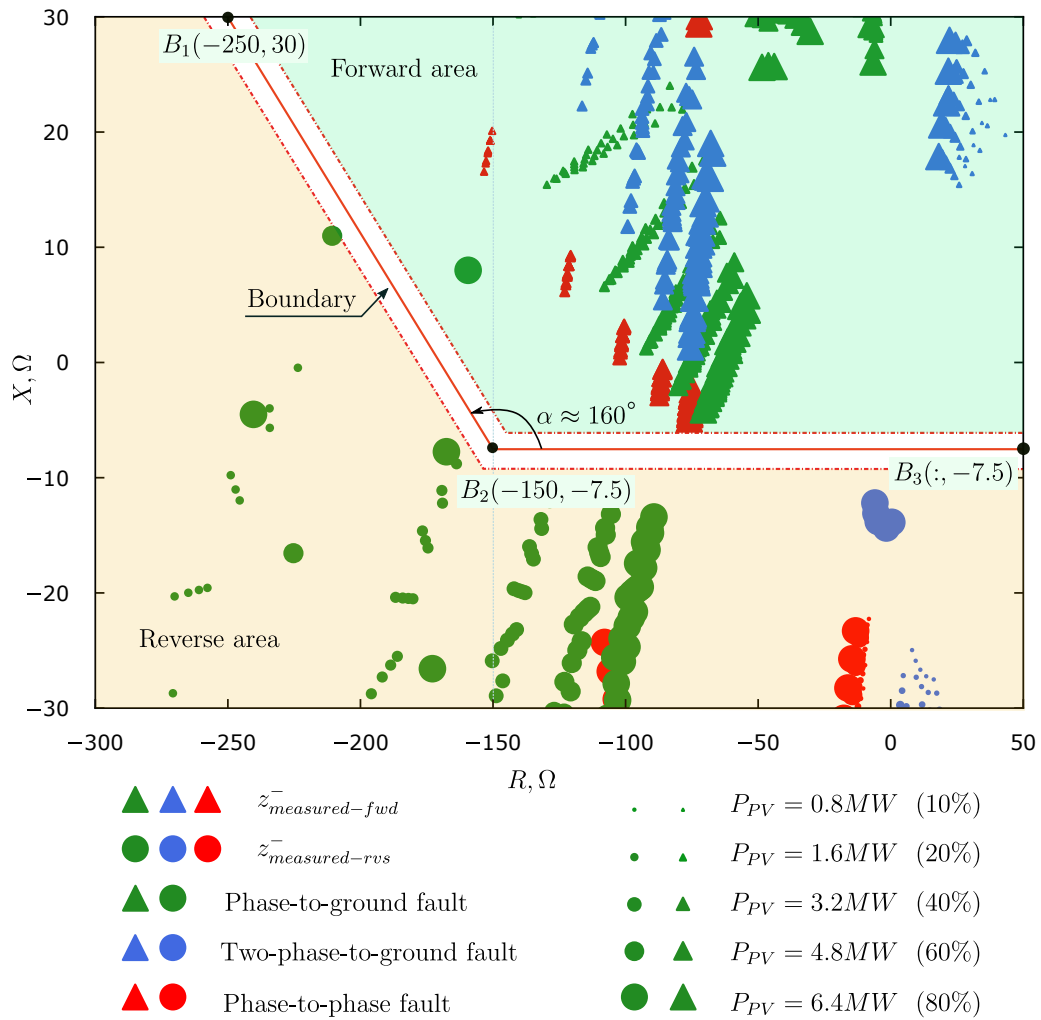


Figure 3.27 – Operating characteristic of the proposed method for all unbalanced faults

are two critical setting factors that should be carefully considered for obtaining the high effectiveness of the proposed RDIR element. The first factor is the boundary line, and the coordinate of the point, at which its slope should be altered. The last parameter is the distance from the central boundary line, based on which the forward and reverse boundary lines are drawn.

3.7 Procedure for fault direction determination

Since the proposed RDIR method relies upon the prefault voltage, an algorithm for detecting the exact moment of fault occurrence shall be equipped with a fault detector to avoid any possible overlap between the prefault and during-fault data, [78]. Figure 3.28 shows the flow chart of the algorithm. The during-fault data shall be collected for two cycles after the fault detection. The fault detector may be in kind of Instantaneous Overcurrent Protection (PIOC) or Under-Voltage Protection (PTUV) elements.

The method is explained as follows. Once a fault has been detected, the RDIR element processes the current signals to determine the precise sample number N_{in} , at which

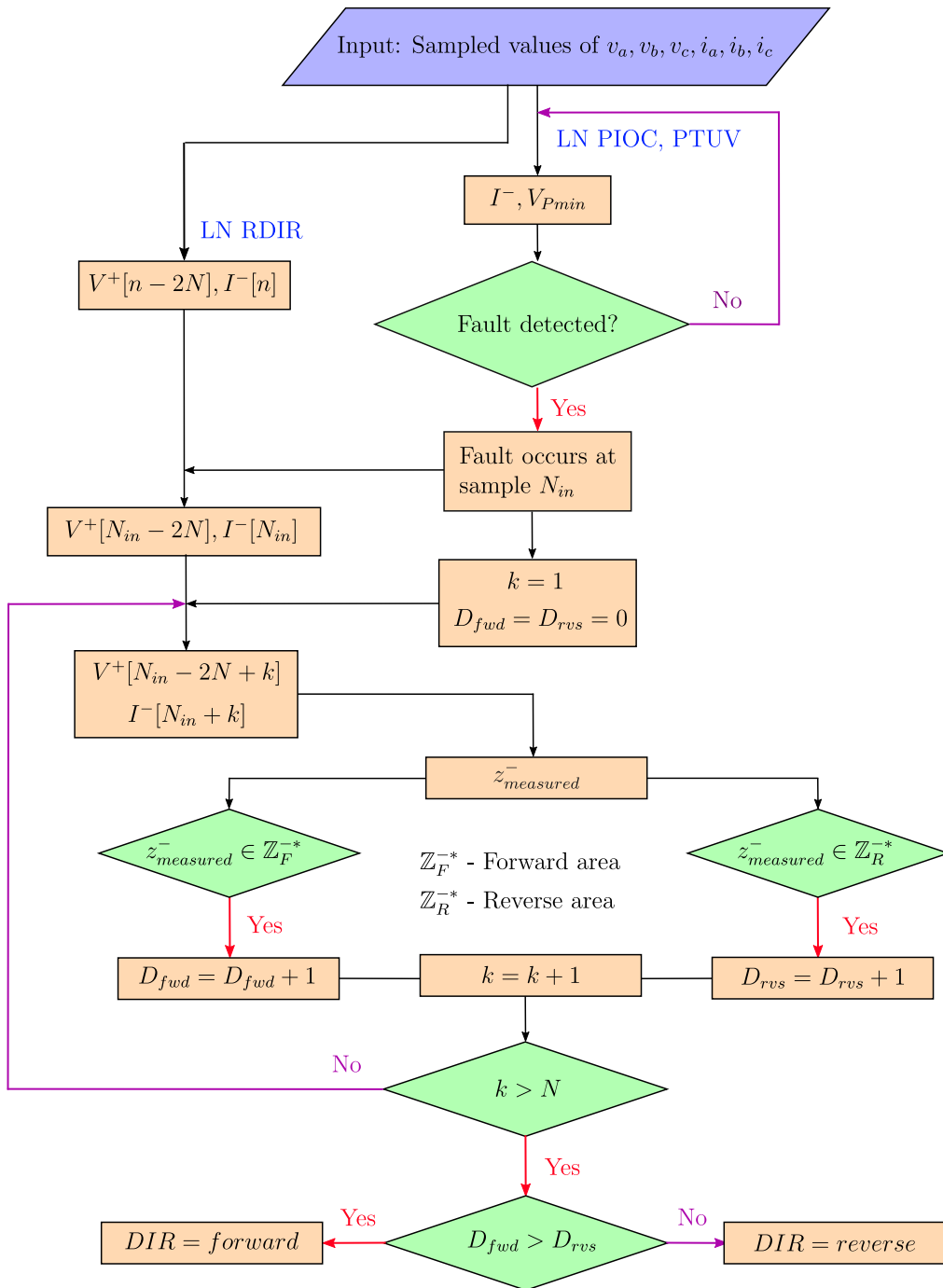


Figure 3.28 – Flowchart of fault direction detection process

the fault has happened. Then, the RDIR element computes the criterion values for fault direction determination by using Equation 3.11 for each sampled value as:

$$z_{measured}^{-}[k] = \frac{V^{+}[N_{in} - 2N + k]}{I^{-}[N_{in} + k]} \quad (3.33)$$

where N is the number of samples per cycle and is equal to the number of samples per data window.

For a reliable operation of the fault direction detection, the calculation of $z_{measured}^-$ is repeated N times. For each value of $z_{measured}^-$ situated in the forward area of Figure 3.27, a so-called index D_{fwd} increases by 1; otherwise, index D_{rvs} increases by 1. The RDIR element calculates N consecutive values of $z_{measured}^-$ i.e., from the sample at N_{in} to the sample at $N_{in} + N$. At the end of the iteration process, the RDIR element compares D_{fwd} with D_{rvs} . If D_{fwd} is larger than D_{rvs} , the fault is forward; otherwise fault is reverse.

3.8 Conclusion

First, the chapter conducted a review of state-of-the-art directional methods used for distribution networks. Then, fault characteristics of inverter-based PV systems under the control strategy proposed in Section 2.7 were also obtained. Based on these characteristics, several limitations of the existing methods for distribution networks with high penetration of PV systems were analyzed and indicated in Appendix F.8. Evaluation results showed that the phase displacement between the NS current and voltage of the inverter-based PV systems did not remain the same as that of conventional synchronous sources. Indeed, this angular relationship depends not only on the fault loop impedance but also on the PV control strategy. In some typical fault scenarios, the traditional RDIR element may misoperate as shown in Figure F.5.

From the knowledge about the drawbacks indicated above, a new directional algorithm that relies on the ratio between the prefault voltage and during-fault NS current was developed. First, we eliminated the non-linear relationship between the NS current and prefault voltage by expressing $z_{measured}^-$ through impedances of the involved components for each fault type by using circuit transformation method. These equations were then used for the numerical analysis and the results showed that there would be a clear separation for distinguishing between forward and reverse faults. Finally, Grid-2 was used to evaluate the proposed method under different fault scenarios by simulations in DlgSILENT | PowerFactory. The simulation results indicated the same pattern of $z_{measured}^-$ compared with those results obtained from the numerical approach. The consistency between the evaluation results of the numerical and the simulation approaches confirmed the correctness of the designed PV model and its control strategy. The proposed algorithm demonstrated its high performance and accuracy under different influencing factors, such as fault impedances, PV penetration levels, fault locations as well as other factors such as load imbalance, short circuit capacity of the external grid. In the next chapter, the proposed RDIR will be applied for developing various protection schemes for MV distribution networks and their included LV microgrids.

Chapter 4

Development of distribution protection schemes with high PV penetration

Contents

4.1	Introduction	88
4.2	State-of-the-art of distribution protection	89
4.2.1	LV microgrid protection	89
4.2.2	MV network protection	92
4.3	Proposition of PV FRT-compliant interface protection	95
4.3.1	Voltage-based protection settings	96
4.3.2	Frequency-based protection settings	96
4.4	Protection scheme for LV microgrids	97
4.4.1	Considered LV microgrid	97
4.4.2	Proposition of the developed protection scheme	98
4.4.3	Protection scheme for grid-connected mode	100
4.4.4	Protection algorithm for the islanded mode	102
4.4.5	Case study	103
4.5	Protection scheme for MV networks	113
4.5.1	Proposition of the protection scheme	113
4.5.2	Case study	117
4.6	Conclusion	119

4.1 Introduction

In traditional distribution networks, fault currents usually flow in a single direction, from the substation to the fault location, and fault detection is not complicated. Hence, the protection systems of these networks are designed for unidirectional energy flow. Fault detection is carried out by comparing the magnitude of the current waveform with a predefined threshold value, without the need for special signal processing. These protection systems must meet the following objectives [57]: (i) to ensure the continuity of supply to consumers, (ii) to safeguard the safety of persons and property, and (iii) to avoid the partial or total destruction of equipment.

With the increase in the PV penetration into distribution networks, many grid codes provided in [21, 22, 23, 24, 25], require that PV systems remain connected in terms of **Fault Ride Through (FRT)** and simultaneously support the grid voltage during the fault in terms of dynamic grid support by injecting reactive power as already mentioned in Chapter 1. Therefore, **Distributed Energy Resource (DER)**s in general, and PV systems in particular, have been significantly involved in the grid transient process during fault events, and their impacts on the fault behavior of the systems should, therefore, be taken into account. In particular, many issues may occur, such as blinding and false tripping, low fault currents, malfunction of traditional directional methods, which are studied in depth in Appendix F and Section F.8. Hence, the current protection systems of **MV** and **LV** distribution networks with high **DER** penetration may no longer function properly.

As far as the **LV** distribution grid is concerned, as many research studies indicate, high integration of PV systems can transform a **LV** grid into a new grid called the **LV** microgrid [35]. This new type of **LV** distribution grid may be necessary to be able to operate in both grid-connected and isolated modes and should be protected against all kinds of faults. One of the essential requirements for successful islanding of the microgrids is to ensure the **FRT** capacity of the connected PV systems, which significantly enhances the post fault active power balance. Besides, the dynamic voltage support of the remaining connected PV systems also increases the voltage quality of the islanded microgrid. The study of the ability of PV systems to support **FRT** is of significant importance, and therefore, has already been developed in Section 2.7. However, the existing interface protection of PV systems cannot guarantee their **FRT** capability. Moreover, even in the case of **FRT** capability realization, the present fuse-based protection system of a **LV** network may not be able to handle the considerable difference in fault currents when the **LV** microgrid switches from one operating mode to another and vice versa [28, 29, 30, 31, 32].

In the isolated mode, the exceptionally high fault current provided by the external HV grid is not present. The low level of the fault current supplied by PV systems, and possibly Battery Energy Storage System (BESS) is not sufficient for the responsible protection devices to operate within an acceptable time frame. In addition, fast and accurate operation of the **LV** microgrid interface protection must be ensured to guarantee successful islanding of the microgrid. Currently, the **LV** microgrid is connected to the **MV** network via a **MV/LV** transformer protected by a fuse or a Circuit Breaker (CB) with an integrated

Instantaneous Overcurrent Protection (PIOC) or Time Overcurrent Protection (PTOC) elements. These protective devices cannot detect external faults to facilitate the islanding of the LV microgrid due to the low fault currents contributed from PV systems inside the concerned LV microgrid.

Concerning the MV distribution protection, the operation of feeder overcurrent relays are time-delayed in order to guarantee the selective operation with the downstream LV network protections. In France, these time delays are typically in range of 0.5 s [54] that appears too long for meeting the PV FRT requirements. For instance, for a fault on the backbone of the MV feeder, its Circuit Breaker (CB) is tripped by its protection relay within 0.5 s. If the time delay of PV interface protection, as recommended in the version 2017 of the VDE-AR-N 4105 standard [116], or BDEW grid code [24], or the IEEE Std 1547-2018 [26, 117], is set at 0.2 s, all the PV systems connected to the LV microgrid are tripped unnecessarily. The successful islanding of the LV microgrid containing these PV systems cannot be realized.

In light of these drawbacks of the conventional MV and LV distribution protection systems, in this chapter, we intend to propose new protection schemes that can not only satisfy the FRT requirement of connected PV systems, but also ensure the successful islanding of included LV microgrids. The operation of the respective protection elements in the LV and MV networks is carried out quickly and correctly in a selective manner. The protection systems are mainly based on the principles of overcurrent, undervoltage, and underfrequency functions. The RDIR algorithm developed in Chapter 3 is deployed to support these elements in differentiating between forward and reserve faults. A communication network is needed to transfer interlocking signals between different protection levels of the two LV and MV networks in order to reduce the coordination time, and then, in turn, ensure the efficient islanding of the LV microgrids.

4.2 State-of-the-art of distribution protection

4.2.1 LV microgrid protection

4.2.1.1 Protection schemes without communication requirement

A relaying system capable of protecting the LV microgrid in both modes of operation without communication support is presented in [118]. This system is mainly based on the principles of overcurrent and undervoltage. The load fuses do not need to be replaced. All types of faults, including high impedance faults, are correctly detected at a very reasonable implementation cost. Reference [119] suggests an adaptive protection strategy without the need for a communication system. Fault detection is based on the discrimination of voltage drops due to short-circuit incidents, and those caused by overloads. A study published in [120] deployed the components of fault voltages and currents at the protection locations to determine the system impedance. The settings of the instantaneous overcurrent protection could be automatically adjusted by comparing the impedances of the external grid with that of protected microgrids. A paper in [121]

presents a protection system that has the same protection strategy for both isolated and grid-connected modes of operation. A study in [122] proposes a new method for detecting and suppressing symmetrical and asymmetrical faults for looped microgrids with converter-interfaced DERs, without the use of expensive protection devices or physical communication links.

Disadvantages: The main disadvantage of the above methods is that time coordination starts at the lowest level of protection, i.e., the lateral fuses. At low fault levels, the melting time of these fuses may be too long, which negatively affects the FRT capability of the connected DERs. Additionally, the operational coordination between the feeder protection element and the lateral fuses may result in a very long delay in the feeder protection. DERs connected to a non-faulty feeder may suffer from spurious tripping. For example, as presented in [118], a two-phase fault on a feeder line is suppressed by a time overcurrent element after 0.286 s that exceeds the usual 0.2 s time delay of the DER interface protection. Another minor shortage of the above approaches is that they do not take into account the interface protection of the connected DERs.

4.2.1.2 Adaptive protection

In [123], a complete adaptive protection system for LV microgrids was developed. The LV feeders are segmented into different protection zones using a large number of switchboards and CBs. The study presents a protection concept that the setting thresholds of the protection elements can be automatically adjusted to adapt to the change of network configuration. Also, the time-current curve of the Molded-Case Circuit Breaker (MCCB) electronic trip unit is continuously modified to adapt to the considerable modification of the network. A similar protection scheme for LV microgrids has also been published in [124]. A central protection unit capable of communicating with the downstream protection relays has been set up. This communication was necessary to calculate and update the pickup thresholds, as well as to detect the fault direction. The authors sorted the relays into pairs, and time coordination was performed within each pair. An advantage of the proposal is that it does not require a fast real-time communication channel for protection purposes, but only a slower and cheaper serial communication link for updating the operating states of the DERs and loads. However, the overall configuration of the whole network, which should consist of operating curves or setting parameters for all the concerned protection elements, was still lacking. A similar adaptive protection scheme has also been presented in [125], where an islanding detection approach is deployed to identify the network operation states. The setting thresholds of the relevant overcurrent relays are then updated to adapt to the new operating state of the network. In [126], a microgrid configuration and its protection scheme with real digital relays and a Generic Objective Oriented Substation Event (GOOSE)-based communication network were developed. The proposed system could handle different fault locations, e.g., fault at utility feeder or at interface bus. However, the grading margin between two protection levels was only 0.02 s, which seems technically unfeasible with the available equipment.

Disadvantages: The disadvantage of the proposed methods is the high investment cost due to the need for real-time communication channels and a large number of CBs

with integrated digital relays. For LV microgrids typically spanning about 1 km, such a large number of expensive advanced devices seems hardly justified. Also, the FRT requirements for connected DERs imposed by the new grid codes have been neglected.

4.2.1.3 Impedance/Admittance protection

Researches in [127, 128] proposed protection methods utilizing the total admittance of the protected line segment. The method can detect and isolate faults in both operation modes. Another paper in [129] measured the impedance to protect against different faults with various fault impedances. The communication-assisted impedance-differential protection scheme was developed for rapidly eliminating faults. The inverse-time low-impedance protection with the inverse-time tripping curve serves as a backup function for protecting single-end feeders alone.

Disadvantages: However, as the LV conductors are always short with a normal range of only 1 km, the protection can only cover a very small part of the segment. Moreover, harmonics, transient behaviors of the fault currents, and fault resistance can degrade the accuracy of the extraction of the fundamental components.

4.2.1.4 Protection schemes considering the FRT requirements

Several researches that focused on the development of the FRT capability of PV systems were provided in [130, 131]. Also, references [132, 133] have proposed an intelligent protection concept dedicated to the protection of LV microgrids taking into account the FRT requirements of the connected DERs. In these articles, the authors divided a LV microgrid into different protection zones, each of which is covered by a protection element corresponding to each operating mode. A very fast and advanced communication network based on the IEC 61850 protocol is proposed to be installed to obtain an adequate selectivity between the protections of the customer and the host feeder.

Disadvantages: Although the above methods have shown very high performance, the high investment cost cannot be justified in the context of protecting small LV microgrids. The number of LV networks with a limited capacity of about 500 to 1000 kVA can reach hundreds of thousands. Therefore, the construction of such a large number of communication facilities may not be cost-effective. In addition, the real-time communication protocol dedicated for protection purposes, such as the transmission of interlocking signals, should be based on GOOSE messages. However, this communication mechanism is limited in the substation area if other measures such as Virtual Local Network Area (VLAN) encapsulation are not considered.

4.2.1.5 Conclusion

As mentioned above, although a series of studies focusing on the protection issues of microgrids with a high proportion of DERs in general, and PV systems in particular, has been published, some researches have not examined the functioning of the interface protection of the connected DERs. In contrast, others have focused only on the Fault

Ride Through (FRT) capability of the **DERs** themselves. In addition, several papers have proposed the use of communication and new digital protective devices to protect **LV** microgrids. Although the idea is quite consistent with the new trend of research topics in smart grids, such implementation requires very high investment costs in reference to the limited capacity and number of customers of **LV** networks. Therefore, in this chapter, a protection scheme for **LV** microgrids is proposed, taking **FRT** capability of the connected PV systems into consideration. The setting parameters of this protection system are the foundation of elaborating the protection scheme of the host **MV** distribution network. The proposed system includes several setting groups that can adapt to changes in the operating modes of the protected **LV** microgrids. The transfer of control signals for changing the protection setting groups and also the control strategies of the connected **DERs** does not require dedicated, fast, and expensive communication channels. It can be integrated into the existing communication infrastructure of utility companies or into new low-cost infrastructures. The proposed protection system is evaluated by applying for protecting **LV** microgrid 1 of Figure 2.8 under various fault scenarios in the software environment **DIgSILENT | PowerFactory**. The **LV** microgrid 1 is connected to Node-06 of the **MV** Grid-1 of Figure 2.7.

4.2.2 MV network protection

4.2.2.1 Adaptive protection

In [102], a practical implementation of an adaptive protection system was described. A network automation controller has been set up, which is responsible for the automatic control action and the change of the setting groups. The interface protection of the installed **DERs** was based on voltage/frequency measurements. The authors also took into account the **FRT** requirements of the connected **DERs**. However, the study focused mainly on network control and islanding instead of protection. Another adaptive protection system for the adaptability of the setting thresholds was mentioned in [134]. Compared with the conventional overcurrent protection, the proposed method updated the operating state of the connected **DERs** prior to recalculating the pickup values. Two adaptive protection elements were implemented, one covering about 80% of the protected line and the other the remaining 20%. A simulation result for a phase-to-phase fault was provided. Similar techniques also could be found in [135, 136, 137].

Reference [138] presented a hybrid framework for adaptive protection of the distribution network based on the IEC 61850 standard. Interlocking logic and fault current direction detection logic has been integrated into each of the local controllers. Besides, local controllers could communicate with each other and with the central controller via a common communication network. Signals required for protection purposes, such as trip and block signals, and status changes, were exchanged using the **GOOSE** message mechanism. However, the mechanism for coordination between the protection elements of the different protection levels was still lacking.

A study in [139] deployed superimposed sequence currents for network protection, which was demonstrated by mathematical formulas. Depending on the type of connected

DERs, an adaptive factor was derived from calculating the setting thresholds of the deployed inverse-time overcurrent relay. The simulation results demonstrated the high performance of the proposed method, which was also validated using a Hardware-In-the-Loop test platform. In [140, 141], an adaptive directional inverse-time overcurrent protection scheme was designed and also verified for specific fault scenarios. The coordination started with the determination of the operating state of the DERs. By calculating the system impedances, the peak current can be obtained.

A scheme presented in [142] applied an optimization technique to determine the optimal delay for each relay. All faults were correctly detected and isolated, as demonstrated by the results of the Hardware-In-the-Loop tests. Similar methods of adaptive calculation of pick-up values for the overcurrent relays involved can be found in [143, 144]. Several studies that have used Phase Measurement Unit (PMU) to implement adaptive protection systems have been reported in [145, 146]. The authors proposed to use PMU real-time measurements for estimating the actual topology of the protected network. Any substantial change in network configuration would result in the recalculation of the settings of the inverse-time relays by using optimization techniques.

Disadvantages: Although the studies mentioned above can be very effective and accurate, various issues need to be taken into consideration. Firstly, some of the methods required to implement a large number of expensive devices such as PMU, digital relays, fast communication channels. Secondly, most of them neglected the FRT requirements of the connected DERs and the coordination with downstream LV microgrid protection. The critical time for successful islanding of the LV microgrids was not taken into account.

4.2.2.2 Differential protection

Papers in [147, 99] proposed differential protection systems by using communication assisted digital relays on each line segment. Primary protection is provided by the instantaneous differential relays, while the relays on adjacent feeders offer backup protection. In the event of a communication or relay failure, a protection scheme based on voltage comparison is used as tertiary protection. Moreover, the proposed approach can handle high impedance faults by relying on the high sensitivity of Current Transformers (TCTR). However, it is not possible to detect all faults, which inevitably leads to dead zone protection. Another article described in [148] has also developed a differential scheme that is based on conventional overcurrent relays and a communication link for data exchange. It is necessary to transfer the current measurements from the relays located at the end of the feeder to those located in the substation zone. Dedicated protection schemes have been designed for the feeders and the LV bus. The protection of the DER interface is based on the principles of under/overvoltage and reverse power flow. However, back-up protection has not been taken into account. The performance of the proposed systems could be affected by load imbalances and switching transients.

A similar protection idea was described in [149], but the difference in energy level between two measuring points was used instead. Many types of faults were detected and isolated correctly, even with high impedance faults. However, this approach required a

large number of measuring points as well as a dedicated communication channel for data transfer. The calculation time for the protection criterion was not mentioned. In [150], communication-assisted multi-terminal differential protection was designed. A central protection unit has been implemented to adjust the operating and restraint thresholds of the multi-terminal protection zone. However, only the protection concept was presented; validation or test results were not mentioned. Another research in [151] applied the Wimax communication network for the differential protection. However, the authors focused only on communication aspects instead. The research in [152] is a combination of two studies in [150] and [151]. However, validation results were still not available. Reference [153] proposed another differential scheme that is based on a data mining model. The results of the performance comparison showed that the proposed system achieved higher accuracy in fault detection (99.7% on average) compared to overcurrent (70%) and differential (85.5%) protections. However, an essential protection factor namely the processing time, that is most concerned in a data mining application for protection purposes, has not been studied.

Disadvantages: The above protection systems require very sensitive TCTRs and a dedicated, fast, and reliable optical communication network, which seems quite expensive to use in distribution networks. The number of MV distribution networks can reach several thousand, and therefore requires a huge budget for large-scale implementation. Moreover, the authors neglected many factors affecting the performance of a differential scheme such as unbalanced loads, harmonics, asynchronous measurements, TCTR saturation, and inrush currents. We should note that the load imbalance, which significantly influences the sensitivity of the differential protection, is an inherent nature of the distribution networks. The issue is more common in the United States where MV single-phase loads are rather common as mentioned in Chapter 2.

4.2.2.3 Multiagent-based protection scheme

A Multiagent System (MAS) protection system for the MV network was mentioned in [154]. The network was divided into different segments that were protected by corresponding protection agents installed on the bus bars interconnecting different areas of the network. A communication channel is required for the exchange of fault data between the adjacent relay agents. Based on the measured and received fault current signals, each relay agent calculated the fault direction using wavelet transform and communicated this value to its neighbors in order to locate the fault. Another MAS-based protection scheme was presented in [155]. Only simplified binary status signals (0 or 1) are required to exchange between adjacent protection agents. Based on the received information, each agent has successfully detected whether the fault is internal or external before making the final tripping decision. The simulation results showed that this protection system correctly tripped all types of faults. A similar system was also published in [156].

Disadvantages: Although the research mentioned above has demonstrated its high performance, several problems have not been mentioned, such as selective operation with connected DERs, islanding of LV microgrids, delays of the protection elements.

4.2.2.4 Distance protection

A distance protection system dedicated to distribution networks containing converter-based DERs was presented in [157]. The converter was represented by a voltage source to obtain the formulas for calculating impedance parameters. The theoretical results calculated by Matlab have closely matched the results simulated in PSCAD/EMTDC. A RDIR element was also required to control the distance relay. The different types of faults were correctly eliminated. Another scheme found in [158] is also based on the distance measurements. Two protection zones with a margin of 0.2 s covering the entire protected line were set up. Impacts of the intermediate DERs have been investigated.

Disadvantages: A similar shortcoming is that they did not consider the FRT requirement of the DERs. Besides, operation coordination was not mentioned. Various influencing factors such as ZS currents, earthing systems, load imbalance have been ignored.

4.2.2.5 Conclusion

The extensive review of the previous literature indicates that the studies on MV protection mainly considered MV networks as an independent protection entity. None of these methods focused on the operational coordination between the protection devices of the MV network and the integrated LV microgrids. The delay of the MV feeder protection is the decisive factor for the successful islanding of the LV microgrids and also the FRT requirements of the PV systems connected to the MV and LV feeders. Therefore, in the following, a protection scheme for MV grids that ensures selective operation with those of LV microgrids and the FRT capability of PV systems is developed. A communication channel for the transfer of the interlocking signal must be set up.

4.3 Proposition of PV FRT-compliant interface protection

This part aims to describe the requirements imposed by the new grid codes on the DER interface protection. Up to now, many countries have revised their grid codes in the sense that DERs in general, and PV systems, in particular, should be able to remain connected during external disturbances to contribute to system stability. This requirement is called "fault ride through", as already presented in Chapter 1. The FRT requirements differ from country to country as illustrated in Figure 1.4. Therefore, in this study, we propose to take the German grid code as the reference for developing PV interface protections thanks to its detailed specification for the PV interconnection requirements in both MV and LV networks. Also, we propose that those PV systems connected to LV level are required to meet the FRT requirements. According to the considered voltage or frequency FRT requirements, one can suggest three different zones as, [117]:

- 1 Zone 1: must trip;
- 2 Zone 2: ride-through or trip is allowed - "voluntary ride-through";
- 3 Zone 3: must ride-through operation.

In order to achieve these above FRT capability, the interface protection of PV systems and their corresponding setting thresholds should be coordinated with the FRT capability in order to avoid any violation. Generally, two kinds of PV protection function are distinguished from its FRT requirements, including voltage FRT versus undervoltage protection functions, and frequency FRT versus underfrequency protection functions.

4.3.1 Voltage-based protection settings

The Under-Voltage Protection (PTUV) settings must be coordinated to avoid conflict with the voltage FRT requirements, [117]. This means that the time delays of the PTUV elements must be set at a margin sufficient to the duration requirements of the voltage FRT. Within the margin between the "mandatory passage" and "mandatory trip" regions, the FRT voltage requirement is optional. To correctly determine the time delays of the PTUV elements, the clearance times of the protection schemes of external networks must be taken into account. Typical clearance times for HV and EHV systems are presented in [117]. EHV transmission networks are usually protected by two high-speed protection schemes, e.g., differential protection or teleprotection. In general, the primary protection operates instantaneously without any intentional delay. The operation time of such a protection scheme is between 0.07 s and 0.1 s. Backup protection systems used to deal with interphase or phase-to-ground faults, or CB or relay failures are tripped with an intentional delay of between 0.16 s and 0.32 s [117].

On the other hand, HV transmission lines are usually protected by distance schemes with much slower clearance times. For faults occurring in zone 1 of the distance protection, clearance times can be in the range of 0.1 s to 0.16 s. Faults detected by zone 2 are eliminated within a range of 0.2 s to 0.42 s. For high impedance faults, clearance times are often set in the range of 0.5 s to 0.92 s. As a result, we propose to implement two tripping levels for the phase PTUV element as recommended in the guideline of the German Association of Energy and Water Industry [24] for MV-connected PV systems and VDE-AR-N 4105:2011 [11] for LV-connected PV systems. The overall setting parameters for the undervoltage element of PV interface protection are provided in Table 4.1.

4.3.2 Frequency-based protection settings

Similarly to the phase PTUV element setting, the pickup values and time delays of the Under-Frequency Protection (PTUF) element are also derived from the standards given in [11] and [24]. The setting values are provided in Table 4.1.

Table 4.1 – Settings of PV undervoltage and underfrequency functions

Function	Description	Level	Threshold	Unit	Time, s
PTUV1	Undervoltage protection	High-set	0.45	<i>p.u.</i>	0.2
PTUV 2	Undervoltage protection	Low-set	0.8	<i>p.u.</i>	1.2
PTUF1	Underfrequency protection	High-set	46	<i>Hz</i>	2
PTUF2	Underfrequency protection	Low-set	47	<i>Hz</i>	3

4.4 Protection scheme for LV microgrids

The **Low Voltage (LV)** microgrids must be able to operate correctly in both modes of operation, including grid-connected and islanded operation [35]. Moreover, they must be able to switch smoothly to islanding, intentionally, or unintentionally. Intentional islanding takes place typically after reaching power balance in isolated LV microgrids. Unintentional islanding occurs in case of failure of external MV distribution networks. To achieve a power balance for the intentional and unintentional islanding of the LV microgrid, we propose to implement a Central Control Unit (CCU) and a master unit.

The CCU is responsible for the economical and energy-efficient operation of the network while meeting the technical boundary conditions in grid-connected and islanded operation modes. In the study, the authors focus only on the technical aspects related to the network concerned. The master unit deployed in the study is a kind of Battery Energy Storage System (BESS), providing voltage and frequency control functions. Its capacity is assumed to be sufficient to cover the total demand of the highest priority customers for a certain pre-specified period. In the case of unintentional islanding, an essential role of the CCU and the BESS system is to achieve the post-fault active power balance to guarantee the stability of the islanded LV microgrid. The model of the BESS with the necessary control functionalities has already been presented in the Section 2.8.

The developed protection scheme must ensure the safe operation of such a flexible subnetwork, not only in the grid-connected operation mode but also in the islanded mode. A fixed set of protecting parameters seems impractical for protecting the LV microgrid due to the wide range of fault currents between the two operation modes. Therefore, different setting groups should be pre-specified in the protection devices to adapt to each operating condition of the network concerned, resulting in an adaptive protection scheme for the LV microgrids. We propose that the CCU assumes the responsibility for changing the setting groups of all relevant protection devices when the LV microgrid is switched from one mode to the other.

4.4.1 Considered LV microgrid

The concerned network is the LV microgrid 1 of Figure 2.8. When the microgrid is transferred to the islanded mode, the BESS assumes responsibility for frequency control. All the PV systems that are remained connected after isolation of external disturbances should participate in voltage control by injecting a certain amount of reactive power as presented in Section 2.7.5. With the proposed control strategy, the network is able to come into steady-state operation with frequency and voltage in permitted ranges after islanding. Moreover, when detecting a transition between operation modes by monitoring the status position of the interface Circuit Breaker (CB), i.e. CB0 in the case, the CCU sends control signals to all protective devices to change their setting groups corresponding to the present operation mode. The changing process should be delayed long enough to avoid any possible malfunction due to postfault transients of current and voltage. In this part, a protection scheme for an islanded LV microgrid is developed.

4.4.2 Proposition of the developed protection scheme

Since the LV microgrid is able to operate in two modes, the coordination of all relevant protection devices must be considered for different operating conditions. To meet the Fault Ride Through (FRT) requirements imposed by the new grid codes presented in Section 1.2, the PV interface protection must be reconfigured according to the operating parameters given in Table 4.1. Besides, it should be noted that the time delays of the other protections must be compatible with those of the PV interface protection. Therefore, the protection time limit of the PV interface is considered as the basis for the development of the LV microgrid protection scheme.

Naturally, the FRT requirements of inverter-based PV systems present a demand for feeder and load protections to respond very quickly to faults. As indicated in the Appendix F, the fault currents provided by inverter-based PV systems may not be large. Therefore, a fuse-based protection system seems unable to protect a certain LV microgrid in both modes of operation. In this study, we suggest replacing all feeder fuses with CBs controlled by intelligent protection relays, abbreviated to Feeder Intelligent Electronic Device (FIED). Moreover, the islanded LV microgrid is very sensitive to disturbances due to a lack of inertia, requiring fast and reliable switching devices to achieve unintentional islanding. Therefore, a fast-operating static switch (CB0) controlled by a Central Intelligent Electronic Device (CIED) replaces the step-down transformer fuse in Figure 2.3 and Figure 2.4 to ensure quick and smooth islanding of the LV microgrid.

Additionally, the fuses installed at the beginning of each lateral, i.e. fuses in Figure 2.3 and fuses AD in Figure 2.4 have to be replaced as their fixed melting times will be significantly extended due to a low level of fault currents in the islanded mode. A long delay in clearing faults may lead to unwanted disconnection of the PV systems, causing instability of the islanded network. Moreover, as indicated in [159], if the customer's fuses remain unchanged as presented in Subsection 2.3.1, selectivity between FIEDs and fuses seems to be barely achieved, since these devices should then trip in a few tens of milliseconds. Hence, the study proposes to replace the lateral fuses by Molded-Case Circuit Breaker (MCCB)s with integrated electronic trip units. The electronic trip units allow precise settings both in terms of disconnection times and current thresholds. Modern electronic MCCBs can trip faults in less than 0.03 s and can handle a wide range of current ratings from 15 A to 2500 A, [160].

A remarkable feature of MCCBs is that their tripping curves are adjustable, allowing selectivity to be achieved with the FIEDs. Besides, the electronic release circuit of MCCBs offers a solution for protection against small earth faults called function G, improving the earth protection sensitivity. One of the advantages of function G is that a fault on the supply side of a MCCB, i.e., a fault between the transformer secondary winding and its connecting conductors across the terminals of the MCCB, does not cause the MCCB to intervene. The reason is that the fault current does not affect either the Current Transformer (TCTR) of the phase or the TCTR of the neutral. When the microgrid changes to a new operating mode, the CCU sends a signal to all MCCB controllers to modify their tripping curves. The simplified diagram of the protection scheme is shown in Figure 4.1.

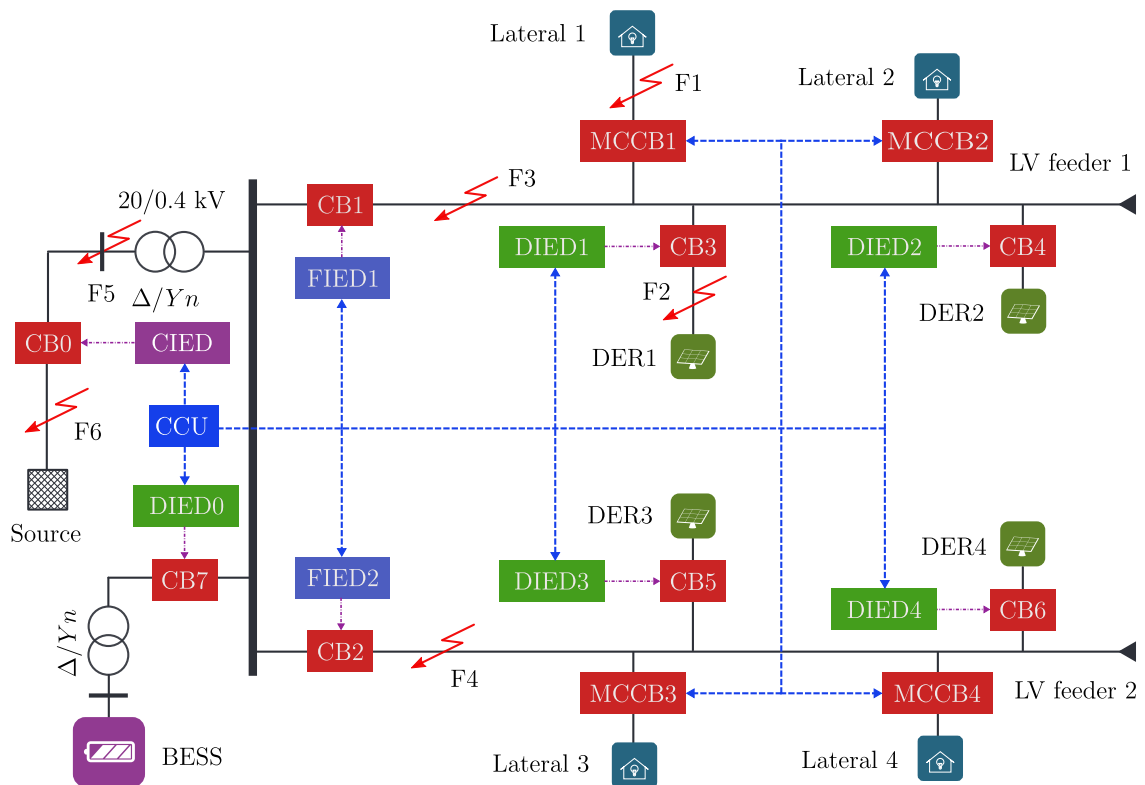


Figure 4.1 – Protection scheme for a LV microgrid

Overall, four typical protective devices are required to protect a *LV* microgrid:

- 1 CIED: interconnection network protective device that replaces the traditional D circuit breaker of Figure 2.4 or FMT fuse of Figure 2.3, and is responsible for network interconnection;
- 2 FIED: *LV* feeder protective device that replaces the conventional feeder FD fuse. It covers faults on the respective feeder, and also provide backup protection for downstream elements, such as lateral MCCBs or DIEDs;
- 3 MCCB: lateral protective devices that replaces lateral FC fuse. It disconnects the respective lateral for faults within its coverage;
- 4 DER Intelligent Electronic Device (DIED): PV interface and facility protection element, including protection of master unit, i.e. BESS. The former isolates PV systems from the network when a fault occurs on the host feeder while the later deals with the internal faults.

We developed two predefined sets for each operating mode. However, operators can design more setting groups to adapt to different practical operating conditions according to network configuration and load and generation capacities. As mentioned earlier, when a transition between these two modes occurs, the CUU sends control signals to FIEDs to modify their setting groups. The configuration and protection coordination between the protection devices concerned are presented below.

Overall, the developed protection scheme of the LV microgrid is mainly based on Time Overcurrent Protection (PTOC) and Under-Voltage Protection (PTUV) elements. The RDIR element that provides a very sensitive selectivity between two levels of protection to meet the PV FRT capability is required. However, under fault conditions involving significant fault impedances, neither the fault current nor the voltage drop could be sufficient for the phase current or voltage protections to detect faults or distinguish between overload and fault conditions [161]. Therefore, additional fault detection algorithms should be added to provide backup protection if the primary ones fail. We propose to use NS and ZS currents and voltages, to serve as redundant fault detection mechanisms. Since these components only appear under unbalanced conditions, the setting thresholds can be set at a level lower than the nominal values. However, to avoid malfunction caused by unbalanced loads, these thresholds must be chosen carefully. Finally, high impedance faults causing fault currents in the same order with load currents that cannot be detected by the fundamental current and voltage components are outside the scope of the study.

4.4.3 Protection scheme for grid-connected mode

Since the setting thresholds for protection functions change case by case, in this part we only focus on the time grading between different protection levels. A detailed set of configuration parameters is provided in a case study.

4.4.3.1 Lateral protection

For any type of fault occurring inside a lateral area, its protective device must eliminate the fault as quickly as possible. As already presented in Subsection 2.3.1, we can choose different MCCBs with ratings according to the load capacity of protected laterals, [160]. The very short tripping time of only 0.03 s greatly improves protection selectivity. Such a short clearance time also ensures that lateral faults are isolated before the time delay of PV interface protection has elapsed.

4.4.3.2 PV protection system

In the proposed scheme, protection of the PV systems is composed of, [31]:

- 1 PTOC element: facility protection for protecting against overloads and faults inside the PV installation.
- 2 PTUV and PTUF elements: interface protection for tripping the PV systems, preventing them from unwanted islanded operation.

In a similar way to the lateral protection, the PV PTOC elements must be coordinated with those of the host feeders. We propose to install an additional MCCB at the PV PCC to provide facility protection. The selection of the operating parameters for the trip unit is made in a same way as for the lateral MCCBs. Therefore, all faults in the PV installation are eliminated before the host feeder PTOC time delay goes by.

A DER Intelligent Electronic Device (DIED) with a separate CB is installed for the interface protection, whose setting parameters are derived from Table 4.3. The clearance times of these protections, which are normally equal to 0.2 s, are the time constraints for the design of the LV feeder protection in order to guarantee the FRT requirements.

4.4.3.3 LV feeder protection

A LV feeder protection unit, i.e. FIED, includes:

- 1 Forward Time Over-Current Protection (PTOCF) element: provides primary protection against faults in its covered area and controlled by a RDIR element. The RDIR function is necessary to avoid any possible false tripping, although it seems unlikely to occur in LV microgrids dominated by inverter-based PV systems. In addition, the PTOC element must serve as a redundant back-up protection for the MCCBs of the PV systems and the laterals downstream;
- 2 Reverse Under-Voltage Protection (PTUVR) element: provides backup for the microgrid CIED or neighboring feeder protections. This element is controlled by a RDIR element that only allows it to trip in the reverse direction.

Regarding coordination in the forward direction, in order to not only quickly eliminate severe faults but also to be sufficiently sensitive to low fault levels, the feeder PTOCF element must have at least two tripping levels, including a fast high-set module, i.e. PTOCF1, and a slow low-set modules, i.e. PTOCF2. The delay of the PTOCF1 level should be shorter than that of the PV interface protection, i.e. PTUV element. Moreover, it should be long enough to be coordinated with the MCCBs. As the trip time of the MCCBs in the instantaneous part is less than 0.03 s, (Figure 4.2), we set the time delay of the PTOCF1 to 0.13 s. On the other hand, that of the PTOCF2 is fixed at 0.45 s to be graded with the MCCB time-delayed part, (Figure 4.2).

The significant delay of the PTOCF2 is not likely to have any impact on the FRT capability of the PV systems connected to neighboring feeders. The voltage drop caused by fault on one feeder is generally low, and therefore corresponds to the PV PTUV2 delay, i.e., 1.2 s (Table 4.1). In conclusion, the feeder PTOCF element, which is only allowed to operate in the forward direction, has two operating thresholds, one is triggered by the high fault current for 0.13 s, and the other is initiated by the low fault currents for 0.45 s. These time delays are fully compatible with the maximum disconnection times for fault protection on TN earthing systems recommended by IEC 60364-4-41 [162].

Concerning the settings of the backup protection, i.e., the PTUVR element, its time delay should be set to an appropriate value to ensure coordination with the PTUV element of the microgrid interconnection protection, i.e., CIED, and PTOCF elements of adjacent FIEDs. Besides, this time delay shall be long enough to allow the PV PTUV2 elements to trip their respective CBs before the fault is completely eliminated, avoiding undesirable islanding. Therefore, a delay of 1.5 s is chosen to ensure a minimum grading margin of 0.2 s with that of the PTUV2 element of the PV systems.

4.4.3.4 Secondary transformer protection

The protection of a MV/LV transformer in a LV microgrid with high PV penetration also has two operating levels. The high-set level protects against severe faults with fault currents up to ten times the transformer rated current, or 1.5 times the maximum fault current at its LV side. This trip level must trip instantaneously for any fault current exceeding the setting threshold. A time delay of 0.1 s is selected. The low-set level is allowed to operate at a much lower current, approximately 1.5 to 2 times the transformer rated current with a delay of 0.65 s to ensure a 0.2 s grading margin with the feeder PTOCF1 elements. This function can also provide backup for the LV feeder protection.

4.4.3.5 Protection against external faults

The ability to quickly and accurately detect and eliminate external faults must be achieved to ensure a successful islanding of the microgrid. External faults are detected and eliminated by the operation of the CIED Reverse Under-Voltage Protection (PTUVR) element, which is allowed to trip only in the reverse direction. Once a voltage drop below the pickup threshold coinciding with the fault current in the reverse direction is detected, the PTUVR element trips CB0 (Figure 4.1) after a predefined delay. The respective microgrid is switched into an isolated mode. The faster the operation of the PTUVR element for external faults, the lower the risk of instability imposed on the LV microgrid after islanding. Therefore, we propose that the PTUVR element should have two tripping levels. The high-set PTUVR1 should trip within 0.13 s to prevent the PV systems located inside the concerned microgrid from undesirable disconnection. The delay of the PTUVR2 is 0.5 s, which is sufficient to be coordinated with the 1.2 s delay of the PV PTUV2 element.

4.4.4 Protection algorithm for the islanded mode

4.4.4.1 Lateral protection

For a network with high PV penetration, the fault currents in islanded mode are relatively low compared to those in grid-connected mode [119]. A low fault level means a longer fault clearance time if tripping curves of the MCCBs remain unchanged. Hence, we propose to decrease the tripping thresholds of the MCCB to achieve fast responses at low fault levels. The solution is rather promising since, in islanded mode, only the most priority customers are maintained in service. Other loads that are not important are usually shed. Since the ground fault level does not depend on the capacity of the load, the setting of function G remains the same.

4.4.4.2 PV and BESS interface protection

The PTUV and PTUF parameters of PV systems and BESS remain the same as in regular operation to ensure the FRT capability of the PV systems. The BESS facility protection must be equipped with an additional Reverse Time Over-Current Protection (PTOCR) element to prevent the BESS from feeding a fault in case of failures of the feeder primary

protection. Such an element must be coordinated with the feeder PTOCF elements. In general, it has only one trip threshold with a time delay of 0.53 s.

4.4.4.3 Feeder protection

The feeder protection for islanded operation is based on the PTUV element:

- 1 Forward Under-Voltage Protection (PTUVF) element: provides primary protection against faults in the forward direction. Two tripping levels are required. The high-set PTUVF1 eliminates faults that cause considerable voltage drops in less than 0.13 s. Such a delay is required to avoid undesirable disconnection of PV systems connected to neighboring feeders. The low-set PTUVF2 is delayed for 0.45 s to coordinate with the slow part of Molded-Case Circuit Breaker (MCCB) tripping curves.
- 2 Reverse Under-Voltage Protection (PTUVR) element: provides backup protection for PTUVF element of the adjacent feeders and is delayed for 1.5 s.

Besides, in the case of two-phase faults with high fault impedances, the voltage drop of the system may be slight due to the injection of reactive power by the BESS. The feeder PTUVF element may not be sensitive enough to detect such faults. It is, therefore, necessary to implement an additional two-set Forward Negative-sequence Time Over-Current Protection (PTOCQF) element, i.e., PTOCQF1 and PTOCQF2, with time delays of 0.13 and 0.45 s, respectively. To protect against earth faults, unrestricted earth fault protection, which has already been used for a grid-connected mode of operation, is also deployed.

4.4.5 Case study

In this part, the performance of the proposed protection scheme is evaluated by implementing it on the LV microgrid 1 in Figure 2.8. The network and proposed protection scheme are simulated in the software environment DIGSILENT|PowerFactory. The detailed configurations are explained in Appendixes G.1 and G.2.

4.4.5.1 Grid-connected mode

4.4.5.1.1 Configuration results

The overall settings are provided in Table 4.2. The current-time-based coordination results for different protection levels including lateral, LV feeder and microgrid interface protections, for instance, MCCB7-FIED1-CIED3, during grid-connected mode is illustrated in Figure 4.2. The voltage-based and frequency-based coordination of three elements DIED1-FIED1-CIED3 is shown in Figure 4.3 and Figure 4.4.

4.4.5.1.2 Evaluation

Various fault scenarios have been simulated for the LV microgrid 1 in Figure 2.8, and provided in Appendix G.3. We assume that all faults occur at $t = 1$ s. Table G.1 presents

Table 4.2 – Overall setting parameters for grid-connected operation mode

Device	Function	(1) ¹	(2) ²	(3) ³	(4) ⁴	(5) ⁵	(6) ⁶	(7) ⁷	8) ⁸
MCCB7	PTOCP1	N	I	kA	High-set	3.0	0.03	F1	None
	PTOCP2	N ⁹	I	kA	Low-set	1.5	0.25	F1	None
	PTOCG1	N	I^0	kA	High-set	0.12	0.03	F1	None
	PTOCG2	N	I^0	kA	Low-set	0.05	0.25	F1	None
DIED1	PTUV1	N	V	$p.u.$	High-set	0.45	0.2	F3, F4	F1, F5, F6
	PTUV2	N	V	$p.u.$	Low-set	0.8	1.2	F3, F4	F1, F5, F6
	PTUF1	N	f	Hz	High-set	47.5	0.2	F3, F4	F1, F5, F6
	PTUF2	N	f	Hz	Low-set	48.5	3	F3, F4	F1, F5, F6
	PTOCP	N	I	kA	–	0.1	0.03	F2	F3, F4, F5, F6
	PTOCG	N	I^0	kA	–	0.03	0.03	F2	F3, F4, F5, F6
FIED1	PTOCPF1	F ¹⁰	I	kA	High-set	8.66	0.13	F3, F4	F1, F5, F6, F2
	PTOCPF2	F	I	kA	Low-set	1.44	0.45	F3, F4	F1, F5, F6, F2
	PTOCQF1	F	I^-	kA	High-set	1.1	0.13	F3, F4	F1, F5, F6, F2
	PTOCQF2	F	I^-	kA	Low-set	0.62	0.45	F3, F4	F1, F5, F6, F2
	PTOCGF1	F	I^0	kA	High-set	0.42	0.13	F3, F4	F1, F5, F6, F2
	PTOCGF2	F	I^0	kA	Low-set	0.17	0.45	F3, F4	F1, F5, F6, F2
	PTUVPR	R ¹¹	V	$p.u.$	–	0.8	1.5	None	F8, F9, F11
	PTUVQR	R	V^-	$p.u.$	–	0.05	1.5	None	F8, F9, F11
CIED3	PTOCP1	N	I	kA	High-set	27.4	0.1	F10	F3, F4, F8, F9
	PTOCP2	N	I	kA	Low-set	2.89	0.65	F10	F3, F4, F8, F9
	PTOCQ1	N	I^-	kA	High-set	14.1	0.1	F10	F3, F4, F8, F9
	PTOCQ2	N	I^-	kA	Low-set	1.35	0.65	F10	F3, F4, F8, F9
	PTOCG1	N	I^0	kA	High-set	9.9	0.1	F10	F3, F4, F8, F9
	PTOCG2	N	I^0	kA	Low-set	0.4	0.65	F10	F3, F4, F8, F9
	PTUVPR1	R	V	$p.u.$	High-set	0.7	0.13	F11	None
	PTUVPR2	R	V	$p.u.$	Low-set	0.8	0.7	F11	None
	PTUVQR1	R	V^-	$p.u.$	High-set	0.08	0.13	F11	None
	PTUVQR2	R	V^-	$p.u.$	Low-set	0.05	0.7	F11	None

¹ Trip direction.

² Operating quantity in which I stands for current, V for voltage, and f for frequency.

³ Unit of operating quantity.

⁴ Tripping stage.

⁵ Value of operating quantity.

⁶ Operating time, s .

⁷ Faults covered by the function as a primary protection.

⁸ Faults covered by the function as a backup protection.

⁹ None directional.

¹⁰ Forward direction.

¹¹ Reverse direction.

some of the obtained results for solid faults at various locations. If the primary protection fails to eliminate faults, other pre-configured protection elements function correctly as backup protection. The operating time of each protection function in the result tables is counted on the time between the fault occurrence moment and the moment when the protection function concerned issues the trip.

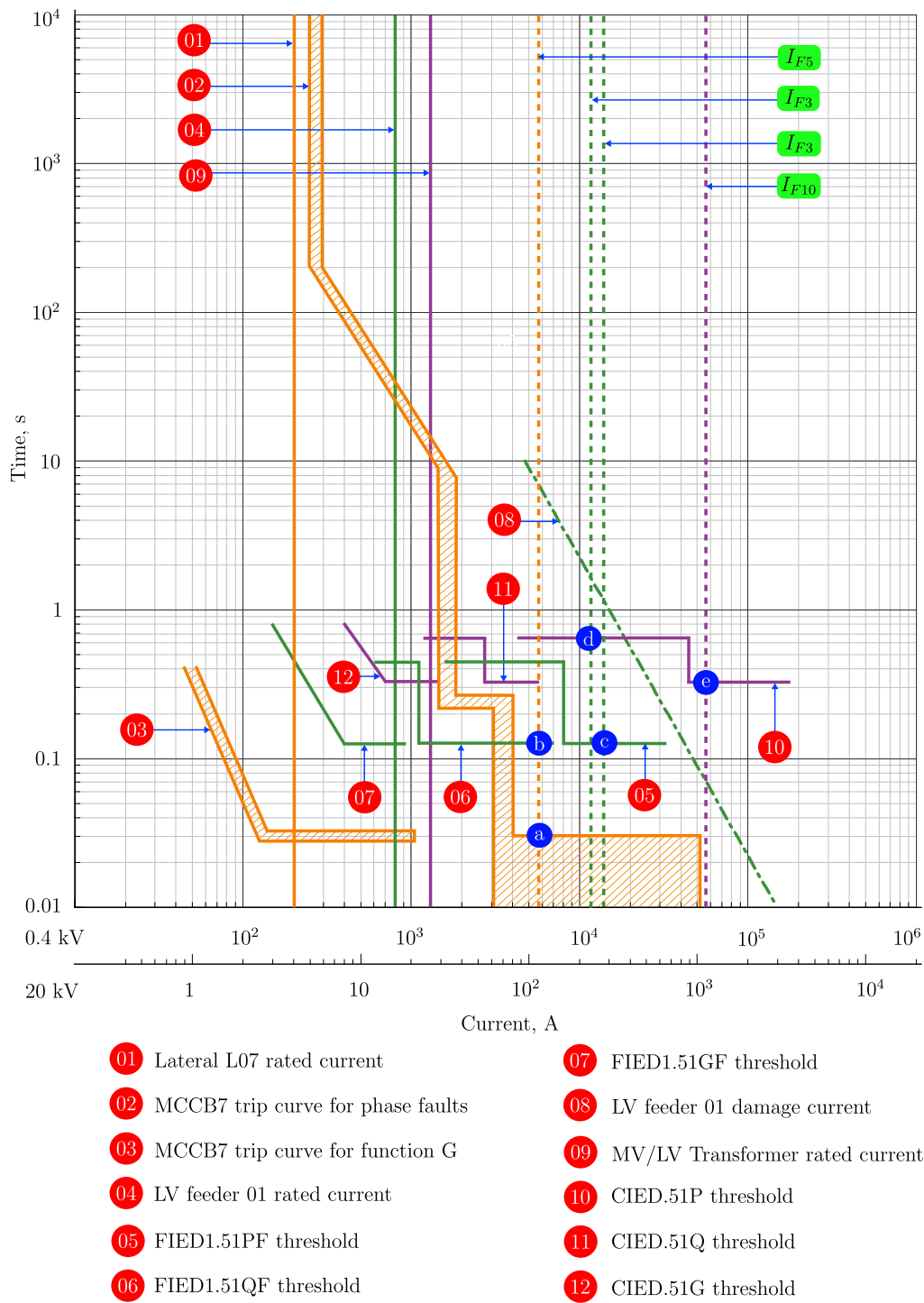


Figure 4.2 – Current-time coordination of LV microgrid 1 in grid-connected mode

For example, Figure 4.2 indicates that, for a phase-to-phase fault with $R_f = 0.01 \Omega$ occurring at the end of the lateral (F5 of Figure 2.8), the fault current level is 4.76 kA . According to the tripping curve shown in Figure 4.2, MCCB9 trips in approximately 0.03 s indicated by node a; the high-set module Forward Negative-sequence Time Over-Current Protection (PTOCQF1) of FIED1 does not trip CB-F1 despite the fault detection. If MCCB9 trip circuit does not work for any reason, FIED1.PTOCQF1 provides a backup trip after

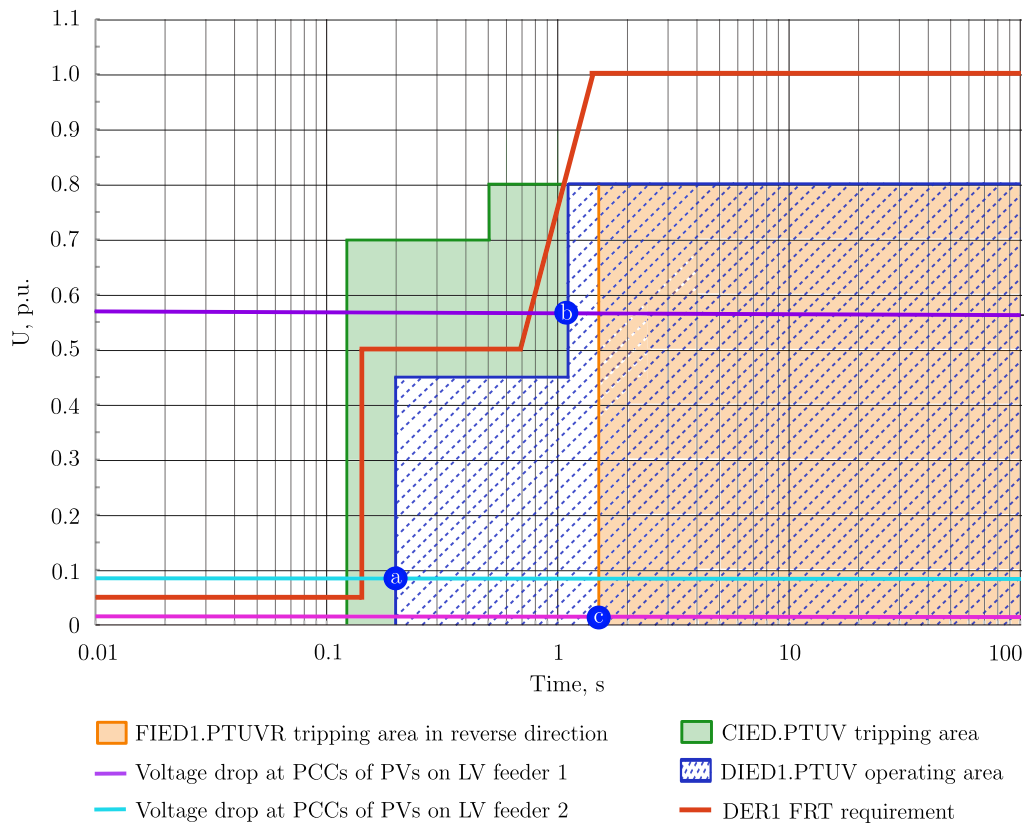


Figure 4.3 – Voltage-time coordination for grid-connected operation mode

0.13 s as illustrated by node b in Figure 4.2. Shortly afterwards, all PV systems connected to the LV Feeder 1 are also disconnected by their phase PTUV1 elements within 0.2 s following the FIED1 trip. All the operating quantities are provided in Table G.2.

Another example is a three-phase fault at F3 with $R_f = 0.01 \Omega$, i.e., a fault at the beginning of the LV Feeder 1 backbone, the fault level is 14.65 kA (node c in Figure 4.2). The high-set FIED1.PTOCPF1 element correctly detects the fault and triggers its corresponding CB-F1 after 0.13 s. All PV systems connected to the LV Feeder 2 succeed in overriding the fault. Also, since the voltage drops at the Point of Common Coupling (PCC) (horizontal cyan line in Figure 4.3) are less than 0.5 p.u., the PV systems connected to the faulty feeder line are disconnected by their PTUV1 elements after 0.2 s (node a in Figure 4.3), preventing them from unintentional islanding.

If CB-F1 does not operate, Phase Time Over-Current Protection (PTOCP)2 element of the CIED3 operates with a fault current of 12.5 kA after 0.65 s (node d in Figure 4.2). The difference between the fault currents detected by the FIED1 and the CIED3 (14.65 kA vs. 12.5 kA) is due to the fault current contribution of the PV systems on the healthy feeders. All PV systems on the healthy feeder, i.e., LV Feeder 2, are disconnected from the grid within 1.2 s (node b in Figure 4.3) after the fault occurrence. Such a long delay is due to the high level of voltages at all the PCCs of these PV systems (the violet line in Figure 4.3). Finally, all the feeder PTUVR elements provide backup operation by tripping their respective CBs after 1.5 s (node c and the pink horizontal line in Figure 4.3).

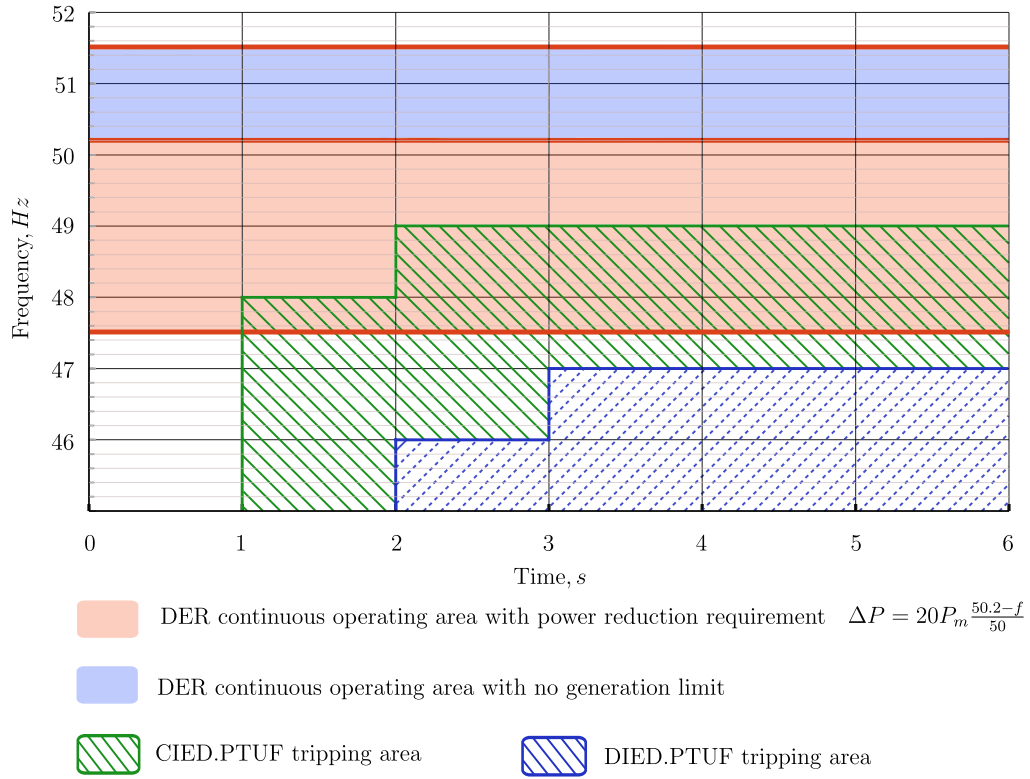


Figure 4.4 – Frequency-time coordination for grid-connected operation mode

Similarly, for faults on adjacent feeders, e.g. a fault occurring at F8 on the **LV** Feeder 2 (Figure 2.8), the module Forward Phase Time Over-Current Protection (PTOCPF)1 of FIED2 identifies a forward fault and trips its CB-F2 within 0.13 s. The FIED1.PTUVR element also detects a fault due to a considerable voltage drop on the **LV** busbar. However, its trip is delayed by 0.33 s since the FIED1.RDIR element has detected a reverse fault. If CB-F2 does not open for any reason, the fault lasts more than 0.13 s. Therefore, the FIED1.PTUVR element trips its corresponding CB-F1 after 1.5 s. When a disturbance occurs due to an internal transformer fault, i.e., at F10, depending on the fault levels, the fault is suppressed either by a high-set PTOC1 or a low-set PTOC2 modules of Central Intelligent Electronic Device (CIED) of the **LV** microgrid 1. In our case, we assume a two-phase fault with $R_f = 5 \Omega$ occurring on the primary side of the MV/LV transformer. The fault level is 1.154 kA on the 20 kV side, or 57.7 kA when referred to 0.4 kV, and thus is eliminated by CIED3.PTOC1 element in 0.13 s (node e in Figure 4.2).

For an external fault at F11, for example, a three-phase fault with $R_f = 2 \Omega$ in the middle of Section 03-04 in Figure 2.7, the voltage sensed by CIED3 reduces to 0.522 p.u. and thus initiates the operation of the CIED3.PTUV element to trip CB0 in 0.13 s. The **LV** network is switched to islanded operation. The transient behaviors of different grid parameters are shown in Figure 4.5. The BESS controller immediately increases its active power according to the frequency control algorithm presented in Chapter 3, as shown in Figure 4.5e. As a result, the post-fault frequency of the islanded **LV** microgrid 1 is maintained within the permitted limits (Figure 4.5b). In addition, after islanding, the variations of the PV operating parameters, such as voltage, current, active and reactive

powers, gradually stabilize and reach steady-state conditions, as shown in figures 4.5e to 4.5h. If CB0 operates unsuccessfully, the feeder PTUV element commands their CBs to open after the time delay of 1.5 s delay has elapsed.

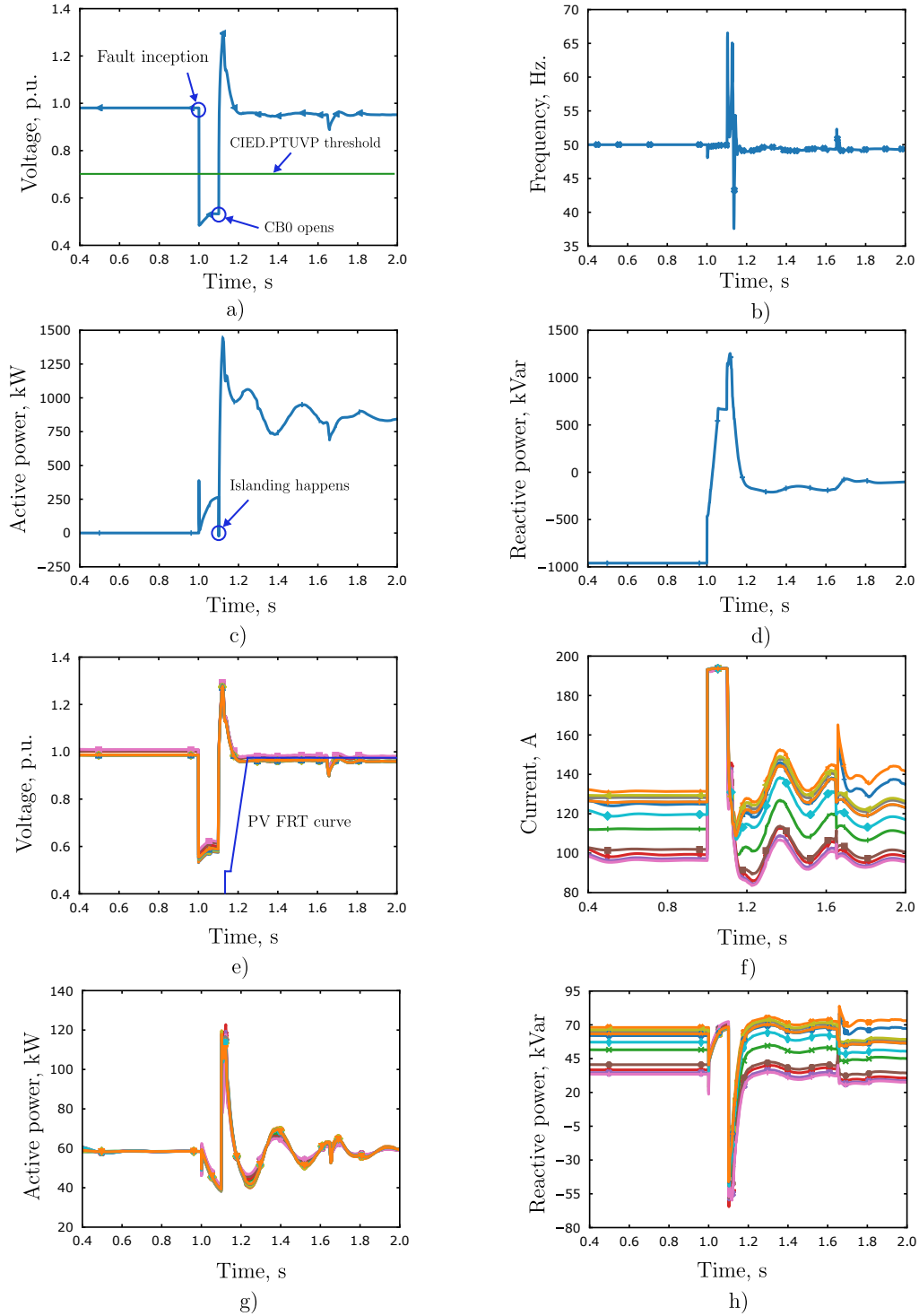


Figure 4.5 – Variations of (a) voltage at MV/LV transformer LV busbar, (b) LV microgrid 1 frequency, (c) BESS active power, (d) BESS reactive power, (e) PV voltages, (f) PV currents, (g) PV active powers, and (h) PV reactive powers during a three-phase fault at F11 with $R_f = 2 \Omega$ in grid-connected mode

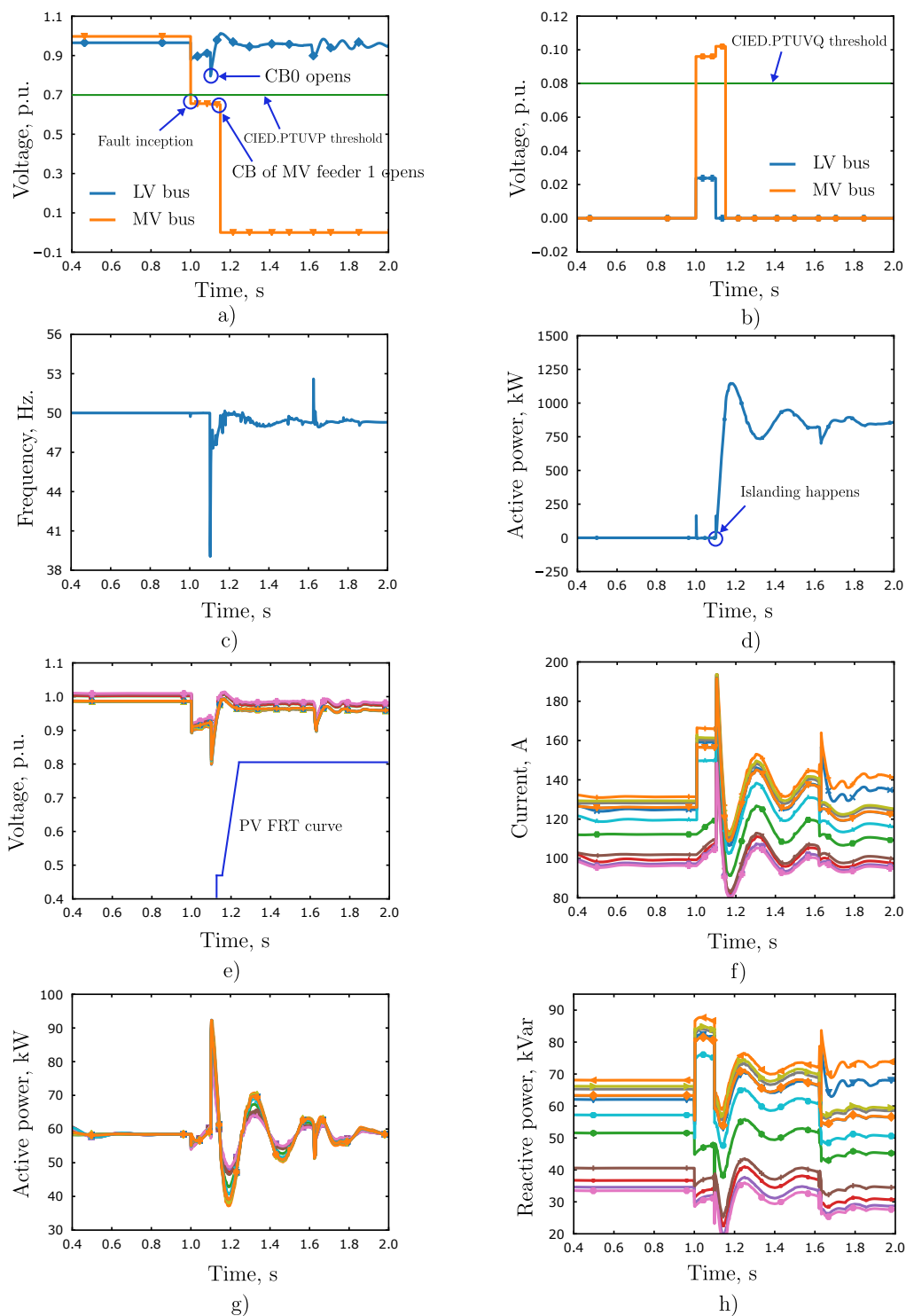


Figure 4.6 – Variations of (a) phase voltages at transformer MV and LV sides, (b) NS voltages at transformer MV and LV sides, (c) LV microgrid 1 frequency, (d) BESS active power, (e) PV voltages, (f) PV currents, (g) PV active powers, and (h) PV reactive powers during a phase-A-to-ground fault at F11 with $R_f = 5 \Omega$ in grid-connected mode

When a disturbance happens due to a transformer internal fault, i.e. at F10, depending on fault levels, the fault is cleared either by a high-set PTOC1 or a low-set PTOC2

elements of the transformer protection. In our case, we assume a phase-A-to-ground fault with $R_f = 5 \Omega$ applied on the primary side of the MV/LV secondary transformer, the fault level is 1.154 kA at 20 KV side, i.e. 57.7 kA when referred to 0.4 kV side, the fault is cleared by the CIED3.PTOC1 in 0.13 s (node e in Figure 4.2).

The proposed system can also handle higher impedance ground faults. For this type of fault, the microgrid CIED3.PTUVR fails to detect the fault due to slight drops of phase voltages. The fault is detected and cleared within 0.13 s by Reverse Negative-sequence Over-Voltage Protection (PTOVQR) of CIED3 thanks to the increase of NS voltage up to 0.1 p.u. . As a result, the LV microgrid 1 is successfully islanded with operational parameters such as voltages, and system frequency is stabilized, as shown in Figure 4.6.

It is worth mentioning that the RDIR method developed in Chapter 3 has shown high accuracy and reliability. For all fault scenarios that have been carried out, the developed RDIR algorithm accurately detects the fault direction even for high impedance faults. The results for higher fault impedance cases are given in Tables G.2 and G.3.

4.4.5.2 Islanded mode

4.4.5.2.1 Configuration results

Figure 4.7 illustrates the current-based coordination for the islanded mode. The coordination results for protection elements based on the phase undervoltage principle are shown in Figure 4.8. The overall settings are tabulated in Table 4.3.

4.4.5.2.2 Evaluation

Various fault scenarios have been simulated for the LV microgrid 1 in the islanded mode, and all the results are represented in Appendix G.4. Assuming at $t = 1 \text{ s}$, a direct phase-A-to-ground fault occurring at F5 on lateral L9. The function G of MCCB9 correctly eliminates the fault after 0.03 s thanks to the rise of the ZS current to 730 A (node a in Figure 4.7). All the PV systems have successfully ridden through such a fault. If MCCB9 fails to operate, the unrestricted earth protection of the FIED1 trips after 0.13 s . After, all PV systems connected to LV feeder 1 will be disconnected after 0.2 s .

Concerning faults on the LV feeder backbone, assuming a solid three-phase fault happens at the far end of the LV feeder 1, i.e. at F4 in Figure 2.8. The voltage measured at the LV busbar drops to 0.678 p.u. , leading to the tripping of FIED1.PTUVF1 after 0.13 s (cyan horizontal line and node a in Figure 4.8). The fault is cleared, and the system voltage is recovered. Therefore, all the PV systems on LV feeder 2 remain connected to the grid. Meanwhile, regarding PV systems connected to faulted LV feeder 1, some trip after 0.2 s (violet horizontal line and node b in 4.8) while the others trip after 0.33 s depending on the distance between their PCCs to the fault location. This is because for those PV systems located far from the fault, the voltage drops at their PCCs are only sufficient for triggering their low-set PTUV2. Only after the FIED1.PTUVF1 operation, the voltage at their PCCs reduce below 0.45 p.u. , initiating their PTUV1 to trip after 0.33 s .

Table 4.3 – Overall setting parameters for islanded operation mode

Device	Function	(1) ¹	(2) ²	(3) ³	(4) ⁴	(5) ⁵	(6) ⁶	(7) ⁷	8) ⁸
MCCB7	PTOCP1	N ⁹	I	kA	High-set	3.0	0.03	F1	None
	PTOCP2	N	I	kA	Low-set	1.5	0.25	F1	None
	PTOCG1	N	I^0	kA	High-set	0.125	0.03	F1	None
	PTOCG2	N	I^0	kA	Low-set	0.05	0.25	F1	None
DIED1	PTUV1	N	V	$p.u.$	High-set	0.45	0.2	F3, F4	F1, F5, F6
	PTUV2	N	V	$p.u.$	Low-set	0.8	1.2	F3, F4	F1, F5, F6
	PTUF1	N	f	Hz	High-set	47	2	F3, F4	F1, F5, F6
	PTUF2	N	f	Hz	Low-set	48	3	F3, F4	F1, F5, F6
	PTOCP	N	I	kA	–	0.1	0.03	F2	F1, F5, F6
	PTOCG	N	I	kA	–	0.03	0.03	F2	F1, F5, F6
DIED0	PTUV1	N	V	$p.u.$	High-set	0.45	0.16	F10	F3, F4, F8, F11
	PTUV2	N	V	$p.u.$	Low-set	0.8	1.2	F10	F3, F4, F8, F11
	PTUF1	N	f	Hz	High-set	47	2	F10	F3, F4, F8, F11
	PTUF2	N	f	Hz	Low-set	48	3	F10	F3, F4, F8, F11
	PTOCPR	R ¹⁰	I	kA	–	0.1	0.53	F12	None
	PTOCQR	R	I^-	kA	–	0.02	0.53	F12	None
FIED1	PTUVPF1	F ¹¹	V	$p.u.$	High-set	0.7	0.13	F3, F4	F1, F5, F8, F9
	PTUVPF2	F	V	$p.u.$	Low-set	0.8	0.45	F3, F4	F1, F5, F8, F9
	PTUVQF1	F	V	$p.u.$	High-set	0.1	0.13	F3, F4	F1, F5, F8, F9
	PTUVQF2	F	V^-	$p.u.$	Low-set	0.05	0.45	F3, F4	F1, F5, F8, F9
	PTOCQF1	F	I^-	kA	High-set		0.13	F3, F4	F1, F5, F8, F9
	PTOCQF2	F	I^-	kA	Low-set		0.45	F3, F4	F1, F5, F8, F9
	PTOCGF1	F	I^0	kA	High-set	0.42	0.13	F3, F4	F1, F5, F8, F9
	PTOCGF2	F	I^0	kA	Low-set	0.17	0.45	F3, F4	F1, F5, F8, F9
	PTUVPR	R	V	$p.u.$	–	0.8	1.5	None	F8, F9, F10
PTUVQR	R	V^-	$p.u.$	–	0.05	1.5	None	F8, F9, F10	

¹ Trip direction.

² Operating quantity in which I stands for current, V for voltage, and f for frequency.

³ Unit of operating quantity.

⁴ Tripping stage.

⁵ Value of operating quantity.

⁶ Operating time, s.

⁷ Faults covered by the function as a primary protection.

⁸ Faults covered by the function as a backup protection.

⁹ None directional.

¹⁰ Reverse direction.

¹¹ Forward direction.

The details of the fault voltage levels at the Points of Common Coupling (PCC) of the connected PV systems, and the operating times of their protection are provided in Table G.4. The system responses under such a fault condition is illustrated in Figure 4.9. We can observe that the network frequency is maintained at nearly 50 Hz before and after

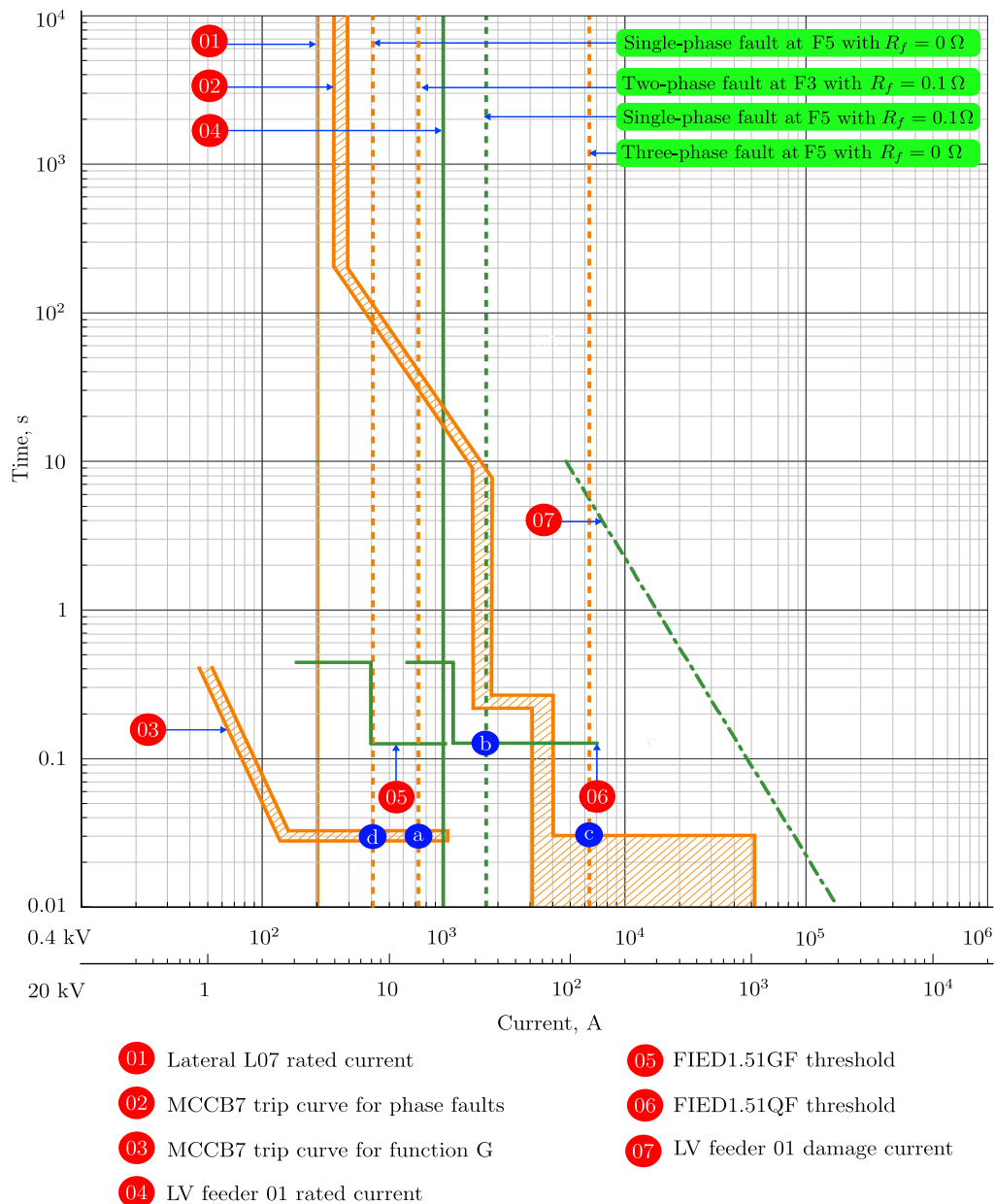


Figure 4.7 – Current-time coordination for islanded operation mode

the fault. Figure 4.9c and d show that after a variation over a short time period, the active powers and currents of the PV systems return their pre-fault levels. Power supply to all customers of LV feeder 1 can be maintained. In case of CB-F1 failure, the fault persists over the trip delay of the Reverse Phase Time Over-Current Protection (PTOCPR) element of the BESS, and thus it trips BESS after 0.53 s by the phase fault current of 5.42 kA.

Consider a phase-B-to-phase-C fault at F3 with a higher fault impedance of $R_f = 0.1 \Omega$, neither the phase nor NS voltage elements, i.e. PTUVF and PTOVQF, have properly detected the faults since the retained phase fault voltage of 0.85 p.u. and NS voltage of 0.03 p.u. are not enough for initiating the corresponding trips. However, fortunately, the fault is successfully removed by the feeder PTOCPF1 element trips in a timely manner

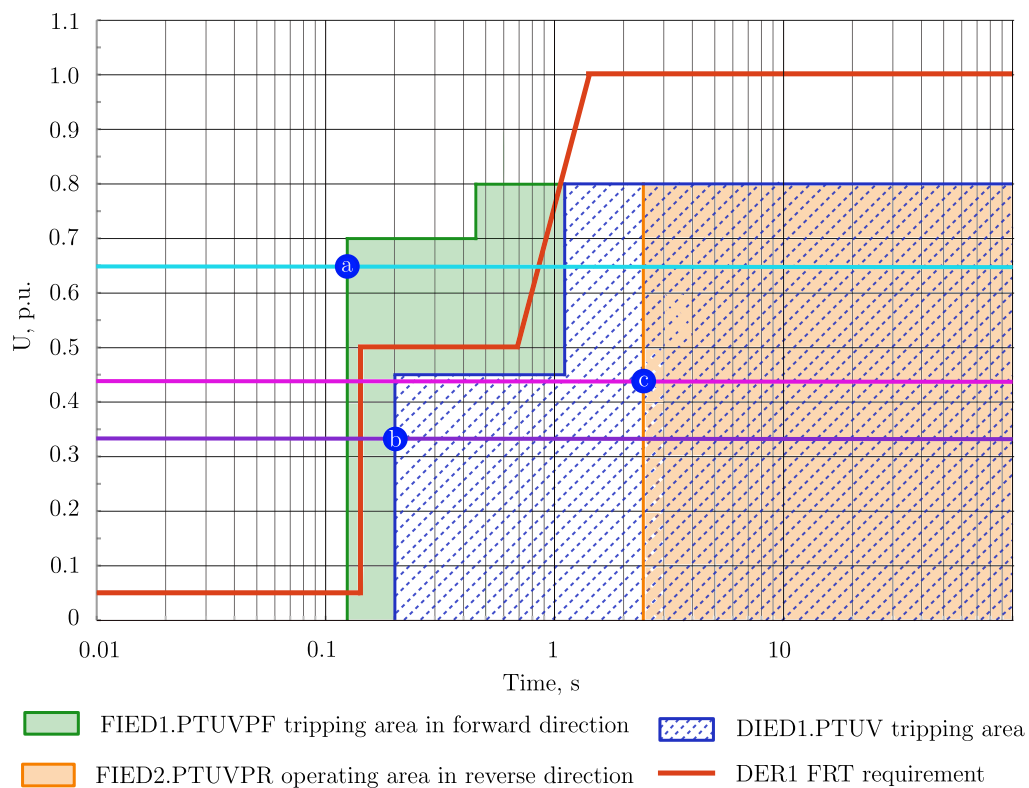


Figure 4.8 – Voltage-time coordination for islanded operation mode

with the **NS** current rising to 1.74 kA (node b in Figure 4.7). All PV systems of **LV** feeder 1 are isolated from the fault by their PTUF element after 2.13 s .

If the fault still exists, only the PTOCQR element of the BESS can detect the fault and trips after 0.53 s . After 1.2 s from the BIED trip, all PV systems are disconnected by their PTUV1 elements. Moreover, the disconnection of BESS also causes a more severe voltage drop of 0.33 p.u. at the **LV** busbar, leading to the operation of the **LV** Feeder 2 PTUVR backup protection after 1.5 s (the horizontal pink line and node c in Figure 4.8).

4.5 Protection scheme for MV networks

4.5.1 Proposition of the protection scheme

The protection scheme of a **MV** distribution network typically can be divided in five different protection areas including: **MV/LV** distribution transformer, PV systems connected to the **MV** feeders, **MV** feeder, **MV** busbar, **HV/MV** distribution transformer.

4.5.1.1 MV/LV transformers and the associated LV microgrids

The protection of the **MV/LV** distribution transformer feeding the connected **LV** microgrids has already been developed in the Section 4.4. Such a protection zone can be regarded as the lowest protection level when coordinating with the protection of the **MV** distribution network. The time delay of the **MV/LV** transformer protection is 0.33 s . If

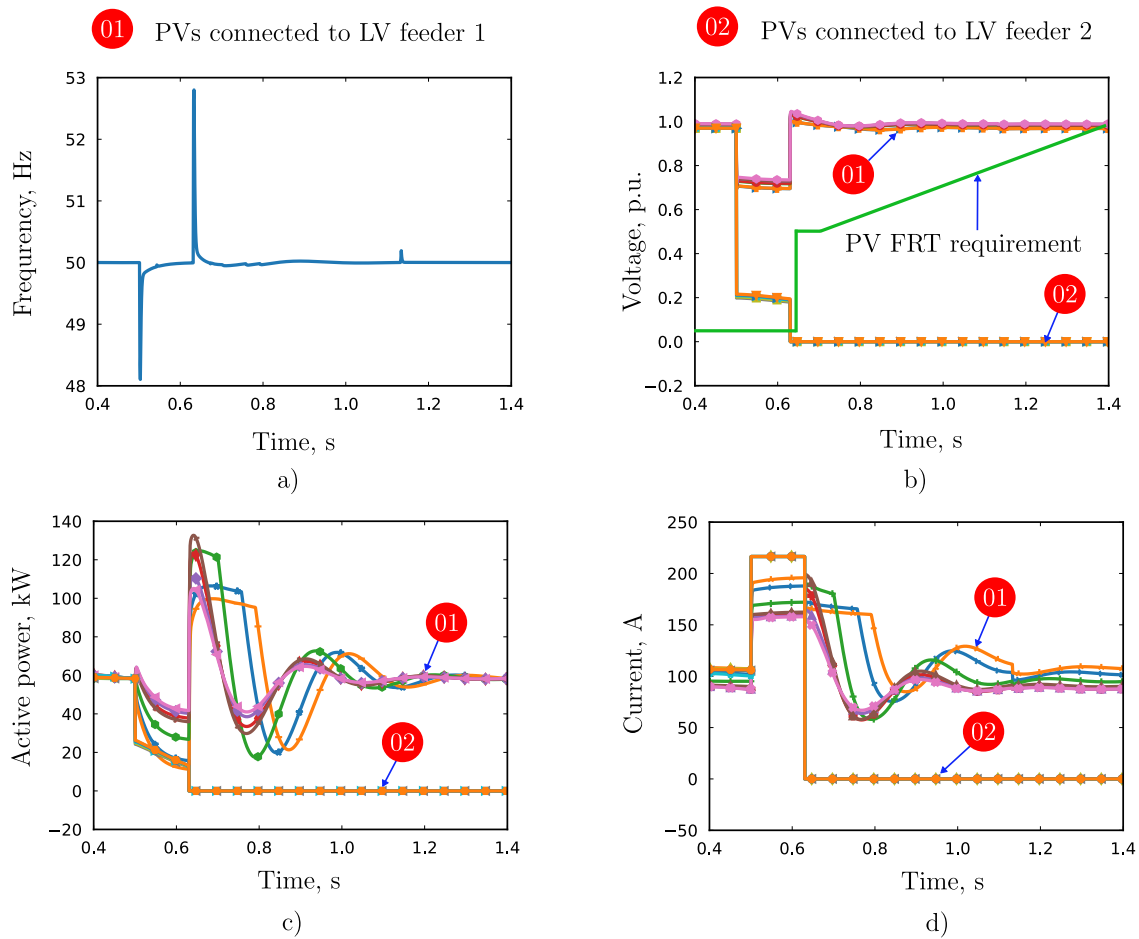


Figure 4.9 – Variations of (a) system frequency, (b) PV voltage, (c) PV active power, and (d) PV current during fault at F4 of LV feeder 1 in islanded operation mode

no additional mean is applied, the time delay of the upper protection level should last longer than 0.53 s for ensuring a minimum discrimination margin of 0.2 s.

4.5.1.2 PV protection

Protection of PV systems should be able to prevent them from unwanted tripping and also protect them from short circuits occurring inside their installation.

4.5.1.3 MV feeder protection

Conventionally, the French MV feeders are equipped with a non-directional Phase Time Over-Current Protection (PTOCP), and a Ground Time Over-Current Protection (PTOCP) elements. The selection of the PTOCP element depends on the magnitude of the ground-fault current, which is, in turn, determined by the system earthing method. In our case, the used system earthing method is a low-impedance grounding system that limits the ground-fault current to 150-300 A in rural systems, and a maximum of 1000 A in urban systems as mentioned previously in Subsection 2.3.2. Therefore, a ground overcurrent element is the typical solution.

On the other hand, a Negative-sequence Time Over-Current Protection (PTOCQ) element is also required when the fault impedance is high, and neither PTOCP nor PTOCG elements can detect the fault. The PTOCQ element can achieve higher sensitivity than the PTOCP element to identify phase-to-phase faults since it is unaffected by the balanced load current. Consequently, its setting thresholds can be set below the feeder rated load current, regardless of the cold load pickup current. Additionally, the PTOCQ element is not affected by the mutual coupling between circuits, [163] and can, thus, provide better fault coverage than a PTOCG element for earth faults at the remote end of a long feeder.

To avoid false trips caused by the possible high level of fault currents provided by the downstream connected PV systems, **Directional Element (RDIR)** should be implemented to control all the deployed PTOC elements. In other words, the PTOC element can time out, but the trip is held pending if the fault direction does not satisfy the predefined one. The principle of operation of the **RDIR** element concerned is derived from that developed in Chapter 3. Besides, a simple Breaker Failure Protection (RBRF) element, which includes a timer triggered by the trip signal from the feeder PTOC element, is also implemented. The settings for various Forward Time Over-Current Protection (PTOCF) elements, must follow the rules below:

- 1 Forward Phase Time Over-Current Protection (PTOCPF): should include a high-set PTOCPF1 and a low-set PTOCPF2 modules. Pickup for PTOCPF1 can be set at ten times the feeder rated current to immediately eliminate severe faults while that for PTOCPF2 should be, at least, two times the feeder rated current to ensure some cold load pickup margin.
- 2 Forward Negative-sequence Time Over-Current Protection (PTOCQF): has only one module whose calculation of pickup current is derived from [164].
- 3 Ground Time Over-Current Protection (PTOCG) element: includes only one tripping level, since the ground-fault current only contributed by the utility source and is determined mainly by the grounding resistance value. The pickup current for the PTOCG element is required to be just higher than the maximum capacitive current of the feeder. A pickup value in a range of 0.1 to 0.3 times the feeder load rated currents is suitable for this case.

The time delay of the **MV** feeder protection, on the one hand, must be sufficiently long to be discriminated from downstream **LV** microgrid protections. On the other hand, it must be fast enough to prevent PV systems connected to adjacent feeders from unwanted tripping. The delay of the **LV** microgrid interface protection, which has already been presented in Section 4.4, is 0.13 s. Thus, the time delay of the host MV feeder protection must be set at least 0.33 s to ensure grading margin of 0.2 s. With such a considerable delay, a fault, which causes a significant voltage drop propagating over the whole **MV** network, may probably affects the **Fault Ride Through (FRT)** requirements of the PV systems connected to the healthy feeders, [118]. Therefore, the protection of **MV** networks without communication support seems difficult to achieve.

To meet the PV **FRT** requirements, the study proposes to implement a communication mechanism for the transfer of interlocking signals between the **LV** microgrid 1 interface protection and the host feeder protection devices, e.g. CIED3 and FIED1 in Figure 2.7. An interlocking signal is directed to the corresponding FIED1 to block its operation only if the CIED3 detects a forward fault. Thus, there is no need to establish discrimination by the time between the CIED3 and the FIED3 in the forward direction. We can set the time delay of the FIED1.PTOCF1, and the FIED1.PTOCF2 elements to 0.1 s and 0.3 s, respectively. To provide backup protections for the transformer and the neighboring feeders, two undervoltage elements, including a Reverse Under-Voltage Protection (PTUVR) and a Reverse Negative-sequence Over-Voltage Protection (PTOVQR), are proposed and allowed to trip after 0.7 s with operating thresholds of 0.7 p.u. and 0.1 p.u., respectively.

Regarding the setting of the Breaker Failure Protection (RBRF) element, its timer has two delay levels. If the Circuit Breaker (CB) concerned does not open, the RBRF element first sends a response to the CB after a predefined delay. If the CB does not open after the end of the second delay, the RBRF element triggers an external trip to the CBs of all adjacent feeders connected to the same **MV** busbar. The RBRF element also sends a control signal to the CIEDs of the **LV** microgrids connected to the adjacent feeders to transform them into islanded operation.

4.5.1.4 MV busbar protection

Similar to the **MV** feeder protection, the busbar protection consists of a PTOCP, a Negative-sequence Time Over-Current Protection (PTOCQ), a PTOCG, and a RBRF elements. To ensure effective backup of the feeder PTOCP element, the bus PTOCP element must be set as low and as fast as possible, while ensuring proper selectivity with the feeder PTOCP element. However, when the bus load current is large compared to the bus phase fault current, it is not possible to set a pick-up current for the bus PTOCP element that is high enough to support the maximum load current with some reserve for cold load pick-up, but sufficiently sensitive to the minimum bus phase fault currents.

Hence, the study proposes to use a Under-Voltage Protection (PTUV) element for holding the bus PTOCP operation until the bus voltage drops below its pickup threshold. With a voltage-based torque control, the bus PTOCP element can be set as close as possible to the phase overcurrent setting of the feeder that has the highest load capacity. The pickup of the bus PTOCQ element is slightly higher than the feeder settings. A pickup value of 1.2 times that of the feeder can be considered reasonable.

The bus PTOC elements must have a time delay long enough to be graded with that of the feeder protection to avoid maloperation upon the occurrence of a fault in the **MV** feeder. Thus, the high-set PTOC1 elements have a time delay of 0.3 s, and the low-set PTOC2 elements have a time delay of 0.5 s. The 0.3 s delay time may in some cases seem too long and a bus interlock protection scheme can be applied. In this scheme, the delay of the bus PTOC elements can be greatly reduced; however, it must be long enough for the feeder protection to send an interlocking signal once a fault is detected in its area.

4.5.1.5 HV/MV transformer protection

For the protection of HV/MV transformers against faults, Phase Differential Protection (PDIF) and Ground Differential Protection (PDIFN) are used as the primary element while a PTOC element is used as a back-up element. The differential protection is of an absolutely selective nature and does not need to coordinate with lower protection levels, such as MV bus and MV feeder protections. Therefore, in this section, we focus only on the configuration of the transformer PTOC protection. In general, transformer PTOC protection consists of three different elements, namely PTOCP, PTOCQ, and PTOCG elements on both sides of the protected transformer.

Protection settings on the primary side: The thresholds for the PTOCP and PTOCQ elements on the HV level should be set at approximately 1.3 times fault currents measured at the primary side for a three-phase solid fault, and a phase-to-phase fault on the secondary side, respectively. The pickups selected in such a way normally exceed the transformer inrush current. For example, with a short-circuit impedance of 7%, a three-phase fault on the 20 kV side of a 63/20 kV transformer causes a fault current of, at most, 15 p.u. Therefore, the pickup current of the PTOCP element would be at least 20.6 p.u., which is above the typical inrush current range. With respect to the ground protection, since the neutral of primary windings are unearthed, there is no ZS current detected at the transformer HV side. The pickup current for the PTOCG element can be adjusted quite sensitively. However, it must be checked for false currents due to the current transformer error during transformer inrush or faults on the secondary side.

Protection settings on the secondary side: The PTOC elements on the secondary side of the transformer must be time-delayed in order to be coordinated with the MV bus PTOC elements. For the PTOCP element, the pickup currents must be set to carry the maximum expected load current of the transformer. Since the transformer is capable of carrying a considerable overload for a certain period of time, the PTOCP threshold is normally set at 2 times the rated current of the transformer. On the other hand, the PTOCQ pickup is set at 0.5 times the rated load current. The PTOCG element provides protection against near-neutral faults at the secondary level of the transformer. It must be coordinated with the bus PTOCG element to allow the bus to trip first, and therefore be set slightly higher than the bus ground pickup, about 1.3 times.

4.5.2 Case study

The proposed protection scheme developed is validated on the Grid-1 of Figure 2.7 in the software environment DIGSILENT | PowerFactory. The overall settings for the Grid-1 protection scheme are tabulated in Table 4.4.

The simulation results included in Appendix H have indicated that the proposed protection scheme could handle all kinds of faults at different locations with different fault impedances. Thanks to the interlocking signal mechanism, the feeder protection MV could quickly eliminate faults within its protected areas, avoiding undesirable disconnection of PV systems connected to adjacent feeders.

Table 4.4 – Overall setting parameters for the proposed MV protection scheme

Element	Function	(1)	(2)	(3)	(4)	(5)	(6)	(7)	(8)
CIED3	PTOCP1	N	I	A	High-set	720	0.33	F1	None
	PTOCP2	N	I	A	Low-set	60	0.65	F1	None
	PTOCQ1	N	I^-	A	High-set	36	0.33	F1	None
	PTOCQ2	N	I^-	A	Low-set	18	0.65	F1	None
	PTUVR1	R	V	$p.u.$	High-set	0.7	0.13	F3, F4	F5, F6, F7
	PTUVR2	R	V	$p.u.$	Low-set	0.8	0.7	F3, F4	F5, F6, F7
	PTUVQR1	R	V^-	$p.u.$	High-set	0.1	0.13	F3, F4	F5, F6, F7
	PTUVQR2	R	V^-	$p.u.$	Low-set	0.05	0.7	F3, F4	F5, F6, F7
	PTUF1	R	f	Hz	High-set	48	1	F3, F4	F5, F6, F7
	PTUF2	R	f	Hz	Low-set	49	2	F3, F4	F5, F6, F7
DIED1	PTUV1	N	V	$p.u.$	High-set	0.45	0.16	F3, F4	F5, F6, F7
	PTUV2	N	V	$p.u.$	Low-set	0.8	1.2	F3, F4	F5, F6, F7
	PTUF1	N	f	Hz	High-set	46	2	F3, F4	F5, F6, F7
	PTUF2	N	f	Hz	Low-set	47	3	F3, F4	F5, F6, F7
	PTOCPF	F	I	A	–	20	0.03	F2	None
	PTOCQF	F	I^-	A	–	12	0.03	F2	None
	FIED1	PTOCPF1	F	I	A	High-set	1155	0.1	F3, F4, F7
PTOCPF2		F	I	A	Low-set	230	0.3	F3, F4, F7	F5, F6, F8
PTOCQF1		F	I^-	A	High-set	125	0.1	F3, F4, F7	F5, F6, F8
PTOCQF1		F	I^-	A	Low-set	52	0.3	F3, F4, F7	F5, F6, F8
PTOCG1		F	I^0	A	High-set	33	0.1	F3, F4, F7	F5, F6, F8
PTOCG2		F	I^0	A	Low-set	11	0.3	F3, F4, F7	F5, F6, F8
PTUVR		R	V	$p.u.$	–	0.7	0.7	None	F5, F6, F8
PTUVQR		R	V	$p.u.$	–	0.1	0.7	None	F5, F6, F8
RBRF		–	–	–	–	–	0.7	None	F3, F4, F7
BIED	PTOCPF	F	I	A	–	692	0.5	F7	F3, F4, F5
	PTOCQF	F	I^-	A	–	75	0.5	F7	F3, F4, F5
	PTOCG	F	I^0	A	–	70	0.5	F7	F3, F4, F5
	PTUVR	R	V	$p.u.$	–	0.7	0.7	None	F9
	PTUVQR	R	V^-	$p.u.$	–	0.1	0.7	None	F9
TIED1	PDIF	N	I	%	–	–	0.08	F8	None
	PDIFN	N	I	%	–	–	0.08	F8	None
	PTOCP	F	I	A	–	5626	0.3	F8	None
	PTOCQ	F	I^-	A	–	599	0.3	F8	None
	PTOCG	F	I^0	A	–	30	0.3	F8	None
TIED2	PTOCP	F	I	A	–	692	0.7	F8	F7
	PTOCQ	F	I^-	A	–	350	0.7	F8	F7
	PTOCG	F	I^0	A	–	90	0.7	F8	F7

¹ Trip direction.² Operating quantity in which I stands for current, V for voltage, and f for frequency.³ Unit of operating quantity.⁴ Tripping stage.⁵ Value of operating quantity.⁶ Operating time, s.⁷ Faults covered by the function as a primary protection.⁸ Faults covered by the function as a backup protection.

In addition, all PV systems connected to the faulty zones were successfully disconnected, thus avoiding unintentional islanding. Other problems, such as blinding or false tripping, were avoided by applying the [RDIR](#) element developed in Chapter 3. In the event of failure of the primary protection, all the back-up protections designed have served as redundant protections, effectively preventing the evolution of the faults.

4.6 Conclusion

In the future, microgrids will be allowed to operate in both operation modes, including grid-connected and islanded mode. The most difficult challenge is to have different sets of operating parameters for the protection systems corresponding to each operation mode. This chapter has proposed different protection systems that can adapt to the different operating modes of the considered microgrids and the associated influencing factors. The results of the simulation have been used to verify the effectiveness of the proposed systems. It is evident that the adaptation characteristics of the protection systems require the implementation of new protection devices, such as IED as well as fast communication networks. Moreover, the developed [MV](#) protection system is capable of not only guaranteeing the safe operation of the [MV](#) networks, but also preventing the unintentional tripping of PV systems connected at the [MV](#) level. It is also coordinated with the protection systems of the [LV](#) microgrids. On the other hand, the protections of the microgrids could ensure their successful islanding in the event of a fault on the [MV](#) or HV grids. All PV systems connected to the [LV](#) level have met the [FRT](#) requirements. Furthermore, after the operation of the respective protection elements, the fault should be located and isolated in order to reconnect the power supply to the disturbed customers as fast as possible. This critical task is handled by the so-called [Fault Location and Isolation System \(FLIS\)](#), whose development and validation are the main objectives of the next chapter.

Chapter 5

Fault location and isolation system for active distribution networks

Contents

5.1	Introduction	123
5.2	State-of-the-art	124
5.3	Proposition of FLISs for active distribution networks	125
5.4	Proposed ANN-based FLIS	126
5.4.1	Multi-layer perceptron classifier-based artificial neural network	126
5.4.2	Data measurement and feature extraction	129
5.4.3	Data set for training and testing the designed ANN	130
5.4.4	Evaluation results	130
5.5	Proposed MAS-based FLIS with IEC 61850-oriented design	130
5.5.1	Multi-agent system	131
5.5.2	Proposed system	132
5.5.3	Functional structure of required FIED and agents	134
5.5.4	Operating principle of the proposed scheme	136
5.6	Validation using cosimulation approach	141
5.6.1	Fundamental of cosimulation method and the proposed system	141
5.6.2	Design of MAS for co-simulation system	141
5.6.3	MatrikonOPC server for cosimulation	143
5.6.4	Optimal placement of controlled switches for Grid-1	144
5.6.5	Results and discussion	144
5.6.6	Conclusion	146
5.7	Validation using CHIL approach	146
5.7.1	Overview of DRTS and CHIL approach in power system domain	146

- 5.7.2 Description of the MAS for the CHIL platform 148
- 5.7.3 CHIL testing platform 149
- 5.7.4 Results and discussion 150
- 5.7.5 Conclusion 152
- 5.8 Conclusion 153

5.1 Introduction

Since faults in the distribution networks account for more than 80% of total power system failures [165], several system reliability indices, such as **System Average Interruption Duration Index (SAIDI)** and **Customer Average Interruption Duration Index (CAIDI)**, mainly depends on the performance of the deployed **Fault Location and Isolation System (FLIS)**. Currently, the most popular type of **FLIS** in distribution networks is mainly based on the coordination between the recloser at the beginning of the feeder and the **Remotely Controlled Switches (RCS)** installed along the feeder [58]. In the French distribution system, **RCS** allocation on each feeder is determined by calculating the product of the power injected into the feeder and its length. This product is called the equivalent grid bag, which is located between the two closest **RCSs**, [58]. These **RCSs** are remotely controlled by the binary inputs received from the control center. The signals are generated manually by the system operator after the analysis of the fault indications received from the fault indicators installed at the **RCS** locations. As mentioned in [58], the operation of the traditional French power restoration system in case of permanent faults can generally be divided into three phases, including ① remotely controlled action, ② manual action, and ③ remedial action, as described in Figure 5.1. The first phase, which is the automatic fault location and isolation, often lasts three to five minutes.

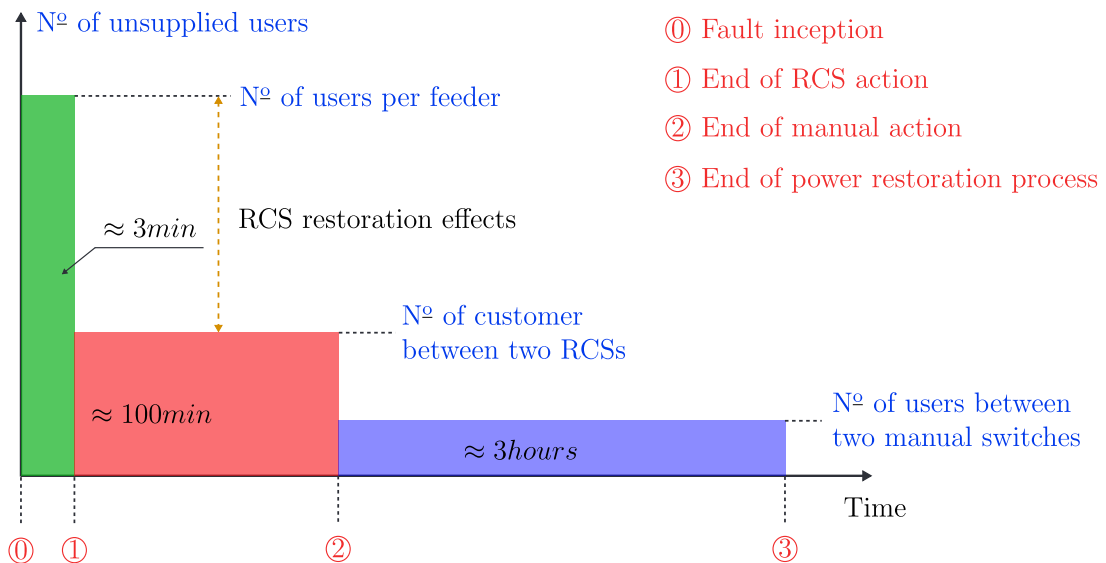


Figure 5.1 – Description of the power restoration process

As mentioned in Chapter 1, traditional single-source radial distribution networks have been transformed into active multi-source networks through the integration of **Distributed Energy Resource (DER)**s, especially PV systems. Multiple power sources supply fault currents, probably leading to the malfunction of the existing **FLIS** due to the lack of directional features or consideration on the fault contribution of the downstream connected **DERs**. Therefore, in this chapter, we intent to pay more attention to developing new **FLISs** dedicated for distribution networks with high share of PV systems. Two different types of **FLIS** are proposed, including an **Artificial Neural Network (ANN)**-based and a **Multiagent System (MAS)**-based **FLISs**.

5.2 State-of-the-art

In general, FLIS can be divided into three categories: centralized, decentralized, and distributed. The first group usually requires all the system data to be sent to the central controller to reach a decision. Impedance- and knowledge-based methods belong to this group. A FLIS can also be carried out in a distributed manner when the two latter approaches are used. MAS-based FLIS can be sorted into this category. In a decentralized scheme, the data can be processed within a substation area without any requirement for Supervisory Control and Data Acquisition (SCADA) implementation. The feeder Intelligent Electronic Device (IED) can issue final decision on fault location based on what it receives from downstream fault indicators. In a distributed system, the data can be processed locally and shared amongst the adjacent controllers to obtain final control decision. In such case, a direct peer-to-peer communication link should be implemented.

One of the most popular centralized methods is impedance-based that can be found in [166, 167, 168, 169]. They are inherited from those developed for transmission networks. The distance between the measurement apparatus and the fault locations is iteratively estimated using three-phase circuit theory. The main drawback of these methods is multiple estimation of the fault locations. Also, many factors such as load imbalances, prefault load currents, fault impedances, mutual coupling may degrade the performance of the methods. Moreover, the one-point measurement of such methods cannot alleviate the impacts of the downstream connected DERs. Travelling wave-based methods, which attract a number of researches, can be the candidate [170, 171, 172, 173]. However, due to the inherently-complicated topology of distribution networks with multiple laterals, sub-laterals, and tapped loads, it may impossible to discriminate the waves reflected from different junctions.

Another solution for developing a FLIS is knowledge-based approaches, such as ANN, expert system, fuzzy logic, or hybrid [174, 175, 176, 177, 178, 179, 180, 181, 182, 183]. The main drawback of these studies is that they did not take into account the transient behavior of the DERs when formulating the data set for developing the methods. As clearly indicated in Section 2.7, the waveforms of fault quantities, such as, currents and voltages of the inverter-based PV systems are imposed by their control strategies, and therefore are far different from those of conventional synchronous generators. Their detailed transient models should be developed before conducting the fault studies.

Moreover, in the context of the new active distribution networks with a high level of complexity and sensitivity, the number of binary measurements and inputs, such as, status positions of the installed RCSs, fault information detected by fault indicators, is very large. Therefore, the centralized category, including impedance- and knowledge-based FLIS, requires a high computing capacity of the hardware devices to manage and process such a large volume of data. They are time consuming and may be affected by personnel intervention or uncertainty of the DERs, [184]. An additional disadvantage of the centralized FLISs is that it may be faced with what is called the single point of failure. For instance, if the central controller is out of order, the whole system is collapsed.

On the other hand, several studies that applied MASs for developing new distributed FLISs have been published in the literature. The IEC 61850 Generic Objective Oriented Substation Event (GOOSE) protocol has also been used to establish a communication channel between these agents. References [185, 186] present MAS-based FLISs, in which the agents act once they have received the lockout signal from the feeder recloser. The disadvantage of these systems is that agents must communicate with the control center, i.e. the IED on the substation side, before making a decision. Another MAS automation architecture based on IEC 61850/61499 intelligent Logical Node (LN) is presented in [187]. The authors proposed to implement additional intelligent LNs that are responsible for decision making and negotiation with other agents. The authors also developed coordination between agents as a complete system.

An article in [188] described a MAS-based distributed FLIS using the GOOSE IEC 61850 protocol. Several agents are installed along with the feeders and communicate with each other using the GOOSE protocol. The authors also proposed to add a RDIR element to the sectionalizing agent for detecting fault direction in the case of feeders with a high DER integration. Reference [189] presents a new approach based on the comparison of the direction information shared between adjacent agents via the GOOSE IEC 61850 protocol. However, we should note that GOOSE messages are only transferred for time-critical applications within substation areas, e.g., protection against CB failures. A mechanism for the exchange of GOOSE messages on an inter-substation scale is still missing from the researches mentioned above.

It is obvious that although the presented studies have offered innovative solutions for FLIS in distribution networks containing DER, the evaluation process was mainly conducted in a pure software environment such as Matlab/Simulink, Digital Real-Time Simulator (DRTS). Performance of the communication network, which plays a crucial role in the information exchange amongst agents and central controllers, was not taken into consideration. The interoperability between the real agents (the actual controllers devices), and the digital relays, or IEDs of a FLIS, has also not been evaluated yet. Currently, Controller Hardware-in-the-Loop (CHIL) is an efficient approach to study and validate the performance of a system that consists of several real hardware devices and simulation tools. Some investigations of adaptive protection based on CHIL were conducted in [190, 191]. However, the application of CHIL to evaluate new generations of FLIS, which are based on MAS and IEC 61850 communication, has been mentioned infrequently.

5.3 Proposition of FLISs for active distribution networks

In the previous section, we have conducted a review of the state-of-the-art studies focusing on FLIS for distribution networks with high DER penetration. We can observe that both centralized and decentralized categories have their own disadvantages. Hence, the selected solution is a compromise between these two groups. Centralized methods are suitable for small-scale grids with reasonable amount of data to be transferred to the central controller. In contrast, the decentralized and distributed approaches yield more benefits for large grids with a lot of substation and feeders. In the study, we propose two

solutions for locating and isolating faults in distribution networks. Each aims to address the issues caused by the increase of the PV penetration. By using the models developed in Section 2.7, the fault behaviors of the PV systems are taken into consideration. Moreover, the intermittency of PV systems and loading conditions is considered by carrying the simulation at different hours during a day.

The first is a ANN-based FLIS. For training the proposed ANN system, a data set covering all possible fault scenarios should be obtained. To achieve this, we decide to consider the Grid-1 in Figure 2.7 due to its short geographical length. A small number of measurement points is sufficient for the developed ANN-based FLIS to properly locate the faulty line-section. First, we divide each MV feeder of the Grid-1 into different sections, in which each section is located between two nearest MV/LV substations, as shown in Figure 2.7. Then, we conduct a variety of fault simulations under different fault impedances, fault sections, fault types, as well as fault hours. All needed values are stored in the database to obtain the complete data set. Next, a part of the data set is used to train the ANN network. Finally, we test the trained ANN network on the remaining data. The effectiveness of the proposed method is based on its correct classification of faulty sections, which are classified on the stage of generating the data set.

The second method is a MAS-based FLIS. All the agents are designed following the Logical Node (LN) description specified in the standard IEC 61850. They can detect the fault direction and exchange this value with their neighboring agents for locating the faulty line-section. Moreover, they can also identify the fault clearance thanks to a fault-counting mechanism, allowing them reaching the final decision on operating its switch without intervention of the network operators. The duration of the power interruption, therefore, can be reduced, improving the system reliability indices, such as SAIDI, and CAIDI. The proposed MAS-based FLIS is first evaluated by developing a cosimulation system. Further, a functional performance test is mandatory to confirm the interoperability of the multi-hardware system. Hence, the proposed FLIS is implemented in a laboratory platform with a CHIL setup. The CHIL platform incorporates a hardware-based MAS model, real IEDs, and an Ethernet-based communication network.

5.4 Proposed ANN-based FLIS

5.4.1 Multi-layer perceptron classifier-based artificial neural network

ANNs are the statistical learning algorithms that are widely used recently in numerous applications, including fault location classification schemes. Many libraries and frameworks are available to develop neural networks. Among these other, Multi-layer Perceptron (MPL) Classifier appears to be one of the most suitable candidates for developing classification purposes. Opposed to other classification methods, such as Support Vector Machines or Naive Bayes Classifier, MPL Classifier applies an underlying Neural Network for conducting classification tasks [192]. Therefore, the study proposes to use the MPL classifier for classifying the faulty line-section thanks to their ability to solve problems stochastically, which often allows approximate solutions for extremely com-

plex problems like fitness approximation. The layer-based architecture of the applied MPL classifier can be observed in Figure 5.2.

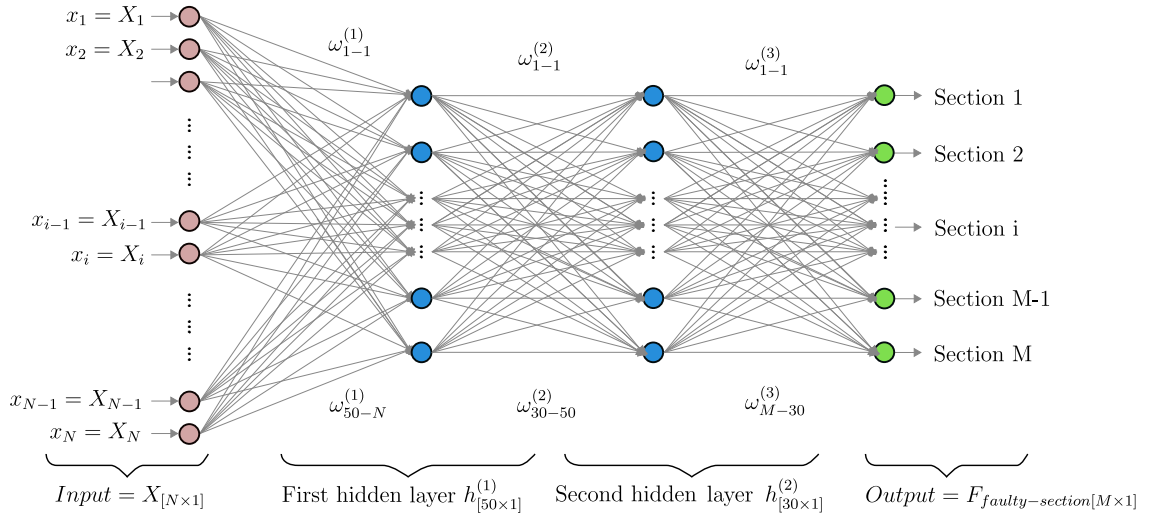


Figure 5.2 – Layer-based architecture of the applied MPL classifier

Each layer of the MPL classifier contains N neurons connecting to the neurons of the previous layer. Each neuron, in turn, receives many inputs from other nodes, and computes a single output based on the inputs and the connection weights. The layers that are between these two are named hidden layers. In our proposal, we applied a two hidden layer neural network. The first layer consists of a set of 50 neurons, whereas the second one comprise a set of 30. The output of the neural network should be equal to the number of sections of the studied network since we intend to find the faulty section. The number of inputs will be justified in Subsection 5.4.2. For properly triggering each layer, a suitable activation function should be chosen according to the application goals, and in our case is the *sigmoid* function. It is defined by:

$$\sigma(z) = \frac{1}{1 + e^{-z}} = \frac{e^z}{e^z + 1} \quad (5.1)$$

The computation that is carried out in the neuron of the first layer would be as:

$$h^{(1)} = [W^{(1)}]^T \cdot X + b^{(1)} \quad (5.2)$$

where X is the input vector, $b^{(1)}$ is the bias vector of all units whose dimension is $[50 \times 1]$, and $W^{(1)}$ is the weight matrix of dimension $[50 \times N]$ described by Equation 5.3:

$$W^{(1)} = \begin{bmatrix} \omega_{1-1}^{(1)} & \cdots & \omega_{1-N}^{(1)} \\ \vdots & \ddots & \vdots \\ \omega_{50-1}^{(1)} & \cdots & \omega_{50-N}^{(1)} \end{bmatrix} \quad (5.3)$$

The calculations in the two hidden layers are defined as:

$$h^{(2)} = [W^{(2)}]^T \cdot \sigma(z^{(1)}) + b^{(2)} \quad (5.4)$$

$$h^{(3)} = [W^{(3)}]^T \cdot \sigma(z^{(2)}) + b^{(3)} \quad (5.5)$$

where $W^{(2)}$ and $W^{(3)}$ are the weight matrix whose dimensions can be obtained from Figure 5.2. The sizes of $b^{(2)}$ and $b^{(3)}$ are $[30 \times 1]$ and $[4 \times 1]$ respectively.

The output neuron of dimension $[m \times 1]$ is calculated as:

$$\hat{y} = \sigma(h^{(3)}) \quad (5.6)$$

The learning of the proposed ANN network is accomplished by altering the weight of the connection. By updating the weight iteratively, the performance of the network is improved. In this developed algorithm, we utilized the Back-propagation method presented in [193]. The Back-propagation approach is a standard method whose goal is to train the neural network for calculating the weights and bias. In this case, we have the known data output (supervised learning), and by a method to lessen the error function E , we can obtain weights $\omega_{ij}^{(l)}$. Further, we can estimate the error for each output neuron by adopting the squared error function, and sum them to find the total error:

$$E = \frac{1}{2} \cdot \sum_{n=1}^N \sum_{i=1}^{m^l} [y_i^l(x_n) - t_{n,i}]^2 \quad (5.7)$$

where x_n is the n -th element of the input vector X , $t_{n,i}$ is the n -th element of the output vector of the i -th class, $y_i^l(x_n)$.

The back-propagation step computes the gradient of E with respect to this input as follows:

$$\omega_{ij}^{(l)} \leftarrow \omega_{ij}^{(l)} - n \cdot \frac{\partial E}{\partial \omega_{ij}^{(l)}} \quad (5.8)$$

where n represents the learning rate.

The learning process of the proposed algorithm is described in Algorithm 1, [193].

Algorithm 1 Learning process of the proposed algorithm

- 1: Feed-forward computation: use equation (5.1), (5.3), (5.4), (5.5) and (5.6) for calculation of each layer. The vectors $h^{(1)}$, $h^{(2)}$ and $h^{(3)}$ are computed and stored. The evaluated derivatives of the activation functions are also stored at each unit
 - 2: Back-propagation to the output layer
 - 3: Back-propagation to the hidden layer
 - 4: Weight updates
-

5.4.2 Data measurement and feature extraction

As mentioned in Chapter 1, with high penetration of PV systems and the introduction of new grid codes, the fault currents have become bidirectional rather than unidirectional. Moreover, the PV systems respond to faults in a way differing from that of conventional well-established synchronous generators. One-point measurement appears impossibly enough for fault location within such an active grid. Hence, after having considered the number of measurement data set, we propose to install three Measurement Units (MU) on the concerned feeder, i.e. Feeder 2 of Grid-1 in Figure 2.7, including MU1 at Node 7, MU2 at Node 14, and MU3 at Node 18. The MU may be in kind of μ PMUs or smart meters that can provide timely and time-synchronized current and voltage phasors effectively for the data analysis in our case, [194]. Each MU samples the measured three-phase current and voltage values at the sampling rate of 800 Hz . The derived currents and voltages are filtered by using a cosine-filtering algorithm that is quite popular in relay technologies, as presented in Figure 5.3, [195]. The signal processing is based on the equations derived from Appendix C.

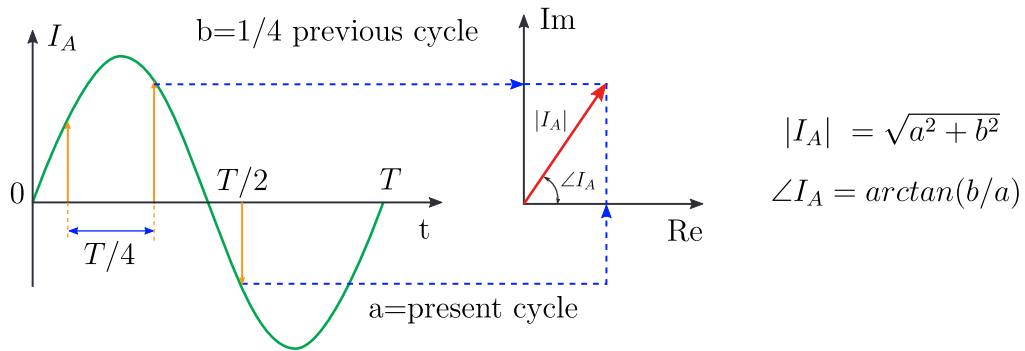


Figure 5.3 – Derivation of current phasor from sampled waveform

Application of machine learning-based approaches for fault location, in particular faulty line-sections, especially for large networks with high level of PV penetration, necessitates a large data set of faults that is composed of a great number of fault scenarios. As already discussed in Section 5.3, we conduct various fault simulations at different hours during a day, from 0 to 20 *hour* by a step of 4 *hour* in order to take into account the impacts of solar variations. Moreover, we consider the influences of fault resistance by increasing R_f from 0 to $60\ \Omega$ by a step of $10\ \Omega$. Faults are assumed to occur on 19 different sections of Feeder 2 (Figure 2.7). By combining these above fault scenarios with 4 fault types, a totally of 3192 faults scenarios were simulated. In the study, faults were assumed to occur at $t = 1.5\text{ s}$, and be cleared at $t = 1.65\text{ s}$, i.e. lasted for 7.5 *cycles*; however, we only made use of 4 samples per cycle per each quantity for a duration of 2 first cycles from the moment of fault inception. So, for each fault scenario, there were 8 data windows taken into consideration.

Based on these sampled values, the data processing unit carried out the calculation of magnitudes and angles of symmetrical sequence currents and voltages, including positive-, negative-, and zero-sequence components. For each data window received

from each MU, 12 quantities would be derived. As a result, we obtain 36 quantities from three MUs plus one quantity standing for the time, a totally of 37 quantities for each data window, as described in Figure 5.4, corresponding to the vector input X in Figure 5.2.

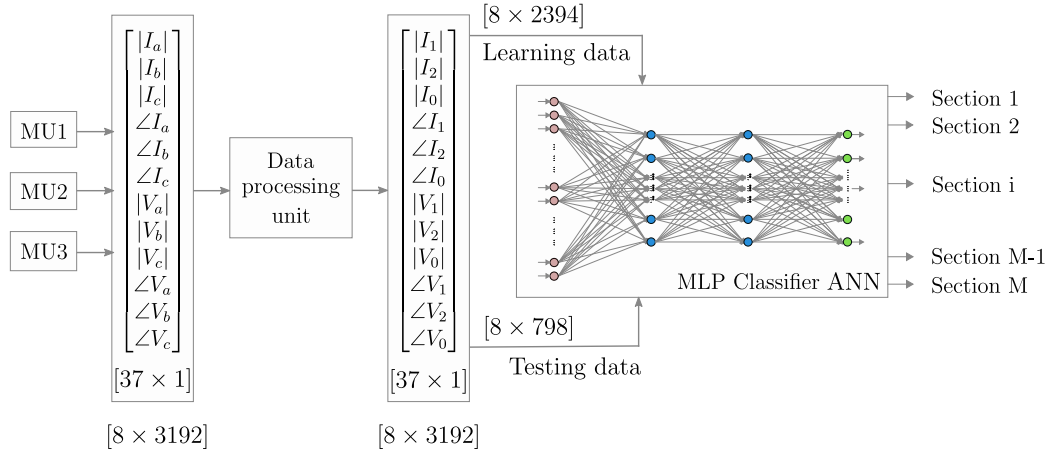


Figure 5.4 – Flowchart of the proposed ANN algorithm

5.4.3 Data set for training and testing the designed ANN

The data set was split into two smaller sets, one for training and another for testing with a ratio of 75:25 correspondingly, as shown in Figure 5.4. Firstly, the first part of the data set was loaded into the designed ANN for learning purposes following the Algorithm 1 described in Subsection 5.4.1. Afterward, the remaining part of the data set was used for testing the proposed approach. Figure 5.4 presents the flowchart of the method.

5.4.4 Evaluation results

The result of testing presented in Table 5.1 indicates that the developed ANN-based FLIS identifies faulty line-sections with high accuracy. The overall average error is lower than 1%. One more notable feature of the proposed approach is that it results in a single estimation for each test. The faulty sections are accurately indicated, minimizing the possible faulty area that needed to be identified by the line crew (stage 2 of the restoration process, Figure 5.1). It can also be observed that the computation time and the error increase at 8, 12, and 16 hours compared with three remaining testing hours. This is due to the participation of PV systems in power production. The location of faults that occur during a high generation of PV systems was more difficult to be identified. It took the designed ANN more time and iteration steps to reach the final results.

5.5 Proposed MAS-based FLIS with IEC 61850-oriented design

The proposed FLIS relies on MAS, which are structured according to and communicate through IEC 61850-based services. Hence, the description of the MAS is introduced first. The overview of the standard IEC 61850 is represented in Appendix I. Further, we provide the details of the structure and operating principle of the proposed scheme with an IEC 61850-oriented design and also a complete procedure for its configuration.

Table 5.1 – Fault location results per hour

Hour	Average computation time, <i>ms</i>	Accuracy, %
0	1.889	100
4	2.036	100
8	2.173	98.7
12	2.325	98.2
16	3.231	98.4
20	1.970	100
Average	2.323	99.3

5.5.1 Multi-agent system

5.5.1.1 Definition

There are diverse types of applications and definitions upon the abstract concept of MAS. Reference [196] has adopted a definition of MAS as systems consisting of multiple autonomous entities with either divergent information, divergent interests, or both. Either in kind of software or hardware entities, an agent can be modeled to act and interact with others in every conceivable manner. Each agent receives information from its environment, processing them based on present or past perceptions, and taking actions via the possible integrated controllers. The working environment of a MAS comprises external entities and resources for the interactions of the included agents. Agents can be described with several characteristics as follows, [196, 197]:

- 1 **Autonomous:** Agents exert partial control of their actions and internal state, seeking to influence outcomes without the intervention of humans or other external devices;
- 2 **Social:** Agents can communicate with humans, external devices or other agents to coordinate actions and satisfy their objectives;
- 3 **Reactive:** Agents react in a timely fashion to changes in their environment.
- 4 **Proactive:** Agents exhibit goal-oriented behaviors and take the initiative to satisfy objectives.

5.5.1.2 Layer structure in MAS applications

To show how MASs could be used to communicate and make intelligent decisions in power system applications, a two-layer structure is commonly used, [198]. Depending on the application, an agent may be associated with a controllable entity in the power grid. However, the functioning of the agents is not clarified because the structure cannot distinguish the relationship between agents, actuators, and controllers. We, therefore, propose to use a structure that is represented in, [198]. This architecture is composed of three layers: the device layer, the control layer, and the agent layer. It can distinctly

present the connection between the agents and the devices of the power system. In particular, it can highlight the communication network between the agents that plays a more important role in a modern power system, as well as the link between the agents and the local controllers. The three layers are as follows:

- 1 *Device layer* is located at the lowest position in the system structure. This layer includes the actual devices that are electrically connected to an electrical system, e.g., loads, PV systems, Wind Turbines, BESS, measuring devices, protection devices... From the *Device layer*, local instantaneous signals, i.e. three-phase currents and voltages, are captured and transmitted to the agent layer. Other information, such as switch or CB position status is sent to the *Control layer*. The operation of the power components in the *Device layer* is regulated by the control signals received from the *Control layer*.
- 2 *Control layer* consists of a group of local controllers of controllable entities located in the *Device layer*. In our case, local controllers, which receive control signals from their agents, are used for controlling the corresponding switches.
- 3 *Agent layer* is a **MAS** operated in a communication network, in which each agent is capable of receiving measured values from its corresponding device, exchanging data with other agents, performing assigned actions, and then returning necessary signals to the local controller. The structure of **MAS** depends mainly on application purposes. In a centralized architecture, a central agent that is responsible for coordinating all other agents is required while in a distributed scheme, all agents play the same roles and need only consult its neighbors for making control actions.

5.5.2 Proposed system

As mentioned in Chapter 1, conventional **FLIS** cannot handle faults on multi-source feeders due to the lack of directional features. For example, considering a permanent fault at F2 in Figure 5.5, all fault indicators detect and report a fault. Without information on the fault direction, the system operator cannot determine in which section the fault is located and therefore, cannot make a remote decision for eliminating the fault. If it can be assumed that the system operator has been able to process the fault successfully, the fault isolation time can be as long as several minutes, which degrades the system reliability indices, such as **System Average Interruption Duration Index (SAIDI)**, and **Customer Average Interruption Duration Index (CAIDI)**. Also, as shown in Figure 5.1, the number of clients who are recovered after the **RCS** operation is significant. Reducing the duration of this phase would have a significant benefit on system reliability indices. We have therefore proposed to set up a new **FLIS** whose operation is based on a **MAS** system with desired features. In such a system, each agent should be able to detect the fault direction and talk to its neighbors to make remedial decisions. It should also report the position of its switch to the central controller on the substation side for the feeder re-connection. The automatic operation capability of the proposed **FLIS** can reduce the duration of the first stage of the power restoration process to only a few tens of seconds.

In the proposed FLIS, communication between agents and Feeder Intelligent Electronic Devices (FIED) is of significant importance. The IEC 61850 communication standard is now widely used in the substation automation systems worldwide. The IEC 61850 **Generic Objective Oriented Substation Event (GOOSE)** protocol has been applied not only for the control and monitoring of primary equipment and FIED status, but also for the status interaction between FIEDs, including protective relays, by replacing the conventional method of using binary and wire I/O with the communication of GOOSE messages over Ethernet cables/fibers, [199]. GOOSE messages are multicast messages whose operating principle is based on a data exchange mechanism between the publisher and the subscriber. FIEDs in a Local Area Network publish GOOSE messages on that network, and also subscribe to certain predefined GOOSE messages published by other FIEDs.

Thus, we propose to replace all fault indicators and controllers of the RCSs with agents with IEC 61850-oriented design that are described in the next subsection 5.5.3. This means that an agent locally controls its switch. An additional function is added for reclosing the feeder CB once permanent faults are fully removed by the respective agents. Two mechanisms for data exchange between the involved devices are also proposed. The transfer of information between substation devices is based on a GOOSE message, e.g., the trip signal from a feeder IED to its corresponding CB, or the position status of a CB to a recloser element, as these applications are time-critical. On the other hand, the data exchange between adjacent agents is based on the TCP/IP protocol since this information is used for non-time critical applications. The structural diagram of the proposed FLIS is shown in Figure 5.5.

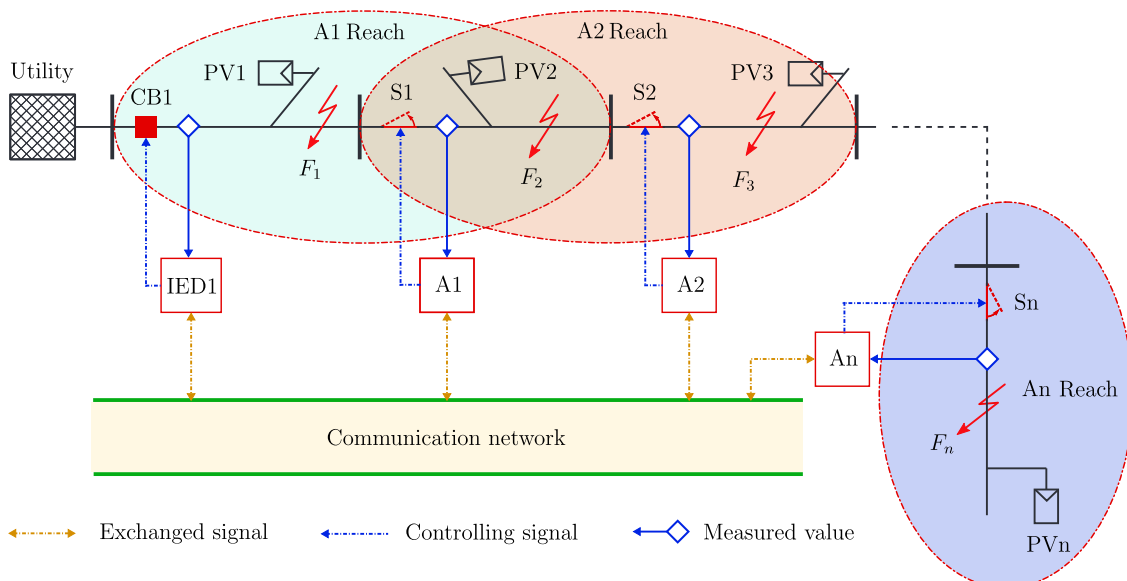


Figure 5.5 – Structural diagram of the proposed MAS-based FLIS

Figure 5.5 indicates that each agent covers two sections that are physically and directly linked to its switch. A fault is considered internal if it occurs within the agent's covered zone; otherwise it is regarded as external. The agents continuously monitor the

operating state of the feeder by comparing the RMS values of the measured currents or voltages with the predefined operating thresholds. The agents determine whether the fault is internal or external based on fault direction information exchanged with the adjacent agents. There are two types of agents, marginal, and intermediate. The former type is assigned to two agents, one just after the feeder FIED, i.e. $A1$, and the other at the section, i.e. An . Intermediate agents Ak are those located between these two marginal agents. Each intermediate agent is a client receiving messages sent from its two neighboring agents, one upstream and one downstream.

In contrast, marginal agents only wait for data from the agent next to them. Moreover, the operating principle of their direction comparison block differs slightly from that of the intermediate agents. When the first agent $A1$ determines a reserve fault, it immediately declares that the fault is between the feeder FIED and himself without comparing his direction value with that received from $A2$. Similarly, when the last agent An detects a forward fault, it concludes that the fault occurred in the last section without consulting the fault direction of the preceding agent, i.e. $A(n - 1)$. The messages exchanged between agents and FIEDs involved in the proposed method are explained in Table 5.2. The detailed operating mechanism of the proposed FLIS is elaborated in Subsection 5.5.4.

Table 5.2 – Data package sent by the agent Ak

Message ID	Description	Value
$Ak.RDIR.Dir.dirGeneral$	Direction value	00= <i>unknown</i>
		01= <i>forward</i>
		10= <i>backward</i>
		11= <i>both</i>
$Ak.XSWI.Pos.stVal$	Switch position	00= <i>intermediate</i>
		01= <i>off</i>
		10= <i>on</i>
		11= <i>bad-state</i>
$Ak.RSWF.OpEx.general$	Switch failure protection	1= <i>true</i>
		0= <i>false</i>

5.5.3 Functional structure of required FIED and agents

We model the FIEDs and agents by using Logical Nodes (LN) specified in IEC 61850-5. Depending on the desired functionality of each device, a set of LNs taken from Table 2.2 should be assigned accordingly, [200]. As mentioned in Section 2.2.2, French MV distribution networks are normally divided into rural and urban types with different operating mechanisms of their FLIS. Recloser is allowed in rural networks. However, despite these differences, the operating principle of the proposed FLIS remains the same for both types of networks. To achieve this objective, we propose to implement an additional fault counter counting the number of fault currents that pass its switch over a pre-specified period of time. The fault counter indicates a permanent fault if the counted number of faults exceeds a predefined value, [201]. This number is typically chosen to be equal to the num-

ber of reclosing attempts of the recloser. For urban networks, the application of a recloser is prohibited, and thus this number is equal to 0. In the following parts, the FIED and agent structures required for the implementation of the developed scheme is presented.

5.5.3.1 Required functionalities of FIED

Figure 5.6 shows the IEC 61850-based architectures for all the controllers and protection devices of a rural MV feeder. On the substation side, there are several logic devices, for instance, measurement, i.e. Current Transformer (TCTR) and Voltage Transformer (TVTR) or Circuit Breaker (CB), i.e. XCBR. In feeder protection device FIED1, LN Instantaneous Overcurrent Protection (PIOC) and Time Overcurrent Protection (PTOC) are responsible for fault detection, LN Directional Element (RDIR) is for determining the fault direction, and LN Autoreclosing Element (RREC) is the reclosing element. For an urban network, LN RREC is withdrawn. The description of remaining LNs of an FIED and an agent have already been specified in Table 2.2.

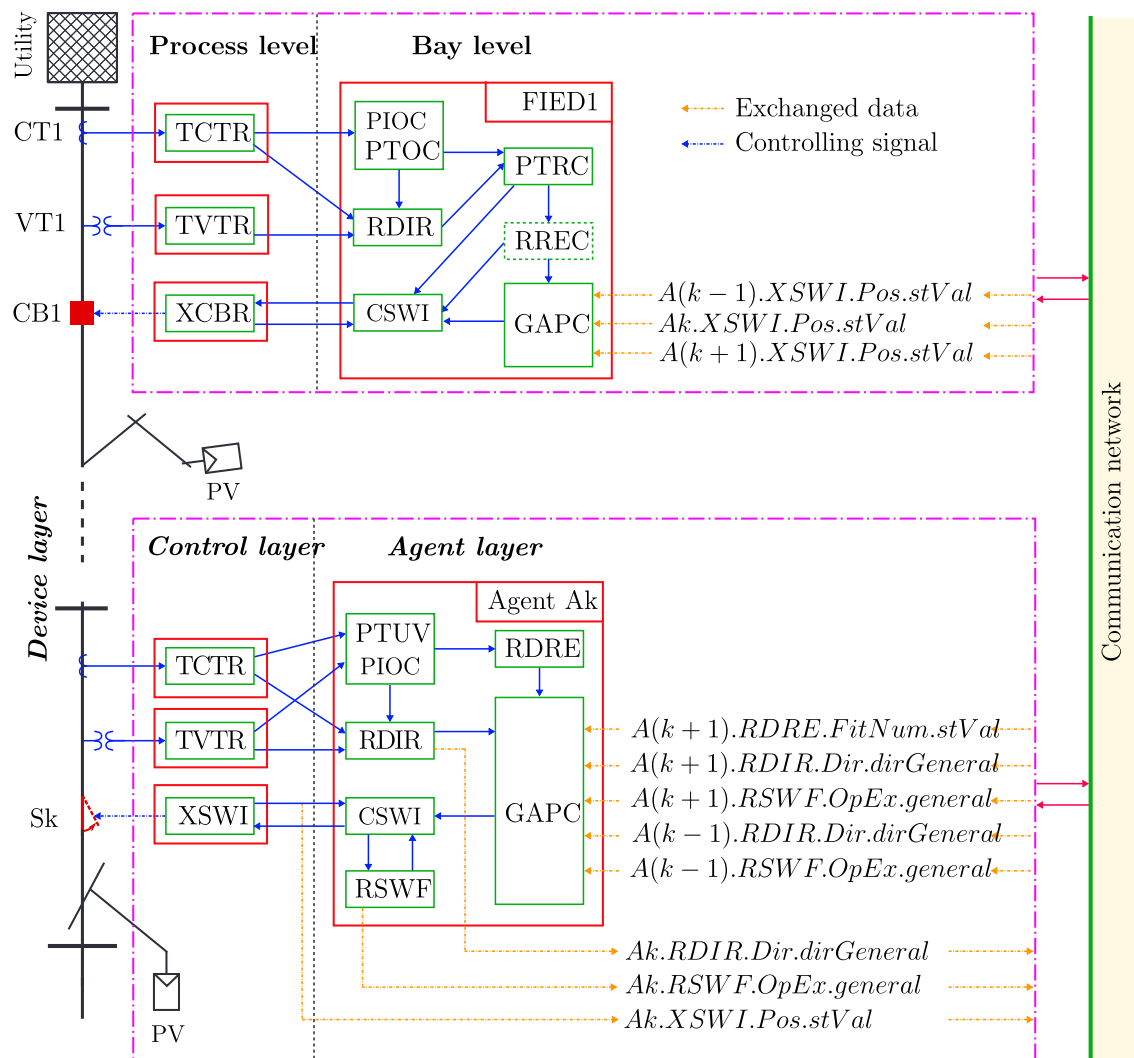


Figure 5.6 – IEC 61850-5-based functions of IED and agent used for a rural MV feeder

Let us consider the FIED1, it receives the measured values from TCTR and TVTR, and transfers them to PIOC, PTOC, and RDIR elements. When a fault is identified by PIOC or PTOC, or both, a signal then is sent to LN Protection Trip Conditioning (PTRC) for issuing a trip signal to LN Circuit Breaker (XCBB) to open CB1. During this time, RREC is also triggered by the trip signal sent by PTRC, and releases CB1 after a predefined delay. The users set the number of reclosing attempts. Besides, LN Generic Automatic Process Control (GAPC) is added to the FIED1 for automatically reclosing CB1 in case of a permanent fault. It monitors the status positions of the switches controlled by those agents that have determined the fault as internal.

5.5.3.2 Required functionalities of the designed agent

Likewise, we propose to implement PIOC and Under-Voltage Protection (PTUV) in each agent for fault detection, RDIR for direction, and RDRE for counting the fault current passing. The use of PTUV avoids maloperation when fault currents are too low for PIOC to detect. These conditions can occur when agents are downstream of the fault, and the connected PV systems are operating under conditions of low or even no solar irradiation. Also, each agent must be able to send several required data to and receive the data transferred by its neighbors. The GAPC block coordinates the information sent by the other LNs within the hosted agent, and all required data from its neighbors to issue the control output.

5.5.4 Operating principle of the proposed scheme

A certain agent A_k should request fault direction data sent by its neighbors, i.e. $A(k-1)$ and $A(k+1)$. The process of fault direction determination for the agents has been already presented in Section 3.7. On the other hand, the FIED must wait for the position status of operated switches reported by the agents that take actions during faults. Figure 5.7 shows an operational logic diagram of an agent dedicated to rural networks. A logic diagram of GAPC of the FIED1 that mentioned in Figure 5.6 is also described.

5.5.4.1 Normal operation

In normal conditions, the criterion values, i.e. I^- or V_{Pmin} , do not fulfill operating conditions, and thus neither the agent PIOC nor PTUV is initiated. Value of the data attribute $GAPC.Op$ is held at *general = False*, resulting in no trip signal to be transferred to LN Switch Controller (CSWI). Therefore, its output trip signal is de-asserted. All the CB and switches remain closed.

5.5.4.2 Transient faults

When a temporary fault occurs, the operation of FIED1 is described as follows:

- 1 Either PIOC or PTOC, or both detect a fault, and thus issue a trip signal.
- 2 PTRC generates a trip command, the CSWI has been configured to receive this trip command. A trip message is then sent to XCBB to open CB1. Meanwhile,

PTRC also sends information to RREC, including *start* of starting element in *FIED1.PTRC.Str.general* and *trip* in *FIED1.PTRC.Op.general*.

- 3 The position status value of CB1 changes from *on* to *off*. This change immediately initiates a publication of the **Generic Objective Oriented Substation Event (GOOSE)** message *CB1.XCBR.Pos.stVal* with value *stVal=on* over the network.
- 4 Based on these above data included in the **GOOSE** messages *FIED1.PTRC.Str.general* *FIED1.PTRC.Op.general* and *CB1.XCBR.Pos.stVal*, RREC sends a reclosing signal contained in *FIED1.RREC.Op.general* to CSWI to reclose CB1. It also provide PIOC and PTOC with information included in the message *FIED1.RREC.TrBeh.general* in order to enable the further expected trip to CB1;
- 5 Once having received the reclosing signal, the CSWI closes CB1 after additional processing. If the fault still exists, the fault clearing process repeats these above steps. Since a temporary fault is extinguished after a definite number of reclosing trials, the power supply is restored to the entire customers connected to the affected feeder without long service interruption.

Once an agent realizes fault direction, it immediately transmits this value to its neighbors via an *Ak.RDIR.Dir.dirGeneral* message. Meanwhile, the agent compares its direction result with those obtained from its neighbors, i.e. *A(k-1).RDIR.Dir.general* and *A(k+1).RDIR.Dir.general*, as shown in Figure 5.7. Thus, at this stage, each agent has already determined whether the fault is external or internal. Since a temporary fault goes out after a defined number of reclosing attempts less than the number of faults predefined in Fault Counter Element (RDRE), it does not allow GAPC to send a trip signal to CSWI. Therefore, the value of the data attributes *Ak.GAPC.SPSCO.stVal* remains false. Thus, all agents do not trigger any trip signals, and all switches remain closed.

Although a transient fault is eliminated without prolonged supply interruption, its location must be identified by the system operator to eliminate the root of failure and improve the system Momentary Average Interrupt Frequency Index. Thus, when agents detect an internal fault, they must report this value to the Supervisory Control and Data Acquisitions (SCADA) system located at the control center, allowing system operators to locate the fault location and take appropriate corrective action.

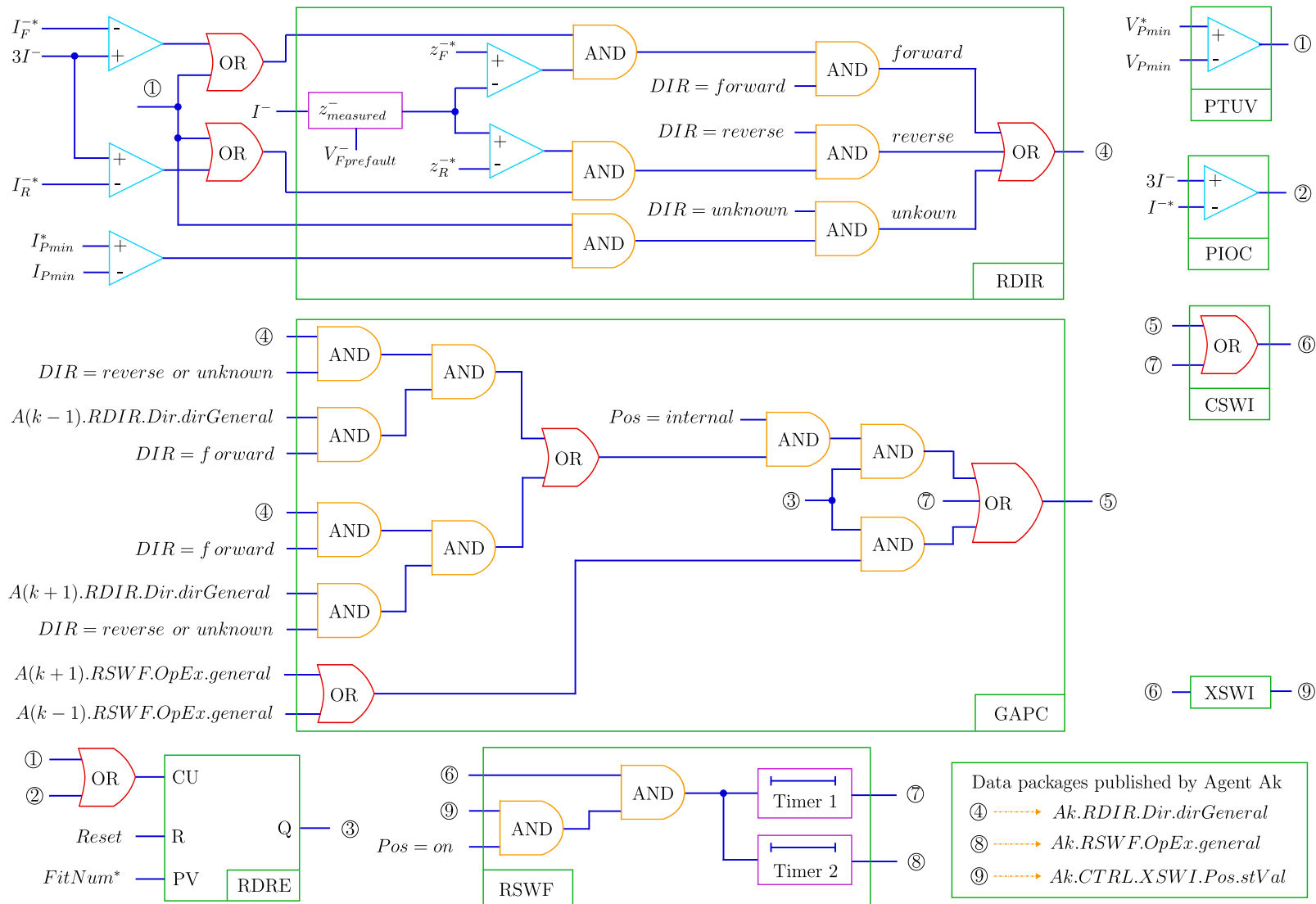


Figure 5.7 – Functional logic diagram of an agent A_k

5.5.4.3 Permanent faults

In the case of a permanent fault, the operation of the proposed FLIS can be divided into two stages namely fault isolation and partial power restoration as follows:

- 1 **Fault isolation:** Autoreclosing Element (RREC) goes into *Lockout* state after the final reclosing attempt, Circuit Breaker (CB)1 remains opened. At this moment, all PV systems connected to the feeder have already been disconnected from the feeder since the time operation of the last recloser trial is longer than that of their interface protection. Hence, all possible sources contributed to the fault current are disconnected, and the fault certainly disappears. Moreover, after the final attempt of RREC, the number of faults counted by Fault Counter Element (RDRE) has exceeded the predefined value and, therefore a logic output *true* is sent to Generic Automatic Process Control (GAPC). Finally, only GAPCs of those agents that have detected an internal fault issue trip signals to the corresponding Switch Controller (CSWI). After the additional process, the switchgear opens the switches. The fault is completely isolated. As soon as $Ak.XSWI.Pos.stVal$ changes its value to *off*, the message is transmitted to FIED1.
- 2 **Partial power restoration:** This task is taken by the additional GAPC of FIED1. As presented above, after the fault isolation by the related switches, there are at least two messages immediately reported to the FIED1. Assuming the fault has occurred at $F2$ as shown in Figure 5.5, the messages received by FIED1 are $A1.XSWI.Pos.stVal$, and $A2.XSWI.Pos.stVal$ with the same value of *off*. The logic diagram of GAPC is described in Figure 5.8 for the considered fault location. Figure 5.8 indicates that when the two subsequent switches have opened, i.e. $XSWI.Pos.stVal=off$, GAPC can realize that the fault is totally isolated by the two switches, one upstream and one downstream the fault. A reclose signal is immediately sent to CSWI to relse CB1, reconnecting the unfaulted zones to the grid, i.e. the zone located from CB1 to $S1$ (Figure 5.5).

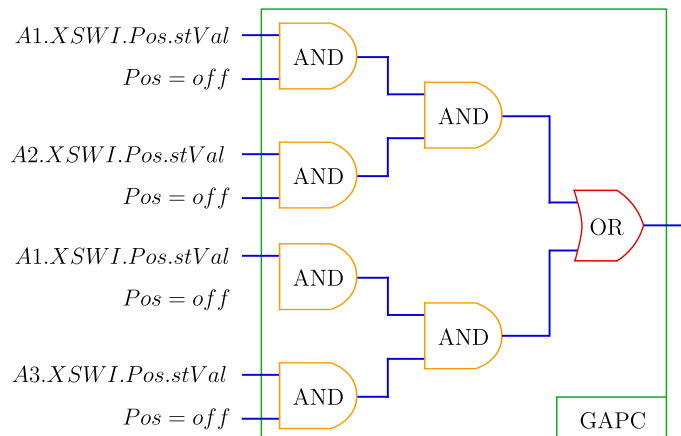


Figure 5.8 – Functional logic diagram of the LN GAPC of FIED1

5.5.4.4 Switch failure protection

A switch that receives a trip signal from its agent may fail to operate due to various reasons, for instance, operating component failure, defective DC source. Faulty line-section must be isolated under sectionalizer failure conditions. In such a case, an appropriate adjacent switch should be tripped by implementing a new dedicated Switch Failure Protection (RSWF) in each agent. This kind of protection is similar to Breaker Failure Protection (RBRF), according to IEC 61850-7-4. The RSWF logic diagram is represented in the bottom of Figure 5.7. The working principle of RSWF of an agent, for instance agent *A2*, can be explained by considering a permanent fault at *F2* in Figure 5.5.

RSWF of the agent *A2* is initiated by the trip signal from its GAPC via the message *A2.GAPC.Op.stVal*. The operating criterion for RSWF is the fault current with the setting *RSWF.FailMod=current* and *SWE.Det.Val.A*. At the first step, RSWF sends a retrip order to the switch *S2* by changing the value of attribute *A2.RSWF.OpIn.general* to *true* after a certain time delay. If it does not open after the second time delay is elapsed, the message *A2.XSWI.Pos.stVal* still has a value different from *off* (Table 5.2). RSWF triggers an external trip by changing the attribute *general* of the data *A2.RSWF.OpEx* to *true*. Figure 5.7 shows that the agent *A1*, which is set to wait for this datum, incorporates it with the *true* value from RDRE and operates to open switch *S3* of Figure 5.5. The fault *F2* is isolated, and then GAPC of FIED1 can issue a reclose message to close the CB1 since both data attributes *A1.XSWI.Pos.stVal* and *A3.XSWI.Pos.stVal* in Figure 5.8 have become *true*. The supply is restored to those customers that are located between CB1 and *S1*, leaving those loads from *S1* to the end of the feeder suffering from outage. The time for total power restoration may last for several hours depending on each utility.

5.5.4.5 Operation of the proposed FLIS in case of no PV generation

One of the most noticeable disadvantages of solar energy is its intermittency. During a day, the power generation of the PV systems may vary in a wide range due to the variation of solar irradiation. For instance, during peak hours of solar irradiation, the power output may reach a very high level while during the night, no power is generated. In such no power generation, the distribution feeder with only PV integration becomes single-source. The logic for the trip decision, therefore, differs from what previously presented. Let us again assume that there is a fault happening at *F2* of Figure 5.5 during no-generation hours of the connected PV systems. In such a situation, there is no fault current flowing through switch *S2*, and thus its direction detector cannot properly operate. However, Under-Voltage Protection (PTUV) of the agent *A2* still detects a fault since voltage drop always spreads across a network. An additional comparator block is implemented to prevent agents from false direction decisions. In this case, there is only load current with limited magnitude flowing through *S2*, and thus the output of the comparator block is *true*. Combining this value with the output from Under-Voltage Protection (PTUV), Directional Element (RDIR) declares the direction of this fault as *unknown*. As described in Figure 5.7, both agents *A1* and *A2* still correctly detect an internal fault, and thus open their corresponding switch, and the fault is therefore isolated.

5.5.4.6 Restoration of power to customer downstream the fault location

In the context of smart grids, the islanded microgrid is a concept that allows a part of the grid to operate autonomously when being decoupled from the external grid [202, 203]. The connected DERs usually feed this kind of small grid. Hence, if in each zone covered by an agent, there is an appropriate set of voltage and frequency control facilities, those zones that are not affected but be isolated from the utility grid during an event of a fault can be allowed to operate in isolated operation mode. We consider a permanent fault event at $F2$ in Figure 5.5 again. As specified above, the only partial load is re-connected to the source while those located from $S2$ to the end of the feeder remain unsupplied. Hence, PV3 to PVn of 5.5 can be re-connected to this part of the grid to feed the loads if there is an additional BESS capable of controlling frequency and voltage.

5.6 Validation using cosimulation approach

5.6.1 Fundamental of cosimulation method and the proposed system

A cosimulation system consists of a group of interfaced software environments working cooperatively. Each environment has its computing method and runs simultaneously and independently on its models, [204]. The software tools are coupled by dynamically connecting the models using their input and output signals so that the outputs of one software environment become the inputs of the other and vice versa. Data exchange, time synchronization, and execution management are usually facilitated during execution by a so-called master algorithm, which organizes the overall process.

In this section, we develop a cosimulation system composed of three software environments, including DlgSILENT | PowerFactory, the OPC-DA server, and Python programming language. The cosimulation system is used to prove the MAS-based effectiveness of the operational coordination of the proposed FLIS when being applied for a typical network, e.g. Grid-1 in case. We use PowerFactory for simulating the dynamic behavior of the studied grid under different fault scenarios, and performing signal processing on fault currents and voltages. The MAS is modeled using the Python language. Data exchange between the agents and the simulated grids is performed via the OPC-DA server, while communication between agents is based on the Remote Procedure Call (RPC) client/server approach. The combined simulator structure is shown in Figure 5.9.

5.6.2 Design of MAS for co-simulation system

The MAS and feeder FIED is developed in Python using various open-access libraries, and hosted on a computer. The communication between the agents, which is based on the RPC method, is carried out in a client/server manner. Figure 5.10 illustrates the implementation of the RPC mechanism, [205]. Each agent acts as a server that requests data from its clients, i.e. adjacent agents, and then distributes it to method calls. The method calls in our case are the control and protection functions required for the proposed FLIS. After additional processes, the results are sent back to the adjacent agents who are in

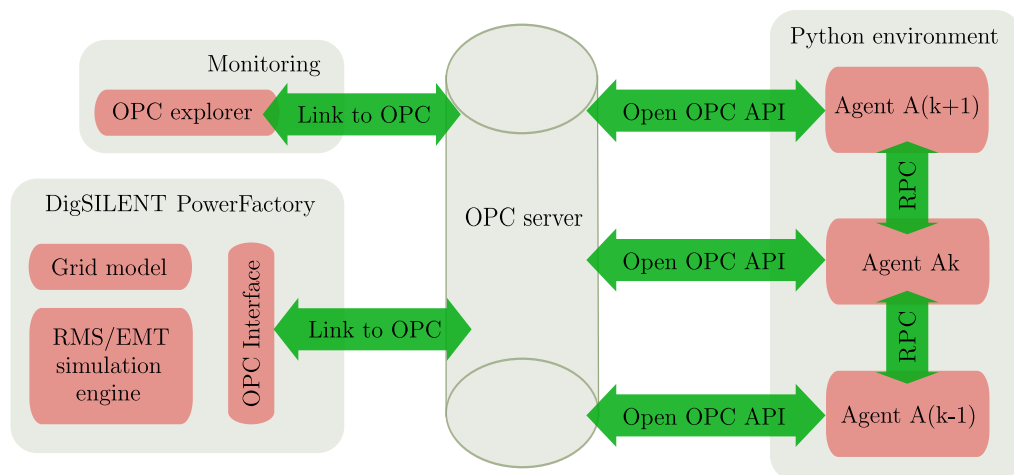


Figure 5.9 – Structural diagram of the cosimulation mechanism between Python and DigSILENT | PowerFactory via OPC-DA server

turn servers of the agent in question. Thus, each agent is programmed using the Python programming language to obtain the following characteristics, [198]:

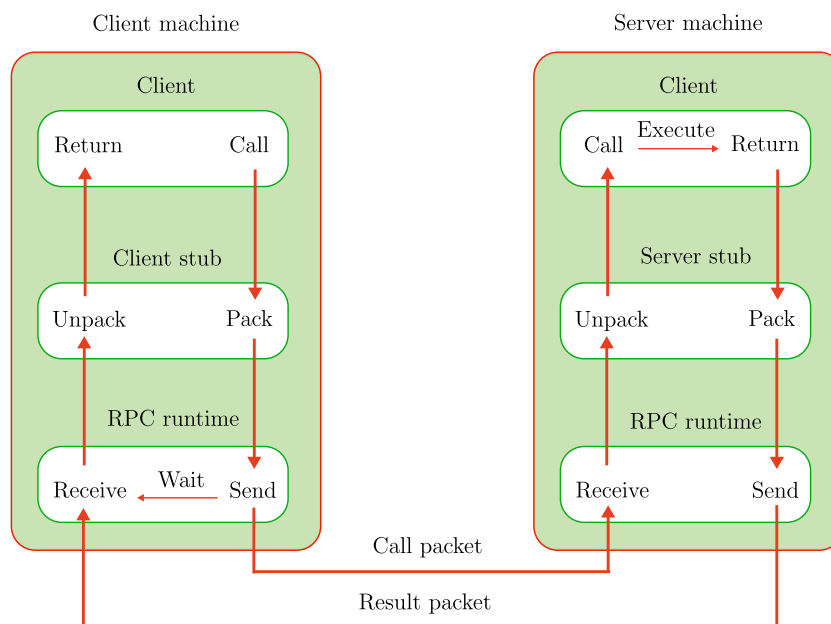


Figure 5.10 – Implementation of RPC mechanism

- 1 Exchanging data with the OPC-DA server to receive measurements from, and return control or status signals to the grid simulated in PowerFactory;
- 2 Performing the desired functions represented in Figure 5.6;
- 3 Acting as RPC server: an agent can be regarded as a RPC server, always being in a state of waiting to collect data from RPC clients of neighboring agents;
- 4 Acting as RPC client: an agent is also the client of the neighboring RPC server to provide its calculation results.

Therefore, the agent functions presented in Subsection 5.5.4 and the communication socket are programmed and stored in Python files. The communication socket enables these agents to generate, pack, or unpack data packets and deliver them to the adjacent agents using UDP/IP communication protocol. Considering an intermediate agent $A(k)$ with two neighboring agents $A(k-1)$ and $A(k+1)$, its structure is shown in Figure 5.11.

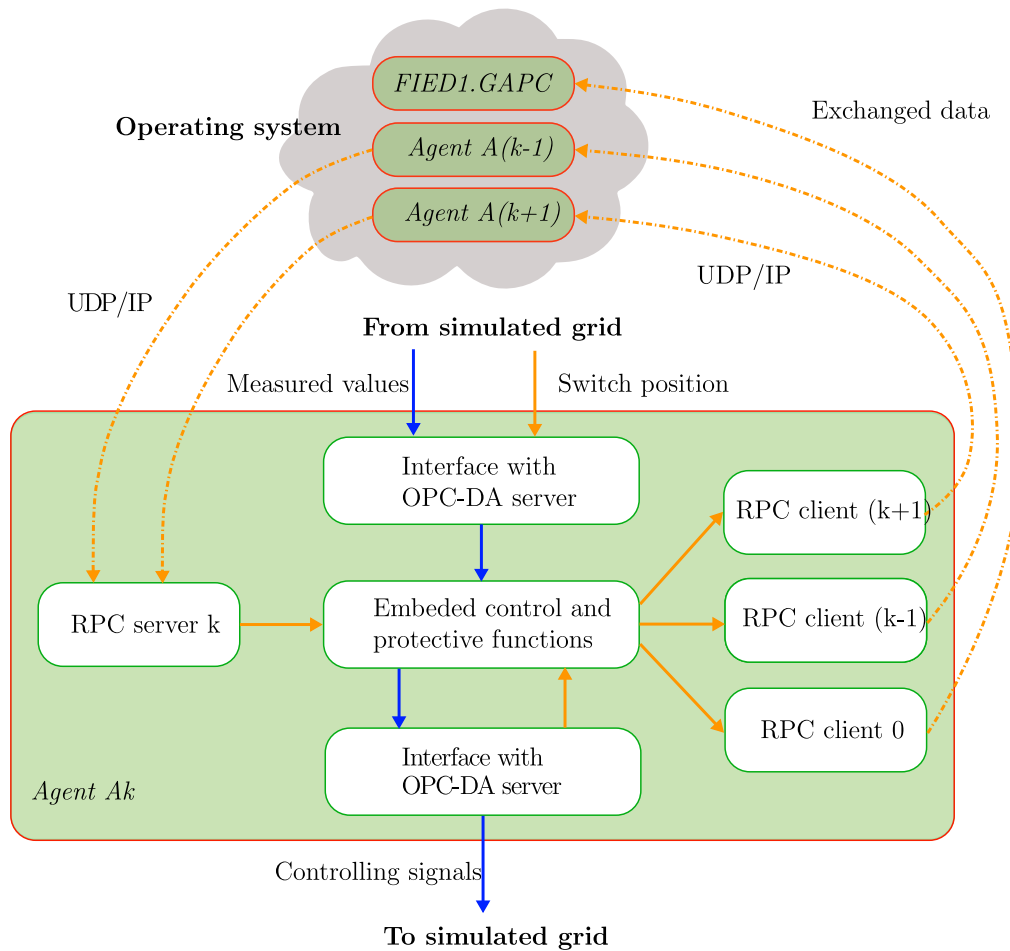


Figure 5.11 – Structural diagram of an agent for co-simulation system

5.6.3 MatrikonOPC server for cosimulation

A MatrikonOPC server is an open software that allows clients to access data in real-time. It is therefore used as a server for exchanging measurement data and control signals between Python-based agents and Powerfactory. Powerfactory sends the measured signals to the MatrikonOPC server, and the agents access this server to obtain data and vice versa. Each variable to be transferred must have an ID number and be preconfigured using the OPC naming convention system. All the preconfigured OPC elements are then loaded on the OPC server. The connection between the OPC server and Powerfactory is made by activating an OPC interface provided in the PowerFactory library. On the other hand, Python agents interface with the OPC server by importing the OpenOPC package.

5.6.4 Optimal placement of controlled switches for Grid-1

As mentioned earlier in Section 5.3, the location of **Remotely Controlled Switch (RCS)** is defined by a term called grid-bag. However, in this work, we use a tool available in PowerFactory library named "*Optimal RCS placement*" for determining the most appropriate number, and location of controlled switches for our proposed **FLIS**. This tool is based on the minimization principle of energy not supplied, [206]. Location of proposed controlled switches is shown in Figure 2.7. So, we have three controlled switches for Feeder 1, and four for Feeder 2. At each switch location, there is one agent for controlling the switch. The feeder FIEDs are also modeled and embedded in DIgSILENT | PowerFactory.

5.6.5 Results and discussion

For the following case studies, we consider Feeder 1 and 2, to which several **LV** microgrids with integrated PV systems are connected. We should note that the feeders in Grid-1 are composed of underground cables; therefore, the deployment of a reclosing element is not allowed. The *FitNum* parameter in the data attribute *Ak.RDRE.FitNum* of each agent is set to 0. The feeder FIED trips the corresponding CB after a delay of 0.5 s from the moment of fault detection.

5.6.5.1 Faults on Feeder 1

As shown in Table 5.3, the proposed **FLIS** has proven its effectiveness. All fault locations are correctly identified and then isolated by the respective agents. CB1 then recloses to restore power to some customers. The number of customers being resupplied depends on the location of the faults. The further away the fault is from the substation, the higher the number of customers is reconnected. Since PV systems in Feeder 1 are connected to the **LV** microgrids, they have no dynamic voltage support. Their contribution to fault currents is limited. Therefore, for faults occurring downstream of the agent location, the agent cannot detect the direction of the fault and therefore returns the results of the direction as *unknown* to its neighbors. By following the logic scheme shown in Figure 5.7, the agents that should be working have been operated correctly. The fault is isolated without any malfunction. Interruption time significantly decreases.

5.6.5.2 Fault on Feeder 2

As with the above fault scenarios, the proposed **FLIS** has demonstrated its effectiveness through the correct fault localization and isolation. The results of the performance validation are shown in Table 5.4. Besides, the proposed system reduced the outage time to only a few tens of seconds, compared to the average three minutes for existing systems [58]. It can also function properly in the case of low or no PV output.

5.6.5.3 Switch failure

To demonstrate the performance of the proposed **FLIS** against switch failure, assuming that a fault occurs at *F7*, and switch *S5* does not respond to the trip signal issued

Table 5.3 – Performance of the proposed FLIS for faults on Feeder 1

Fault point	Fault direction			Fault location			System operation	
	A1	A2	A3	A1	A2	A3	Action sequences	Time, s
F1	U	U ¹	U	I ³	E ⁴	E	① CB1 opens ② S1 opens ③ CB1 recloses	12.3
F2	F ²	U	U	I	I	E	① CB1 opens ② S1 & S2 open ③ CB1 recloses	13.5
F3	F	F	U	E	I	I	① CB1 opens ② S2 & S3 open ③ CB1 recloses	12.7
F4	F	F	F	E	E	I	① CB1 opens ② S3 opens ③ CB1 recloses	12.9

¹ Unknown fault;² Forward fault;³ Internal fault;⁴ External fault.

Table 5.4 – Performance of the proposed FLIS for faults on Feeder 2

Fault point	Fault direction				Fault location				System operation	
	A4	A5	A6	A7	A4	A5	A6	A7	Action sequences	Time, s
F5	R ¹	R	U ²	U	I ⁴	E ⁵	E	E	① CB2 opens ② S4 opens ③ CB2 recloses	13.7
F6	F ³	R	U	U	I	U	E	E	① CB2 opens ② S4 & S5 open ③ CB2 recloses	12.1
F7	F	F	U	U	E	I	I	E	① CB2 opens ② S5 & S6 open ③ CB2 recloses	13.5
F8	F	F	F	U	E	E	I	I	① CB2 opens ② S6 & S7 open ③ CB2 recloses	13.4
F9	F	F	F	F	E	E	E	I	① CB2 opens ② S7 opens ③ CB2 recloses	12.2

¹ Reverse fault;² Unknown fault;³ Forward fault;⁴ Internal fault;⁵ External fault.

by agent A5. After a predefined delay, agent A4 decides to trip switch S4 following the switch failure protection logic of Figure 5.7, and the position status of switch S4 is reported to FIED2. After processing, FIED2 recloses CB2, restoring power to the customers located between CB2 and switch S4.

5.6.6 Conclusion

In this part, the proposed FLIS is validated using a cosimulation system based on the combination of Python and PowerFactory simulators via the OPC-DA server. The obtained results show that such a FLIS can handle all fault locations despite the contribution of PV systems. The duration of the first phase of the overall power restoration process has considerably reduced. Consequently, several system reliability indices, such as SAIDI and CAIDI, have been improved, even if they are not quantified here. In the next section, the validation of the proposed FLIS is performed using a Controller Hardware-in-the-Loop (CHIL) platform on Grid-3 of Figure 2.10.

5.7 Validation using CHIL approach

5.7.1 Overview of DRTS and CHIL approach in power system domain

The Digital Real-Time Simulator (DRTS) is an approach that represents the behavior of the real electrical system being modeled by reproducing its output waveforms (current/voltage) with the desired accuracy. To achieve these objectives, the time required for a real-time digital simulator to solve the system equations for one time step should not be longer than the real-world clock time, [207]. Depending on the specific applications and study objectives, the DRTS can be divided into two groups: (i) fully real-time numerical simulation and (ii) Hardware-In-the-Loop real-time simulation. In the former, the entire system, including control, protection, and other equipment, must be fully modeled within the real-time simulators, without any connection to real external devices. However, in the second system, parts of the system being simulated may be replaced by hardware devices. The Hardware-In-the-Loop system is referred to as CHIL if it involves only hardware controllers or other devices operating with low-voltage signals that interact with the rest of the simulated system. Another type of Hardware-In-the-Loop system is called Power-Hardware-In-the-Loop if it interfaces with external real power devices such as power inverters, synchronous compensators..., through power amplifier devices. In the thesis, the CHIL approach is taken into account since it is necessary to validate the performance of the proposed method, which involves real controllers and FIEDs.

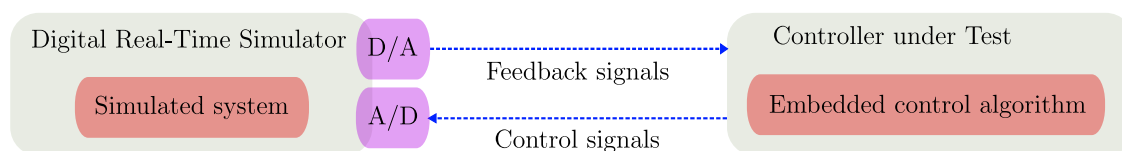


Figure 5.12 – Basic concept of CHIL simulation

Figure 5.12 represents the basic concept for the CHIL configuration, [207]. In such

a simulation platform, the power system is fully virtualized inside a real-time digital simulator, and the proposed control algorithm is integrated into real external controllers. The real controllers receive the measured signals from the simulators in real-time, process them, and send the control signals back to the system inside the simulator. In the study, the agents that form the MAS for the proposed FLIS act as controllers. Their structure is described in Subsection 5.7.2.

Since the first fully digital real-time simulator ARENE introduced by Electricité de France in 1996 [207], various DRTS systems have been made available such as NETOMAC from SIEMENS, RTDS from RTDS technologies, dSPACE, Typhoon RTDs, xPC Target, VTB, eMEGAsim and HYPERSIM from OPAL-RT Technologies [198]. Although different producers have shared the market, as described in [207], most DRTSs share the following common characteristics:

- 1 a hardware platform consisting of multiple operating-in-parallel processors for running the simulated power system in real-time;
- 2 a host computer for: (i) building the model offline and then compiling and loading it to the target platform, and (ii) monitoring the results returned by the target platform;
- 3 Input/Output ports for interfacing with actual devices connected externally such as an amplifier, power electronic devices, controller;
- 4 a communication network for transmitting data between multiple targets if the model is divided into multiple subsystems. A separate communication network is required for data exchange between the host and the target.

In the study, the eMEGAsim OP5600 simulator from OPAL-RT Technologies is used for implementing the CHIL testing platform. The target computer (simulator) is connected to a host computer directly or via a Ethernet network switch or a local area network. OPAL-R Technologies provides a dedicated software named RT-LAB with Matlab/Simulink integration for modeling and preparing the studied electric power system. Normally, the users should follow the following basic steps to perform a real-time simulation using eMEGAsim, [198]:

- 1 *Edit*: open the Simulink model directly through RT-LAB;
- 2 *Compile*: transform the Simulink model into a real-time simulation;
- 3 *Load*: load the compiled model into the target platform;
- 4 *Execute*: run the simulation on real time target using multiple cores;
- 5 *Interact*: change controls and acquire data by using graphical interface.

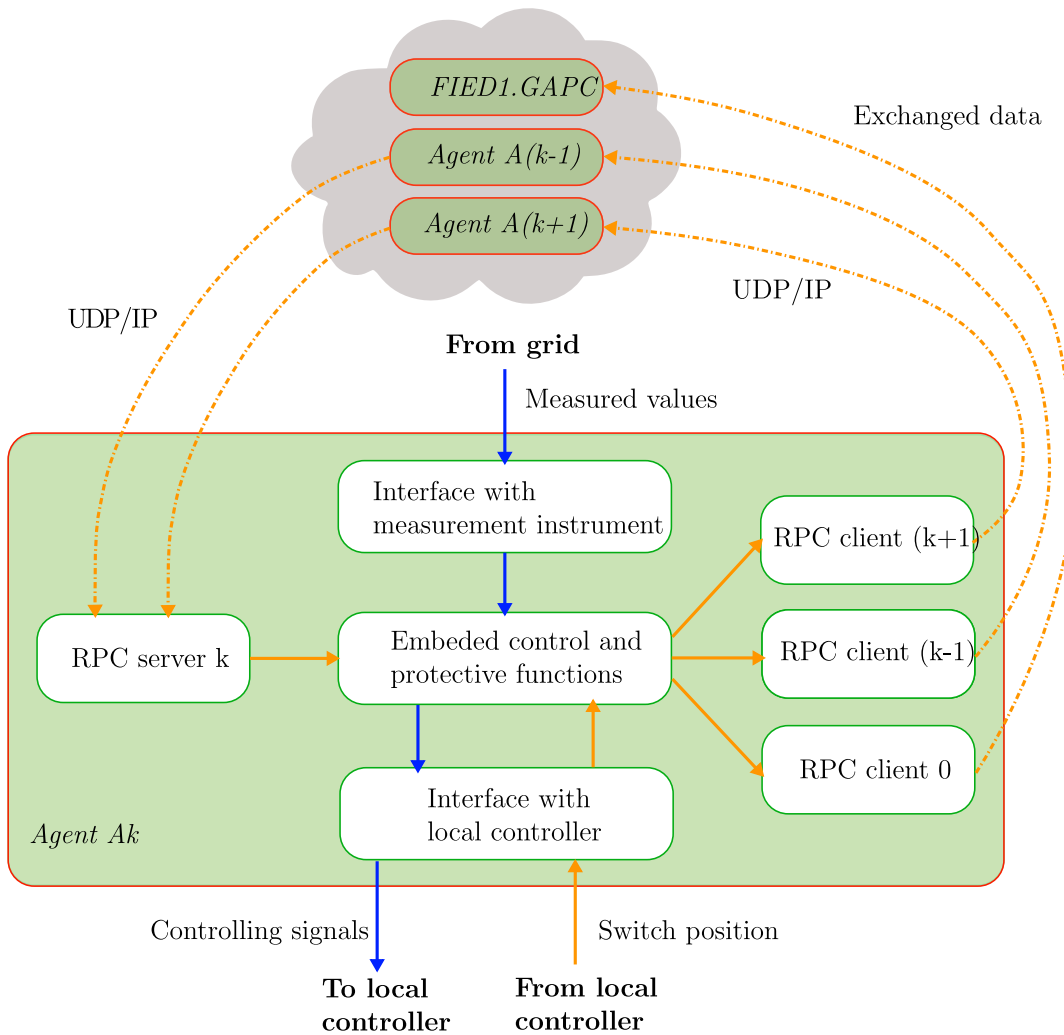


Figure 5.13 – Structural diagram of an agent for CHIL validation

5.7.2 Description of the MAS for the CHIL platform

The **Multiagent System (MAS)** testbed deployed in the study is a cluster of ten Raspberry Pis connected to a local area network. Communication between agents is conducted in a client/server manner. Each agent acts as a server that requests data from its clients, i.e. adjacent agents, and then distributes them to method calls. The method calls in our case are the control and protection functions required for the proposed **FLIS**. After processing, the results are sent back to the adjacent agents who are in turn servers of the agent in question. Thus, each agent is programmed using the Python programming language to obtain the following characteristics, [198]:

- 1 Feature of exchanging data with DRTS to receive measured current/voltage values from and return control or status signals to the grid simulated in DRTS;
- 2 Feature of performing the functions required by the proposed **FLIS** depicted in Figure 5.6;

- 3 Feature of RPC server: an agent is always in a state of waiting signals from its adjacent agents. So a agent can be considered as an RPC server to collect data from RPC neighboring clients;
- 4 Feature of RPC client: an agent is also the client of the neighboring RPC server to provide its calculation results.

Therefore, the designed functions of the agents presented in Subsection 5.5.4 and IEC 61850-based communication socket are programmed, and then hosted and executed on these Raspberry PIs. The IEC 61850-based communication socket enables these agents to generate, pack, or unpack data packets and deliver them over the networks. Considering an intermediate agent A_k with two neighboring agents $A^{(k-1)}$ and $A^{(k+1)}$, its structure is illustrated in Figure 5.13.

5.7.3 CHIL testing platform

The CHIL simulation platform implemented in the study includes the real-time simulator eMEGAsim OP5600 from OPAL-RT Technologies, ABB relay REF615, and three Raspberry PIs with corresponding IP addresses from 192.168.1.101 to 192.168.1.103, as shown in Figure 5.14. The relay REF615 is identified by its MAC address 00:21:c1:25:08:a2 that was configured by its manufacturer.

5.7.3.1 Studied feeder

The network concerned in this part is Grid-3 depicted in Figure 2.10. All PV systems are modeled as voltage-controlled current sources with fault currents limited to 1.2 times their nominal currents. Also, the simulated PV systems are disconnected within 0.2 s after the fault detection by their interface protection to avoid undesirable islanding. On the other hand, the feeder CB and switches with their control circuits are simulated in the OPAL/RT simulator. Besides, we have set the operating time of the CBs and the switches to 0.03 s and 0.1 s, respectively, to consider their actual operation times.

5.7.3.2 Feeder IED and agents

Agents receive current and voltage measurements from the OPAL-RT eMEGAsim 5600 via an Ethernet switch, which are filtered by an integrated full window cosine filter to eliminate aliased signals. The sampling rate is fixed at 1000 Hz, so that the window length is 20. Since Grid-3 is a rural network, the time delay of the feeder Time Overcurrent Protection (PTOC) element is set at 0.15 s as mentioned in Section 2.2.2. The function Autoreclosing Element (RREC) of each feeder FIED has two cycles, a fast one with a delay of 0.3 s, and a slow one with a delay of 10 s (Section 2.2.2). When a fault occurs, the FIED1 triggers the CB1 emulated in the eMEGAsim 5600 by a [Generic Objective Oriented Substation Event \(GOOSE\)](#) message. The real-time simulator must be configured to receive this message. For the feeder FIED1 to be able to publish GOOSE messages on the network, we need to group the messages from each one into data sets and configure the [GOOSE Control Block \(GCB\)](#). The feeder FIED1 and the eMEGAsim 5600 have a

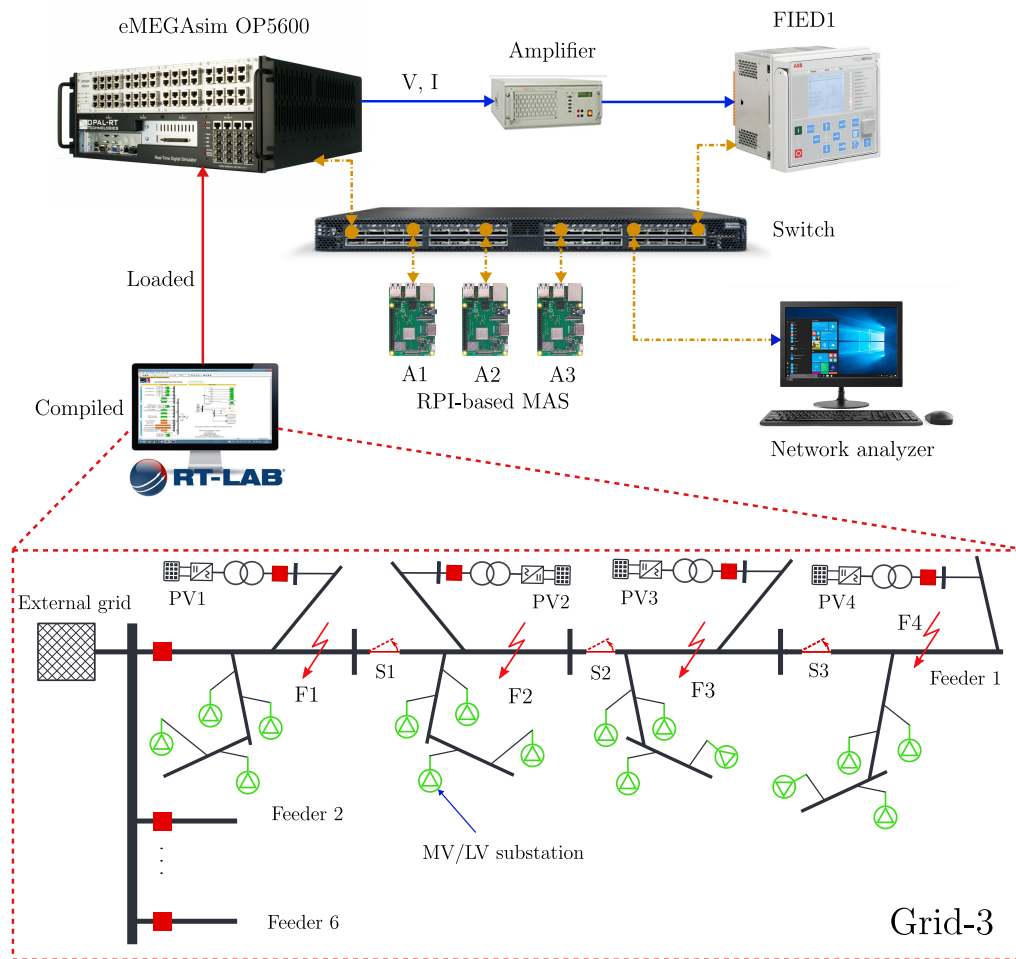


Figure 5.14 – CHIL testing setup

MAC IP address that must be included in the GCB. In the study, we focus only on validating the overall performance of the proposed FLIS; therefore, an Ethernet-based local area network is applied for the communication between the agents and the feeder FIED. However, a delay of 0.5 s has been assigned to the communication blocks to take into account the data propagation delay between the agents and the feeder FIED that occurs outside the substation area,

5.7.4 Results and discussion

5.7.4.1 Evaluation of data exchange

The performance of the GOOSE-based communication capability of the feeder protection relay, i.e. FIED1, and the real time simulator eMEGAsim OP5600 was tested using Wireshark software tool. A segment of the data set of the GOOSE messages published by the feeder FIED is illustrated in Figure 5.15. The tests have shown that the feeder FIED and DRTS have successfully published and subscribed to the required GOOSE messages that were previously presented in Subsection 5.5.4.

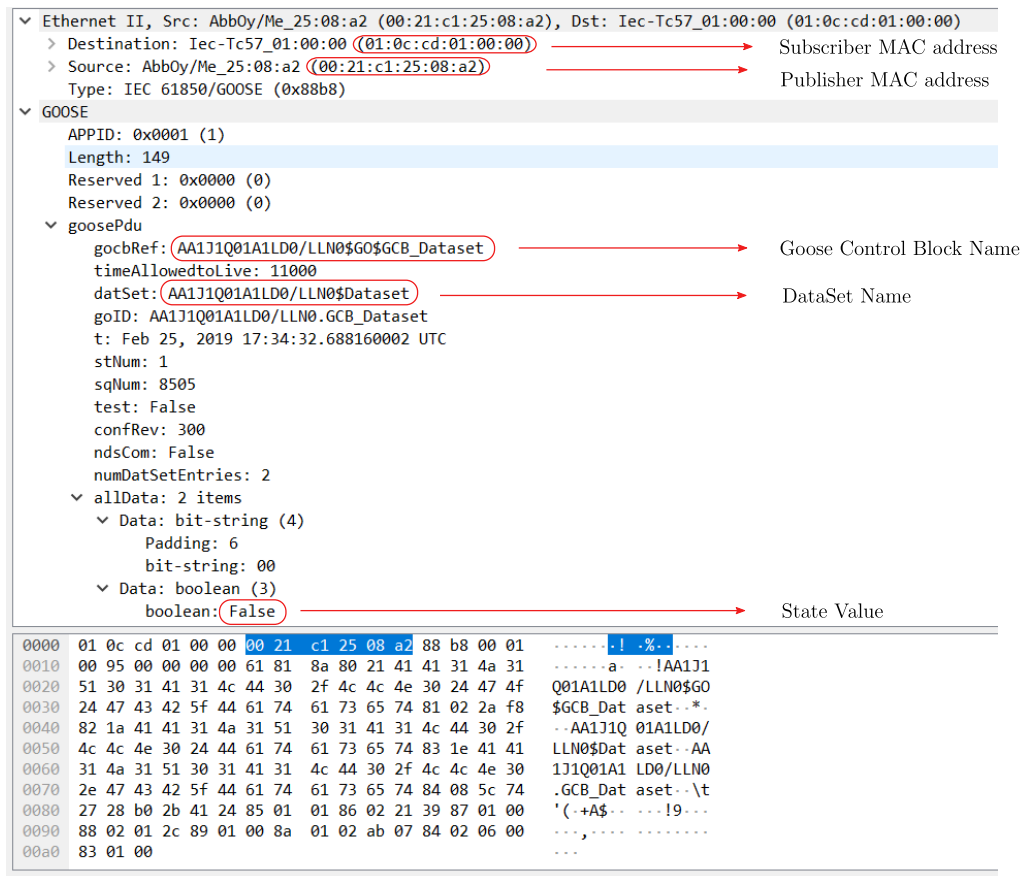


Figure 5.15 – GOOSE packets captured by Wireshark software tool

5.7.4.2 Evaluation of the proposed scheme

The proposed FLIS has proven its effectiveness by successfully dealing with a variety of fault scenarios, which are presented in Table 5.5 and graphically illustrated in Figure 5.16. The total operating time is calculated from the time at which the fault occurs to the time the CB closes completely after the successful operation of the respective switches. It is evident that the fault clearing time of the proposed FLIS has been significantly reduced to only less than 15 s compared with 3 minutes or more of the existing methods, [58].

Figure 5.16a shows the current-time curves measured by the feeder IED for a permanent three-phase fault at F3 in Figure 5.14 with $R_f = 10 \Omega$. It clearly shows that after the fast then slow cycles, the reclosing function of the IED is locked out, and the IED has tripped the CB again. Once the CB opened, agents A2 and A3 opened the switches S2 and S3. In the final stage, the central controller closed the CB; however, the supply was only restored to a portion of the customers between the IED and switch S2. The decrease in currents after 6.88 s demonstrates this. The results for a permanent single-phase-to-ground fault are also shown in Figure 5.16b. Similarly, the agents correctly detected the faulty line section and then operated the switches to open them, thus isolating the fault.

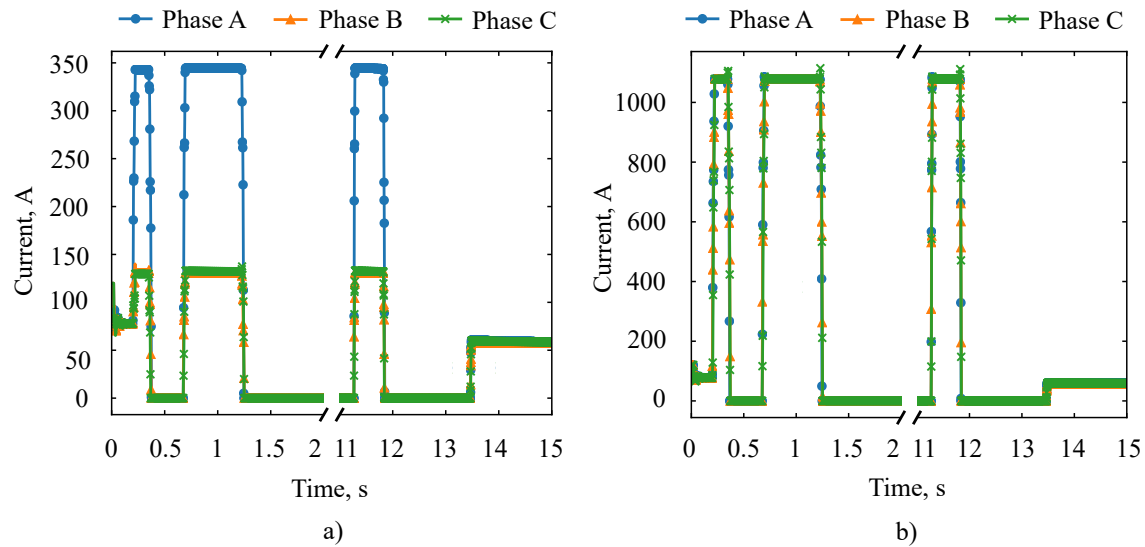


Figure 5.16 – IED time-current curves in the event of a permanent a) single-phase fault with $R_f = 20 \Omega$ and b) three-phase fault with $R_f = 10 \Omega$

Table 5.5 – CHIL test results

Fault location	Operation sequences	Operation time, s
$F1$	① CB opens \mapsto ② RREC operates and locks out \mapsto ③ CB opens	12.03
$F2$	① CB opens \mapsto ② RREC operates and locks out \mapsto ③ CB opens \mapsto ④ $S1$ & $S2$ open \mapsto ⑤ CB recloses	13.68
$F3$	① CB opens \mapsto ② RREC operates and locks out \mapsto ③ CB opens \mapsto ④ $S2$ & $S3$ open \mapsto ⑤ CB recloses	13.52
$F4$	① CB opens \mapsto ② RREC operates and locks out \mapsto ③ CB opens \mapsto ④ $S3$ opens \mapsto ⑤ CB recloses	13.64

5.7.5 Conclusion

In this subsection, the proposed FLIS has been validated using a CHIL platform involving a real-time simulator, as well as a real protection relay and RPI-based controllers. The obtained results show that the proposed FLIS can handle all fault locations despite the contribution of PV systems. The duration of the first phase of the overall power restoration process has considerably reduced. System indices, such as SAIDI and CAIDI, have therefore been improved. The correct detection and isolation of faulty line-section also confirms the interoperability between the controllers involved and the real devices.

5.8 Conclusion

In this chapter, two **FLIS** have been developed. The first scheme is based on **Artificial Neural Network (ANN)**, and the second system relies on **Multiagent System (MAS)** and IEC 61850 communication. In the first proposal, an **ANN** network based on the Multi-layer Perceptron (MPL) classifier technique has been formulated and validated by a set of data obtained from multiple simulations. The second scheme is mainly based on local measurements, and fault direction information exchanged via the communication network. An agent only needs to talk to his neighbors to decide whether or not the fault is within his protection zone. We use the same network, i.e. Grid-1 illustrated in Figure 2.7, for evaluating the **ANN**-based **FLIS**, and the **MAS**-based **FLIS** by using cosimulation approach; and another network, i.e. Grid-3 in Figure 2.10, for validating the **MAS**-based **FLIS** by using **Controller Hardware-in-the-Loop (CHIL)** platform.

The test results show the high accuracy of the proposed **ANN**-based **FLIS**. It could accurately indicate the faulty line-section located between two manual switches, facilitating the restoration process thanks to its fast computation time. On the other hand, the evaluation results, obtained by using the cosimulation system and the **CHIL** platform, show that the **MAS**-based **FLIS** system has achieved high performance on different networks under various fault scenarios. The faulty line-section located between two switches, locally controlled by their agents, are rapidly isolated. A further step is to send a line crew to the field to open the two manual switches that are nearest to the fault location.

However, the impact of communication networks in terms of communication losses and delays and other severe fault conditions were not considered. Therefore, future studies should focus on these issues. Also, an algorithm for precisely locating fault points should be developed based on the proposed schemes.

6.1 Conclusion

The rapid increase in the penetration level of the inverter-based PV systems, combined with the imposition of new grid codes in many countries, has changed the distribution network conditions profoundly both in normal steady-state operation and in the event of faults.

The fundamental direction of the thesis has been the fault conditions under which the proper fault behavior of inverter-based PV systems under the new grid code conditions is of importance. Therefore, in the first stage of the thesis, all new grid codes issued by authorities in many countries were investigated. Based on these requirements, a control strategy for PV systems was developed. This control strategy not only ensured that the PV systems met the new grid code requirements during fault but also facilitated the detection of unbalanced faults. The results of the evaluation indicated that the PV systems under the proposed control algorithm actively participated in recovering the system voltage during fault events by injecting additional reactive power. Also, [Negative Sequence \(NS\)](#) current generation increased the sensitivity of the overcurrent protections. **(Contribution 1)**

In addition, the possibility of bidirectional fault currents, which are caused by the increasing contribution of the PV systems connected downstream of the measuring devices, motivated the proposal of a new directional method. Hence, in the thesis, a new [Directional Element \(RDIR\)](#) that can achieve high performance under high penetration of electronic inverter-based production units was developed, evaluated by an analytical approach, and then validated by numerous simulations on real networks in the software environment DIGSILENT|PowerFactory. The consistency between the different evaluation methods confirmed the accuracy of the developed PV models and the formulas representing the [RDIR](#) method. Also, the simulation results showed that the proposed [RDIR](#) method could be effectively used for the protection as well as fault location and isolation of distribution networks with in high-penetration of inverter-based PV systems. **(Contribution 2)**

Next, a comprehensive protection strategy that could entirely protect [Medium Voltage \(MV\)](#) distribution networks containing [Low Voltage \(LV\)](#) microgrids was implemented.

Results obtained from simulations on a real network in the software environment DIgSILENT | PowerFactory proved that a protection strategy without communication support can be sufficient to protect the LV microgrids in both modes of operation. All connected LV microgrids could successfully transit to islanding if there were faults in the external networks. Moreover, the installed PV systems achieved their required Fault Ride Through (FRT) capability. The protection systems for the MV and LV distribution networks effectively operated in a selective and coordinated manner. Besides, at each level of protection, when a primary function failed to trip for any reason, a designed back-up function was able to provide redundant trips, thus preventing the fault from propagating. **(Contribution 3)**

Further, two Fault Location and Isolation System (FLIS) systems for MV distribution networks with high integration of PV systems were accomplished. The first Artificial Neural Network (ANN)-based method can be considered centralized, while the second Multiagent System (MAS)-based approach can be regarded as distributed. In the first scheme, the developed ANN network was trained and then tested on fault data derived from multiple fault simulations in the software environment DIgSILENT | PowerFactory. The test results showed its high accuracy and faulty line sections could be correctly identified after a very short time. Additionally, this method required only three measuring points for an entire MV feeder with high penetration of PV systems. On the other hand, the second method has enabled faulty line sections to be obtained by local controllers, i.e., agents, using fault information received from neighboring agents. The performance of the MAS-based FLIS was evaluated using a cosimulation system, and then a CHIL platform. The results of the cosimulation method indicated that the designed agents could communicate with each other for fault information exchange to make final control decisions. Also, the implemented Controller Hardware-in-the-Loop (CHIL) platform allowed for the verification of interoperability between the relevant control elements, including the actual agents and IED. **(Contributions 4, 5, and 6)**

Finally, we can conclude that all the algorithms and methods developed in the study have achieved their high-performance thanks to the validation results obtained by different methods. The use of different real networks also improved the validation results. All problems, which are caused by high PV penetration to protection systems as well as fault location and isolation systems in distribution networks, have been solved.

6.2 Perspectives

Based on what has been achieved in the thesis, several research topics that can be put forward as follows:

- 1 An investigation into the application of Artificial Intelligence for determination of the operating boundary between forward and reverse faults for the proposed directional method;
- 2 An expansion in analyzing the impacts of different network configurations, such as grounding systems, high fault impedances, short-circuit capacity of

external grids on the developed directional algorithm;

- 3 **CHIL** simulation of the proposed protection schemes involving DRTS and real IED such as feeder and transformer numerical relays. IEC 61850-based communication between devices within substation areas, as well as communication protocols on inter-substation scales, also deserves more attention. The **CHIL** simulation results would be more reliable and realistic than those from pure simulations, and thus can be considered as a next stage toward the realization of the developed protection schemes;
- 4 A tool for automatic configuration of **MAS**-based **FLIS**. Such a tool can significantly facilitate the configuration process of the system on a large-scale;
- 5 Optimal algorithm for the restoration process that follows the operation of the proposed **FLIS**. The system **System Average Interruption Duration Index (SAIDI)**, **Customer Average Interruption Duration Index (CAIDI)** and other economic indicators would be significantly improved if the duration of the restoration process can be reduced and carried out in an optimal pattern.

Bibliography

- [1] P. Kundur, N. J. Balu, and M. G. Lauby, *Power system stability and control*, vol. 7. McGraw-hill New York, 1994.
- [2] "Global electricity generation." <https://www.eia.gov/international/data/world/electricity/>. Accessed: 2015-03-15.
- [3] FAOSTAT, "Carbon dioxide (CO2) emissions by sector," 2017.
- [4] A. A. Sallam and O. P. Malik, *Electric distribution systems*. John Wiley & Sons, 2018.
- [5] W. El-Khattam and M. M. Salama, "Distributed generation technologies, definitions and benefits," *Electric power systems research*, vol. 71, no. 2, pp. 119–128, 2004.
- [6] Q. T. Tran, "Lecture notes in solar energy," October 2018.
- [7] "Distribution of power across the network levels." <https://www.ren21.net/reports/global-status-report/http://www.energymap.info/energieregionen/DE/105.html/>. Accessed: 2015-03-15.
- [8] I. Fraunhofer, "Recent facts about photovoltaics in germany," *Fraunhofer Institute for Solar Energy Systems ISE, Germany, Tech. Rep*, vol. 25, 2015.
- [9] B. Crăciun, T. Kerekes, D. Séra, and R. Teodorescu, "Overview of recent grid codes for pv power integration," in *2012 13th International Conference on Optimization of Electrical and Electronic Equipment (OPTIM)*, pp. 959–965, May 2012.
- [10] F. Blaabjerg, R. Teodorescu, M. Liserre, and A. V. Timbus, "Overview of control and grid synchronization for distributed power generation systems," *IEEE Transactions on industrial electronics*, vol. 53, no. 5, pp. 1398–1409, 2006.
- [11] Y. Bae, T.-K. Vu, and R.-Y. Kim, "Implemental control strategy for grid stabilization of grid-connected pv system based on german grid code in symmetrical low-to-

- medium voltage network," *IEEE Transactions on Energy Conversion*, vol. 28, no. 3, pp. 619–631, 2013.
- [12] S. Jain and V. Agarwal, "A single-stage grid connected inverter topology for solar pv systems with maximum power point tracking," *IEEE transactions on power electronics*, vol. 22, no. 5, pp. 1928–1940, 2007.
- [13] R. Teodorescu, M. Liserre, and P. Rodriguez, *Grid converters for photovoltaic and wind power systems*, vol. 29. John Wiley & Sons, 2011.
- [14] M. Gaetan, O. Sinead, and R. Manoel, "Global market outlook," *EPIA - European Photovoltaic Industry Association.*, p. 60, 2018.
- [15] "Renewables 2018: Global status report." <https://www.ren21.net/reports/global-status-report/>. Accessed: 2019-10-30.
- [16] H. M. Hasanien, "An adaptive control strategy for low voltage ride through capability enhancement of grid-connected photovoltaic power plants," *IEEE Transactions on power systems*, vol. 31, no. 4, pp. 3230–3237, 2015.
- [17] T. Stetz, F. Marten, and M. Braun, "Improved low voltage grid-integration of photovoltaic systems in germany," *IEEE Transactions on sustainable energy*, vol. 4, no. 2, pp. 534–542, 2012.
- [18] M. Arnold, W. Friede, and J. Myrzik, "Challenges in future distribution grids-a review," *Proc. of ICREPQ'13*, pp. 1–6, 2013.
- [19] G. Mokhtari, A. Ghosh, G. Nourbakhsh, and G. Ledwich, "Smart robust resources control in lv network to deal with voltage rise issue," *IEEE Transactions on Sustainable Energy*, vol. 4, no. 4, pp. 1043–1050, 2013.
- [20] H. Wirth and K. Schneider, "Recent facts about photovoltaics in germany," *Fraunhofer ISE*, vol. 92, 2015.
- [21] V. V. d. E. E. Informationstechnik, "ev,"power generation systems connected to the low-voltage distribution network-technical minimum requirements for the connection to and parallel operation with low-voltage distribution networks," tech. rep., VDE-AR, 2011.
- [22] C. E. Italiano, "Reference technical rules for connecting users to the active and passive lv distribution companies of electricity," *CEI 0*, vol. 21, 2011.
- [23] A. Cagnano, E. De Tuglie, M. Liserre, and R. A. Mastromauro, "Online optimal reactive power control strategy of pv inverters," *IEEE Transactions on Industrial Electronics*, vol. 58, no. 10, pp. 4549–4558, 2011.
- [24] W. Bartels, F. Ehlers, K. Heidenreich, R. Huttner, H. Kuhn, T. Meyer, T. Kumm, J. Salzmann, H. Schafer, and K. Weck, "Generating plants connected to the medium-voltage network," *Technical Guideline of BDEW*, 2008.

- [25] E.-E. N. Code, "Requirements for grid connection applicable to all generators," *ENTSO-E: Brussels, Belgium*, 2013.
- [26] T. Basso, S. Chakraborty, A. Hoke, and M. Coddington, eds., *IEEE 1547 Standards advancing grid modernization*, vol. 1 of 1, (USA), 2015 IEEE 42nd Photovoltaic Specialist Conference, PVSC 2015, IEEE, 7 2015.
- [27] R. Bründlinger, "Advanced smart inverter and der functions requirements in latest european grid codes and future trends," *Solar Canada*, vol. 8, 2015.
- [28] P. P. Barker and R. W. De Mello, "Determining the impact of distributed generation on power systems. i. radial distribution systems," in *2000 Power Engineering Society Summer Meeting (Cat. No. 00CH37134)*, vol. 3, pp. 1645–1656, IEEE, 2000.
- [29] I. K. Tarsi, A. Sheikholeslami, T. Barforoushi, and S. M. B. Sadati, "Investigating impacts of distributed generation on distribution networks reliability: A mathematical model," in *Proceedings of the 2010 Electric Power Quality and Supply Reliability Conference*, pp. 117–124, IEEE, 2010.
- [30] F. T. Dai, "Impacts of distributed generation on protection and autoreclosing of distribution networks," in *10th IET International Conference on Developments in Power System Protection (DPSP 2010). Managing the Change*, pp. 1–5, March 2010.
- [31] J. González, A. Dyško, and G. Lloyd, "The impact of renewable energy sources and distributed generation on substation protection and automation," *43rd International Conference on Large High Voltage Electric Systems 2010, CIGRE 2010*, vol. 57, 01 2010.
- [32] C. Mozina, "Impact of green power inverter-based distributed generation on distribution systems," in *2014 67th Annual Conference for Protective Relay Engineers*, pp. 264–278, IEEE, 2014.
- [33] C. A. Plet, M. Brucoli, J. D. McDonald, and T. C. Green, "Fault models of inverter-interfaced distributed generators: Experimental verification and application to fault analysis," in *2011 IEEE Power and Energy Society General Meeting*, pp. 1–8, IEEE, 2011.
- [34] J. Rocabert, A. Luna, F. Blaabjerg, and P. Rodriguez, "Control of power converters in ac microgrids," *IEEE transactions on power electronics*, vol. 27, no. 11, pp. 4734–4749, 2012.
- [35] B. Lasseter, "Microgrids distributed power generation," in *2001 IEEE power engineering society winter meeting. Conference proceedings (Cat. No. 01CH37194)*, vol. 1, pp. 146–149, IEEE, 2001.
- [36] N. Hadjsaid and J.-C. Sabonnadière, *Electrical distribution networks*. John Wiley & Sons, 2013.
- [37] A. Girgis and S. Brahma, "Effect of distributed generation on protective device coordination in distribution system," in *LESCOPE 01. 2001 Large Engineering Systems Conference on Power Engineering. Conference Proceedings. Theme: Powering Beyond 2001 (Cat. No. 01ex490)*, pp. 115–119, IEEE, 2001.

- [38] R. Bründlinger, "Grid codes in europe for low and medium voltage," in *6th International Conference on Integration of Renewable and Distributed Energy Resources, Kyoto, Japan*, vol. 18, 2014.
- [39] H. Kobayashi, "Fault ride through requirements and measures of distributed pv systems in japan," in *2012 IEEE Power and Energy Society General Meeting*, pp. 1–6, IEEE, 2012.
- [40] "Revision of power generating plants in the low voltage grid." <https://www.vde.com/en/fnn/topics/technical-connection-rules/power-generating-plants>. Accessed: 2019-10-30.
- [41] M. Kraiczy, L. Fakhri, T. Stetz, and M. Braun, "Do it locally: Local voltage support by distributed generation—a management summary: Management summary of iea task 14 subtask 2—recommendations based on research and field experience," *IEA International Energy Agency: Fribourg, Switzerland*, 2017.
- [42] E. On, "Grid code high and extra high voltage," *On Netz GmbH: Bayreuth, Germany*, 2006.
- [43] J. Boemer, J. Torres, E. van Ruitenbeek, K. Skaloumpakas, and M. van der Meijden, "Evolution of low voltage generator behaviour in low-voltage events german: Weiterentwicklung des verhaltens von erzeugungsanlagen am niederspannungsnetz im fehlerfall-systemsicherheitsaspekte," in *Technische Universität Delft im Auftrag des Forum Netztechnik/Netzbetrieb im VDE eV, Tech. Rep*, 2015.
- [44] H. Kobayashi and I. Kurihara, "Research and development of grid integration of distributed generation in japan," in *2009 IEEE Power & Energy Society General Meeting*, pp. 1–8, IEEE, 2009.
- [45] K. Fujii, N. Yamada, Y. Okuma, and N. Kanao, "Fault ride through capability for solar inverters," *EPE Journal*, vol. 22, no. 2, pp. 30–36, 2012.
- [46] A. Q. Al-Shetwi, M. Z. Sujod, and N. L. Ramli, "A review of the fault ride through requirements in different grid codes concerning penetration of pv system to the electric power network," *ARNP journal of engineering and applied sciences*, vol. 10, no. 21, pp. 9906–9912, 2015.
- [47] Y. Yang, P. Enjeti, F. Blaabjerg, and H. Wang, "Wide-scale adoption of photovoltaic energy: Grid code modifications are explored in the distribution grid," *IEEE Industry Applications Magazine*, vol. 21, no. 5, pp. 21–31, 2015.
- [48] Y. Yang, F. Blaabjerg, and Z. Zou, "Benchmarking of grid fault modes in single-phase grid-connected photovoltaic systems," *IEEE Transactions on Industry Applications*, vol. 49, no. 5, pp. 2167–2176, 2013.
- [49] M. Datta, T. Senjyu, A. Yona, T. Funabashi, and C.-H. Kim, "A frequency-control approach by photovoltaic generator in a pv–diesel hybrid power system," *IEEE Transactions on Energy Conversion*, vol. 26, no. 2, pp. 559–571, 2010.

- [50] H. Xin, Y. Liu, Z. Wang, D. Gan, and T. Yang, "A new frequency regulation strategy for photovoltaic systems without energy storage," *IEEE Transactions on Sustainable Energy*, vol. 4, no. 4, pp. 985–993, 2013.
- [51] T. A. Short, *Electric power distribution handbook*. CRC press, 2018.
- [52] S. Papathanassiou, N. Hatziaargyriou, K. Strunz, *et al.*, "A benchmark low voltage microgrid network," in *Proceedings of the CIGRE symposium: power systems with dispersed generation*, pp. 1–8, 2005.
- [53] I. E. Commission *et al.*, "Iec 60364-5-54: 2011 low-voltage electrical installations–part 5-54: Selection and erection of electrical equipment earthing arrangements and protective conductors is," 2010.
- [54] R. Apel, C. Jaborowicz, and R. Kussel, "Fault management in electrical distribution networks," in *16th International Conference and Exhibition on Electricity Distribution, 2001. Part 1: Contributions. CIRED. (IEE Conf. Publ No. 482)*, vol. 3, pp. 5 pp. vol.3–, June 2001.
- [55] C. Puret, "MV public distribution networks throughout the world," *E/Ct*, vol. 155, no. March 1992, 1992.
- [56] A. Guldbrand, "System earthing," *Report, Sweden*, 2006.
- [57] T. M. C. Le, *Couplage Onduleurs Photovoltaïques et Réseau, aspects contrôle/commande et rejet de perturbations*. PhD thesis, Grenoble INP, Grenoble, 1 2012.
- [58] T. Wagner, "Impact of remote controlled switches on distribution grid recovering processes," 2010.
- [59] R. M. Kamel, A. Chaouachi, and K. Nagasaka, "Comparison the performances of three earthing systems for micro-grid protection during the grid connected mode," *Smart Grid Renew Energy*, vol. 2, no. 3, pp. 206–215, 2011.
- [60] DIgSILENT GmbH, *DigSILENT PowerFactory 18, User manual*.
- [61] W. Xiao, F. F. Edwin, G. Spagnuolo, and J. Jatskevich, "Efficient approaches for modeling and simulating photovoltaic power systems," *IEEE journal of photovoltaics*, vol. 3, no. 1, pp. 500–508, 2012.
- [62] H. Kawamura, K. Naka, N. Yonekura, S. Yamanaka, H. Kawamura, H. Ohno, and K. Naito, "Simulation of i–v characteristics of a pv module with shaded pv cells," *Solar Energy Materials and Solar Cells*, vol. 75, no. 3-4, pp. 613–621, 2003.
- [63] S. Saravanan and N. R. Babu, "Maximum power point tracking algorithms for photovoltaic system—a review," *Renewable and Sustainable Energy Reviews*, vol. 57, pp. 192–204, 2016.
- [64] H.-s. Song and K. Nam, "Dual current control scheme for pwm converter under unbalanced input voltage conditions," *IEEE transactions on industrial electronics*, vol. 46, no. 5, pp. 953–959, 1999.

- [65] M. Mirhosseini, J. Pou, B. Karanayil, and V. G. Agelidis, "Positive-and negative-sequence control of grid-connected photovoltaic systems under unbalanced voltage conditions," in *2013 Australasian Universities Power Engineering Conference (AUPEC)*, pp. 1–6, IEEE, 2013.
- [66] F. Wang, J. L. Duarte, and M. A. Hendrix, "Pliant active and reactive power control for grid-interactive converters under unbalanced voltage dips," *IEEE transactions on power electronics*, vol. 26, no. 5, pp. 1511–1521, 2010.
- [67] P. Rodriguez, A. V. Timbus, R. Teodorescu, M. Liserre, and F. Blaabjerg, "Flexible active power control of distributed power generation systems during grid faults," *IEEE transactions on industrial electronics*, vol. 54, no. 5, pp. 2583–2592, 2007.
- [68] S. Alepuz, S. Busquets-Monge, J. Bordonau, J. A. Martínez-Velasco, C. A. Silva, J. Pontt, and J. Rodríguez, "Control strategies based on symmetrical components for grid-connected converters under voltage dips," *IEEE Transactions on Industrial Electronics*, vol. 56, no. 6, pp. 2162–2173, 2009.
- [69] F. A. Magueed, A. Sannino, and J. Svensson, "Transient performance of voltage source converter under unbalanced voltage dips," in *2004 IEEE 35th Annual Power Electronics Specialists Conference (IEEE Cat. No. 04CH37551)*, vol. 2, pp. 1163–1168, IEEE, 2004.
- [70] K. Jia, C. Gu, Z. Xuan, L. Li, and Y. Lin, "Fault characteristics analysis and line protection design within a large-scale photovoltaic power plant," *IEEE Transactions on Smart Grid*, vol. 9, no. 5, pp. 4099–4108, 2017.
- [71] A. Yazdani and R. Iravani, *Voltage-sourced converters in power systems*, vol. 34. Wiley Online Library, 2010.
- [72] S. M. Alhejaj and F. M. Gonzalez-Longatt, "Investigation on grid-scale bess providing inertial response support," in *2016 IEEE International Conference on Power System Technology (POWERCON)*, pp. 1–6, IEEE, 2016.
- [73] A. Mahmud, "Large scale renewable power generation," 2014.
- [74] W. Sonnemann, "A study of directional element connections for phase relays," *Transactions of the American Institute of Electrical Engineers*, vol. 69, no. 2, pp. 1438–1451, 1950.
- [75] K. Zimmerman and D. Costello, "Fundamentals and improvements for directional relays," in *2010 63rd Annual Conference for Protective Relay Engineers*, pp. 1–12, IEEE, 2010.
- [76] A. (Firm), *Network protection & automation guide*. Alstom, 2002.
- [77] J. L. Blackburn and T. J. Domin, *Protective relaying: principles and applications*. CRC press, 2014.

- [78] A. Ukil, B. Deck, and V. H. Shah, "Current-only directional overcurrent protection for distribution automation: challenges and solutions," *IEEE Transactions on Smart Grid*, vol. 3, no. 4, pp. 1687–1694, 2012.
- [79] Le, Trung Dung and Petit, Marc, "Directional relays for distribution networks with distributed generation," in *11th IET International Conference on Developments in Power Systems Protection (DPSP 2012)*, (Birmingham), pp. 72–78, IET, 2012.
- [80] A. Pradhan, A. Routray, and S. M. Gudipalli, "Fault direction estimation in radial distribution system using phase change in sequence current," *IEEE Transactions on Power Delivery*, vol. 22, no. 4, pp. 2065–2071, 2007.
- [81] M. Eissa, "Current directional protection technique based on polarizing current," *International Journal of Electrical Power & Energy Systems*, vol. 44, no. 1, pp. 488–494, 2013.
- [82] A. v. C. Warrington, *Protective Relays: Their Theory and Practice Volume One*. Springer Science & Business Media, 2012.
- [83] J. Roberts and A. Guzman, "Directional element design and evaluation," in *proceedings of the 21st Annual Western Protective Relay Conference, Spokane, WA, 1994*.
- [84] J. B. Roberts and E. O. Schweitzer III, "Negative sequence directional element for a relay useful in protecting power transmission lines," Sept. 20 1994. US Patent 5,349,490.
- [85] J. B. John Appleyard, "Considerations in choosing directional polarizing methods for ground overcurrent elements in line protection applications: Technical report to the line protection subcommittee of the pes, power systems relaying committee completion date: May 2015 members," in *2017 70th Annual Conference for Protective Relay Engineers (CPRE)*, pp. 1–67, April 2017.
- [86] A. Guzman, J. Roberts, and D. Hou, "New ground directional elements operate reliably for changing system conditions," in *23rd Annual Western Protective Relay Conference, 1996*.
- [87] P. McLaren, G. Swift, Z. Zhang, E. Dirks, R. Jayasinghe, and I. Fernando, "A new directional element for numerical distance relays," *IEEE Transactions on Power Delivery*, vol. 10, no. 2, pp. 666–675, 1995.
- [88] T. Sidhu, H. Singh, and M. Sachdev, "Design, implementation and testing of an artificial neural network based fault direction discriminator for protecting transmission lines," *IEEE Transactions on Power Delivery*, vol. 10, no. 2, pp. 697–706, 1995.
- [89] M. Sanaye-Pasand and O. Malik, "Power transmission lines fault direction estimation using artificial neural networks," in *Proceedings of 1996 Canadian Conference on Electrical and Computer Engineering*, vol. 2, pp. 758–761, IEEE, 1996.

- [90] Gang, Wang and Jiali, He and Yao, Li and Xiaodan, Yu and Zhongpu, Liu, "Neural network application in directional comparison carrier protection of EHV transmission lines," in *APSCOM-97. International Conference on Advances in Power System Control, Operation and Management*, (Hong Kong), pp. 89–94, IET, 1997.
- [91] Y.H. Song; A.T. Johns ; Q.Y. Xuan ; J.Y. Liu, "Generic algorithm based neural network applied to fault classification for EHV transmission lines with a UPFC," in *6th International Conference on Developments in Power Systems Protection*, (Nottingham), pp. 278–281, IET, 1997.
- [92] A. O. Fernandez and N. K. I. Ghonaim, "A novel approach using a firann for fault detection and direction estimation for high-voltage transmission lines," *IEEE Transactions on Power Delivery*, vol. 17, no. 4, pp. 894–900, 2002.
- [93] U. Lahiri, A. Pradhan, and S. Mukhopadhyaya, "Modular neural network-based directional relay for transmission line protection," *IEEE Transactions on Power Systems*, vol. 20, no. 4, pp. 2154–2155, 2005.
- [94] A. Yadav and A. Swetapadma, "Improved first zone reach setting of artificial neural network-based directional relay for protection of double circuit transmission lines," *IET Generation, Transmission & Distribution*, vol. 8, no. 3, pp. 373–388, 2013.
- [95] A. G. Phadke and J. S. Thorp, *Computer relaying for power systems*. Wiley Online Library, 2009.
- [96] W. A. Elmore, *Protective relaying: theory and applications*, vol. 1. CRC press, 2003.
- [97] R. Lavorin, D. Hou, H. J. Altuve, N. Fischer, and F. Calero, "Selecting directional elements for impedance-grounded distribution systems," in *proceedings of the 34th Annual Western Protective Relay Conference, Spokane, WA*, 2007.
- [98] J. Roberts, H. J. Altuve, and D. Hou, "Review of ground fault protection methods for grounded ungrounded and compensated distribution systems," *USA, SEL*, pp. 1–40, 2001.
- [99] E. Sortomme, J. Ren, and S. Venkata, "A differential zone protection scheme for microgrids," in *2013 IEEE Power & Energy Society General Meeting*, pp. 1–5, IEEE, 2013.
- [100] B. Bak-Jensen, M. Browne, R. Calone, R. C. González, A. Craib, G. Donnart, D. Dumitrascu, M. Engel, R. Hanuš, H. Hoidalén, *et al.*, "Protection of distribution systems with distributed energy resources," *CIGRE*, 2015.
- [101] Ł. Huchel and H. H. Zeineldin, "Planning the coordination of directional overcurrent relays for distribution systems considering dg," *IEEE Transactions on Smart Grid*, vol. 7, no. 3, pp. 1642–1649, 2015.
- [102] H. Laaksonen, D. Ishchenko, and A. Oudalov, "Adaptive protection and microgrid control design for hailuoto island," *IEEE Transactions on Smart Grid*, vol. 5, no. 3, pp. 1486–1493, 2014.

- [103] M. A. Zamani, A. Yazdani, and T. S. Sidhu, "A communication-assisted protection strategy for inverter-based medium-voltage microgrids," *IEEE transactions on smart grid*, vol. 3, no. 4, pp. 2088–2099, 2012.
- [104] X. Liu, M. Shahidehpour, Z. Li, X. Liu, Y. Cao, and W. Tian, "Protection scheme for loop-based microgrids," *IEEE Transactions on Smart Grid*, vol. 8, no. 3, pp. 1340–1349, 2016.
- [105] M. Petit, X. Le Pivert, and L. Garcia-Santander, "Directional relays without voltage sensors for distribution networks with distributed generation: Use of symmetrical components," *Electric Power Systems Research*, vol. 80, no. 10, pp. 1222–1228, 2010.
- [106] T. D. Le and M. Petit, "Directional relays without voltage sensors for distribution grids: Optimal boundaries for fault direction estimation," in *2013 IEEE Grenoble Conference*, pp. 1–6, IEEE, 2013.
- [107] A. Hooshyar and R. Iravani, "A new directional element for microgrid protection," *IEEE Transactions on Smart Grid*, vol. 9, no. 6, pp. 6862–6876, 2017.
- [108] E. Muljadi, N. Samaan, V. Gevorgian, J. Li, and S. Pasupulati, "Short circuit current contribution for different wind turbine generator types," in *IEEE PES General Meeting*, pp. 1–8, IEEE, 2010.
- [109] V. Diedrichs, H. Lorenzen, I. Mackensen, and S. Gertjegerdes, "Asymmetrical current injection addressed by entso-e draft network code," in *Proc. Workshop on Large-Scale Integration of Wind Power into Power Systems as well as on Transmission Networks for Offshore Wind Farms*, 2012.
- [110] Q. Wang, N. Zhou, and L. Ye, "Fault analysis for distribution networks with current-controlled three-phase inverter-interfaced distributed generators," *IEEE Transactions on Power Delivery*, vol. 30, no. 3, pp. 1532–1542, 2015.
- [111] M. Castilla, J. Miret, A. Camacho, J. Matas, and L. G. de Vicuña, "Voltage support control strategies for static synchronous compensators under unbalanced voltage sags," *IEEE transactions on industrial electronics*, vol. 61, no. 2, pp. 808–820, 2013.
- [112] J. Schlabbach and I. of Electrical Engineers, *Short Circuit Currents (IEE Power and Energy Series; 51)*. Institution of Engineering and Technology-IET, 2005.
- [113] R. Marguet, *Improved fault localization method for electrical power distribution networks*. PhD thesis, Grenoble INP, Grenoble, France, 7 2015.
- [114] R. Yan and T. K. Saha, "Investigation of voltage imbalance due to distribution network unbalanced line configurations and load levels," *IEEE Transactions on Power Systems*, vol. 28, no. 2, pp. 1829–1838, 2012.
- [115] S. Chattopadhyay, M. Mitra, and S. Sengupta, "Electric power quality," in *Electric Power Quality*, pp. 5–12, Springer, 2011.

- [116] L. Schwartfeger, D. Santos-Martin, A. Wood, N. Watson, and A. Miller, "Review of distributed generation interconnection standards," in *The 2014 Electricity Engineers' Association Conference, At Auckland*, pp. 15–19, EEA, 2014.
- [117] "Recommended settings for voltage and frequency ride-through of distributed energy resources." <https://www.epri.com/#/pages/product/3002006203/?lang=en-US/>.
- [118] M. A. Zamani, T. S. Sidhu, and A. Yazdani, "A protection strategy and microprocessor-based relay for low-voltage microgrids," *IEEE transactions on Power Delivery*, vol. 26, no. 3, pp. 1873–1883, 2011.
- [119] R. Tumilty, M. Brucoli, G. Burt, and T. Green, "Approaches to network protection for inverter dominated electrical distribution systems," in *3rd IET International Conference on Power Electronics, Machines and Drives (PEMD 2006)*, (Dublin, Ireland), pp. 622–626, 2006.
- [120] Y. Han, X. Hu, and D. Zhang, "Study of adaptive fault current algorithm for microgrid dominated by inverter based distributed generators," in *The 2nd International Symposium on Power Electronics for Distributed Generation Systems*, pp. 852–854, IEEE, 2010.
- [121] H. Nikkhajoei and R. H. Lasseter, "Microgrid protection," in *2007 IEEE Power Engineering Society General Meeting*, pp. 1–6, IEEE, 2007.
- [122] K. O. Oureilidis and C. S. Demoulias, "A fault clearing method in converter-dominated microgrids with conventional protection means," *IEEE Transactions on Power Electronics*, vol. 31, no. 6, pp. 4628–4640, 2015.
- [123] A. Oudalov and A. Fidigatti, "Adaptive network protection in microgrids," *International Journal of Distributed Energy Resources*, vol. 5, no. 3, pp. 201–226, 2009.
- [124] T. S. Ustun, C. Ozansoy, and A. Ustun, "Fault current coefficient and time delay assignment for microgrid protection system with central protection unit," *IEEE Transactions on power systems*, vol. 28, no. 2, pp. 598–606, 2012.
- [125] P. Mahat, Z. Chen, B. Bak-Jensen, and C. L. Bak, "A simple adaptive overcurrent protection of distribution systems with distributed generation," *IEEE Transactions on Smart Grid*, vol. 2, no. 3, pp. 428–437, 2011.
- [126] M. H. Cintuglu, T. Ma, and O. A. Mohammed, "Protection of autonomous microgrids using agent-based distributed communication," *IEEE Transactions on Power Delivery*, vol. 32, no. 1, pp. 351–360, 2016.
- [127] M. Dewadasa, A. Ghosh, and G. Ledwich, "Fold back current control and admittance protection scheme for a distribution network containing distributed generators," *IET generation, transmission & distribution*, vol. 4, no. 8, pp. 952–962, 2010.
- [128] J. M. D. Dewadasa, *Protection of distributed generation interfaced networks*. PhD thesis, Queensland University of Technology, 2010.

- [129] W. Huang, T. Nengling, X. Zheng, C. Fan, X. Yang, and B. J. Kirby, "An impedance protection scheme for feeders of active distribution networks," *IEEE transactions on power delivery*, vol. 29, no. 4, pp. 1591–1602, 2014.
- [130] K. Skaloumpakas, J. C. Boemer, E. van Ruitenbeek, M. Gibescu, and M. A. M. M. van der Meijden, "Response of low voltage networks with high penetration of photovoltaic systems to transmission network faults," in *3rd Renewable Power Generation Conference (RPG 2014)*, pp. 1–6, Sep. 2014.
- [131] J. Miret, M. Castilla, A. Camacho, L. G. de Vicuña, and J. Matas, "Control scheme for photovoltaic three-phase inverters to minimize peak currents during unbalanced grid-voltage sags," *IEEE transactions on Power Electronics*, vol. 27, no. 10, pp. 4262–4271, 2012.
- [132] H. Laaksonen and K. Kauhaniemi, "Smart protection concept for lv microgrid," *International Review of Electrical Engineering*, vol. 5, no. 2, 2010.
- [133] H. J. Laaksonen, "Protection principles for future microgrids," *IEEE Transactions on Power Electronics*, vol. 25, no. 12, pp. 2910–2918, 2010.
- [134] J. Ma, C. Mi, T. Wang, J. Wu, and Z. Wang, "An adaptive protection scheme for distributed systems with distributed generation," in *2011 IEEE Power and Energy Society General Meeting*, pp. 1–6, IEEE, 2011.
- [135] K. Dang, X. He, D. Bi, and C. Feng, "An adaptive protection method for the inverter dominated microgrid," in *2011 International Conference on Electrical Machines and Systems*, pp. 1–5, IEEE, 2011.
- [136] S. Bukhari, R. Haider, M. Zaman, Y. Oh, G. Cho, M. Kim, J. Kim, and C. Kim, "Adaptive centralized protection scheme for microgrids based on positive sequence complex power," *IPST, Seoul, Republic of Korea*, 2017.
- [137] A. Gupta, A. Varshney, O. G. Swathika, and S. Hemamalini, "Dual simplex algorithm aided adaptive protection of microgrid," in *2015 International Conference on Computational Intelligence and Communication Networks (CICN)*, pp. 1505–1509, IEEE, 2015.
- [138] A. Hussain and H.-M. Kim, "A hybrid framework for adaptive protection of microgrids based on iec 61850," *International Journal of Smart Home*, vol. 10, no. 5, pp. 285–296, 2016.
- [139] H. Muda and P. Jena, "Superimposed adaptive sequence current based microgrid protection: a new technique," *IEEE Transactions on Power Delivery*, vol. 32, no. 2, pp. 757–767, 2016.
- [140] V. A. Papaspiliotopoulos, G. N. Korres, and N. D. Hatziargyriou, "Protection coordination in modern distribution grids integrating optimization techniques with adaptive relay setting," in *2015 IEEE Eindhoven PowerTech*, pp. 1–6, IEEE, 2015.

- [141] Y. Ates, A. R. Boynuegri, M. Uzunoglu, A. Nadar, R. Yumurtacı, O. Erdinc, N. G. Paterakis, and J. P. Catalão, "Adaptive protection scheme for a distribution system considering grid-connected and islanded modes of operation," *Energies*, vol. 9, no. 5, p. 378, 2016.
- [142] M. K. Singh and P. N. Reddy, "A fast adaptive protection scheme for distributed generation connected networks with necessary relay coordination," in *2013 Students Conference on Engineering and Systems (SCES)*, pp. 1–5, IEEE, 2013.
- [143] Y. Ates, M. Uzunoglu, A. Karakas, A. R. Boynuegri, A. Nadar, and B. Dag, "Implementation of adaptive relay coordination in distribution systems including distributed generation," *Journal of Cleaner Production*, vol. 112, pp. 2697–2705, 2016.
- [144] H. Muda and P. Jena, "Real time simulation of new adaptive overcurrent technique for microgrid protection," in *2016 National Power Systems Conference (NPSC)*, pp. 1–6, IEEE, 2016.
- [145] M. N. Alam, S. Chakrabarti, A. Sharma, and S. C. Srivastava, "An adaptive protection scheme for ac microgrids using μ pmu based topology processor," in *2019 IEEE International Conference on Environment and Electrical Engineering and 2019 IEEE Industrial and Commercial Power Systems Europe (EEEIC/I&CPS Europe)*, pp. 1–6, IEEE, 2019.
- [146] M. S. Elbana, N. Abbasy, A. Meghed, and N. Shaker, " μ pmu-based smart adaptive protection scheme for microgrids," *Journal of Modern Power Systems and Clean Energy*, vol. 7, no. 4, pp. 887–898, 2019.
- [147] E. Sortomme, S. Venkata, and J. Mitra, "Microgrid protection using communication-assisted digital relays," *IEEE Transactions on Power Delivery*, vol. 25, no. 4, pp. 2789–2796, 2009.
- [148] M. Dewadasa, A. Ghosh, and G. Ledwich, "Protection of microgrids using differential relays," in *AUPEC 2011*, pp. 1–6, IEEE, 2011.
- [149] S. Samantaray, G. Joos, and I. Kamwa, "Differential energy based microgrid protection against fault conditions," in *2012 IEEE PES Innovative Smart Grid Technologies (ISGT)*, pp. 1–7, IEEE, 2012.
- [150] T. S. Ustun, C. Ozansoy, and A. Zayegh, "Differential protection of microgrids with central protection unit support," in *IEEE 2013 Tencon-Spring*, pp. 15–19, IEEE, 2013.
- [151] R. H. Khan, T. S. Ustun, and J. Y. Khan, "Differential protection of microgrids over a wimax network," in *2013 IEEE International Conference on Smart Grid Communications (SmartGridComm)*, pp. 732–737, IEEE, 2013.
- [152] T. S. Ustun and R. H. Khan, "Multiterminal hybrid protection of microgrids over wireless communications network," *IEEE Transactions on Smart Grid*, vol. 6, no. 5, pp. 2493–2500, 2015.

- [153] S. Kar, S. Samantaray, and M. D. Zadeh, "Data-mining model based intelligent differential microgrid protection scheme," *IEEE Systems Journal*, vol. 11, no. 2, pp. 1161–1169, 2015.
- [154] N. Perera and A. Rajapakse, "Agent-based protection scheme for distribution networks with distributed generators," in *2006 IEEE Power Engineering Society General Meeting*, pp. 6–pp, IEEE, 2006.
- [155] T. Kato, H. Kanamori, Y. Suzuoki, and T. Funabashi, "Multi-agent based control and protection of power distributed system-protection scheme with simplified information utilization," in *Proceedings of the 13th International Conference on, Intelligent Systems Application to Power Systems*, pp. 49–54, IEEE, 2005.
- [156] Z. Xiangjun, K. Li, W. Chan, and S. Sheng, "Multi-agents based protection for distributed generation systems," in *2004 IEEE International Conference on Electric Utility Deregulation, Restructuring and Power Technologies. Proceedings*, vol. 1, pp. 393–397, IEEE, 2004.
- [157] J. M. Dewadasa, A. Ghosh, and G. Ledwich, "Distance protection solution for a converter controlled microgrid," in *Proceedings of the 15th National Power Systems Conference*, 2008.
- [158] S. Voima and K. Kauhaniemi, "Using distance protection in smart grid environment," in *IEEE PES innovative smart grid technologies, Europe*, pp. 1–6, IEEE, 2014.
- [159] H. Laaksonen, "Technical solutions for low-voltage microgrid concept," *Acta Wasaensia*, vol. 241, p. 251, 2011.
- [160] "Distribution systems and protection against indirect contact and earth fault." <http://www04.abb.com/global/seitp/seitp202.nsf/0/5bddbcb7217300a6c125761f004f9837/\protect\T1\textdollarfile/Vol.3.pdf/>.
- [161] A. Zamani, T. Sidhu, and A. Yazdani, "A strategy for protection coordination in radial distribution networks with distributed generators," in *IEEE PES General Meeting*, pp. 1–8, IEEE, 2010.
- [162] I. E. Commission *et al.*, "IEC 60364-4-41: 2017 Low-voltage electrical installations—Part 4-41: Protection for safety—Protection against electric shock," 2017.
- [163] A. F. Elneweihi, "Useful applications for negative-sequence overcurrent relaying," in *22nd Annual Western Protective Relay Conference, Spokane, Washington, October*, pp. 24–26, 1995.
- [164] A. Elneweihi, E. Schweitzer, and M. Feltis, "Negative-sequence overcurrent element application and coordination in distribution protection," *IEEE Transactions on Power Delivery*, vol. 8, no. 3, pp. 915–924, 1993.
- [165] L. Xu, M.-Y. Chow, J. Timmis, and L. S. Taylor, "Power distribution outage cause identification with imbalanced data using artificial immune recognition system

- (airs) algorithm," *IEEE Transactions on Power Systems*, vol. 22, no. 1, pp. 198–204, 2007.
- [166] E. Senger, G. Manassero, C. Goldemberg, and E. Pellini, "Automated Fault Location System for Primary Distribution Networks," *IEEE Transactions on Power Delivery*, vol. 20, pp. 1332–1340, apr 2005.
- [167] R. Salim, M. Resener, A. Filomena, K. Rezende Caino de Oliveira, and A. Bretas, "Extended Fault-Location Formulation for Power Distribution Systems," *IEEE Transactions on Power Delivery*, vol. 24, pp. 508–516, apr 2009.
- [168] S. Das, N. Karnik, and S. Santoso, "Distribution Fault-Locating Algorithms Using Current Only," *IEEE Transactions on Power Delivery*, vol. 27, pp. 1144–1153, jul 2012.
- [169] M. Majidi and M. Etezadi-Amoli, "A New Fault Location Technique in Smart Distribution Networks Using Synchronized/Nonsynchronized Measurements," *IEEE Transactions on Power Delivery*, vol. 33, pp. 1358–1368, jun 2018.
- [170] H. Hizman, P. A. Crossley, P. F. Gale, and G. Bryson, "Fault section identification and location on a distribution feeder using travelling waves," in *IEEE Power Engineering Society Summer Meeting*, vol. 3, pp. 1107–1112 vol.3, July 2002.
- [171] A. Dwivedi and X. Yu, "Fault location in radial distribution lines using travelling waves and network theory," in *2011 IEEE International Symposium on Industrial Electronics*, pp. 1051–1056, June 2011.
- [172] M. El-Hami, L. L. Lai, D. J. Daruvala, and A. T. Johns, "A new travelling-wave based scheme for fault detection on overhead power distribution feeders," *IEEE Transactions on Power Delivery*, vol. 7, pp. 1825–1833, Oct 1992.
- [173] D. P. Coggins, D. W. P. Thomas, B. R. Hayes-Gill, Y. Zhu, E. T. Pereirat, and S. H. L. Cabral, "A new high speed fpga based travelling wave fault recorder for mv distribution systems," in *2008 IET 9th International Conference on Developments in Power System Protection (DPSP 2008)*, pp. 579–583, March 2008.
- [174] C. Teo and H. Gooi, "Artificial intelligence in diagnosis and supply restoration for a distribution network," *IEE Proceedings-Generation, Transmission and Distribution*, vol. 145, no. 4, pp. 444–450, 1998.
- [175] J. d. Souza, M. Rodrigues, M. T. Schilling, and M. B. Do Coutto Filho, "Fault location in electrical power systems using intelligent systems techniques," *IEEE Transactions on power delivery*, vol. 16, no. 1, pp. 59–67, 2001.
- [176] H. Zayandehroodi, A. Mohamed, H. Shareef, and M. Mohammadjafari, "Performance comparison of mlp and rbf neural networks for fault location in distribution networks with dgs," in *2010 IEEE International Conference on Power and Energy*, pp. 341–345, Nov 2010.
- [177] F. Dehghani and H. Nezami, "A new fault location technique on radial distribution systems using artificial neural network," in *22nd International Conference and Exhibition on Electricity Distribution (CIRED 2013)*, pp. 1–4, June 2013.

- [178] D. Thukaram, H. P. Khincha, and H. P. Vijaynarasimha, "Artificial neural network and support vector machine approach for locating faults in radial distribution systems," *IEEE Transactions on Power Delivery*, vol. 20, pp. 710–721, April 2005.
- [179] M. U. Usman, J. Ospina, and M. O. Faruque, "Fault classification and location identification in a smart distribution network using ann," in *2018 IEEE Power Energy Society General Meeting (PESGM)*, pp. 1–6, Aug 2018.
- [180] P. Ray and D. Mishra, "Artificial intelligence based fault location in a distribution system," in *2014 International Conference on Information Technology*, pp. 18–23, Dec 2014.
- [181] F. S. V. Petite, R. Caneloi dos Santos, and P. T. L. Asano, "A scheme based on anns for single-phase fault location in distribution systems with dg," in *2017 IEEE Manchester PowerTech*, pp. 1–6, June 2017.
- [182] P. Ray, D. P. Mishra, and D. D. Panda, "Hybrid technique for fault location of a distribution line," in *2015 Annual IEEE India Conference (INDICON)*, pp. 1–6, Dec 2015.
- [183] P. H. A. Barra, A. L. d. S. Pessoa, T. S. Menezes, G. G. Santos, D. V. Coury, and M. Oleskovicz, "Fault location in radial distribution networks using ann and superimposed components," in *2019 IEEE PES Innovative Smart Grid Technologies Conference - Latin America (ISGT Latin America)*, pp. 1–6, Sep. 2019.
- [184] A. Zidan, M. Khairalla, A. M. Abdrabou, T. Khalifa, K. Shaban, A. Abdrabou, R. El Shatshat, and A. M. Gaouda, "Fault Detection, Isolation, and Service Restoration in Distribution Systems: State-of-the-Art and Future Trends," *IEEE Transactions on Smart Grid*, vol. 8, pp. 2170–2185, sep 2017.
- [185] M. J. Ghorbani, M. A. Choudhry, and A. Feliachi, "A multiagent design for power distribution systems automation," *IEEE Transactions on Smart Grid*, vol. 7, no. 1, pp. 329–339, 2015.
- [186] J. Ghorbani, M. A. Choudhry, and A. Feliachi, "Fault location and isolation using multi agent systems in power distribution systems with distributed generation sources," in *2013 IEEE PES Innovative Smart Grid Technologies Conference (ISGT)*, pp. 1–6, IEEE, 2013.
- [187] G. Zhabelova and V. Vyatkin, "Multiagent smart grid automation architecture based on iec 61850/61499 intelligent logical nodes," *IEEE Transactions on Industrial Electronics*, vol. 59, no. 5, pp. 2351–2362, 2011.
- [188] P. Jamborsalamati, A. Sadu, F. Ponci, and A. Monti, "Implementation of an agent based distributed flisr algorithm using iec 61850 in active distribution grids," in *2015 International Conference on Renewable Energy Research and Applications (ICR-ERA)*, pp. 606–611, IEEE, 2015.

- [189] A. Dede, D. Della Giustina, F. Franzoni, and A. Pegoiani, "Iec 61850-based logic selectivity scheme for the mv distribution network," in *2014 IEEE International Workshop on Applied Measurements for Power Systems Proceedings (AMPS)*, pp. 1–5, IEEE, 2014.
- [190] V. A. Papaspiliotopoulos, G. N. Korres, V. A. Kleftakis, and N. D. Hatzargyriou, "Hardware-in-the-loop design and optimal setting of adaptive protection schemes for distribution systems with distributed generation," *IEEE Transactions on Power Delivery*, vol. 32, no. 1, pp. 393–400, 2015.
- [191] L. Montoya, D. Montenegro, and G. Ramos, "Adaptive protection testbed using real time and hardware-in-the-loop simulation," in *2013 IEEE Grenoble Conference*, pp. 1–4, IEEE, 2013.
- [192] A. Music and S. Gagula-Palalic, "Classification of leaf type using multilayer perceptron, naive bayes and support vector machine classifiers," *Southeast Europe Journal of Soft Computing*, vol. 5, no. 2, 2016.
- [193] R. Rojas, *Neural networks: a systematic introduction*. Springer Science & Business Media, 2013.
- [194] M. U. Usman, J. Ospina, and M. O. Faruque, "Fault classification and location identification in a smart distribution network using ann," in *2018 IEEE Power & Energy Society General Meeting (PESGM)*, pp. 1–6, IEEE, 2018.
- [195] W. Rebizant, J. Szafran, and A. Wiszniewski, *Digital signal processing in power system protection and control*. Springer Science & Business Media, 2011.
- [196] Y. Shoham and K. Leyton-Brown, *Multiagent systems: Algorithmic, game-theoretic, and logical foundations*. Cambridge University Press, 2008.
- [197] A. Kantamneni, L. E. Brown, G. Parker, and W. W. Weaver, "Survey of multi-agent systems for microgrid control," *Engineering applications of artificial intelligence*, vol. 45, pp. 192–203, 2015.
- [198] T. L. Nguyen, *Agent-based distributed control and optimization in microgrids with Hardware-in-the-Loop implementation*. PhD thesis, Université Grenoble Alpes, 2019.
- [199] R. E. Mackiewicz, "Overview of iec 61850 and benefits," in *2006 IEEE Power Engineering Society General Meeting*, pp. 8–pp, IEEE, 2006.
- [200] A. Saleem, N. Honeth, and L. Nordström, "A case study of multi-agent interoperability in iec 61850 environments," in *2010 IEEE PES Innovative Smart Grid Technologies Conference Europe (ISGT Europe)*, pp. 1–8, IEEE, 2010.
- [201] R. E. Brown, *Electric power distribution reliability*. CRC press, 2017.
- [202] N. A. Luu, *Control and management strategies for a microgrid*. PhD thesis, Grenoble INP, Grenoble, 12 2014.

- [203] L. Tao; and C. Schwaegerl, "Advanced architecture and control concepts for more microgrids," *EC Project, Tech. Rep. SES6-019864, Tech. Rep.*, vol. 2, no. 1, pp. 1–145, 2009.
- [204] P. Palensky, A. A. Van Der Meer, C. D. Lopez, A. Joseph, and K. Pan, "Cosimulation of intelligent power systems: Fundamentals, software architecture, numerics, and coupling," *IEEE Industrial Electronics Magazine*, vol. 11, no. 1, pp. 34–50, 2017.
- [205] "Remote procedure call in operating system." <https://www.geeksforgeeks.org/remote-procedure-call-rpc-in-operating-system/>.
- [206] M. Stojkov, S. Nikolovski, and V. Mikulicic, "Estimation of electrical energy not supplied in reliability analysis of distribution networks," in *Proceedings of the 12th IEEE Mediterranean Electrotechnical Conference (IEEE Cat. No. 04CH37521)*, vol. 3, pp. 967–970, IEEE, 2004.
- [207] M. O. Faruque, T. Strasser, G. Lauss, V. Jalili-Marandi, P. Forsyth, C. Dufour, V. Dinavahi, A. Monti, P. Kotsampopoulos, J. A. Martinez, *et al.*, "Real-time simulation technologies for power systems design, testing, and analysis," *IEEE Power and Energy Technology Systems Journal*, vol. 2, no. 2, pp. 63–73, 2015.
- [208] P. Rioual, H. Pouliquen, and J.-P. Louis, "Regulation of a pwm rectifier in the unbalanced network state using a generalized model," *IEEE Transactions on Power Electronics*, vol. 11, no. 3, pp. 495–502, 1996.
- [209] M. E. Baran and I. El-Markaby, "Fault analysis on distribution feeders with distributed generators," *IEEE transactions on power systems*, vol. 20, no. 4, pp. 1757–1764, 2005.
- [210] P. Pillay and M. Manyage, "Definitions of voltage unbalance," *IEEE Power Engineering Review*, vol. 21, no. 5, pp. 50–51, 2001.
- [211] P. M. Anderson and P. M. Anderson, *Analysis of faulted power systems*, vol. 445. IEEE press New York, 1995.
- [212] H. A. Ferrer, I. D. Verduzco, and E. V. Martinez, "Fourier and walsh digital filtering algorithms for distance protection," *IEEE Transactions on power systems*, vol. 11, no. 1, pp. 457–462, 1996.
- [213] G. Benmouyal and J. Roberts, "Superimposed quantities: Their true nature and application in relays," in *Proceedings of the 26th Annual Western Protective Relay Conference, Spokane, WA*, 1999.
- [214] S. M. Brahma and A. A. Girgis, "Microprocessor-based reclosing to coordinate fuse and recloser in a system with high penetration of distributed generation," in *2002 IEEE Power Engineering Society Winter Meeting. Conference Proceedings (Cat. No. 02CH37309)*, vol. 1, pp. 453–458, IEEE, 2002.
- [215] J. Blair, G. Hataway, and T. Mattson, "Solutions to common distribution protection challenges," in *2018 IEEE Rural Electric Power Conference (REPC)*, pp. 81–91, IEEE, 2018.

- [216] S. Santoso and T. A. Short, "Identification of fuse and recloser operations in a radial distribution system," *IEEE transactions on power delivery*, vol. 22, no. 4, pp. 2370–2377, 2007.
- [217] E. O. Schweitzer, M. W. Feltis, and A. Einweih, "Improved sensitivity and security for distribution bus and feeder relays," in *IEEE WESCANEX 93 Communications, Computers and Power in the Modern Environment-Conference Proceedings*, pp. 337–339, IEEE, 1993.

Appendix A

Model parameters

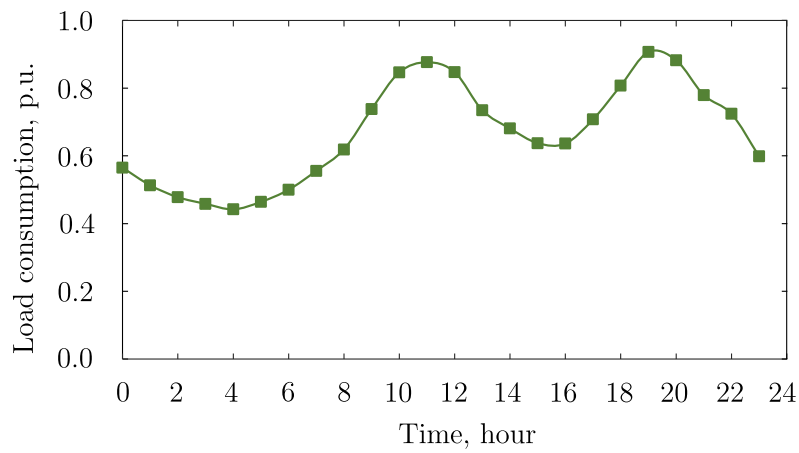


Figure A.1 – Load characteristic during a day

Table A.1 – Parameters required for modeling PV arrays in the study

Parameter	Symbol	Value	Unit
Open-circuit voltage at STC	$V_{oc,STC}$	43.8	V
Maximum voltage at STC	$V_{mpp,STC}$	35	V
Short-circuit current at STC	$I_{sc,STC}$	5	A
Maximum current at STC	$I_{mpp,STC}$	4.58	A
Temperature correction factor for voltage	α_v	-0.367	1/K
Temperature correction factor for current	α_i	0.043	1/K
Series resistance	R_S	0.33	Ω
Parallel resistance	R_P	389.9	Ω
Cell number per module	N_{cell}	96	PV cell
Number of modules in series per string	n_{series}	20	PV module
Number of strings in parallel per array	$n_{parallel}$	140	PV string

Table A.2 – Theoretical results of PV array modelling

Parameter	Symbol	Value	Unit
Maximum voltage	$V_{mpp,PV}$	578.16	V
Open-circuit voltage	$V_{oc,PV}$	876	V
Maximum current	$I_{mpp,PV}$	643.25	A
Short-circuit current	I_{shc}	700	A
Maximum output power	P_{mpp}	436.2	kW

Table A.3 – Parameters of the battery model

Parameter	Symbol	Value	Unit
State of charge	SOC	0.8	<i>p.u.</i>
Single cell capacity	C	60	Ah
Minimum voltage of empty cell	V_{min}	12	V
Maximum voltage of full charged cell	V_{max}	13.85	V
Number of cells connected in parallel	N_p	40	Cell
Number of cells connected in series	N_s	65	Cell
Nominal voltage of DC-voltage source	V_{nom}	0.9	V
Cell internal impedance	Z_i	0.001	Ω

Appendix B

PV modeling

B.1 Transformation from abc- to dual PS and NS dq-frames

Any unbalanced three-phase state variable in abc-frame, denoted by $\{v_a, v_b, v_c\}$, e.g. three-phase voltage $\{V_a, V_b, V_c\}$ or three-phase current $\{I_a, I_b, I_c\}$ can be described by the sum of two orthogonal symmetrical **Positive Sequence (PS)** and **Negative Sequence (NS)** components as, [208]:

$$v_{dq} = e^{j\omega t} v_{dq}^+ + e^{-j\omega t} v_{dq}^- \quad (\text{B.1})$$

$$v_{dq} = \frac{1}{3} \left(2v_a + e^{j\frac{2\pi}{3}} v_b + e^{j\frac{4\pi}{3}} v_b + e^{j\frac{2\pi}{3}} v_c + e^{j\frac{4\pi}{3}} v_c \right) \quad (\text{B.2})$$

$$v_{dq}^+ = v_d^+ + jv_q^+ \quad (\text{B.3})$$

$$v_{dq}^- = v_d^- + jv_q^- \quad (\text{B.4})$$

where the term with $e^{j\omega t}$ indicates the **PS** component, and the other with $e^{-j\omega t}$ represents the **NS** component; ω is the angular frequency, equal to $2\pi f$ where $f = 50, Hz$.

B.2 Formulation of PV equivalent sequence circuits

From Equations B.1, B.3 and B.4, we have known that any **PS** and **NS** variables can be derived from sequence components in dq-frame by:

$$v^+ = e^{j\omega t} v_{dq}^+ = e^{j\omega t} (v_d^+ + jv_q^+) \quad (\text{B.5})$$

$$v^- = e^{-j\omega t} v_{dq}^- = e^{-j\omega t} (v_d^- + jv_q^-) \quad (\text{B.6})$$

From Equations 2.28, B.5, and B.6, we have:

$$I_{dqref}^+ = \left(I_{dref}^+ + jI_{qref}^+ \right) = \frac{2}{3} \left(\frac{P_{ref}}{D} - j\frac{Q_{ref}}{G} \right) (V_d^+ + jV_q^+) \quad (\text{B.7})$$

$$I_{dqref}^- = \left(I_{dref}^- + jI_{qref}^- \right) = \frac{2}{3} \left(\frac{P_{ref}}{D} + j\frac{Q_{ref}}{G} \right) (V_d^- + jV_q^-) \quad (\text{B.8})$$

Based on these above equations, the coefficients D and G also can be rewritten as:

$$D = |V_{dq}^+|^2 + |V_{dq}^-|^2 = |e^{-2j\omega t}||V^+|^2 + |e^{2j\omega t}||V^-|^2 = |V^+|^2 + |V^-|^2 \quad (\text{B.9})$$

$$G = |V_{dq}^+|^2 - |V_{dq}^-|^2 = |e^{-2j\omega t}||V^+|^2 - |e^{2j\omega t}||V^-|^2 = |V^+|^2 - |V^-|^2 \quad (\text{B.10})$$

where V^+ and V^- are the **PS** and **NS** voltages at the Point of Common Coupling (PCC) of the considered PV system.

As a result, reference values of **PS** and **NS** currents can be obtained from I_{dqref}^+ and I_{dqref}^- as:

$$I_{ref}^+ = \frac{2}{3} \left(\frac{P_{ref}}{|V^+|^2 + |V^-|^2} - j \frac{Q_{ref}}{|V^+|^2 - |V^-|^2} \right) V^+ \quad (B.11)$$

$$I_{ref}^- = \frac{2}{3} \left(\frac{P_{ref}}{|V^+|^2 + |V^-|^2} + j \frac{Q_{ref}}{|V^+|^2 - |V^-|^2} \right) V^- \quad (B.12)$$

As indicted in [209], transient phase of PV fault currents can be nearly neglected in fault analysis due to the quick response of the current controller to sudden system changes. Thus, if we assume the actual values of the postfault PV active and reactive power are $P_{postfault}$ and $Q_{postfault}$ respectively, the sequence currents injected by the PV system during fault can be determined as:

$$I_{PV}^+ = \frac{2}{3} \left(\frac{P_{postfault}}{|V^+|^2 + |V^-|^2} - j \frac{Q_{postfault}}{|V^+|^2 - |V^-|^2} \right) V^+ = \frac{V^+}{Z_{PV}^+} \quad (B.13)$$

$$I_{PV}^- = \frac{2}{3} \left(\frac{P_{postfault}}{|V^+|^2 + |V^-|^2} + j \frac{Q_{postfault}}{|V^+|^2 - |V^-|^2} \right) V^- = \frac{V^-}{Z_{PV}^-} \quad (B.14)$$

where Z_{PV}^+ and Z_{PV}^- denote the virtual **PS** and **NS** impedances of the PV system respectively.

B.3 Equations of angles of PV fault sequence impedances

From Equations B.13 and B.14, Equations describing **PS** and **NS** impedances of PV system during fault can be determined as follows:

$$Z_{PV}^+ = \frac{V^+}{I_{PV}^+} = \frac{3}{2} \frac{(1 - \beta^4) [P_{postfault}(1 - \beta^2) + jQ_{postfault}(1 + \beta^2)]}{P_{postfault}^2(1 - \beta^2)^2 + Q_{postfault}^2(1 + \beta^2)^2} |V^+|^2 \quad (B.15)$$

$$Z_{PV}^- = \frac{V^-}{I_{PV}^-} = \frac{3}{2} \frac{(1 - \beta^4) [P_{postfault}(1 - \beta^2) - jQ_{postfault}(1 + \beta^2)]}{P_{postfault}^2(1 - \beta^2)^2 + Q_{postfault}^2(1 + \beta^2)^2} |V^+|^2 \quad (B.16)$$

where $\beta = |V^-|/|V^+|$ is voltage unbalance factor as defined in [210].

Based on Equations B.15 and B.16, one can gain the characteristic angle of PV **PS** and **NS** impedances, as follows:

$$\theta_{Z_{PV}^+} = \arctan \frac{Q_{postfault}(1 + \beta^2)}{P_{postfault}(1 - \beta^2)} \quad (B.17)$$

$$\theta_{Z_{PV}^-} = -\arctan \frac{Q_{postfault}(1 + \beta^2)}{P_{postfault}(1 - \beta^2)} \quad (B.18)$$

These above expressions reveal that the phase angles of **PS** and **NS** impedances of a PV system are completely defined by its postfault active and reactive powers and the unbalance level of the fault voltage. If we assume that prior to the fault, the voltage level at the PCC is well-regulated, i.e. $V_0 = 1$ in Equations 1.1b and 1.1c, so the PV system is not required to participate in static voltage support. In other words, the PV system injects no reactive power in normal operation, and therefore $I_{qpre-fault} = 0$. Hence, the postfault active and reactive powers can be defined by:

$$\left\{ \begin{array}{l} \left\{ \begin{array}{l} Q_{postfault} = 2(1-\gamma)\gamma S_n = aS_n \\ P_{postfault} = \sqrt{S_n^2 - Q_{postfault}^2} = \sqrt{1-a^2}S_n \end{array} \right. \quad \text{if } 0.5 \leq \gamma < 0.9 \quad (\text{B.19a}) \\ \left\{ \begin{array}{l} Q_{postfault} = S_n \\ P_{postfault} = 0 \end{array} \right. \quad \text{if } \gamma < 0.5 \quad (\text{B.19b}) \end{array} \right.$$

where $\gamma = V/V_n$ indicating the voltage drop level, $a = 2(1-\gamma)\gamma$, and $S_n = V_n I_n$ is the inverter nominal apparent power.

If we substitute for $P_{postfault}$ and $Q_{postfault}$ from Equations B.19a and B.19b to Equations B.17 and B.17, the final equations describing the phase angle characteristics of the PS and NS impedances of the considered PV system under unbalanced faults would be as follows:

$$\left\{ \begin{array}{l} \left\{ \begin{array}{l} \theta_{Z_{PV}^+} = \arctan \frac{(1+\beta^2)a}{(1-\beta^2)\sqrt{1-a^2}} \\ \theta_{Z_{PV}^-} = -\theta_{Z_{PV}^+} \end{array} \right. \quad \text{if } 0.5 \leq \gamma < 0.9 \quad (\text{B.20a}) \\ \left\{ \begin{array}{l} \theta_{Z_{PV}^+} = \frac{\pi}{2} \\ \theta_{Z_{PV}^-} = -\frac{\pi}{2} \end{array} \right. \quad \text{if } \gamma < 0.5 \quad (\text{B.20b}) \end{array} \right.$$

B.4 Equations of magnitudes of PV fault sequence impedances

From Equations B.13 and B.14, the magnitudes of PS and NS impedances of the PV system are similar and defined as:

$$|Z_{PV}^+| = |Z_{PV}^-| = \frac{3}{2} \frac{(1-\beta^4) |V^+|^2}{\sqrt{P_{postfault}^2 (1-\beta^2)^2 + Q_{postfault}^2 (1+\beta^2)^2}} \quad (\text{B.21})$$

By substituting for $P_{postfault}$ and $Q_{postfault}$ from Equations B.19a and B.19b to Equation B.21, we obtain the final express for $|Z_{PV}^+|$ and $|Z_{PV}^-|$ as:

$$\left\{ \begin{array}{l} |Z_{PV}^+| = |Z_{PV}^-| = \frac{3}{2} \frac{(1-\beta^4) |V^+|^2}{S_n \sqrt{1+2\beta^2(2a^2-1)+\beta^4}} \quad \text{if } 0.5 \leq \gamma < 0.9 \quad (\text{B.22a}) \\ |Z_{PV}^+| = |Z_{PV}^-| = \frac{3}{2} \frac{(1-\beta^4) |V^+|^2}{S_n (1+\beta^2)} \quad \text{if } \gamma < 0.5 \quad (\text{B.22b}) \end{array} \right.$$

As stated in Subsection 3.3.1, the sequence circuit of the PV system is opened to the Zero Sequence (ZS) current; thus, the voltage is a sum of only PS and NS voltages. Moreover, the NS voltage phasor is in the opposite direction with the PS one in case of single-phase-to-ground fault [211], thus:

$$V = V^+ + V^- = (1-\beta) V^+ \quad (\text{B.23})$$

Since $V = \gamma V_n$, we have:

$$|V^+| = \frac{\gamma}{1-\beta} V_n \quad (\text{B.24})$$

Finally, by substituting for $|V^+|$ from Equation B.24 to Equations B.22a and B.22b, formulae representing $|Z_{PV}^+|$ and $|Z_{PV}^-|$ are acquired as follows:

$$\left\{ \begin{array}{l} |Z_{PV}^+| = |Z_{PV}^-| = \frac{3}{2} \frac{(1 - \beta^4) \gamma^2 V_n^2}{S_n (1 - \beta)^2 \sqrt{1 + 2\beta^2(2a^2 - 1) + \beta^4}} \quad \text{if } 0.5 \leq \gamma < 0.9 \quad (\text{B.25a}) \\ |Z_{PV}^+| = |Z_{PV}^-| = \frac{3}{2} \frac{(1 + \beta) \gamma^2 V_n^2}{S_n (1 - \beta)} \quad \text{if } \gamma < 0.5 \quad (\text{B.25b}) \end{array} \right.$$

Appendix C

Signal processing and data measurement

C.1 Signal processing

In today digital relay technology, the needed signals are usually processed by using finite impulse response filters with sine and cosine windows [212]. The output signals of a pair of orthogonal FIR filters deploying full cycle sine and cosine windows can be computed from a series of input signals as [195]:

$$y_c[n] = \sum_{k=0}^{N-1} x[n-k] \cos \left[\left(\frac{N-1}{2} - k \right) \frac{2\pi}{N} \right] \quad (\text{C.1})$$

$$y_s[n] = \sum_{k=0}^{N-1} x[n-k] \sin \left[\left(\frac{N-1}{2} - k \right) \frac{2\pi}{N} \right] \quad (\text{C.2})$$

where $y_c[n]$ and $y_s[n]$ are output signals at n^{th} sample of cosine and sine filters, respectively, x are input signal samples; N is the number of samples within a data window equal to the number of samples per cycle, i.e. $N = \frac{f_s}{f}$, where f_s is the sampling rate and f is the fundamental electrical frequency.

C.2 Measurement of criterion values

If we have on disposal the output signals of the two cosine and sine filters, the magnitude and phase angle of the input signal can be obtained by [195]:

$$X_m[n] = \frac{2}{N} \sqrt{y_c[n]^2 + y_s[n]^2} \quad (\text{C.3})$$

$$\theta_X[n] = \arctan \left(\frac{y_c[n]}{y_s[n]} \right) + \left(1 - \frac{\pi}{N} \right) - \frac{2n\pi}{N} \quad (\text{C.4})$$

where X_m and θ_X is the magnitude and phase angle of the input signal.

Moreover, resistance and reactance can be derived from current and voltage input signals as:

$$R = \frac{u_c[n]i_c[n] + u_s[n]i_s[n]}{i_c[n]^2 + i_s[n]^2} \quad (\text{C.5})$$

$$X = \frac{u_s[n]i_c[n] - u_c[n]i_s[n]}{i_c[n]^2 + i_s[n]^2} \quad (\text{C.6})$$

where $u_c[n]$, $u_s[n]$, $i_c[n]$, and $i_s[n]$ are the orthogonal components of current and input signals determined by Equations C.1 and C.2.

C.3 Measurement of symmetrical sequence quantities

Studies related to unbalanced faults within power system normally necessitate the symmetrical components [211]. If orthogonal components of three-phase sinusoidal signals, such as current and voltage, are given then their symmetrical components can be represented by corresponding orthogonal quantities as:

$$\begin{bmatrix} x_c^+ \\ x_c^- \\ x_c^0 \end{bmatrix} = \frac{1}{3} \begin{bmatrix} 1 & 1 & 1 \\ 1 & a_R & a_R \\ 1 & a_R & a_R \end{bmatrix} \begin{bmatrix} x_{ac} \\ x_{bc} \\ x_{cc} \end{bmatrix} - \frac{1}{3} \begin{bmatrix} 0 & 0 & 0 \\ 0 & a_I & -a_I \\ 0 & -a_I & a_I \end{bmatrix} \begin{bmatrix} x_{as} \\ x_{bs} \\ x_{cs} \end{bmatrix} \quad (\text{C.7})$$

$$\begin{bmatrix} x_s^+ \\ x_s^- \\ x_s^0 \end{bmatrix} = \frac{1}{3} \begin{bmatrix} 1 & 1 & 1 \\ 1 & a_R & a_R \\ 1 & a_R & a_R \end{bmatrix} \begin{bmatrix} x_{as} \\ x_{bs} \\ x_{cs} \end{bmatrix} + \frac{1}{3} \begin{bmatrix} 0 & 0 & 0 \\ 0 & a_I & -a_I \\ 0 & -a_I & a_I \end{bmatrix} \begin{bmatrix} x_{ac} \\ x_{bc} \\ x_{cc} \end{bmatrix} \quad (\text{C.8})$$

where $a_R = 0.5$; $a_I = \frac{\sqrt{3}}{2}$; x_{ac} , x_{bc} , x_{cc} and x_{as} , x_{bs} , x_{cs} are orthogonal sets of the three-phase sinusoidal signals x_a , x_b , x_c , respectively.

Based on these above orthogonal components, magnitudes and phase angles of symmetrical components can be derived from Equations C.3 and C.4. Follow the same procedure, one can obtain the desired sequence impedance and its components, i.e. resistance and reactance.

Appendix D

Analysis of fault circuits containing PV systems

D.1 Superposition principle and superimposed quantities

Let assume a fault happening at F_{fwd} of Figure 3.1. The superposition theory for fault circuit analysis declares that a faulted network in Figure D.1a can be decomposed into two networks including pre-fault network, Figure D.1b, and superimposed network, Figure D.1c, [213]. Moreover, all the sources should be short-circuited in a superimposed network, and a driving voltage should be placed at the fault point. This voltage source should have a magnitude equal to the pre-fault voltage level at the fault location but with an opposite direction as represented in Figure D.1c.

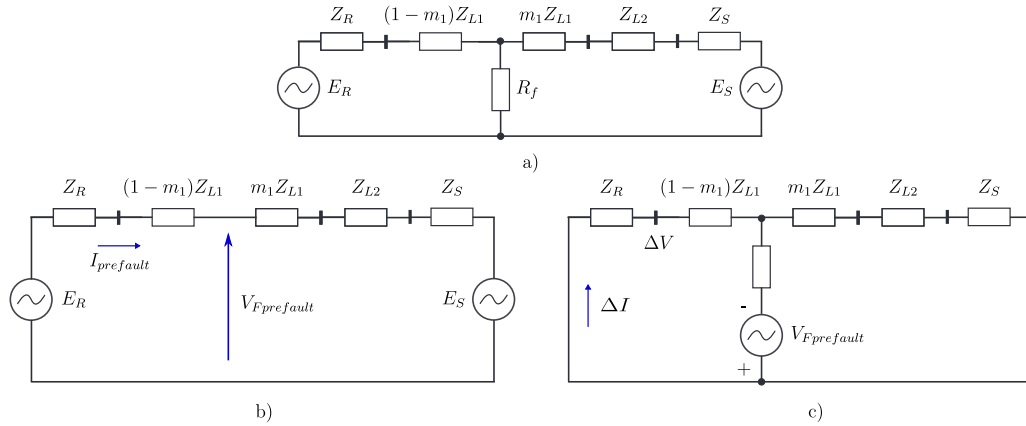


Figure D.1 – Superposition principle with (a) Faulted network, (b) Prefault network, and (c) Superimposed network

Consider a phase-A-to-ground fault at F_{fwd} of Figure 3.1, its pure-fault network is as shown in Figure 3.7a. From this Figure, we can state that all sequence voltage and currents are represented as superimposed quantities with prefix Δ . By using simple circuit transform and rearrangement, one can obtain the relationship between the pre-fault voltage at the fault point with the superimposed **Negative Sequence (NS)** current with ease. Nonetheless, the **NS** superimposed quantity is not of our interest but the **NS** one that can be derived from three-phase currents as:

$$I^- = I_A + a^2 I_B + a I_C \quad (D.1)$$

The superimposed NS current at fault is given as:

$$\Delta I^- = \Delta I_A + a^2 \Delta I_B + a \Delta I_C \quad (D.2)$$

The superimposed and sequence quantities relate to each other via the below expression:

$$I^- = \Delta I^- + I_{prefault}^- \quad (D.3)$$

If we assume that the pre-fault network is balanced, then the pre-fault **NS** load current can be canceled. As a result, the superimposed **NS** current obtained from the pure-fault network can be considered as the **NS** current measured by the DIR element. The proposed directional method, therefore, could be demonstrated by using only the pure-fault network provided in Figure 3.7.

D.2 Equivalent sequence circuits

Any unbalanced fault can be represented by using three-component method including **PS**, **NS**, and **ZS** circuits, [211]. Depending on the type of fault there is corresponding connection of these sequence circuits. Let us evaluate the way a equivalent diagram corresponding to each sequence circuit can be represented before stepping forward to the detailed analysis of each fault type.

D.2.1 PS equivalent circuit

The equivalent diagram of **PS** networks for a forward and reverse unbalanced fault of Figure 3.3 are provided in Figure D.2.

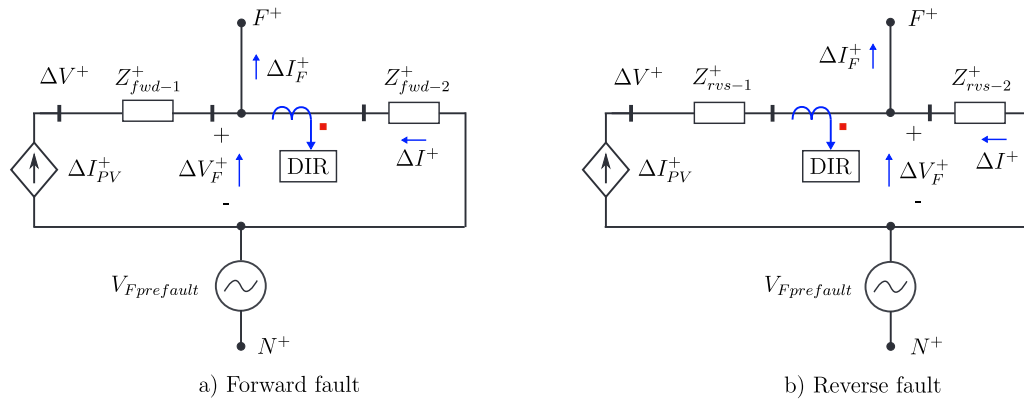


Figure D.2 – PS equivalent networks for an unsymmetrical fault

All the equivalent impedances involved in Figure D.2 are derived from those impedances in Figure 3.3 and defined as follows:

$$Z_{fwd-1}^+ = Z_{fwd-1}^- = Z_T + (1 - m_1)Z_{L1} \quad (D.4)$$

$$Z_{fwd-2}^+ = Z_{fwd-2}^+ = m_1 Z_{L1} + Z_{L2} + Z_S \quad (D.5)$$

$$Z_{rvs-1}^+ = Z_{rvs-1}^- = Z_T + Z_{L1} + m_2 Z_{L2} \quad (D.6)$$

$$Z_{rvs-2}^+ = Z_{rvs-2}^+ = (1 - m_2)Z_{L2} + Z_S \quad (D.7)$$

The necessary expressions of voltage and currents for forward and reverse faults for further analysis are also provided in Table D.1. For a forward fault, the directional element measures the **NS** current injected by the source, thus the **PS** current and voltage at the fault point should be represented via this sequence current. In contrast, for a reverse fault, the **PS** produced by the PV system should be the quantity describing all remaining current and voltage in the ultimate expression of the proposed impedance in Equation 3.11.

Table D.1 – Relationship between PS current and voltage quantities

Quantity	Forward fault	Reverse fault
c^+	$c_{fwd}^+ = (Z_{fwd-2}^+ + Z_{fwd-1}^+ + Z_{PV}^+) / (Z_{fwd-1}^+ + Z_{PV}^+)$	$c_{rvs}^+ = (Z_{rvs-2}^+ + Z_{rvs-1}^+ + Z_{PV}^+) / Z_{rvs-2}^+$
ΔI_F^+	$c_{fwd}^+ \Delta I^+$	$c_{rvs}^+ \Delta I_{PV}^+$
ΔV_F^+	$-Z_{fwd-2}^+ \Delta I^+$	$-(Z_{rvs-1}^+ + Z_{PV}^+) \Delta I_{PV}^+$

D.2.2 NS equivalent circuit

The equivalent diagram of NS networks for a forward and reverse unbalanced fault of Figure 3.3 are provided in Figure D.3.

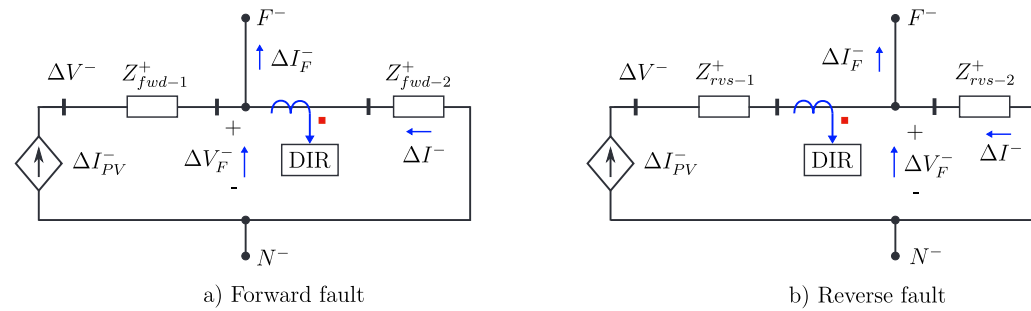


Figure D.3 – NS equivalent networks for an unsymmetrical fault

The necessary expressions of voltage and currents for forward and reverse faults for further analysis are also provided in Table D.2. For a forward fault, we need to represent the NS current and the voltage at the directional location through the NS current fed from the source side. In contrast, the NS current caused by the PV system should be only current left in the ultimate expression of the measured impedances.

Table D.2 – Relationship between NS current and voltage quantities

Quantity	Forward fault	Reverse fault
c^-	$c_{fwd}^- = (Z_{fwd-2}^+ + Z_{fwd-1}^+ + Z_{PV}^-) / (Z_{fwd-1}^+ + Z_{PV}^-)$	$c_{rvs}^- = (Z_{rvs-2}^+ + Z_{rvs-1}^+ + Z_{PV}^-) / Z_{rvs-2}^+$
ΔI_F^-	$c_{fwd}^+ \Delta I^-$	$c_{rvs}^+ \Delta I_{PV}^-$
ΔV_F^-	$-Z_{fwd-2}^+ \Delta I^-$	$-(Z_{rvs-1}^+ + Z_{PV}^-) \Delta I_{PV}^-$

D.2.3 ZS equivalent circuit

The ZS circuit is only included in the ground faults. Figure D.4 depicts the equivalent diagram of ZS networks for a ground fault of Figure 3.3. The necessary expressions of voltage and currents for forward and reverse faults for further analysis are also provided in Table D.3. Likewise, the NS voltage at the fault location should be represented by the corresponding NS current that flows through the Current Transformer (TCTR) of the directional element.

All the equivalent impedances involved in Figure D.4 are derived from those impedances in Figure 3.3 and defined as follows:

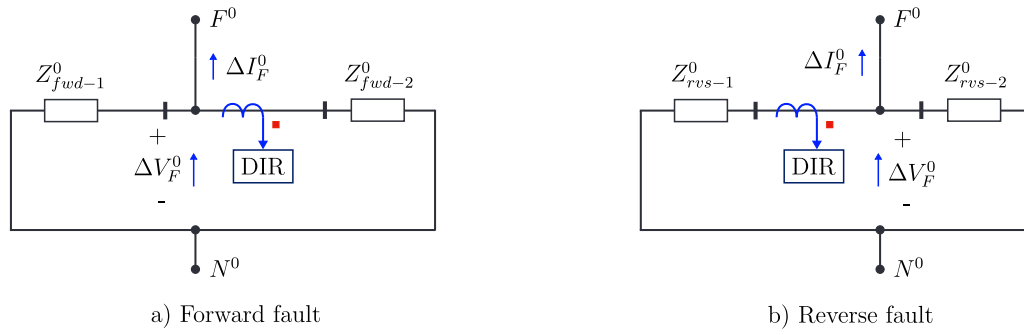


Figure D.4 – ZS equivalent networks for an earthed fault

$$Z_{fwd-1}^0 = Z_T + 3(1 - m_1)Z_{L1} \quad (D.8)$$

$$Z_{fwd-2}^0 = 3m_1Z_{L1} + 3Z_{L2} + 3Z_S \quad (D.9)$$

$$Z_{rvs-1}^0 = Z_T + 3Z_{L1} + 3m_2Z_{L2} \quad (D.10)$$

$$Z_{rvs-2}^0 = 3(1 - m_2)Z_{L2} + 3Z_S \quad (D.11)$$

Table D.3 – Relationship between NS current and ZS voltage

Quantity	Forward fault	Reverse fault
Z_{Σ}^0	$Z_{\Sigma fwd}^0 = Z_{fwd-1}^0 Z_{fwd-2}^0 / (Z_{fwd-1}^0 + Z_{fwd-2}^0)$	$Z_{\Sigma rvs}^0 = Z_{rvs-1}^0 Z_{rvs-2}^0 / (Z_{rvs-1}^0 + Z_{rvs-2}^0)$
ΔV_F^0	$-Z_{\Sigma fwd}^0 \Delta I_F^-$	$-Z_{\Sigma rvs}^0 \Delta I_F^-$

Appendix E

Evaluation results of the proposed DRIR method

E.1 Two-phase fault

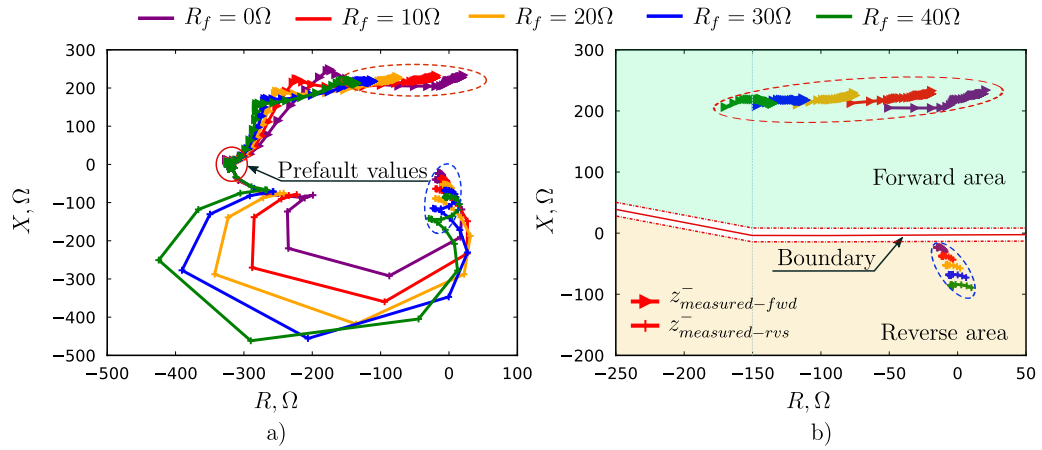


Figure E.1 – Evaluation results for two-phase fault with $R_f \in [0 : 40] \Omega$ with $P_{PV} = 20\%$, (a) entire trajectory in the R-X plane, and (b) a part zoomed in on R-axis with $R \in [-250 : 50] \Omega$

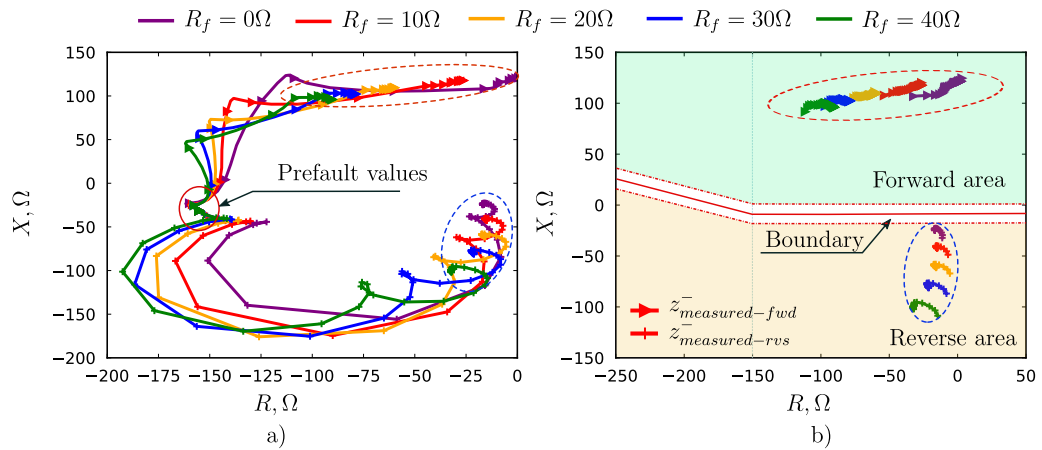


Figure E.2 – Evaluation results for two-phase fault with $R_f \in [0 : 40] \Omega$ with $P_{PV} = 40\%$, (a) entire trajectory in the R-X plane, and (b) a part zoomed in on R-axis with $R \in [-250 : 50] \Omega$

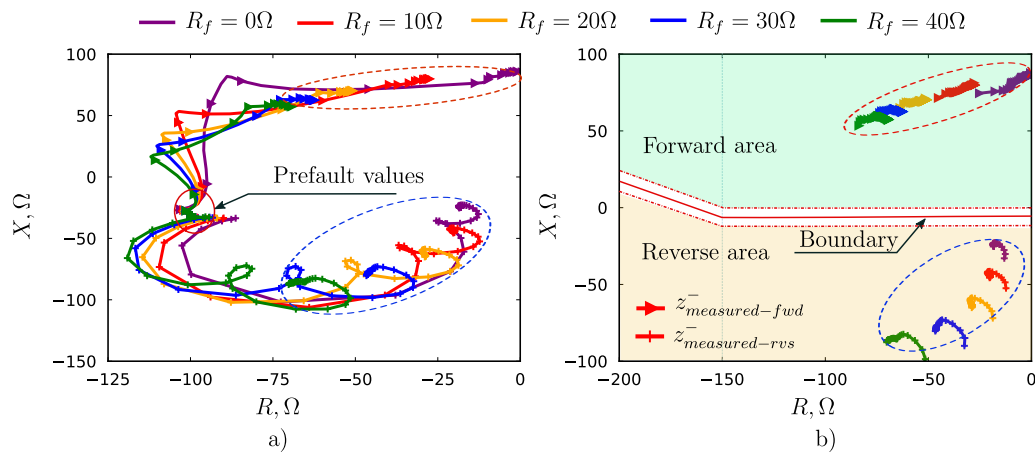


Figure E.3 – Evaluation results for two-phase fault with $R_f \in [0 : 40] \Omega$ with $P_{PV} = 60\%$, (a) entire trajectory in the R-X plane, and (b) a part zoomed in on R-axis with $R \in [-200 : 0] \Omega$

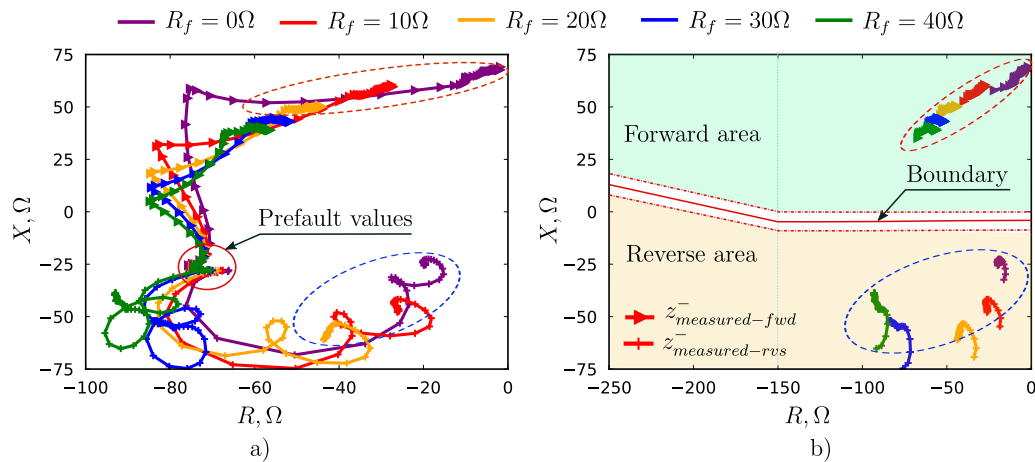


Figure E.4 – Evaluation results for two-phase fault with $R_f \in [0 : 40] \Omega$ with $P_{PV} = 80\%$, (a) entire trajectory in the R-X plane, and (b) a part zoomed in on R-axis with $R \in [-250 : 0] \Omega$

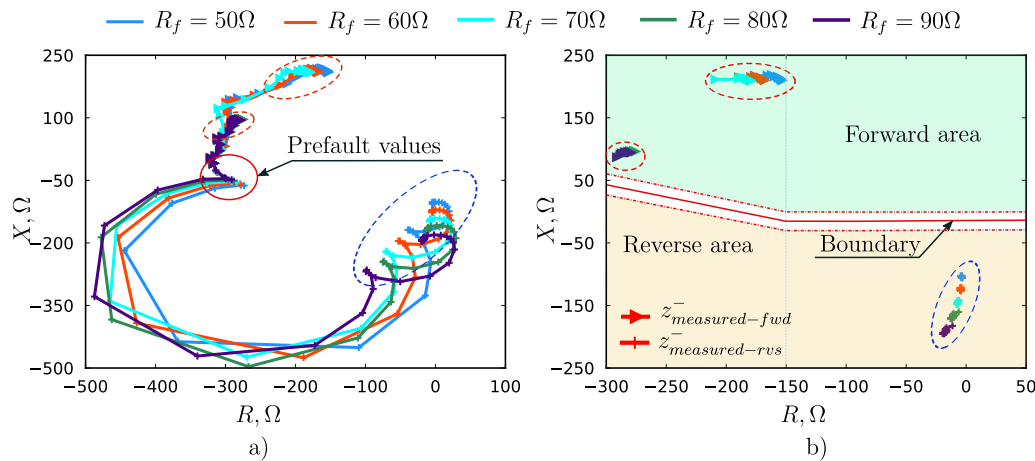


Figure E.5 – Evaluation results for two-phase fault with $R_f \in [50 : 90] \Omega$ with $P_{PV} = 40\%$, (a) entire trajectory in the R-X plane, and (b) a part zoomed in on R-axis with $R \in [-300 : 50] \Omega$

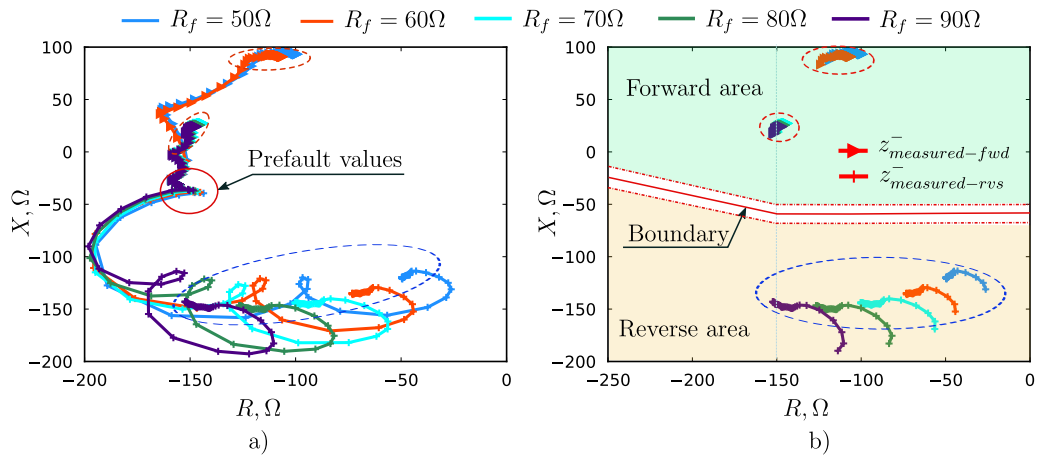


Figure E.6 – Evaluation results for two-phase fault with $R_f \in [50 : 90] \Omega$ with $P_{PV} = 40\%$, (a) entire trajectory in the R-X plane, and (b) a part zoomed in on R-axis with $R \in [-250 : 0] \Omega$

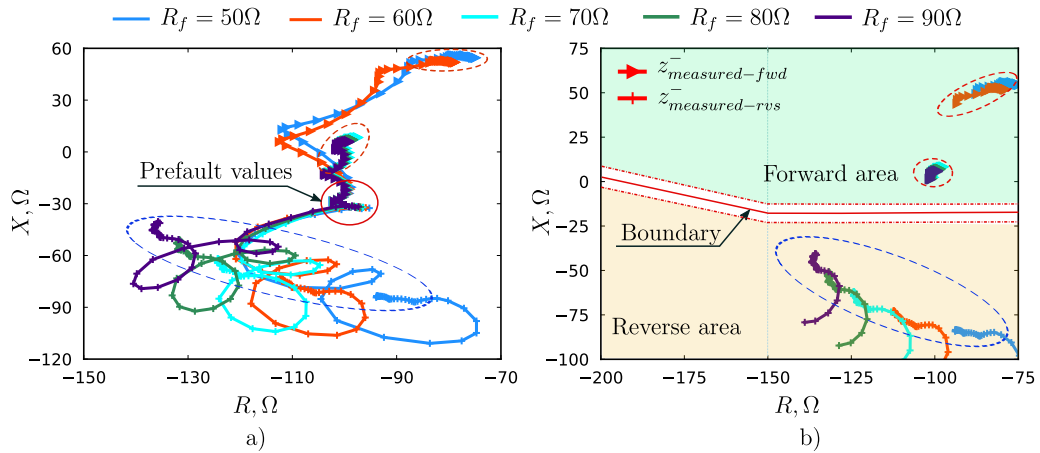


Figure E.7 – Evaluation results for two-phase fault with $R_f \in [50 : 90] \Omega$ with $P_{PV} = 60\%$, (a) entire trajectory in the R-X plane, and (b) a part zoomed in on R-axis with $R \in [-200 : -75] \Omega$

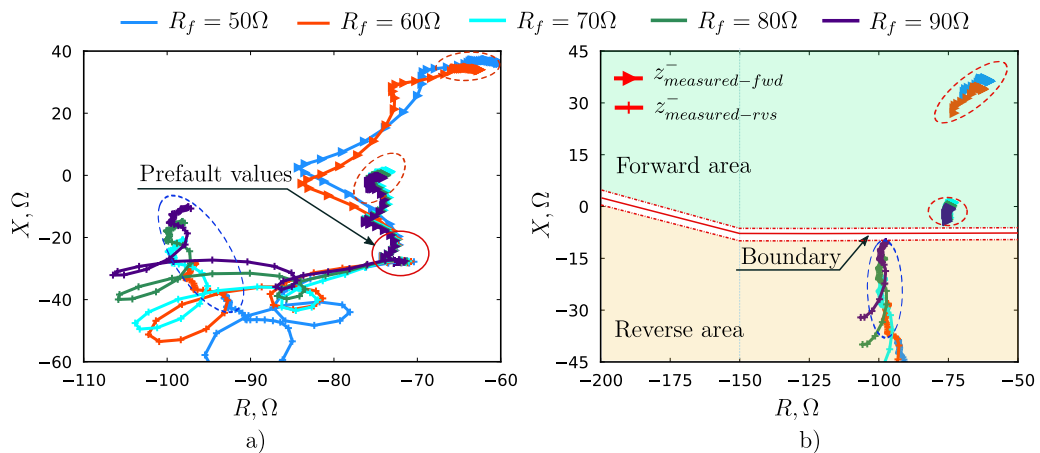


Figure E.8 – Evaluation results for two-phase fault with $R_f \in [50 : 90] \Omega$ with $P_{PV} = 80\%$, (a) entire trajectory in the R-X plane, and (b) a part zoomed in on R-axis with $R \in [-200 : -50] \Omega$

E.2 Two-phase-to-ground fault

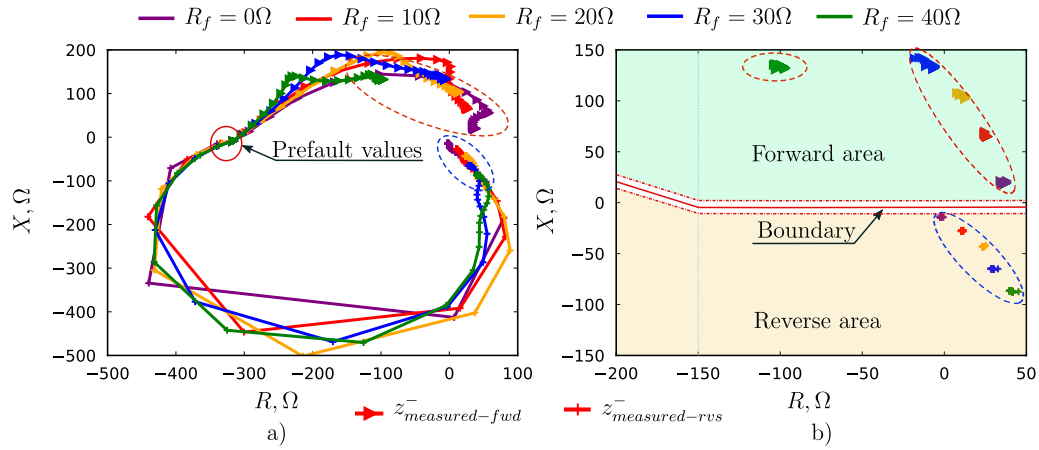


Figure E.9 – Evaluation results for two-phase-ground fault with $R_f \in [0 : 40] \Omega$ with $P_{PV} = 20\%$, (a) entire trajectory in the R-X plane, and (b) a part zoomed in on R-axis with $R \in [-250 : 50] \Omega$

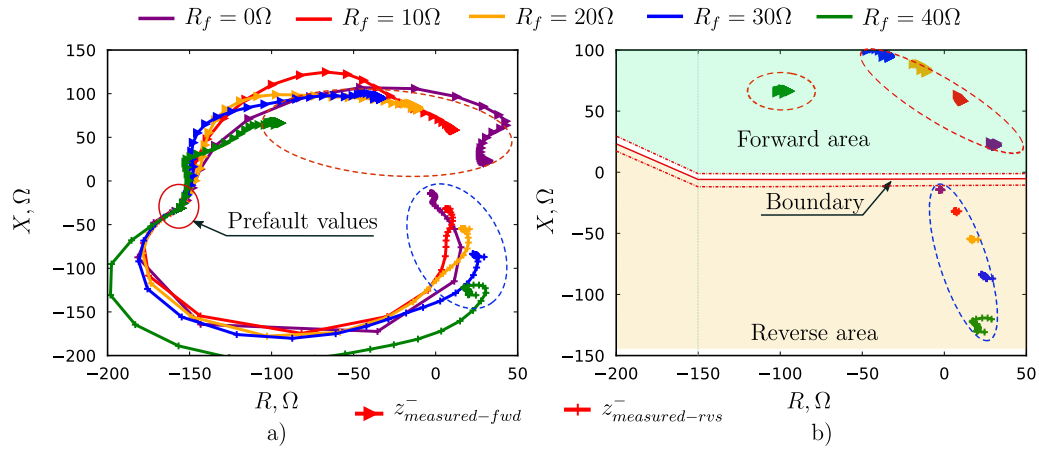


Figure E.10 – Evaluation results for two-phase-ground fault with $R_f \in [0 : 40] \Omega$ with $P_{PV} = 40\%$, (a) entire trajectory in the R-X plane, and (b) a part zoomed in on R-axis with $R \in [-250 : 50] \Omega$

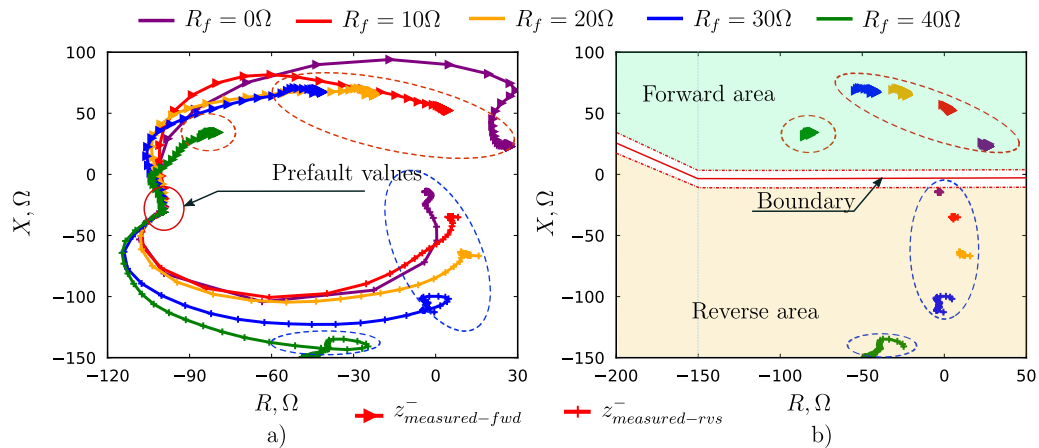


Figure E.11 – Evaluation results for two-phase-ground fault with $R_f \in [0 : 40] \Omega$ with $P_{PV} = 60\%$, (a) entire trajectory in the R-X plane, and (b) a part zoomed in on R-axis with $R \in [-250 : 50] \Omega$

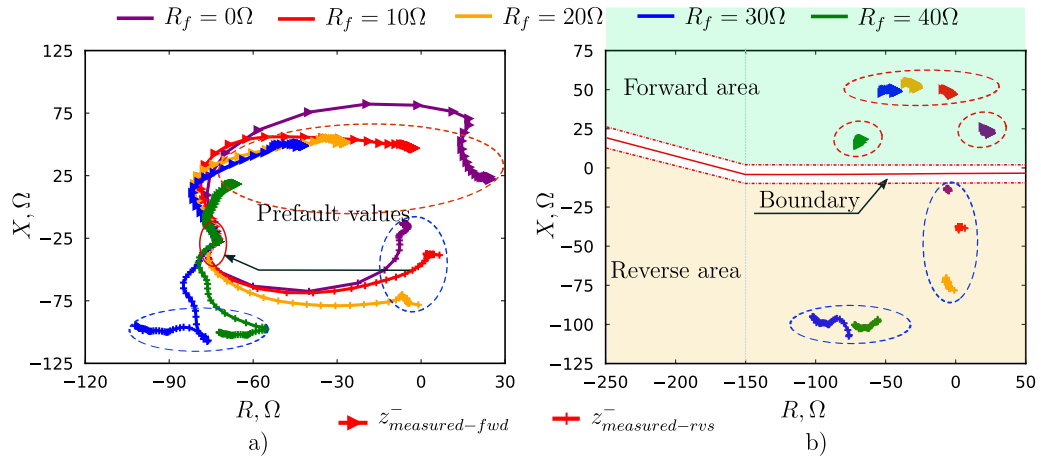


Figure E.12 – Evaluation results for two-phase-ground fault with $R_f \in [0 : 40] \Omega$ with $P_{PV} = 80\%$, (a) entire trajectory in the R-X plane, and (b) a part zoomed in on R-axis with $R \in [-250 : 50] \Omega$

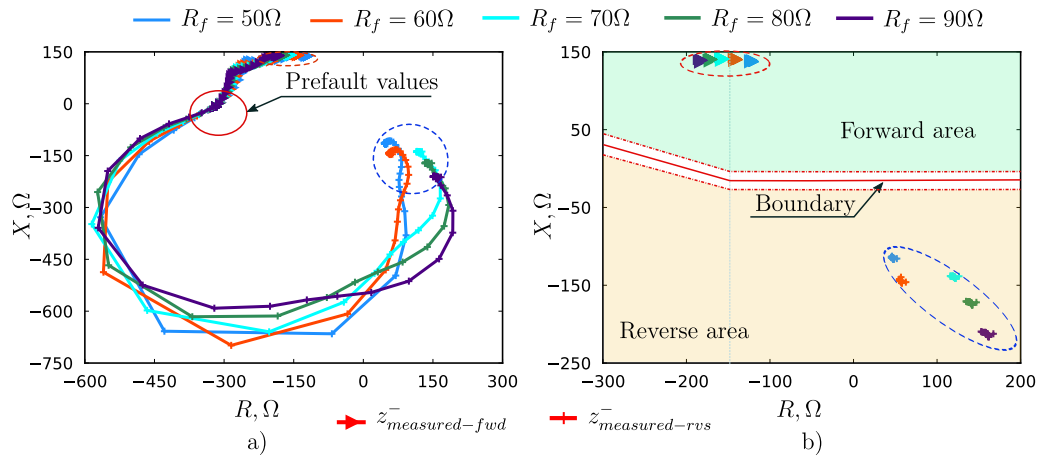


Figure E.13 – Evaluation results for two-phase-ground fault with $R_f \in [50 : 90] \Omega$ with $P_{PV} = 40\%$, (a) entire trajectory in R-X plane, and (b) a part zoomed in on R-axis with $R \in [-300 : 200] \Omega$

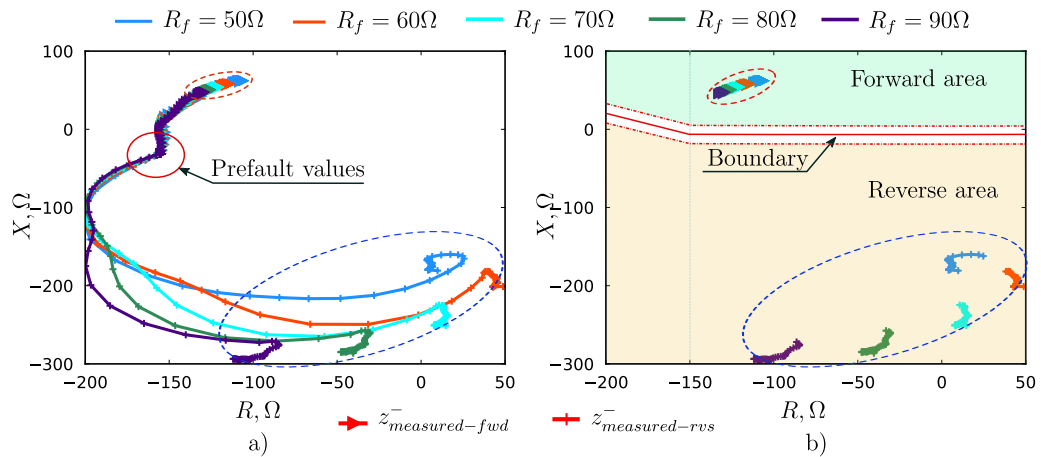


Figure E.14 – Evaluation results for two-phase-ground fault with $R_f \in [50 : 90] \Omega$ with $P_{PV} = 40\%$, (a) entire trajectory in R-X plane, and (b) a part zoomed in on R-axis with $R \in [-20 : 50] \Omega$

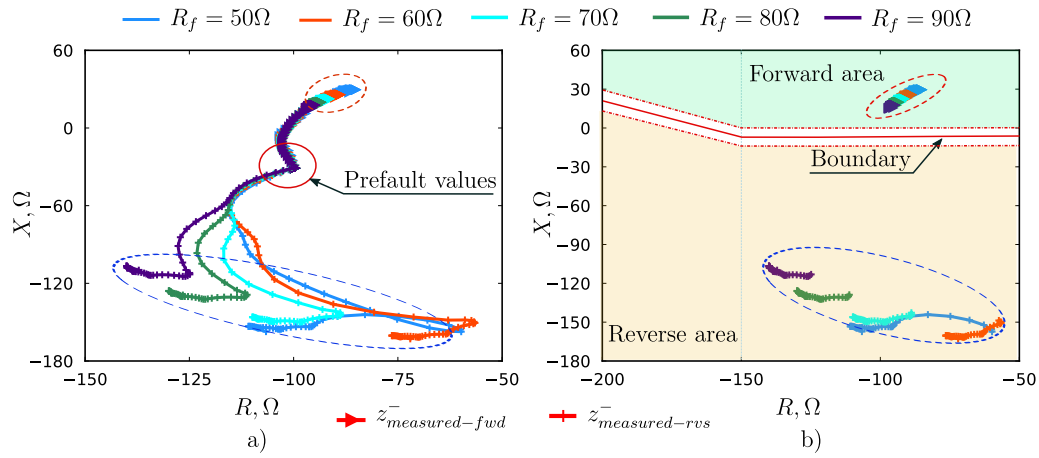


Figure E.15 – Evaluation results for two-phase-ground fault with $R_f \in [50 : 90] \Omega$ with $P_{PV} = 60\%$, (a) entire trajectory in the R - X plane, and (b) a part zoomed in on R -axis with $R \in [-200 : -50] \Omega$

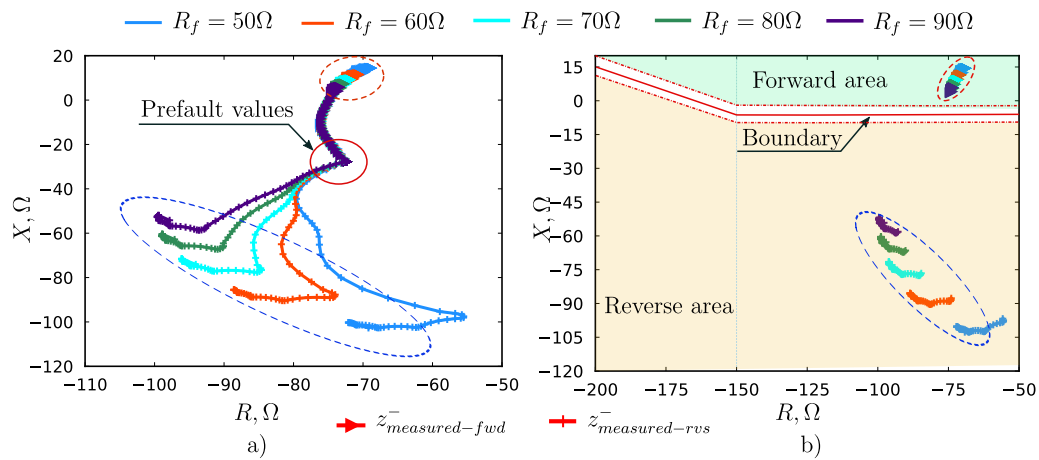


Figure E.16 – Evaluation results for two-phase-to-ground fault with $R_f \in [50 : 90] \Omega$ with $P_{PV} = 80\%$, (a) entire trajectory in the R - X plane, and (b) a part zoomed in on R -axis with $R \in [-200 : -50] \Omega$

Appendix F

Impacts of high penetration of DERs on distribution protection

Consider a simple system consisting of an external source feeding two **Medium Voltage (MV)** feeders and a **Distributed Energy Resource (DER)** of in a type of a small hydroelectric plant connected to Feeder 1, as shown in Figure F.1. The necessary parameters of the network components are provided in Table F.1.

Table F.1 – Parameters of network components

Component	Parameter
Source	$S = 200 \div 1000$ MVA
DER	$S_{DER} = 5 \div 25$ MVA, $V_n = 6.3$ kV, $x_d'' = 0.15$ p.u.
Transformer	$S_T = 25$ MVA, 22/6.3 kV, $u_n = 15\%$
Feeder 1	AC 150 mm ² , $L = 2 \div 20$ km, $z_0 = 0.2 + j0.1 \Omega/km$, $I_{rated} = 1$ kA
Feeder 2	AC 150 mm ² , $L = 2 \div 20$ km, $z_0 = 0.2 + j0.1 \Omega/km$, $I_{rated} = 1$ kA
Fuse 1	200E
Fuse 2	150E

F.1 Blinding tripping

As mentioned above, the **MV** distribution networks is generally covered by time-definite and inverse time overcurrent relays. Since the fault current flows from the external network to the fault location and is often of large amplitude, these traditional simple schemes which are based on the coordination of current and time can achieve high performance. Nevertheless, in the presence of **DER** downstream of the relay location, fault currents can come from different directions, which can cause phenomena such as blinding and false tripping.

Assuming that a fault occurs at F1 of Figure F.1, the equivalent circuit of the network studied for this fault location is shown in Figure F.2a. As required by the new grid codes, the **DER** should participate in the dynamic grid voltage support during and after faults instead of being disconnected immediately. In particular, the **DER** must be able to inject additional reactive currents into the network, [24]. The analysis of Figure F.2a allows to determine the total fault current flowing to F1:

$$I_{F1} = \frac{E_{\Sigma 1}}{Z_{\Sigma 1}} \quad (F.1)$$

where $E_{\Sigma 1}$ and $Z_{\Sigma 1}$ are the equivalent voltage and impedance of the network in Figure F.1 that are defined by:

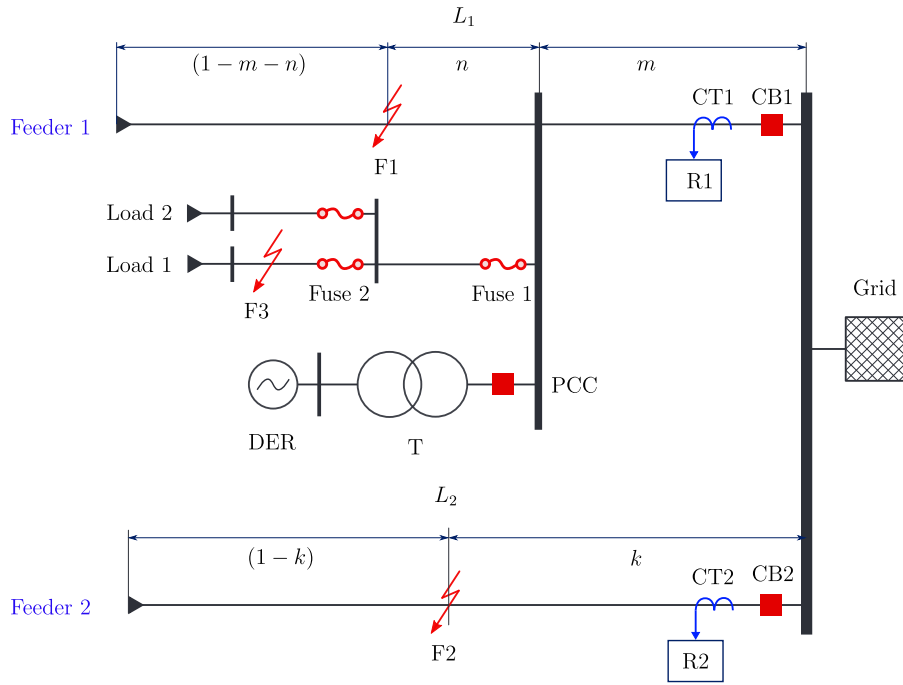


Figure F.1 – Single-diagram of the studied network

$$E_{\Sigma 1} = \frac{E_S Z_{DER} + E_{DER} (Z_S + mZ_{L1})}{Z_S + mZ_{L1} + Z_{DER}} \quad (F.2)$$

$$Z_{\Sigma 1} = \frac{Z_{DER} (Z_S + mZ_{L1})}{Z_S + mZ_{L1} + Z_{DER}} + nZ_{L1} \quad (F.3)$$

where Z_{DER} is the aggregate of the DER and its interface transformer impedance.

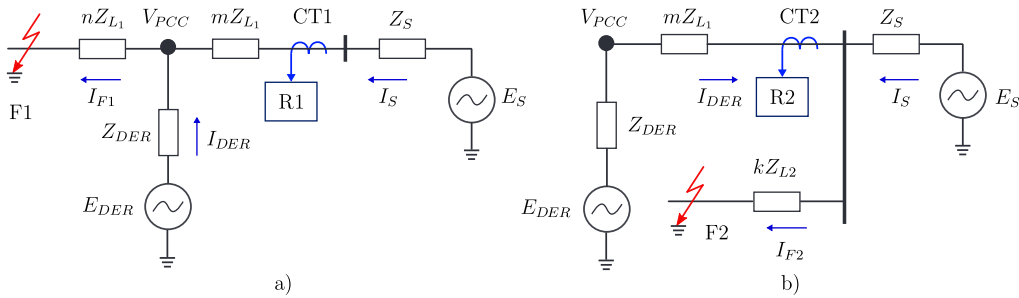


Figure F.2 – Equivalent diagrams for faults at (a) F1 and (b) F2

Consequently, the current contributed by the source for fault at F1 is computed as:

$$I_S = I_{F1} \frac{Z_{DER}}{Z_S + mZ_{L1} + Z_{DER}} \quad (F.4)$$

By substituting F.1 in F.4, the expression for the current fed to relay R1 is defined by:

$$I_S = \frac{E_{\Sigma 1}}{(Z_s + mZ_{L1}) + nZ_{L1} \left(\frac{Z_s + mZ_{L1}}{Z_{DER}} + 1 \right)} \quad (F.5)$$

Equation F.5 indicates that the current sensed by the Feeder 1 relay in the event of a fault downstream of the DER location depends on the following factors, including source and DER impedances, the distance between the source and the DER, and the fault location. To consider the worst case condition, assume that the DER capacity reaches 200% of the maximum allowable load of Feeder 1 which is equal to 34.64 MVA corresponding to the 1000 A rated current in Table F.1; any higher level of DER penetration is considered unrealistic [214]. As a further contribution to the worst-case situation, it can be assumed that the DER transformer has a very low leakage impedance, i.e. 5% [214]. Furthermore, it is assumed that the DER is located in the middle of the feeder. Therefore, when the short-circuit capacity of the source is 200 MVA, the magnitude of the fault current at the end of the feeder 1 measured by the relay would be approximately equal to 1.394 kA. Depending on Section 2.2.2, the pickup current of relay 2 should be greater than 1.5 times the maximum load of the protected feeder line, or 1.5 kA. Relay R1 fails to detect this fault. The sensitivity of the relay may worsen as the fault impedance increases.

F.2 False tripping

Unlike the blinding problem, false tripping occurs when the DERs connected to one feeder contribute to a fault on an adjacent feeder connected to the same MV busbar. The fault current supplied by the DERs may exceed the operating threshold of its feeder overcurrent relay, causing the healthy feeder to false trip before the actual fault is cleared. False tripping can be classified as a selectivity problem. DERs make a substantial contribution to the fault current when they and the fault are located close to the primary substation. A possible condition that can lead to a false trip is when a weak source feeds a long feeder covered by a definite time overcurrent relay. In this case, a fault occurring at the end of the supply line would have a minimum fault current, but the relay must have to detect it reliably. The relay pickup current must therefore be low enough to ensure its sensitivity, and in this case the DER has a negative impact on the safety of the feeder relay. To demonstrate the possibility of false tripping, let us consider a fault that occurs at F2 as shown in Figure F.1. The equivalent diagram of the fault scenario is illustrated in Figure F.2b. Similarly, the current contributed by the DER is defined by :

$$I_{DER} = \frac{E_{\Sigma 2}}{(mZ_{L1} + Z_{DER}) + kZ_{L2} \left(\frac{mZ_{L1} + Z_{DER}}{Z_S} + 1 \right)} \quad (F.6)$$

where $E_{\Sigma 2}$ is the equivalent voltage of network in Figure F.1 that can be expressed by:

$$E_{\Sigma 2} = \frac{E_S (Z_S + mZ_{L1}) + E_{DER} Z_S}{Z_S + mZ_{L1} + Z_{DER}} \quad (F.7)$$

Again, we assume a worst-case condition in which a three-phase solid fault and a DER are located near the substation. Using equation F.6, the fault current contributed by the DER can reach up to 1.7 kA, exceeding the setting threshold of the feeder relay R1 and causing CB1 to trip incorrectly.

F.3 Impacts on reclosing performance

The inclusion of DERs in the distribution system could interrupt the normal operation of the re-closure system. The DER can be switched to unintentional islanded mode in the event of a fault by continuing to supply fault current during auto-reclose attempts. For example, for a transient earth fault, after the first tripping of the feeder, the fault may not be completely eliminated since

the DER may remain connected to the grid in unintentional islanded mode. Therefore, if the feeder CB is reset by automatic reclosing prior to the DER interface protection operation, the fault will not be extinguished and may turn into a more serious fault. This may cause severe damage to the synchronous DER turbine or add to the cumulative stress due to out-of-phase synchronization. Additionally, the feeder CB may be damaged due to the non-synchronous coupling.

To address the above problem, delaying the recloser operation time to trip the DER before the first reclosing attempt may be an acceptable solution. In this case, the recloser operating time should be graded with those of the Under-Voltage Protection (PTUV) protections, especially when the Fault Ride Through (FRT) requirements are applied. From the point of view of the DER, this solution can be easily achieved; the recloser delay time can be chosen between 1.2 and 2 s for the feeder with the presence of the DER [31], i.e. longer than the release time of the low-set delay of the DER PTUV protection. However, the overall reliability of the system and the quality of the power supply are negatively influenced.

F.4 Impacts on coordination between recloser and fuse

To investigate adverse influences of the high integration of the DER on the performance of the recloser-fuse saving scheme, we assume that one recloser and two fuses are applied on Feeder 1, [215]. The characteristics of the fuses are taken from [216]. The fuse saving scheme typically uses a high-set Instantaneous Overcurrent Protection (PIOC) element, which will trip the feeder CB before the lateral fuse blows, and the CB is then recloses. The high-set PIOC element is automatically blocked after the first trip, so if the fault is persistent, the low-set inverse time elements must operate to trip the CB. The long delay of the inverse low-set element gives time for the fuse of the faulty circuit to blow if the fault is beyond it. For instance, the coordination time curves that are applied for Feeder 1 are shown in Figure F.3.

Figure F.3 indicates that in the absence of DERs, the fault current for solid three-phase fault at F3 is about $I_{Fuse2}^1 = 2.34 \text{ kA}$. However, by integrating a high-capacity DER into the bus connected to Fuse 1, the fault current can increase up to $I_{Fuse2}^2 = 3.5 \text{ kA}$. At such a high fault level, the melting curve of Fuse 2 is below the fast operating time of the feeder recloser, as shown in Figure F.3. The fuse therefore blows before CB1 is tripped, leading to the loss of coordination between the recloser and the fuse. It can be suggested to move the fast operating curve of the recloser downwards. However, this seems impossible due to the speed limit of the recloser operation time. Another suggestion is to increase the minimum melting curve of the fuse. Unfortunately, the melting curve is limited by the slow curve of the recloser which, in turn, should be less than a time limit imposed by the upstream protection element. Therefore, the improvement of the existing recloser-fuse saving scheme is a compromise between the different levels of distribution protection system and seems complicated, requiring a very thorough investigation.

F.5 Impacts on distance protection

The high penetration of the DER may also affect the performance of distance relays which are currently implemented in distribution networks in several countries, for example Germany. Indeed, the fault current contribution of the downstream connected DER may reduce the range covered by the first protection zone of the distance relays. For example, for a fault at F1 in Figure F.1, the impedance measured by relay R1, i.e., Z_{R1} , is calculated by:

$$Z_{R1} = (m + n) Z_{L1} + \frac{I_{RES}}{I_S} n Z_{L1} \quad (\text{F.8})$$

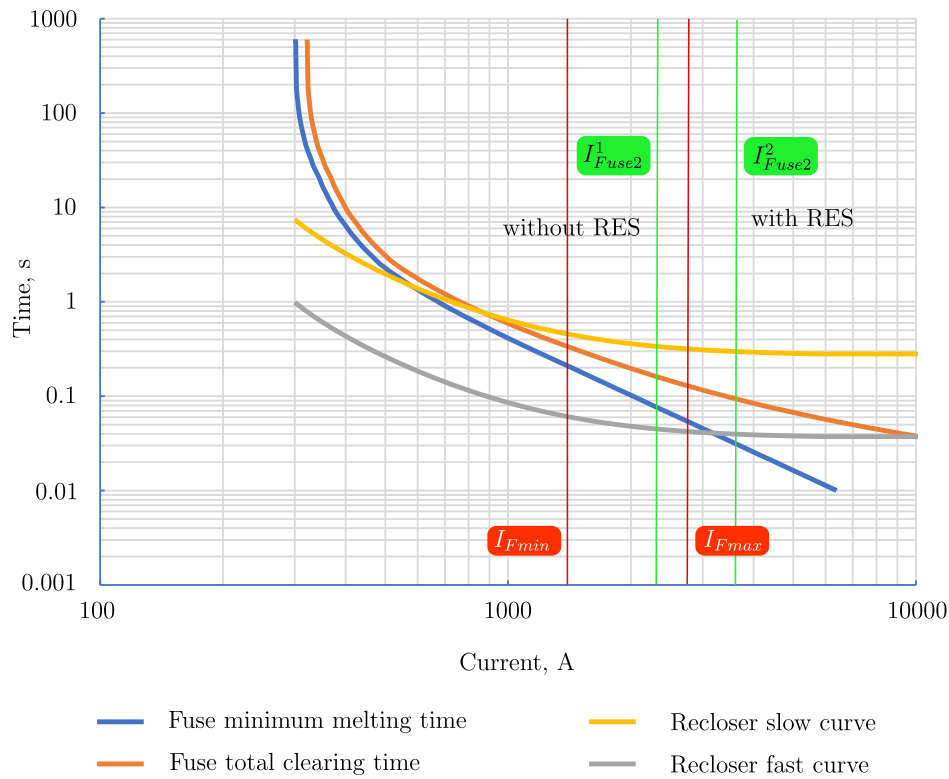


Figure F.3 – Fuse-recloser coordination for fuse-saving scheme

Equation F.8 shows that the impedance measured by R1 is greater than the actual fault impedance, which is equal to $(m + n)Z_{L1}$. Therefore, the fault may be cleared by zone 2 of distance element R1 with a longer tripping time instead of by instantaneous zone 1. Other issues caused by the DER tapped connection are as follows [31]:

- 1 Impacts of prefault load on the impedance seen by the distance element;
- 2 Unsuccessful trip an internal fault due to the current flowing out at on end;
- 3 False tripping for an external fault because of high current contributed by large DER connected very closely to the relay location.

F.6 Issues related to low level of PV fault currents

The major impact is that PV systems often provide unnecessary earth fault currents for faults in the supply circuit, e.g. the fault at F1 in Figure F.1, and thus reduce the current from the source via CB1. As mentioned earlier, this can lead to a lot of issues related to relay coordination. Let us consider several faults illustrated in Figure F.1; the potential consequences can be, [32]:

- 1 If fault F1 occurs on the remote end of Feeder 1, the ground fault current at the substation side may reduce significantly, leading to ground overcurrent function of R1 failing to detect the fault;
- 2 If a fuse-saving scheme is used for Feeder 1, the decrease of fault current contributed by the source, and the increase in fault current seen by Fuse 2 in case of fault at F3 may lead to failure to over trip fuses and the loss of recloser-fuse coordination;

- 3 For fault at F2, the resulting ground fault current flow through CB1 may cause the R1 to issue a false trip to CB1.

Another problem that should be mentioned is the intermittent nature of several types of DER, such as solar or wind energy. The electricity production of these DERs can vary to a large extent, especially in the case of high penetration of PV systems. The output power reaches its highest-level during hours of peak solar irradiation, while it can be reduced to zero at night. Consequently, the fault currents are very different for faults occurring at different times. Such a large variation in fault currents does not exist in the case of traditional synchronous generators on which the power distribution protection system is designed. A fixed set of setting thresholds that are generally used no longer seems possible.

F.7 Overvoltage of healthy phases during ground faults

Another problem that may arise is overvoltage of the healthy phases in the event of a permanent single-phase ground fault in the distribution network with ungrounded neutral after the CB of the faulted feeder has been tripped. Let us consider, for instance, a single-phase-to-ground fault at F1 in Figure F.1. After the tripping of CB1, the MV/LV connected downstream of the CB1 and the lightning arresters may be subjected to an overvoltage which may reach the line-to-line voltage level. The phenomenon is more likely to occur if the DER is located close to the load capacity [32]. As a result, MV/LV transformers that generally operate at the knee in the saturation curve may be saturated.

F.8 Impacts of inverter-based PV systems on the conventional directional method

Practical applications have shown the effectiveness of the **Negative Sequence (NS) Directional Element (RDIR)** previously mentioned in Subsubsection 3.2.2.2. However, it should be noted that, for these above directional principles to accomplish accurate performance, the characteristics of NS quantities should be similar to those of conventional synchronous generator-based sources. The NS equivalent circuit of a synchronous generator is just a single impedance, as demonstrated in [211]. As a result, in the network dominated by synchronous generator-sources, the NS current is largely dependent on the driving NS voltage caused by the fault and the impedance of the fault loop. Synchronous generator-based DERs such as gen-sets or wind generators of Type 1 (Squirrel Cage Induction Generator) and Type 2 (Wound-Rotor Induction Generator with Variable External Rotor Resistance) may respond to faults in the same way with conventional synchronous generators, [108].

In contrast, as demonstrated in Section 3.3, the response of inverter-based PV systems to faults largely depends on their control strategy, and therefore, their fault current and voltage waveforms are different from those of conventional synchronous machines. The NS currents contributed by the PV systems are defined by their control algorithm instead of fault loop NS impedances [34], leading to unconventional patterns of the phase displacement between the NS current and NS voltage. The performance of existing directional algorithms, which is based on the above displacement as shown in Equation 3.5, within the context of high penetration of converter-based DERs is, therefore, affected.

For instance, let us consider a phase-A-to-ground fault at $t = 0.2$ s in the middle of the line L_1 of Grid-2 (Figure 3.3), which appears to be a forward fault to the RDIR element. For this fault

location, the NS current provided to the RDIR element is the NS current contributed by the PV systems under the operation of their inverter controller. Figure F.4 represents the extremely low voltage at phase A and a rise in fault current of this phase.

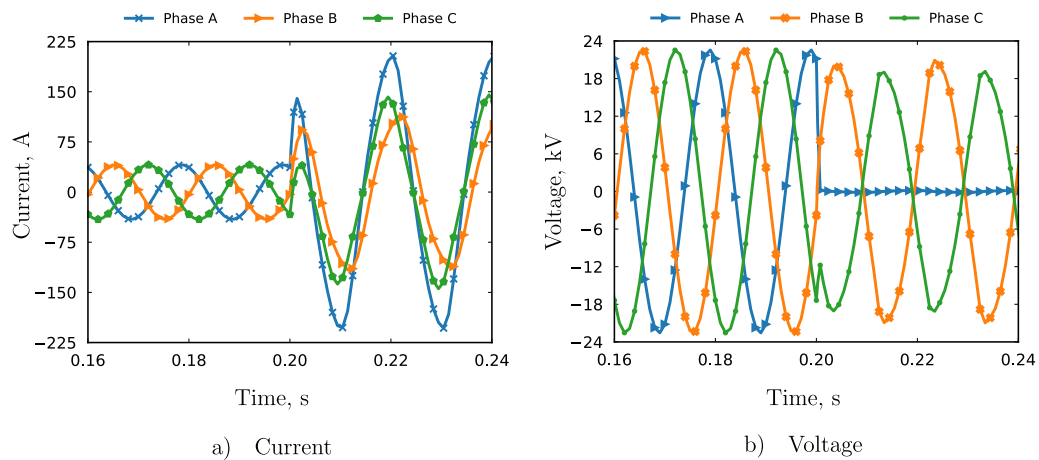


Figure F.4 – Three-phase current and voltage measured at the RDIR location during a direct phase-A-to-ground forward fault

As investigated in Section 3.3.2, the PV NS current leads the NS voltage at the PV terminal by an angle within a range of 10 to 40°, as illustrated in Figure 3.5b, depending on the unbalance voltage level and fault severity. If the NS line impedance angle is 68° then the angle of the cosine term of the NS torque-product T^- for this fault would be within the range of 78 to 108°, possibly leading to the spurious negative values of NS torque T^- for a forward faults if θ_{T^-} larger than 90°. The typical range of NS torque angle can be observed through simulation results of various fault scenarios as shown in Figure F.5. It is clear that the values of the NS torque angle exceed 90° for all fault conditions. For case of severe faults, the voltage drops below 0.5p.u.. So, according to Equation B.20b, the phase displacement between NS current and voltage can reach up to 90°, leading to larger value of NS torque-product phase angle, i.e. may exceed 150°. It is obviously that the traditional RDIR element outputs false direction identification.

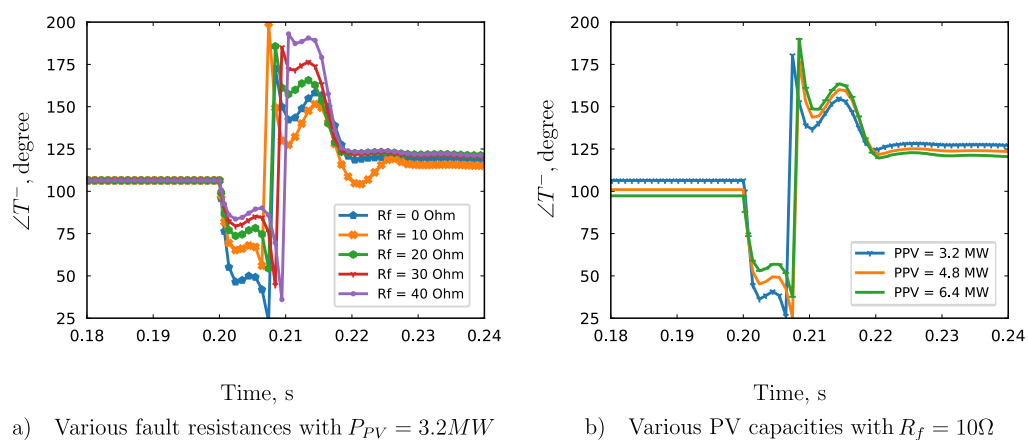


Figure F.5 – NS torque angle computed by conventional method for various fault impedances and PV capacities during a forward fault

Appendix G

LV distribution protection

G.1 Protection configuration for grid-connected mode

G.1.1 MCCB time-current curve settings

The selection of the Molded-Case Circuit Breaker (MCCB) rating for each lateral is based on its maximum load current. The higher the rating, the greater the fault current required to trip the MCCB. Therefore, the selectivity between the MCCBs and the feeder Forward Time Over-Current Protection (PTOCF) must be checked with the time-current curve of the MCCB with the longest release time. On LV Feeder 1 in Figure 2.8, the lateral L07 has the highest load capacity of 130 kW, with a power factor of 0.9 lag, and its time-current curve is therefore chosen as the initial curve for the protection coordination. An MCCB of 250 A is selected. The operating curve of the MCCB for phase faults is divided into three different sections, as shown in Figure 4.2. Long-term tripping responds to an overload condition, short-term tripping responds to a fault current of about 6 times the rated current of the MCCB, and instantaneous time-tripping responds to extremely high fault current. The simulation results using Digsilent I PowerFactory show that the lowest fault current at the lateral areas is about 3200 A, which means that the MCCB can guarantee the elimination of all faults in only 0.03 s. For setting the G function of the MCCB against earth fault, the current thresholds for the high- and low- set level are set at 0.5 times and 0.2 times the rated current of the MCCB, respectively.

G.1.2 Feeder protection setting thresholds

For the feeder PTOCF function, we must implement three different elements for detecting different types of fault that only trip forward. The direction detection algorithm has already been developed and validated in Chapter 3.

- 1 Forward Phase Time Over-Current Protection (PTOCPF): includes a high-set PTOCPF1 and a low-set PTOCPF2, whose pickups are 12 times and 1.5 times the feeder maximum load current, respectively. For LV Feeder 1 of 500 kVA rating, the pickups for PTOCPF1 and PTOCPF2 are 8.66 and 1.44 kA, respectively.
- 2 Forward Negative-sequence Time Over-Current Protection (PTOCQF): can be set more sensitively than the PTOCPF to detect phase-to-phase faults because the PTOCQF element is insensitive to the balanced load currents. It does not need to be adjusted for cold load or pickup conditions. There are also two different tripping levels PTOCQF1 and PTOCQF2, whose setting calculation is derived from [217, 164]. In particular, the settings are determined by the settings of the MCCBs of the DER and laterals downstream.

- 3 Ground Time Over-Current Protection (PTOCCG): Unrestricted earth fault. This element provides protection against ground faults occurring on the feeder side of the feeder CB. The pickups for PTOCCG1 and PTOCCG2 are 0.5 and 0.2 times the feeder rated current, respectively.

On the other hand, the parameters of the feeder and Reverse Negative-sequence Over-Voltage Protection (PTOVQR), which provide the backup function for the CIED3.PTUVR element, are 0.8 *p.u.* and 0.05 *p.u.*, respectively.

G.1.3 Transformer protection setting thresholds

The setting of the transformer protection, i.e., CIED3, requires not only the detection of faults in the MV/LV transformer but also faults in the MV networks. Like the feeder PTOCF protection, that of CIED3 should also include three elements, namely Phase Time Over-Current Protection (PTOCP), Negative-sequence Time Over-Current Protection (PTOCQ), and Ground Time Over-Current Protection (PTOCCG), whose settings are as follows:

- 1 PTOCP element: the low-set threshold should be at least 2 times the rated current to avoid the cold load pickup currents. For a transformer of 1000 *kVA* rating, the low-set pickup would be 2887 *A*. The high-set pickup is set at 1.3 times the maximum three-phase fault current sensed on the HV side for fault at the LV side. For the studied LV microgrid, this current is equal to 422 *A*, resulting in a high-set pickup of 633 *A* at 20 *kV* or 27430 *A* at 0.4 *kV*.
- 2 PTOCQ element: the pickup values for the protection against phase-to-phase fault follows the rule in [164, 217] and should be coordinated with the feeder PTOCQF.
- 3 PTOCCG element: For ground fault detection, restricted earth fault protection is used, protecting against ground faults occurring between the secondary winding of the transformer and the LV feeder CB. The protection has two trip levels with 9900 *A* for high setting and 400 *A* for the low setting.

G.1.4 Interface protection setting thresholds

The undervoltage element of the CIED3 consists of two elements, one for detecting three-phase and earth faults, and one for phase-to-phase fault and has the corresponding settings as follows:

- 1 PTUVR element: The phase undervoltage element comprises a high setting level, i.e., PTUVR1, operating on a significant voltage drop, and a low setting level, i.e., PTUVR2, being triggered by a smaller voltage drop. We propose to set PTUVR1 at 0.7 *p.u.* and PTUVR2 at 0.8 *p.u.*
- 2 PTOVQR element: Negative-sequence undervoltage element with the settings for both PTOVQR1 and PTOVQR2 elements are 0.08 *p.u.* and 0.05 *p.u.*, respectively.

The voltage-based and frequency-based coordination of three elements DIED1-FIED1-CIED3 is shown in Figure 4.3 and Figure 4.4.

G.2 Protection coordination for islanded operation

Let us re-consider the LV feeder 1 in Figure 2.8. The coordination principle is carried out in a similar way to the grid-connected operation mode. The delay of the lowest protection level, i.e., MCCBs, is the lower time limit.

G.2.1 MCCB time current curve settings

A signal from the CCU decreases the thresholds of the electronic trip units of the MCCBs for phase tripping. The settings for function G remain the same.

G.2.2 DER and BESS protection settings

For the thresholds of the PTOC element of the BESS, thresholds of 1.5 and 0.3 times the BESS rated current is selected to identify three-phase and phase-to-phase faults, respectively.

G.2.3 Feeder protection setting thresholds

The configuration parameters for the feeder PTOCQ and PTOCG elements are derived from those for parallel mode. The configuration of the feeder unrestricted earth protection is proposed to be similar to that of grid-connected mode since the LV side of the transformer, which is directly earthed, remains connected to the islanded microgrid, leading to the constancy of the zero-sequence impedance of the fault loop.

The feeder undervoltage function consists of two elements, one for detection of three-phase faults, i.e., PTUVF, and the other for phase-to-phase faults, i.e., PTOVQF. The pickups for PTUVF1 and PTUVF2 elements are 0.7 *p.u.* and 0.8 *p.u.*, respectively. On the other hand, the values configured for PTUVF1 and PTUVF2 are 0.1 *p.u.* and 0.05 *p.u.*, correspondingly. The setting of the feeder backup protection is carried out similarly. However, each function has only one tripping stage. The values for the PTUVR and PTOVQR functions are 0.8 and 0.05 *p.u.*, respectively.

G.3 Results for grid-connected mode

Table G.1 – Operated functions and corresponding operation times in grid-connected mode under solid fault conditions at different locations

(1)*	Primary protection			Backup protection		
	(2) [†]	(3) [‡]	(4)**	(2)	(3)	(4)
F1 (near substation)						
ABC	MCCB7	17.66	0.03	FIED1.PTOCPF1	16.52	0.13
				DIEDx.PTUV1 [§]	0.18 ÷ 0.23	0.2
AB	MCCB7	16.29	0.03	FIED1.PTOCPF1	15.74	0.13
				FIED1.PTOCQF1	9.12	0.13
				DIEDx.PTUV1	0.57 ÷ 0.62	1.2
AG	MCCB7	8.28	0.03	FIED1.PTOCPF1	7.39	0.13
				FIED1.PTOCQF1	2.72	0.13
				FIED1.PTOCG1	2.51	0.13
F5 (at the lateral on the remote end of LV feeder 1)						
ABC	MCCB9	5.953	0.03	FIED1.PTOCPF1	5.24	0.13
				DIED5.PTUV1	0.37	0.2
				DIED6.PTUV1	0.37	0.2
				DIED7.PTUV1	0.14	0.2
				DIED1.PTUP1	0.73 ↘ [‡] 0.12	0.33
				DIED2.PTUV1	0.73 ↘ 0.12	0.33
				DIED3.PTUV1	0.54 ↘ 0.10	0.33
				DIED4.PTUV1	0.54 ↘ 0.10	0.33
F3 (at the beginning of LV feeder 1 backbone)						
ABC	FIED1.PTOCPF1	30.2	0.13	CIED3.PTOCP1	29.1	0.33
	DIEDx.PTUV1	0.05 ÷ 0.09	0.2	DIEDy.PTUV2	0.63 ↘ 0.12	0.53
				FIED2.PTUVR	0.58 ↘ 0.52	1.5
AC	FIED1.PTOCPF1	29.2	0.13	CIED3.PTOCP1	16.95	0.33
	FIED1.PTOCQF1	17.13	0.13	CIED3.PTOCQ1	7.75	0.33
	DIEDx.PTUV2	0.45 ÷ 0.78	1.2	DIEDx.PTUV1	0.45 ÷ 0.15	0.53
				DIEDy.PTUV1	0.29	0.53
			FIED2.PTOVQR	0.14 ↗ 0.22	1.5	
AG	FIED1.PTOCPF1	15.08	0.13	CIED3.PTOCP1	6.2	0.33
	FIED1.PTOCQF1	5.34	0.13	CIED3.PTOCQ1	23.655	0.33
	FIED1.PTOCG1	5.15	0.13	DIEDy.PTUV2	0.86 ↘ 0.58	1.53
	DIEDx.PTUV1	0.11 ÷ 0.12	0.2	FIED2.PTOVQR	0.047 ↗ 0.25	1.5
F4 (at the end of LV feeder 1 backbone)						
ABC	FIED1.PTOCPF1	6.75	0.13	CIED3.PTOCP1	8.2	0.33
	DIED3.PTUV1	0.39	0.2	DIEDy.PTUV1	0.92 ↘ 0.13	0.53
	DIED4.PTUV1	0.39	0.2	FIED2.PTUVR	0.9 ↘ 0.3	1.85
	DIED5.PTUV1	0.39	0.2			
	DIED6.PTUV1	0.16	0.2			

Continued on next page

Table G.1 – continued from previous page

(1)	Primary protection			Backup protection		
	(2)	(3)	(4)	(2)	(3)	(4)
	DIED7.PTUV1	0.012	0.2			
	DIED1.PTUV1	0.64 ↘ 0.08	0.33			
	DIED2.PTUV1	0.65 ↘ 0.08	0.33			
BC	FIED1.PTOCPF1	6.41	0.13	CIED3.PTOCP1	4.95	0.33
	FIED1.PTOCQF1	3.79	0.13	CIED3.PTOCQ1	1.659	0.33
	DIEDx.PTUV2	0.53 ÷ 0.77	1.2	DIEDx.PTUV1	0.62 ↘ 0.22	0.53
				DIEDy.PTUV1	0.91 ↘ 0.32	0.53
				FIED2.PTUVR	0.95 ↘ 0.04	1.85
BG	FIED1.PTOCPF1	2.386		CIED3.PTOCP1	2.6	0.33
	FIED1.PTOCQF1	932.7		CIED3.PTOCQ1	0.4	0.33
	FIED1.PTOCG1	826.68	0.13	DIEDx.PTUV2	0.70 ↘ 0.08	0.53
	DIED3.PTUV1	0.41	0.2	DIEDy.PTUV2	0.96 ↘ 0.12	0.53
	DIED4.PTUV1	0.41	0.2	FIED2.PTUVR	0.95 ↘ 0.04	1.85
	DIED5.PTUV1	0.17	0.2			
	DIED6.PTUV1	0.17	0.2			
	DIED7.PTUV1	0.13	0.2			
	DIED1.PTUV1	0.70 ↘ 0.23	0.33			
	DIED2.PTUV1	0.70 ↘ 0.18	0.33			
ABG	FIED1.PTOCPF1	5.97	0.13	CIED3.PTOCP1	5.35	0.33
	FIED1.PTOCQF1	3.51	0.13	CIED3.PTOCQ1	1.55	0.33
	FIED1.PTOCG1	0.5	0.13	FIED2.PTUVR	0.95 ↘ 0.04	1.85
	DIED3.PTUV1	0.42	0.2			
	DIED4.PTUV1	0.42	0.2			
	DIED5.PTUV1	0.17	0.2			
	DIED6.PTUV1	0.17	0.2			
	DIED7.PTUV1	0.02	0.2			
	DIED1.PTUV1	0.70 ↘ 0.26	0.33			
	DIED2.PTUV1	0.71 ↘ 0.27	0.33			

*Fault type

†Function that trips

‡Measured values protection criterion

§"x" denotes all PV systems connected to LV feeder 1

||"y" denotes all PV systems connected to LV feeder 2

**Operation time that is counted from the instant of fault inception

‡‡Representing the change in protection criterion values after a certain function operates

Table G.2 – Operated functions and corresponding operation times in grid-connected operation mode under faults with $R_f = 0.01 \Omega$ at different locations

(1)*	Primary protection			Backup protection		
	(2) [†]	(3) [‡]	(4)**	(2)	(3)	(4)
F1 (near substation)						
ABC	MCCB7	10.78	0.03	FIED1.PTOCPF1	10.4	0.13
				DIEDx.PTUV1	0.6 ↘ 0.08	0.2
BC	MCCB7	12.24	0.03	FIED1.PTOCPF1	12.08	0.13
				FIED1.PTOCQF1	6.90	0.13
				DIEDx.PTUF1	43.73	2.13
F5 (at the lateral on the remote end of LV feeder 1)						
AB	MCCB9	4.76	0.03	FIED1.PTOCQF1	5.64	0.13
				DIEDx.PTUV1	0.85 ↘ 0.15	0.33
AG	MCCB9 G	0.72	0.03	FIED1.PTOCG1	0.63	0.13
F3 (at the beginning of LV feeder 1 backbone)						
ABC	FIED1.PTOCPF1	14.65	0.13	CIED3.PTOCP1	12.5	0.33
	DIEDx.PTUV1	0.67 ↘ 0.09	0.2	DIEDy.PTUV1	0.89 ↘ 0.11	0.53
				FIED2.PTUVR	0.89 ↘ 0.12	1.85
AC	FIED1.PTOCPF1	19.62	0.13	CIED3.PTOCQ1	4.9	0.33
	FIED1.PTOCQF1	10.89	0.13	DIEDx.PTUV1	0.79 ↘ 0.17	0.53
	DIEDx.PTUF1	43.74	2	DIEDy.PTUV1	0.97 ↘ 0.22	0.53
				FIED2.PTOVQR	0.09 ↗ 0.2	1.5
AG	FIED1.PTOCPF1	10.48	0.13	CIED3.PTOCQ1	1.6	0.33
	FIED1.PTOCQF1	3.65	0.13	DIEDx.PTUV1	0.48 ÷ 0.12	0.53
	FIED1.PTOCG1	3.5	0.13	DIEDy.PTUV1	0.48 ÷ 0.11	0.53
	DIEDx.PTUV1	0.46 ÷ 0.16	0.33	FIED2.PTOVQR	0.03 ↗ 0.4	1.5
F4 (at the end of LV feeder 1 backbone)						
ABC	FIED1.PTOCPF1	5.53	0.13	CIED3.PTOCP1	7.1	0.33
	DIEDx.PTUV1	0.74 ↘ 0.10	0.33	DIEDx.PTUV1	0.74 ↘ 0.11	0.53
				DIEDy.PTUV1	0.94 ↘ 0.10	0.53
				FIED2.PTUVR	0.92 ↘ 0.15	1.5
BG	FIED1.PTOCG1	0.77	0.13	CIED3.PTOCG1	0.4	0.33
	DIEDx.PTUV1	0.72 ↘ 0.11	0.2	DIEDx.PTUV1	0.72 ↘ 0.11	0.53
				DIEDy.PTUV1	0.92 ↘ 0.08	0.53

Table G.3 – Operated functions and corresponding operation times in normal operation mode under fault with $R_f = 0.1 \Omega$ conditions at different locations

Primary protection				Backup protection		
(1)	(2)	(3)	(4)	(2)	(3)	(4)
F1 (near substation)						
AG	MCCB7	0.64	0.03	FIED1.PTOCG1	0.58	0.13
				DIEDx.PTUF1	44.67	2.13
AC	MCCB7	2.4	0.03	FIED1.PTOCQF1	1.3	0.13
				DIEDx.PTUV2	0.88 ↘ 0.73	1.2
F5 (at the lateral on the remote end of LV feeder 1)						
CG	MCCB9 G	0.42	0.03	FIED1.PTOCG1	0.37	0.13
				DIEDx.PTUV1	0.82 ↘ 0.40	0.33
AC	MCCB9	2.4	0.03	FIED1.PTOCQF1	1.3	0.13
				DIEDx.PTUV2	0.88 ↘ 0.72	1.33
F3 (at the beginning of LV feeder 1 backbone)						
AG	FIED1.PTOCGF1	0.67	0.13	CIED3.PTOCQ1	2.45	0.33
	DIEDx.PTUV1	0.81 ↘ 0.31	0.33	DIEDx.PTUV1	0.33	0.53
				DIEDy.PTUV1	0.33	0.53
F4 (at the end of LV feeder 1 backbone)						
BG	FIED1.PTOCG1	0.77	0.13	CIED3.PTOCG2	0.4	0.65
	DIEDx.PTUV1	0.72 ↘ 0.11	0.33	DIEDx.PTUV1	0.72 ↘ 0.11	0.85
				DIEDy.PTUV1	0.92 ↘ 0.08	0.85
AB	FIED1.PTOCQF1	1.48	0.13			
	DIEDx.PTUV2	0.88 ↘ 0.74	1.33			

G.4 Results for islanded mode

Table G.4 – Operated functions and corresponding operation times in islanded operation mode under solid fault conditions at different locations

(1)*	Primary protection			Backup protection		
	(2) [†]	(3) [‡]	(4)**	(2)	(3)	(4)
F1 (near substation)						
ABC	MCCB7	7.25	0.03	FIED1.PTUVF1	0.47	0.13
				DIEDx.PTUV1	0.12	0.2
AC	MCCB7	6.86	0.03	FIED1.PTOVQF2	0.075	0.33
				DIEDx.PTUF1 [§]	43.8	2.33
BG	MCC7-G	2.41	0.03	FIED1.PTOCG1	2.19	0.13
				DIEDx.PTUV1	0.11	0.2
F5 (at the lateral on the remote end of LV feeder 1)						
AG	MCCB9-G	730	0.03	FIED1.PTOCG1	643	0.13
				DIEDx.PTUV1	0.1	0.2
ABC	MCCB9	5.2	0.03	FIED1.PTUVF1	0.699	0.13
				DIED3.PTUV1	0.38	0.2
				DIED4.PTUV1	0.38	0.2
				DIED5.PTUV1	0.23	0.2
				DIED6.PTUV1	0.23	0.2
				DIED7.PTUV1	0.01	0.2
				DIED1.PTUV1	0.55 ↘ 0.03 ^{‡‡}	0.33
F3 (at the beginning of LV feeder 1 backbone)						
ABC	FIED1.PTUVPF1	0.32	0.13	DIEDy.PTUV1	0.34	0.2
	DIEDx.PTUV1	0.05	0.2	DIED0.PTOCPR	6.3	0.53
				FIED2.PTUVR1	0.32 ↘ 0.02	1.5
BG	FIED1.PTOCG1	4.2	0.13	DIED0.PTOCPR	4.2	0.53
	DIEDx.PTUV1	0.1	0.2	DIEDy.PTUV1	0.73 ↘ 0.19	0.72
				FIED2.PTUVR	0.06 ↗ 0.36	1.5
AB	FIED1.PTOVQF1	0.15	0.13	DIED0.PTOCQR	3.7	0.53
	DIEDx.PTUV1	0.37	0.2	DIEDy.PTUV1	0.61 ÷ 0.46	1.2
				FIED2.PTOVQR	0.15 ↗ 0.45	1.5
F4 (at the end of LV feeder 1 backbone)						
ABC	FIED1.PTUVF1	0.67	0.13	DIEDy.PTUV1	0.71-0.19	0.73
	DIED3.PTUV1	0.33	0.2	FIED2.PTUVR	0.58 ↘ 0.12	1.5
	DIED4.PTUV1	0.30	0.2	DIED0.PTOCPR	2.8	0.53
	DIED5.PTUV1	0.12	0.2	DIED3.PTUV1	0.33	0.2
	DIED6.PTUV1	0.12	0.2	DIED4.PTUV1	0.3	0.2
	DIED7.PTUV1	0.01	0.2	DIED5.PTUV1	0.12	0.2
	DIED1.PTUV1	0.49 ↘ 0.03	0.33	DIED6.PTUV1	0.12	0.2
	DIED2.PTUV1	0.50 ↘ 0.03	0.33	DIED7.PTUV1	0.01	0.2
				DIED1.PTUV1	0.49 ↘ 0.03	0.73

Continued on next page

Table G.4 – continued from previous page

(1)	Primary protection			Backup protection		
	(2)	(3)	(4)	(2)	(3)	(4)
				DIED2.PTUV1	0.50 ↘ 0.03	0.73
AG	FIED1.PTOCG1	1.84	0.13	DIED _y .PTUV1	0.88 ↘ 0.52	1.2
	DIED3.PTUV1	0.38 ↘ 0.02	0.2	FIED2.PTOVQR	0.01 ↗ 0.2	1.5
	DIED4.PTUV1	0.38 ↘ 0.03	0.2	DIED0.PTOCQR	0.86	0.53
	DIED5.PTUV1	0.12 ↘ 0.02	0.2	DIED3.PTUV1	0.39	0.2
	DIED6.PTUV1	0.12 ↘ 0.02	0.2	DIED4.PTUV1	0.38	0.2
	DIED7.PTUV1	0.01	0.2	DIED5.PTUV1	0.2	0.2
	DIED1.PTUV1	0.64 ↘ 0.03	0.33	DIED6.PTUV1	0.2	0.2
	DIED2.PTUV1	0.64 ↘ 0.03	0.33	DIED7.PTUV1	0.01	0.2
				DIED1.PTUV1	0.64 ↘ 0.03	0.73
				DIED2.PTUV1	0.64 ↘ 0.03	0.73

*Fault type

†Function that trips

‡Measured values protection criterion

§"x" denotes all PV systems connected to LV feeder 1

||"y" denotes all PV systems connected to LV feeder 2

**Operation time that is counted from the instant of fault inception

‡‡Representing the change in protection criterion values after a certain function operates

Table G.5 – Operated functions and corresponding operation times in islanded operation mode under faults with $R_f = 0.01 \Omega$ at different locations

Primary protection				Backup protection		
(1)	(2)	(3)	(4)	(2)	(3)	(4)
F1 (near substation)						
ABC	MCCB7	5.15	0.03	FIED1.PTUVF1	0.57	0.13
				DIEDx.PTUV1	0.38	0.2
AC	MCCB7	4.56	0.03	FIED1.PTOCQF1	3.9	0.13
				DIEDx.PTUF1	43.85	2.13
AG	MCCB7 G	1.9	0.03	FIED1.PTOCG1	1.76	0.13
				DIEDx.PTUV1	0.31	0.2
F5 (at the lateral on the remote end of LV feeder 1)						
ABC	MCCB9	3.57	0.03	FIED1.PTUVF2	0.72	0.33
				DIED3.PTUV1	0.47 ↘	0.13 0.53
				DIED4.PTUV1	0.47 ↘	0.13 0.53
				DIED5.PTUV1	0.35 ↘	0.1 0.2
				DIED6.PTUV1	0.35 ↘	0.1 0.2
				DIED7.PTUV1	0.21 ↘	0.1 0.2
				DIED1.PTUV1	0.6 ↘	0.1 0.53
				DIED2.PTUV1	0.6 ↘	0.2 0.53
AG	MCCB9 G	0.61	0.03	FIED.PTOCG1	0.61	0.13
				DIEDx.PTUF1	44.2	2.13
F3 (at the beginning of LV feeder 1 backbone)						
CG	FIED1.PTOCG1	2.87	0.13	DIED0.PTOCQR	2.96	0.53
	DIEDx.PTUV1	0.4	0.2	DIEDy.PTUV1	0.77 ↘	0.25 0.73
				FIED2.PTOVQR	0.04 ↗	0.32 2.03
AB	FIED1.PTUVF1	0.63	0.13	DIED0.PTOCQR	7	0.53
	DIEDx.PTUV2	0.56	1.2	DIEDy.PTUV2	0.67 ÷	0.47 1.73
				FIED2.PTUVR	0.1 ↗	0.42 2.03
F4 (at the end of LV feeder 1 backbone)						
ABC	FIED1.PTUVF1	0.13	0.13	DIED0.PTOCPR	4.2	0.53
	DIEDx.PTUV1	0.4	0.2	DIEDy.PTUV1	0.6 ↘	0.2 0.73
BG	FIED1.PTOCG1	0.44	0.13	DIED0.PTOCQR	1.89	0.53
	DIEDx.PTUV1	0.3	0.2	DIEDy.PTUV1	0.83 ↘	0.32 0.73
				FIED2.PTUVR	0.79 ↘	0.25 2.03

Table G.6 – Operated functions and corresponding operation times in islanded operation mode under faults with $R_f = 0.1 \Omega$ at different locations

Primary protection				Backup protection		
(1)	(2)	(3)	(4)	(2)	(3)	(4)
F1 (near substation)						
AG	MCCB7 G	0.58	0.03	FIED1.PTOCG1	0.53	0.13
				DIEDx.PTUV1	0.80 ↘ 0.44	0.2
BG	MCCB9 G	0.41	0.03	FIED1.PTOCG1	0.36	0.13
				DIEDx.PTUV2	0.79 ÷ 0.53	1.33
F5 (at the lateral on the remote end of LV feeder 1)						
BG	MCCB9 G	0.41	0.03	FIED1.PTOCG1	0.36	0.13
				DIEDx.PTUV2	0.79 ÷ 0.53	1.33
F3 (at the beginning of LV feeder 1 backbone)						
BC	FIED1.PTOCQ1F	1.74	0.13	DIED0.PTOCQR1	1.7	0.53
	DIEDx.PTUF1	43.25	2.13	DIEDx.PTUV1	0.87 ↘ 0.56	1.73
				DIEDy.PTUV1	0.87 ↘ 0.56	1.73
				FIED2.PTUVR	0.63 ÷ 0.46	2.03
CG	FIED1.PTOCG1	2.86	0.13	DIED0.PTOCQR1	2.9	0.53
	DIEDx.PTUV1	0.4	0.2	DIEDy.PTUV1	0.77 ↘ 0.25	0.73
				FIED2.PTOVQR	0.04 ↗ 0.32	2.03
F4 (at the end of LV feeder 1 backbone)						
AG	FIED1.PTOCG1	2.86	0.13	DIED0.PTOCQR1	0.8	0.53
	DIED3.PTUV1	0.42	0.2	DIEDy.PTUV1	0.88 ↘ 0.5	0.73
	DIED4.PTUV1	0.42	0.2	FIED2.PTUVR	0.86 ↘ 0.3	2.03
	DIED5.PTUV1	0.22	0.2			
	DIED6.PTUV1	0.22	0.2			
	DIED7.PTUV1	0.11	0.2			
	DIED1.PTUV1	0.65 ↘ 0.27	0.33			
	DIED2.PTUV1	0.65 ↘ 0.28	0.33			

Appendix H

MV distribution protection

Table H.1 – Operated functions and corresponding operation times under solid fault conditions at different locations for MV protection

(1)*	Primary protection			Backup protection		
	(2) [†]	(3) [‡]	(4)**	(2)	(3)	(4)
F1 (inside PV installation)						
ABC	DIED1.PTOCPF	3384	0.03	FIED1.PTOCPF1	3021	0.13
				DIED2.PTUV1	0.09	0.2
AB	DIED1.PTOCQF	1688	0.03	FIED1.PTOCQF1	1517	0.13
				DIED2.PTUV1	0.41	0.2
BCG	DIED1.PTOCQF	1658	0.03	FIED1.PTOCQF1	1517	0.13
				DIED2.PTU1	0.12	0.2
CG	DIED1.PTOCG	98	0.03	FIED1.PTOCG1	89	0.13
				DIED2.PTUV1	0.02	0.2
F3 (at the end of Feeder 1)						
ABC	FIED1.PTOCPF1	2667	0.13	CIED3.PTUVR1	0.28	0.43
	DIED1.PTUV1	0.34	0.2	BIED.PTOCPF	2453	0.5
	DIED2.PTUV1	0.22	0.2	FIED2.PTUVR	0.27	0.7
	CIED3.PTUVR1	0.24	Locked			
AC	FIED1.PTOCQF1	1327	0.13	CIED3.PTOVQR2	0.42	0.43
	DIED1.PTUV1	0.42	0.2	BIED.PTOCQF	1207	0.5
	DIED2.PTUV1	0.42	0.2	FIED2.PTOVQR	0.38	0.7
	CIED3.PTUVR1	0.42	Locked			
ABG	FIED1.PTOCG1	44.3	0.13	CIED3.PTOVQR1	0.42	0.43
	DIED1.PTUV1	0.18	0.2	BIED.PTOCQF	1182	0.5
	DIED2.PTUV1	0.17	0.2	FIED2.PTOVQR	0.37	0.7
	CIED.PTUVR1	0.25	Locked			
BG	FIED1.PTOCG1	86.5	0.13	CIED3.PTUVR1	0.06	0.43
	DIED1.PTUV1	0.06	0.2	BIED.PTOCG	86.6	0.5
	DIED2.PTUV1	0.05	0.2	FIED2.PTUVR	0.06	0.7
	CIED3.PTUVR1	0.06	Locked			
F6 (at the beginning of Feeder 2)						
ABC	FIED2.PTOCPF1	3480	0.13	DIED1.PTUV1	0.12	0.2

Continued on next page

Table H.1 – continued from previous page

(1)	Primary protection			Backup protection		
	(2)	(3)	(4)	(2)	(3)	(4)
	CIED3.PTUVR1	0.02	0.13	DIED2.PTUV1	0.01	0.2
				CIED1.PTUVR1	0.02	0.33
				CIED2.PTUVR1	0.01	0.33
				BIED.PTOCPF	3132	0.5
				FIED1.PTUVR	0.01	0.7
BC	FIED2.PTOCQF1	1729	0.13	CIED1.PTOVQR1	0.48	0.33
	CIED3.PTOVQR1	0.48	0.13	CIED2.PTOVQR1	0.48	0.33
				BIED.PTOCQF	1534	0.5
				FIED1.PTOVQR	0.48	0.7
				DIED1.PTUV2	0.48 ↗ 0.86	Untrip
				DIED2.PTUV2	0.48 ↗ 0.86	Untrip
				DIED1.PTOF1	51.8	2.5
				DIED2.PTOF1	51.8	2.5
ABG	FIED2.PTOCQF1	1714	0.13	CIED1.PTOVQR1	0.48	0.33
	CIED3.PTOVQR1	0.48	0.13	CIED2.PTOVQR1	0.48	0.33
				BIED.PTOCQF	1527	0.5
				FIED1.PTOVQR	0.48	0.7
				DIED1.PTUV2	0.48 ↗ 0.86	Untrip
				DIED2.PTUV2	0.48 ↗ 0.86	Untrip
				DIED1.PTOF1	52.17	2.5
				DIED2.PTOF1	52.17	2.5
CG	FIED2.PTOCGF1	90.9	0.13	DIED1.PTUV1	0.01	0.2
	CIED3.PTUVR1	0.01	0.13	DIED2.PTUV1	0.01	0.2
				CIED1.PTUVR1	0.02	0.33
				CIED2.PTUVR1	0.02	0.33
				BIED.PTOCG	236	0.5
				FIED1.PTOVQR	0.49	0.7
F7 (Busbar fault)						
ABC	BIED.PTOCPF	3510	0.5	TIED2.PTOCP	3510	0.7
	CIED1.PTUVR1	0.05	0.13	FIED1.PTUVR	0.03	0.7
	CIED2.PTUVR1	0.04	0.13	FIED2.PTUVR	0.03	0.7
	CIED3.PTUVR1	0.04	0.13			
	DIED1.PTUV1	0.04	0.2			
	DIED2.PTUV1	0.04	0.2			
AC	BIED.PTOCQF	174	0.5	TIED2.PTOCP	1723	0.7
	CIED1.PTOVQR1	0.47	0.13	FIED1.PTOVQR	0.47	0.7
	CIED2.PTOVQR1	0.48	0.13	FIED2.PTOVQR	0.47	0.7
	CIED3.PTOVQR1	0.48	0.13			
	DIED1.PTOF1	52.17	0.2			
	DIED2.PTOF1	52.17	0.2			
BG	BIED.PTOCG	238	0.5	TIED2.PTOCG	238	0.7

Continued on next page

Table H.1 – continued from previous page

(1)	Primary protection			Backup protection		
	(2)	(3)	(4)	(2)	(3)	(4)
	CIED1.PTUVR1	0.05	0.13	FIED1.PTOVQR	0.03	0.7
	CIED2.PTUVR1	0.05	0.13	FIED2.PTOVQR	0.03	0.7
	CIED3.PTUVR1	0.05	0.13			
	DIED1.PTUV1	0.04	0.2			
	DIED2.PTUV1	0.04	0.2			

*Fault type

†Function that trips

‡Measured values protection criterion

§"x" denotes all PV systems connected to LV feeder 1

||"y" denotes all PV systems connected to LV feeder 2

**Operation time that is counted from the instant of fault inception

‡‡Representing the change in protection criterion values after a certain function operates

Table H.2 – Operated functions and corresponding operation times under fault conditions with $R_f = 5 \Omega$ at different locations for MV protection

(1)*	Primary protection			Backup protection		
	(2) [†]	(3) [‡]	(4)**	(2)	(3)	(4)
F1 (inside PV installation)						
ABC	DIED1.PTOCPF	1593	0.03	FIED1.PTOCPF1	1431	0.13
				CIED1.PTUVR1	0.73 ↘ 0.1	0.26
				CIED2.PTUVR1	0.75 ↘ 0.1	0.26
				DIED2.PTUV1	0.74 ↘ 0.1	0.33
AB	DIED1.PTOCPF	1991	0.03	FIED1.PTOCQF1	1031	0.13
				CIED1.PTOVQR1	0.9 ↘ 0.49	0.26
				CIED2.PTOVQR2	0.89 ↘ 0.46	0.26
				DIED2.PTUV1	0.89 ↘ 0.45	0.33
BCG	DIED1.PTOCPF	1419	0.03	FIED1.PTOCQF1	703	0.13
				DIED2.PTUV1	0.68 ↘ 0.12	0.33
CG	DIED1.PTOCG	81.3	0.03	FIED1.PTOCG1	81.4	0.13
				DIED2.PTUV1	0.12	0.2
F3 (at the end of Feeder 1)						
ABC	FIED1.PTOCPF1	1346	0.13	CIED3.PTUVR2	0.75	0.5
	CIED1.PTOVQR1	0.26	0.13	BIED.PTOCPF	1361	0.5
	CIED2.PTOVQR2	0.31	0.13	FIED2.PTUVR	0.75	Untrip
	DIED1.PTUV1	0.75 ↘ 0.11	0.33			
	DIED2.PTUV1	0.74 ↘ 0.12	0.33			
AC	FIED1.PTOCQF1	930	0.13	CIED3.PTOVQR1	0.26	0.33
	CIED1.PTOVQR1	0.26	0.13	BIED.PTOCQF	678	0.5
	CIED2.PTOVQR2	0.31	0.13	FIED2.PTOVQR	0.26 ↗ 0.37	0.7
	DIED1.PTUV1	0.88 ↘ 0.42	0.33			
	DIED2.PTUV1	0.88 ↘ 0.44	0.33			
ABG	FIED1.PTOCQF1	658	0.13	CIED3.PTOVQR1	0.19	0.33
	CIED1.PTOVQR1	0.19	0.13	BIED.PTOCQF	658	0.5
	CIED2.PTOVQR2	0.22	0.13	FIED2.PTOVQR	0.19 ↗ 0.36	0.7
	DIED1.PTUV1	0.69 ↘ 0.14	0.33			
	DIED2.PTUV1	0.69 ↘ 0.14	0.33			
BG	FIED1.PTOCGF1	71	0.13	CIED3.PTOVQR1	0.14	0.33
	CIED1.PTOVQR1	0.14	0.13	BIED.PTOCGF	71.3	0.5
	CIED2.PTOVQR2	0.14	0.13	FIED2.PTUVR	0.14	0.7
	DIED1.PTUV1	0.14	0.2			
	DIED2.PTUV1	0.14	0.2			
F6 (at the beginning of Feeder 2)						
ABC	FIED2.PTOCPF1	1621	0.13	BIED.PTOCPF	1499	0.5
	CIED3.PTUVR1	0.14	0.13	CIED1.PTUVR1	0.74 ↘ 0.23	0.63
				CIED2.PTUVR2	0.74 ↘ 0.23	0.63
				DIED1.PTUV1	0.74 ↘ 0.22	0.7

Continued on next page

Table H.2 – continued from previous page

(1)	Primary protection			Backup protection		
	(2)	(3)	(4)	(2)	(3)	(4)
				DIED2.PTUV1	0.74 ↘ 0.22	0.7
				FIED2.PTUVR	0.74 ↘ 0.23	1.2
BC	FIED2.PTOCQF1	1156	0.13	CIED1.PTOVQR1	0.32	0.33
	CIED3.PTOVQR1	0.32	0.13	CIED2.PTOVQR2	0.32	0.3
				BIED.PTOCQF	1021	0.5
				FIED2.PTOVQR	0.32	0.7
				DIED1.PTUV2	0.87 ↘ 0.5	1.7
				DIED2.PTUV2	0.87 ↘ 0.5	1.7
BCG	FIED2.PTOCQ1F	1398	0.13	CIED1.PTOVQR2	0.22	0.33
	CIED3.PTOVQR2	0.22	0.13	CIED2.PTOVQR2	0.22	0.33
				BIED.PTOCQF	680	0.5
				FIED2.PTOVQR	0.22	0.7
				DIED1.PTUV2	0.67 ↘ 0.22	0.7
				DIED2.PTUV2	0.67 ↘ 0.22	0.7
CG	FIED2.PTOCG1	82.5	0.13	CIED1.PTUVQR1	0.1	0.33
	CIED3.PTUVR1	0.1	0.13	CIED2.PTOVQR1	0.1	0.33
				BIED.PTOCG	82.5	0.5
				FIED2.PTUVR	0.11	0.7
F7 (Busbar fault)						
ABC	BIED.PTOCPF	1584	0.5	TIED2.PTOCP	1584	0.7
	CIED1.PTUVR1	0.72 ↘ 0.22	0.63	FIED1.PTUVR	0.72 ↘ 0.22	1.4
	CIED2.PTUVR1	0.72 ↘ 0.22	0.63	FIED2.PTUVR	0.72 ↘ 0.22	1.4
	CIED3.PTUVR1	0.72 ↘ 0.22	0.63			
	DIED1.PTUV2	0.72 ↘ 0.22	0.7			
	DIED2.PTUV2	0.72 ↘ 0.22	0.7			
AB	BIED.PTOCQF	1872	0.5	TIED2.PTOCQ	1872	0.7
	CIED1.PTOVQR1	0.33	0.13	FIED1.PTOVQR	0.33	0.7
	CIED2.PTOVQR1	0.33	0.13	FIED2.PTOVQR	0.33	0.7
	CIED3.PTOVQR1	0.33	0.13			
	DIED1.PTUV2	0.88 ↘ 0.5	1.7			
	DIED2.PTUV2	0.88 ↘ 0.5	1.7			
ACG	BIED.PTOCQF	1306	0.5	TIED2.PTOCQ	1306	0.7
	CIED1.PTOVQR1	0.22	0.13	FIED1.PTOVQR	0.22	0.7
	CIED2.PTOVQR1	0.22	0.13	FIED2.PTOVQR	0.22	0.7
	CIED3.PTOVQR1	0.22	0.13			
	DIED1.PTUV1	0.66 ↘ 0.21	0.7			
	DIED2.PTUV1	0.66 ↘ 0.21	0.7			
CG	BIED.PTOCGF	82.5	0.5	TIED2.PTOCQ	82.6	0.7
	CIED1.PTOVQR1	0.11	0.13	FIED1.PTUVR	0.11	0.7
	CIED2.PTOVQR1	0.11	0.13	FIED2.PTUVR	0.11	0.7
	CIED3.PTOVQR1	0.11	0.13			

Continued on next page

Table H.2 – continued from previous page

(1)	Primary protection			Backup protection		
	(2)	(3)	(4)	(2)	(3)	(4)
	DIED1.PTUV1	0.11	0.2			
	DIED2.PTUV1	0.11	0.2			

*Fault type

†Function that trips

‡Measured values protection criterion

§"x" denotes all PV systems connected to LV feeder 1

|| "y" denotes all PV systems connected to LV feeder 2

**Operation time that is counted from the instant of fault inception

‡#Representing the change in protection criterion values after a certain function operates

Appendix I

Overview of the IEC 61850 standard

I.1 General overview of the standard

The first version of IEC 61850 consisted of 14 different parts which can be divided into 5 main aspects including (i) System aspects: Parts 1 to 5, (ii) Configuration: Part 6, (iii) Abstract data models and communication services: Parts 7-1 to 7-4, (iv) Communication mappings: Part 8-1, 9-1 and 9-2, and (v) Testing: Part 10. The names of these above Parts are provided in Table I.1. For better illustrating the realization process of the IEC 61850 standard, the parts in this standard are divided into 4 fundamental aspects as shown in Figure I.1:

- 1 **Data model:** all data available within a substation area are virtualized by using data models. Example: tripping signals, measurements, Circuit Breaker (CB) status;
- 2 **Services:** specifies methods of using data from the data model. Example: coordination of tripping signals from the sending Intelligent Electronic Devices (IED) for inter-trip, consult of circuit breaker position, control of circuit breaker;
- 3 **Network:** a selection of communication protocols for transmitting the services and data to a real communication network;
- 4 **Configuration:** defines description files needed for the configuration process.

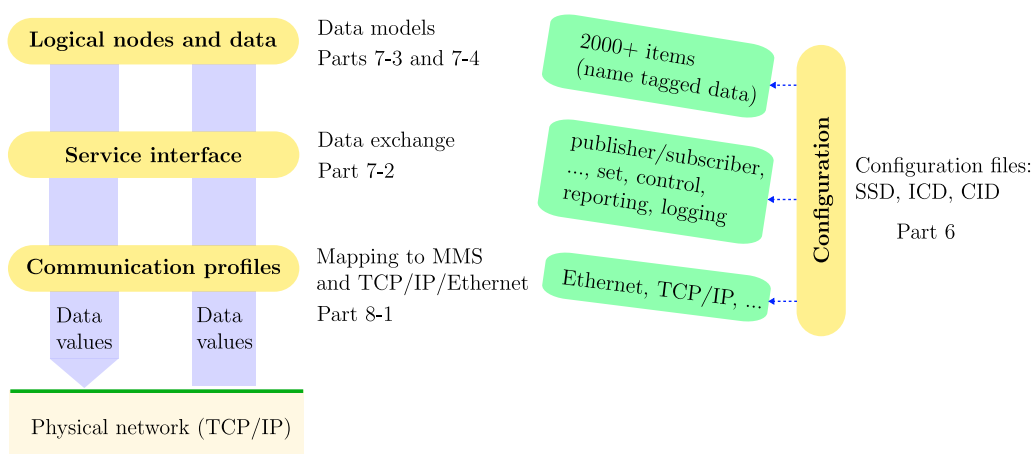


Figure I.1 – IEC 61850 realization process

Parts 3, 4, and 5 of the standard were initiated by identifying the general and specific functional requirements for communication in a substation. These requirements are then deployed to identify the necessary services and data models, the required application protocol, and the under-

Table I.1 – Parts of IEC 61850 standard

System aspects		Data Models	
Part 1:	Introduction and Overview	Part 7-3:	Common Data Classes
Part 2:	Glossary	Part 7-4:	Compatible Logical Node Classes and Data Classes
Part 3:	General requirements	Abstract communication services	
Part 4:	System and project management	Part 7-1:	Principles and Models
Part 5:	Communication requirements for function and device models	Part 7-2:	Abstract Communication Services (ACSI)
Configuration		Testing	
Part 6:	Configuration Language for electrical Substation IEDs	Part 10:	Conformance Testing
Mapping to real Comm. Networks			
Part 8-1:	Mapping to MMS and ISO/IEC 8802-3		
Part 9-1:	Sampled Values over Serial Unidirectional Multidrop Point-to-Point link		
Part 9-2:	Sampled Values over ISO/IEC 8802-3		

lying communication infrastructure that meet the general requirements. Then, based on Part 5, the data models, including logical nodes and data, are described in Parts 7-3 and 7-4, and the interfaces of the communication services for the use of data are defined in Part 7-2. The mapping of the services described in Part 7 to actual communication networks is presented in Parts 8 and 9. In particular, Part 8-1 defines the mapping of the data object and services to the Manufacturing Messaging Specification-MMS2, and Parts 9-1 and 9-2 describe the mapping of the sample values-SV of the measurement data to an Ethernet data frame. As a considerable number of configurations are required to manage all the relevant components, an XML-based substation configuration language to facilitate the configuration process and minimize human error is introduced in Part 6. Since the first edition, IEC 61850 has been extended, and several new parts have been added.

I.2 Data modeling in IEC 61850

As shown in Figure I.1, data modeling is the first step in the implementation of IEC 61850. IEC 61850 is based on the idea of virtualization for data model design. All data available in a real device within a substation is transformed into a virtual world and defined in the standard. A device model in IEC 61850 is started with a physical device that connects to a real communication network. The physical device is the highest level that is normally identified by its given network address. Several logical devices, for example, IEDs, may be located within a physical device. This subdivision makes it possible to organize the data according to their applications. Each logical device can incorporate several different functions or applications called **Logical Node (LN)**s. A set of **LN** necessary for the study is provided in Table 2.2

Depending on their functionality, A **LN** contains a list of data objects related to the purpose of the power system, which is defined in part 7-4. For example, as shown in Figure I.2, CB1 is represented by an **LN** named XCBR1, where the suffix 1 is used as the instance ID of the **LN**. The logic node XCBR1 contains various data objects, e.g., *Pos*, to indicate the status of the CB contact position, *OpCnt*, to count the number of operations.

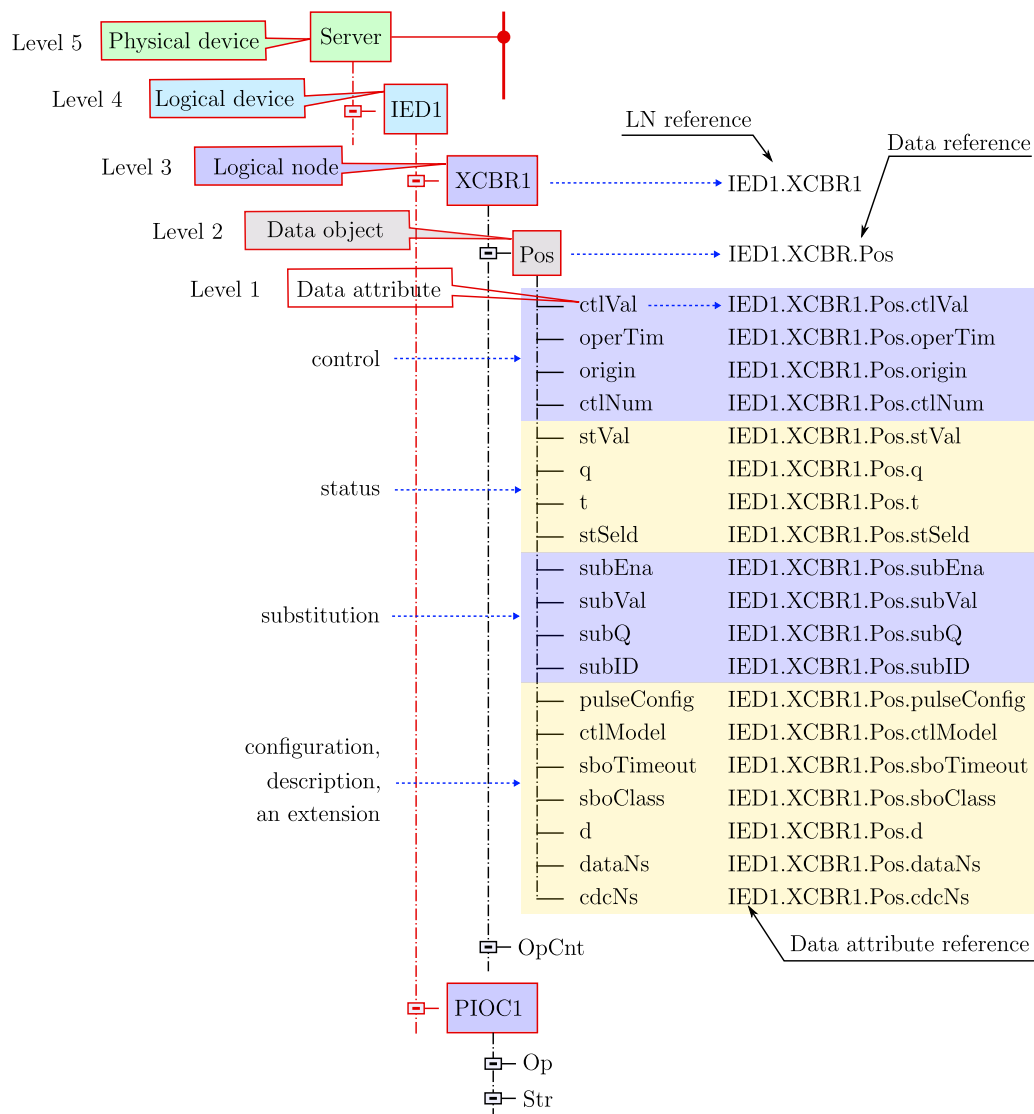


Figure I.2 – A IEC 61850-based circuit breaker model

Each data object in the LN is assigned to a dedicated CDC, specified in part 7-3. A CDC defines the type and structure of the data in the LN. There are 7 dedicated CDC specifications for status information, measurand information, controllable status information, status settings, analogue settings and description information. For example, the *Pos* data object of the XCBBR1 LN in Figure I.2 is confined to the CDC named "Dual Controllable Point - DPC" which is shown in Figure I.3, [199].

Figure I.3 shows that the DPC class is composed of a group of data attributes characterized by a defined name, defined type, and particular functionality. Each data attribute belongs to a data attribute type sorted into functional constraints - FC. For instance, those data attributes of the DPC class are categorized into 5 groups, including control attribute - CO, status attribute - ST, substituted value attribute - SV, configuration attribute, description attribute - DC, and extended attribute - EX. In this example, the control data attribute of the DPC class constitutes control value (*ctlVal*), operating time (*TimeStamp*), originator that causes the change of control value (*Originator*), and *ctlNum* attribute indicating its possible values.

DPC class					
Attribute Name	Attribute Type	FC	TrgOp	Value/Value Range	M/O/C
DataName	Inherited from Data Class (see IEC 61850-7-2)				
DataAttribute					
<i>control and status</i>					
ctlVal	BOOLEAN	CO		off (FALSE) on (TRUE)	AC_CO_M
operTm	TimeStamp	CO			AC_CO_O
origin	Originator	CO, ST			AC_CO_O
ctlNum	INT8U	CO, ST		0..255	AC_CO_O
stVal	CODED ENUM	ST	dchg	intermediate-state off on bad-state	M
q	Quality	ST	qchg		M
t	TimeStamp	ST			M
stSeld	BOOLEAN	ST	dchg		AC_CO_O
<i>substitution</i>					
subEna	BOOLEAN	SV			PICS_SUBST
subVal	CODED ENUM	SV		intermediate-state off on bad-state	PICS_SUBST
subQ	Quality	SV			PICS_SUBST
subID	VISIBLE STRING64	SV			PICS_SUBST
<i>configuration, description and extension</i>					
pulseConfig	PulseConfig	CF			AC_CO_O
ctlModel	CtlModels	CF			M
sboTimeout	INT32U	CF			AC_CO_O
sboClass	SboClasses	CF			AC_CO_O
d	VISIBLE STRING255	DC		Text	O
dU	UNICODE STRING255	DC			O
cdcNs	VISIBLE STRING255	EX			AC_DLNDA_M
cdcName	VISIBLE STRING255	EX			AC_DLNDA_M
dataNs	VISIBLE STRING255	EX			AC_DLN_M
Services					
As defined in Table 31					

Figure I.3 – Controllable double point

Therefore, the IEC 61850 model of a device is a virtual representation starting with an abstract description of the device and its objects, and is defined in Parts 7-3, 7-4, and 7-2. This abstract model is then mapped to a specific protocol stack specified in Part 8-1, e.g., MMS, TCP/IP, and Ethernet. In the process of mapping the IEC 61850 objects to MMS, IEC 61850-8-1 specifies a method of transforming the model information into a named MMS variable object that results in a unique and unambiguous reference for each piece of information in the model. Consider logical device CB1 in Figure I.2 containing an LN XCBR1. If we would consult the status value of the CB1 position, we should refer to the data object with the reference name shown in Figure I.4.

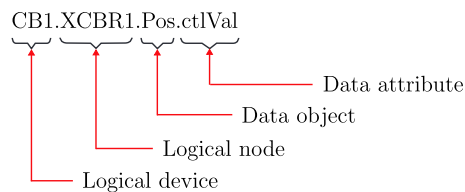


Figure I.4 – A structure of an IEC 61850-based object name

